DISCLAIMER

ANL/NSE-25/71
INL/RPT-25-88160

Argonne NATIONAL LABORATORY

Integrated Molten Salt Reactor Modeling Capabilities in NEAMS Thermal Hydraulics Tools

Nuclear Science & Engineering Division

ANL/NSE-25/71
INL/RPT-25-88160

Integrated Molten Salt Reactor Modeling Capabilities in NEAMS Thermal Hydraulics Tools

prepared by

Travis Mui, Daniel O'Grady, Thanh Hua, Andrés Nicolás Fierro López, Ling Zou, Rui Hu

Nuclear Science and Engineering Division, Argonne National Laboratory

Mauricio Tano, Ramiro Freile, Victor Coppo Leite, David Reger, Mengnan Li, Joshua Hansel, Guillaume Giudicelli, Lise Charlot, Mustafa K. Jaradat

Idaho National Laboratory

Robert Salko

Oak Ridge National Laboratory

September 2025

ABSTRACT

The DOE Nuclear Energy Advanced Modeling and Simulation (NEAMS) program supports a full range of computational thermal fluids analysis capabilities and code developments for a broad range of advanced reactor concepts. The research and development approach under the thermal fluids technical area synergistically combines three length and time scales in a hierarchical multi-scale approach. To enable multi-scale thermal fluids capability using these codes, a key joint effort has been underway to develop an integrated system- and engineering-scale thermal fluids analysis capability, through integration of SAM and Pronghorn codes, both based on the MOOSE framework.

This report summarizes recent advances in developing an integrated system- and engineering-scale modeling capability for the molten salt reactor (MSR) concept, which has gained significant interest in recent years. A consistent framework was established by coupling Pronghorn and SAM through the Saline interface, with thermophysical properties provided by the Molten Salt Thermal Properties Database-Thermophysical (MSTDB-TP). Further improvements were made to the coupling schemes and domain-overlapping strategies, enhancing the stability and robustness of multi-code simulations. Verification and validation efforts demonstrate the accuracy of this integration across a range of benchmark problems, including one-dimensional heated pipe flows, three-dimensional natural convection loops with evolving isotopic compositions, and molten salt reactor experiment (MSRE) demonstration cases.

Within Pronghorn, new capabilities were introduced to model corrosion and noble-metal plating phenomena, supported by an extended thermal-hydraulics framework and refined turbulence treatments. To capture two-phase flow behavior, a multiphase Euler–Euler model was implemented in Pronghorn, including advanced closure relations, high-resolution advection techniques, and capillary force reconstruction. Preliminary verification cases confirm the fidelity of the approach, while planned validation efforts target canonical multiphase benchmarks and application to MSR components such as the MSRE pump bowl.

Finally, updates to SAM's MSR mass transfer modeling were extended to consider noble gas migration into porous structures like graphite. The point kinetics model was updated to include reactivity feedback contributions from any defined species, such as xenon. The gas transport model was expanded for applicability to gas mixtures, bubble efflux phenomena, and species transport between liquid and gas phases. A selection of multi-scale Sherwood number correlations from MOSCATO/NekRS and multi-phase correlations from literature have been added for improved accuracy in calculating mass transfer coefficients. A companion effort on developing system-level redox corrosion has also been incorporated into SAM. Collectively, these enhancements strengthen the predictive capability of SAM and Pronghorn for simulating MSR thermal-hydraulics, corrosion, multiphase behavior, and fission-product transport, providing a more complete toolset for design, safety analysis, and licensing support of next-generation MSRs.

Contents

List of Figures

List of Tables

1 Introduction

1.1 Multiscale thermal fluid modeling

The design and safety analysis of advanced nuclear reactors, including MSR, often involves predicting complex thermal-fluid (T-F) phenomena that occur in various reactor components. Accurately and efficiently predicting such phenomena for long transients remains a key challenge for reactor safety analysis. System thermal hydraulics codes have been traditionally the main workhorse to support reactor design and licensing efforts. These fast-running system analysis tools can provide integrated modeling capabilities to simulate whole system behavior under the simultaneous occurrence of various phenomena and processes. It can provide a wide range of analyses for iterative reactor design optimizations, prototypical conditions for fuels and materials qualification testing, safety analyses in reactor licensing, and can help identify key areas for designers, code developers, and the regulator for additional R&D work where the most progress is needed.

Higher-fidelity modeling and simulation tools, on the other hand, can take advantage of advances in computing power and modern algorithms for solving more complex systems of equations to enable multi-dimensional, closer-to-first-principles solutions. Computational Fluid Dynamics (CFD) methods have proven to be a powerful tool for nuclear applications to complement traditional systems analyses, with improved accuracy. These capabilities can also facilitate a more detailed understanding of the phenomena and reduce the uncertainties in conventional system analysis tools.

The DOE NEAMS program supports a full range of computational thermal fluids analysis capabilities for a broad class of light-water and advanced reactor concepts. The research and development approach under the thermal fluids technical area synergistically combines three length and time scales in a hierarchical multi-scale approach. These three overlapping thermal-fluid scales are defined across all reactor concepts as:

- *Lower Length Scale*: The Lower Length Scale focuses upon resolving the high-resolution physics associated with single and multi-phase, highly turbulent fluid flow and heat transfer with highly resolved thermal boundary layers.
- *Engineering Length scale*: The Engineering Length Scale includes coarse mesh approaches for homogenized multi-dimensional conjugate heat transfer (CHT), such as those found in gas-cooled or salt-cooled pebble-bed reactors, or subchannel capabilities tightly coupled to nuclear fuels performance.
- *System Scale*: System Scale analysis for nuclear reactors is composed of one-dimensional fluid flow pipe networks and zero-dimensional system components, used for steady-state and transient T/F analysis at the full power plant level. These reduced-order systems rely heavily on empirical correlations or models, as many of the flow features and phenomena are no longer resolved.

The connections between different scales and codes can be illustrated in Figure 1.1. At the lower length scale, Nek5000/NekRS will be used to investigate flow patterns and heat transfer for specific reactor components and operating conditions. Constitutive models such as turbulence models, heat transfer or friction correlations can be derived based on lower-length scale simulations and used in the engineering-scale or system-scale simulations. At the engineering length scale, Pronghorn

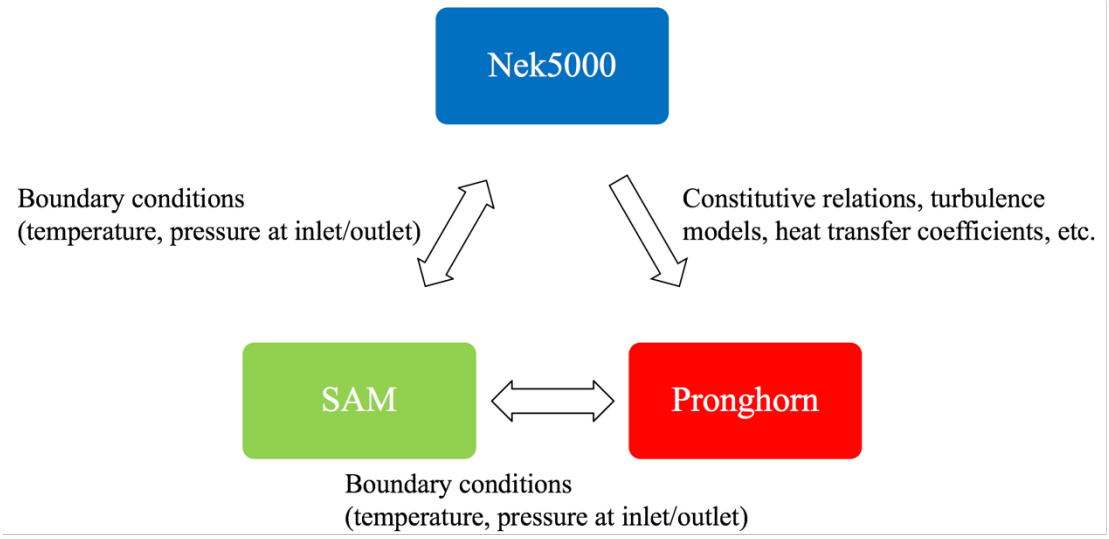

Figure 1.1: Multi-scale integration of Nek5000, Pronghorn and SAM for advanced reactor applications

can be used to model the reactor core or other key reactor components using a coarse-grid CFD approach. Finally, at the reactor plant length scale, SAM will be used to investigate the whole-plant behavior during steady-state operation and transients, which can be coupled with Nek5000/NekRS or Pronghorn when detailed simulations are needed for any specific components or subsystems. Using the Idaho National Laboratory (INL)'s Multi-physics Object-Oriented Simulation Environment (MOOSE) framework, and its MultiApps and Transfers features in particular, multiple space and time scales can be solved simultaneously to achieve a tightly coupled, converged solution. Being able to couple these codes for multi-scale thermal-fluids modeling and simulation is viewed as a critical objective for reactor vendors in the design optimization process towards commercialization.

In recent years, there has been a renewed interest in MSR technology in the development of future advanced nuclear reactors. To support the development and utilization of the NEAMS codes for MSR safety analysis and licensing, continuous efforts have been devoted to enhancing integrated code capabilities and updating reference models for the MSR designs. In a previous work [1], the integrated system- and engineering-scale thermal fluids analysis capability for MSR was developed using SAM-Pronghorn and demonstrated for transient simulations of a reference MSR. The steady state and transient SAM-Pronghorn coupled simulations results provided a successful demonstration of the utilized coupling approaches. However, future work was identified on the improvements in the robustness of the coupling schemes, specifically leveraging the domain overlapping approaches developed in SAM and NekRS coupling [2].

1.2 Pronghorn Overview

Pronghorn is a multidimensional, coarse-mesh, thermal-hydraulics (TH) code for advanced reactors. It serves the intermediate fidelity realm situated between detailed CFD analysis and lumped system models [3]. Pronghorn has successfully transitioned to the Finite Volume Method, recovering all capabilities previously developed with the Finite Element Method (FEM) [4]. The underlying

numerical method is implemented in MOOSE's Navier Stokes module [5], while reactor specifics closures are implemented and maintained in Pronghorn itself. The MOOSE Navier-Stokes module implements an incompressible, a weakly-compressible, and a fully compressible Finite Volume Method (FVM) formulation. For the weakly-compressible FVM formulation, it uses the Boussinesq approximation, a collocated grid and Rhie-Chow interpolation of variables on element faces. Pronghorn also has native support for scalar quantity advection. This is leveraged for precursor advection in molten salt reactors. It also has a corrosion model utilizing the Poisson-Nernst-Planck model for electrochemical species migration.

1.3 SAM Overview

SAM [6][7] is a modern system analysis tool under development at Argonne National Laboratory (ANL) for advanced non-glslwr reactor safety analysis. It aims to provide fast-running, modest-fidelity, whole-plant transient analyses capabilities, which are essential for fast turnaround design scoping and engineering analyses of advanced reactor concepts. While SAM is being developed as a system-level modeling and simulation tool, advanced modeling techniques being implemented include a reduced-order three-dimensional module [8] (which has been mostly moved into MOOSE's Navier Stokes module [5]), pseudo 3-D conjugate heat transfer modeling in reactor core [9], flexible and multi-scale modeling of heat transfer between fluid and structures [10], in addition to the advances in software environments and design, and numerical methods. Significant MSR modeling capabilities have been added to SAM in recent years, such as the reactor kinetics with the flowing fuel, species transport modeling, chemical interactions and corrosion modeling, etc.

This report summarizes FY25 progress in advancing integrated thermal-fluids analysis capabilities for MSRs using SAM and Pronghorn. Efforts focused on improving coupling schemes, incorporating advanced thermophysical property models, and expanding verification and demonstration cases relevant to reactor applications. Chapter 2 details the integration of the Saline thermophysical property interface, based on the MSTDB-TP, into both SAM and Pronghorn, with supporting verification examples. Chapter 3 presents the improved coupling scheme between SAM and Pronghorn, and the verification and demonstration of the coupled SAM–Pronghorn-Saline-based simulations of the MSRE. Chapter 4 introduces improvements in Pronghorn for corrosion and noble-metal plating models, supported by verification and reactor-scale demonstrations. Chapter 5 documents the implementation of two-phase Euler–Euler modeling in Pronghorn, with verification cases and a preliminary MSRE pump bowl study. Chapter 6 highlights updates to SAM's MSR mass transport and reactivity modeling capabilities, and Chapter 7 discusses the verification of the updated SAM capabilities and a system demonstration of integrated xenon transport and reactivity in the MSRE.

2 Pronghorn-Saline and SAM-Saline Integration Scheme using the Molten Salt Thermal Property Database for Thermophysical Properties

2.1 Brief description of Saline and the MSTDB-TP

Saline [11] is an API for MSTDB-TP thermophysical property data. It allows for the integration of density, viscosity, thermal conductivity, and heat capacity into client applications through a collection of classes and methods. Additionally, the Saline submodule in MOOSE introduces conversion functions between enthalpy and temperature through lookup tables for arbitrary temperature-dependent specific heat functions. This approach removes the necessity for users to manually specify the conversion functions between enthalpy and temperature. The interface is predominantly written in C++, and is accessed in MOOSE through the `FluidProperties` module [12] and its Saline application submodule [13].

2.2 Review of Saline integration in SAM

The Saline interface was first integrated into a MOOSE context in FY22 as a submodule and equation of state (EOS) interface in SAM, and was migrated upstream to the `FluidProperties` module [12] in FY23 to be made available to all MOOSE applications. SAM is able to calculate EOS properties through its internal library of fluids, through properties called from the `FluidProperties` module, or through the `SalineInterface` object which is still maintained in SAM but now relies on the Saline submodule being built as a dependency of the `FluidProperties` module [14]. `SalineInterface` also allows users to select from built-in models for surface tension for FLiBe and FLiNaK, which is used by the non-condensable gas transport model. Internal regression tests check that the EOS properties output by SAM match a custom Saline database property file by verifying against a separate Python script that directly calls Saline to compute and compare all EOS properties over a range of temperatures.

2.3 Integration of Saline into Pronghorn

Pronghorn and SAM both access Saline through the `SalineMoltenSaltFluidProperties`. This fluid properties object/class provides the following routines:

- `rho_from_p_T` : density computed using the local pressure and temperature
- `mu_from_p_T` : dynamic viscosity computed using the local pressure and temperature
- `k_from_p_T` : thermal conductivity computed using the local pressure and temperature
- `cp_from_p_T` : specific capacity computed using the local pressure and temperature
- `e_from_p_T` : specific internal energy computed using the local pressure and temperature
- `h_from_p_T` : specific enthalpy computed using the local pressure and temperature
- `T_from_p_h` : temperature computed using the local pressure and specific enthalpy

The first six functions are provided with two signatures: one simply computing the value and the other computing the value and the derivatives with regards to the inputs. The latter enables notably the use of these fluid properties with automatic differentiation. The nonlinear finite-volume discretization available in Pronghorn uses automatic differentiation.

The last routine (`T_from_p_h`) is notably used when using the enthalpy-based equation discretizations available in both the Semi-Implicit Method for Pressure Linked Equations (SIMPLE)-based and the nonlinear (Newton-based) solvers. The temperature is notably used to evaluate the other fluid properties, as the (pressure, specific enthalpy) variable set is not implemented for density, viscosity, thermal conductivity, etc.

In modeling nuclear reactor systems, the temperature dependency of the thermophysical properties is crucial to obtain accurate results. Low-Mach thermal-hydraulics phenomena with temperature-dependent thermophysical properties are modeled using weakly compressible formulations for the mass, momentum and energy conservation. Hence, density does not depend on pressure, and is evaluated at a reference pressure value. Nevertheless, the values for density, specific heat, thermal conductivity and viscosity depend on temperature and are obtained via the fluid properties object detailed above.

The conservation of mass (continuity equation) is given by Equation (2.1):

$$\frac{\partial \rho}{\partial t} + \frac{\partial (\rho u_i)}{\partial x_i} = 0 \tag{2.1}$$

where ρ is the density, u_i is the velocity component in the i-th direction, and x_i represents the spatial coordinates.

The conservation of momentum is described by Equation (2.2):

$$\frac{\partial (\rho u_i)}{\partial t} + \frac{\partial (\rho u_i u_j)}{\partial x_j} = -\frac{\partial p}{\partial x_i} + \frac{\partial}{\partial x_j}\left((\mu + \mu_t)\, \tau_{ij} \right) + F_i \tag{2.2}$$

where p is the pressure, $\tau_{ij} = \left(\frac{\partial u_i}{\partial x_j} + \frac{\partial u_j}{\partial x_i} - \frac{2}{3}\frac{\partial u_i}{\partial x_i} \right)$ is the fluid stress tensor, μ_t is the turbulent viscosity computed via a turbulence model representing the effects of the turbulent fluctuating scales on the mean flow, and F_i is the component of an external body force.

The conservation of internal energy is described by Equation (2.3):

$$\frac{\partial (\rho e)}{\partial t} + \frac{\partial (\rho e u_i)}{\partial x_i} = -p\frac{\partial u_i}{\partial x_i} + \tau_{ij} u_i + \frac{\partial}{\partial x_j}\left((\kappa + \kappa_t)\frac{\partial T}{\partial x_j} \right) + \dot{q}''' \tag{2.3}$$

where κ_t is the turbulent thermal conductivity computed via a turbulence model and q''' is the volumetric heat source.

The relationship between the internal energy of the system e and the specific enthalpy h is

$$h = e + \frac{p}{\rho}. \tag{2.4}$$

Replacing the definition of the specific enthalpy in Eq. (2.3), and neglecting viscous heating terms, leads to the enthalpy conservation equation:

$$\frac{\partial (\rho h)}{\partial t} + \frac{\partial (\rho h u_i)}{\partial x_i} = \frac{\partial}{\partial x_j}\left((\kappa + \kappa_t)\frac{\partial T}{\partial x_j} \right) + \dot{q}'''. \tag{2.5}$$

Furthermore, for low Mach number flows where the influence of pressure variations are negligible, the differential form of enthalpy in terms of the temperature in the system can be stated as

$$dh = c_p dT. \tag{2.6}$$

Through the relationship defined in Eq. (2.6), Eq. (2.5) becomes

$$\frac{\partial(\rho h)}{\partial t} + \frac{\partial(\rho h u_i)}{\partial x_i} = \frac{\partial}{\partial x_j}\left(\frac{(\kappa+\kappa_t)}{c_p}\frac{\partial h}{\partial x_j}\right) + \dot{q}'''. \tag{2.7}$$

which allows for an implicit formulation of the diffusive term when the variable to solve for is the enthalpy.

2.4 Verification and Validation Examples for Pronghorn-Saline integration

2.4.1 1D Heated Pipe Analytical Solution

The nonlinear (Newton-based) solver, solving for temperature, and the SIMPLE-based solver, solving for enthalpy, are both validated against a 1D analytical solution. The input files of the problem have been added to the MOOSE test suite.

The equation for the 1D advection problem with a volumetric heat source is given by

$$\dot{m}dh = \dot{m}c_p(T)dT = q'dx \tag{2.8}$$

where $c_p(T) = A + BT$, and q' is a linear source. Integration from the inlet to the outlet of the domain yields

$$\int_{T_{in}}^{T} \dot{m}c_p(T)dT = \int_0^L q'dx, \tag{2.9}$$

$$\dot{m}\left(AT + \frac{B}{2}T^2 - AT_{in} - \frac{B}{2}T_{in}^2\right) = q'L, \tag{2.10}$$

where $\dot{m}$ is the constant mass flow rate, T_{in} is the inlet temperature, and L is the length of the domain. Solving for temperature, the analytical solution for the outlet temperature is obtained:

$$T_{out} = \frac{1}{B}\left[-A + \sqrt{A^2 - 2B\cdot\left(\frac{-q'L}{\dot{m}} - AT_{in} - \frac{B}{2}T_{in}^2\right)}\right] \tag{2.11}$$

The parameters of the problem are ρ = 2000 kg/m^3, L = 30 m , $\dot{m}$ = 20 kg/s, T_{in} =860 K, A = 976.78 J/kg-K, and B = 1.0634 J/kg-K^2, where the specific heat corresponds to the FLiNaK fluid.

The analytical solution at the outlet is 899.2227 K, the simulation results for both the Newton temperature solver and the Segregated Linear enthalpy solver match the analytical solution within computational error. Figure 2.1 shows the axial temperature profile along the 1D domain for the Newton-temperature and Segregated-enthalpy solvers with the FLiNaK temperature dependent specific heat.

Table 2.1: Outlet temperature in the 1D domain for the analytical solution, the segregated solver, and the Newton solver.

Analytical solution	Newton solver solution	Segregated solver solution
899.2227 K	899.2227 K	899.2227 K

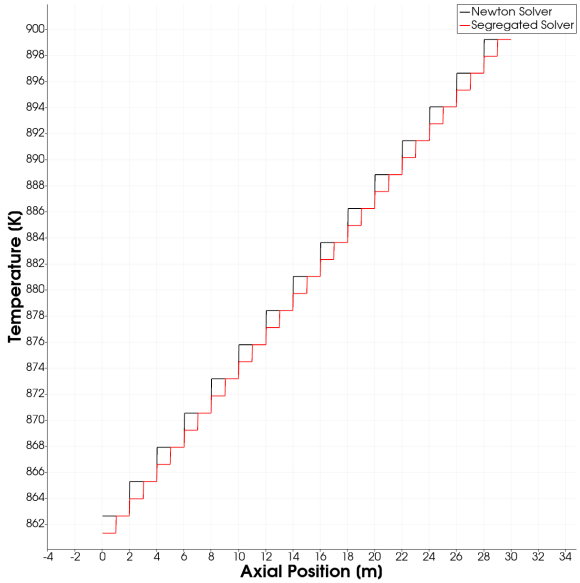

Figure 2.1: Axial temperature profile using the Newton and Segregated solver.

2.4.2 3D Natural convection loop with burnup-like varying composition of U-235

This section presents an additional feature of the Saline library. The MSTDB-TP contains comprehensive information on thermophysical properties as a function of the composition of each of its constituents. The power history of a MSR determines the evolution of species within the salt, influenced by factors such as the depletion of fissile material, leaching and plating on structures, and the corrosion of metal components, among others. These processes result in compositional changes to the working salt in MSRs. As the composition changes, the thermophysical properties can vary significantly, impacting modeling and simulation predictions. The `SalineFluidProperties` user object offers the flexibility to accommodate a time-dependent variable composition, enabling the coupling of thermal-hydraulics, depletion, and chemistry. Consequently, at different stages of the simulation, the thermophysical properties can be automatically recalculated based on the evolving composition of the working salt.

In this subsection, we evaluate the performance of a 3D natural convection loop using NaCl-UCl3 0.67-0.33 as the working salt. The computational domain is illustrated in Figure 2.2. A coarse mesh comprising 55,000 elements is utilized, with 11 radial divisions, 32 angular divisions (refer to Figure 2.2), and an axial aspect ratio of 4. The pipe has a diameter of 2 cm, with the heated and cooled sections each measuring 80 cm in height.

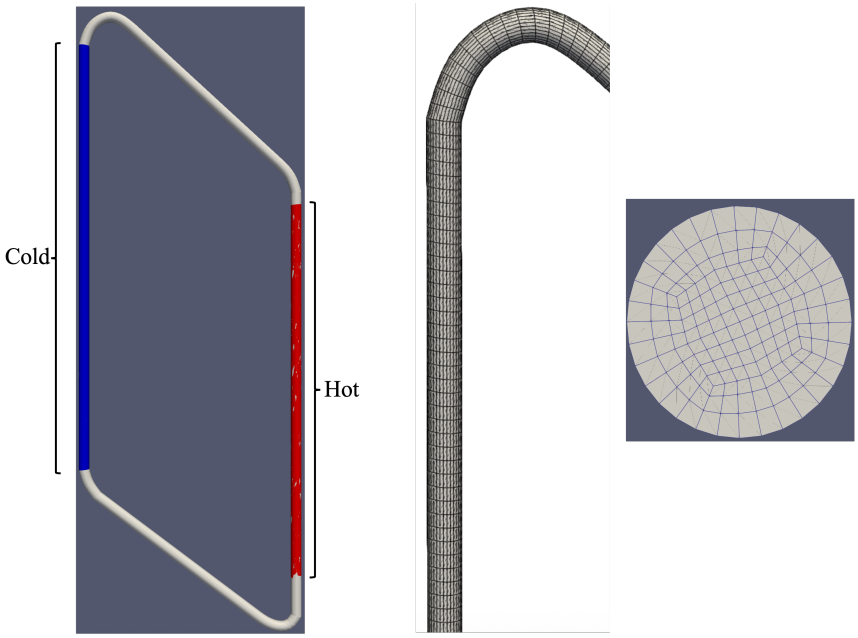

Figure 2.2: Computational domain of the natural convection loop. Loop domain including temperature boundary condition distribution (left). Top left section of computational mesh domain (center). Mesh sketch of the pipe radial section (right).

The PIMPLE solver is applied in conjunction with a generalized buoyancy model to account for the buoyancy force. The momentum equation term provided by the generalized buoyancy model is expressed as $(\rho - \rho_0)\vec{g}$, where ρ is obtained through Saline and ρ_0 represents the reference density. Boundary conditions for temperature are set at 890 K and 910 K for the cold and hot regions of the loop, respectively. No-slip conditions are enforced along the walls. Details regarding the PIMPLE solver, the generalized buoyancy model and a new formulation for pressure boundary conditions along the walls when body forces are present are given in [15].

Figure 2.3 presents the temperature distribution for NaCl-UCl3 0.67-0.33 in the natural convection loop, comparing results from Pronghorn with those obtained using Star-CCM+ on equivalent meshes for verification purposes. Additionally, Figure 2.4 illustrates the vertical velocity field distribution within the loop. In the loop, the salt is heated in the hot region of the vertical pipe, causing it to flow upward. Upon reaching the top region, it mixes to a uniform temperature before entering the cold region, where it cools and flows downward. The salt then remixes at the bottom before re-entering the hot region. An "annular-like" flow pattern is observed in the cold and hot regions of the loop, characterized by higher vertical velocity magnitudes near the walls within the temperature boundary layer, and lower velocities at the center of the pipe. The spatial distribution of flow between Pronghorn and Star-CCM+, including the annular-like flow regions and the mixing regions at the elbows, shows good agreement, indicating consistency between the two simulation tools.

Figure 2.5 compares the vertical velocity profiles obtained from Pronghorn and a reference CFD code as a function of the radial position at the exit of the heated region (left) and the exit of the cooled region (right). In both plots, the annular-like flow pattern is evident, with the vertical velocity peaking near the walls due to maximum buoyancy differences and approaching stagnation at the center of the pipe. The results from both codes show good agreement within the same computational

domain, with a total L2-error of 0.0031 m/s at the outlet of the cold leg and 0.0025 m/s at the outlet of the hot leg. Interestingly, the velocity at the center of the pipe is not only low in magnitude but also exhibits a reversal in direction. This phenomenon is observed in both Pronghorn and Star-CCM+. This detail is further illustrated in Figure 2.6, highlighting the complexity of the flow dynamics within the loop. This extra recirculation due to buoyancy effects contributes to the slight asymmetry of the velocity profile observed in Figure 2.5.

The salt used in the loop has an average Prandtl number of approximately 30, which is four times higher than that of water at atmospheric pressure and 293 K. Consequently, the thermal diffusivity is significantly lower than the momentum diffusivity. This disparity explains the annular flow observed in the heated and cooled regions of the loop. Due to the low thermal diffusivity towards the center of the pipe, the temperature in this region remains relatively unchanged. The temperature at the center is predominantly influenced by the bulk temperature resulting from the mixing at the top and bottom elbows of the loop, following the hot and cold outlet, respectively.

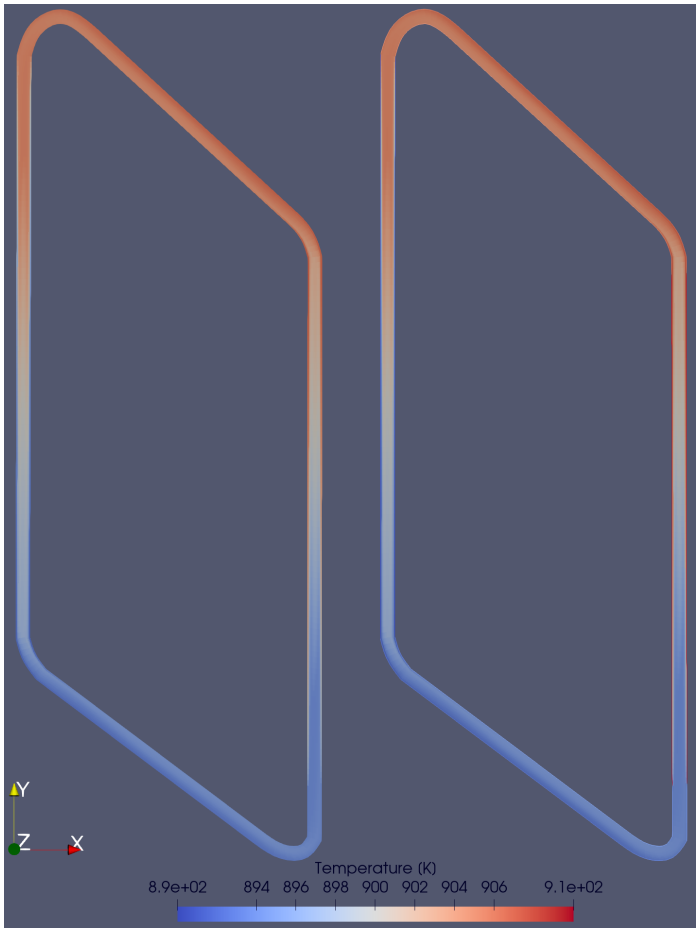

Figure 2.3: Temperature distribution at the midplane of the 3D molten salt loop. Pronghorn natural convection results (left), Reference CFD code results (right).

Next, we examine the effect of depletion in the natural convection loop case. Figure 2.7 depicts a simplified analysis used to obtain the evolution of the U-235 isotope as a result of burnup in a molten

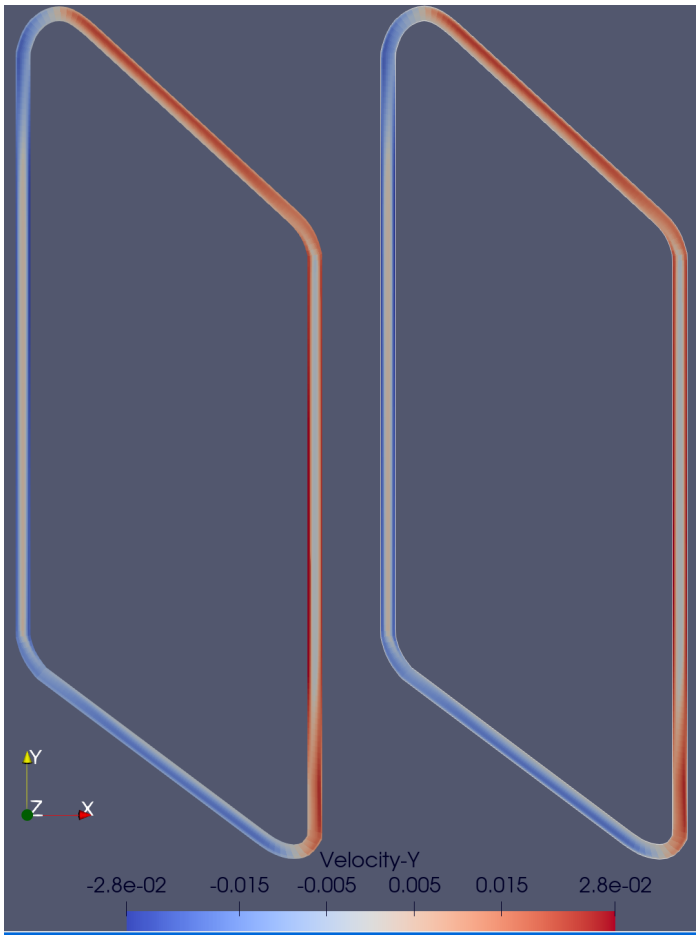

Figure 2.4: Vertical Velocity at the midplane of the 3D molten salt loop. Pronghorn natural convection results (left), Reference CFD code results (right).

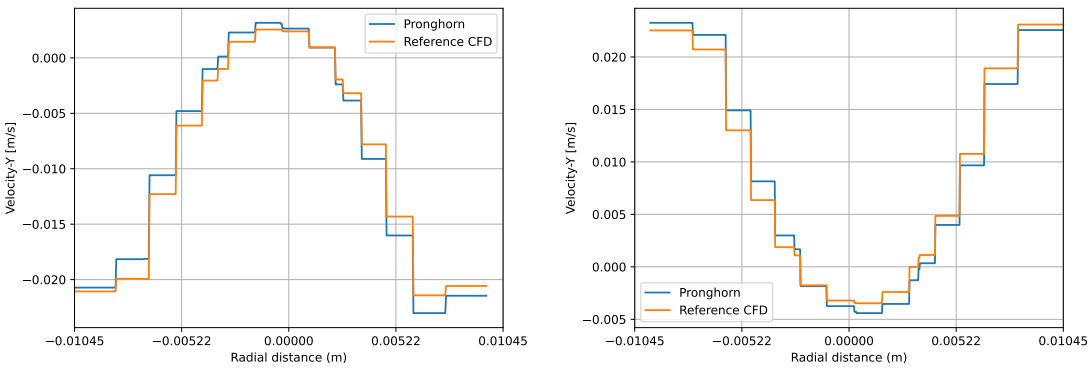

(a) Velocity-Y at the outlet of the cold leg.

(b) Velocity-Y at the outlet of the hot leg.

Figure 2.5: Vertical velocity comparisons between Pronghorn and the reference CFD code

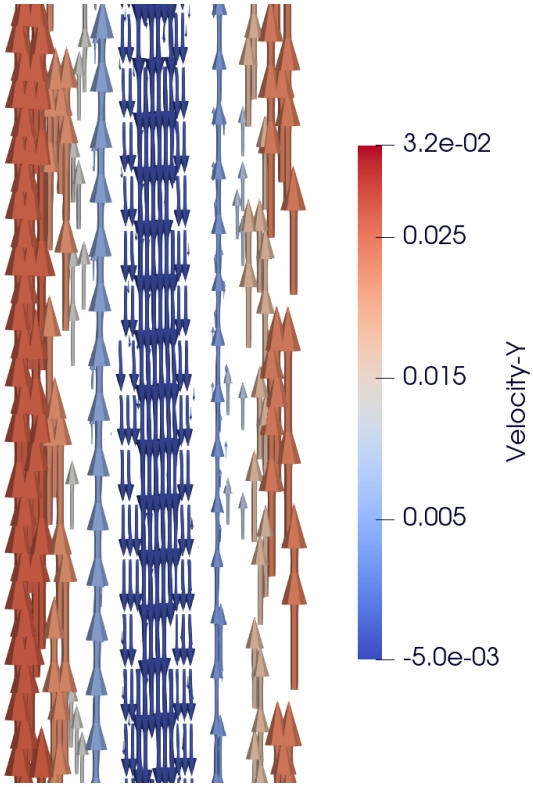

Figure 2.6: Vertical Velocity streamlines in the hot leg predicted by Pronghorn.

salt fuel reactor, assuming no refueling occurs during the power history of the MSR. Starting from an initial salt composition of NaCl-UCl3 0.67-0.33, the final U-235 composition is 0.28 at a burnup value of 150 MWd/kgU.

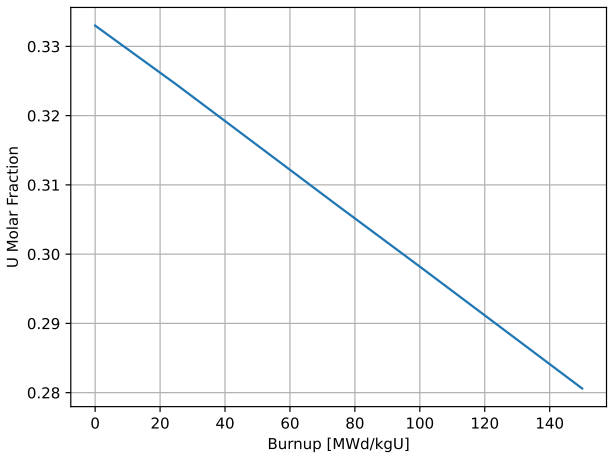

Figure 2.7: Uranium molar fraction evolution as a function of burnup from 0 to 150 MWd/kgU.

The MSTDB-TP contains thermophysical property data for the compositions 0.667-0.333, 0.7-0.3, and 0.716-0.284. Using a nearest neighbor algorithm, the appropriate salt composition is queried based on the evolving composition during the burnup process. This approach ensures that the thermophysical properties used in the simulations accurately reflect the changing composition of the salt mixture throughout the reactor's operation. Table 2.2 details the thermophysical properties for different compositions of NaCl-UCl3 used in the simulations.

Table 2.2: Approximate thermophysical properties for the composition evolution of NaCl-UCl3. Temperature values are in Kelvin.

Property	Low Burnup	Medium Burnup	High Burnup
Molecular weight [g/mol]	153.66	144.22	139.65
Density [kg/mˆ3]	4220 - 1.03*T	3960 - 0.925*T	3850 - 0.885*T
Viscosity [Pa.s]	$10^{\left(-1.23+\frac{1602}{T}\right)}$	$10^{\left(-1.218+\frac{1557}{T}\right)}$	$10^{\left(-1.18+\frac{1388}{T}\right)}$
Specific Heat [J/kg mol]	102.9	88	85
Thermal Conductivity [W/mK]	0.4	0.35	0.3

Figure 2.8 illustrates the vertical velocity profiles for three different salt compositions at various burnup levels at the exit of the cold leg. There is no significant variation observed between the 0 MWd/kgU and 50 MWd/kgU burnup levels. However, at 150 MWd/kgU, the velocity at the external radius is higher compared to the other two cases. Additionally, the backflow at the center is more pronounced. This behavior can be attributed to the decrease in viscosity and thermal conductivity as the burnup level increases. The outlet temperatures of the hot leg and cold leg, as well as the natural convection mass flow rates for the three different burnup levels, are compared in Table 2.3. As uranium depletes, the linear coefficient of the density temperature-dependent func-

tion decreases, as shown in Table 2.2. This results in a lower buoyancy force. Simultaneously, the viscosity decreases with burnup. Therefore, two competing effects are at play: on one hand, the buoyancy force decreases with burnup, while on the other hand, the counteracting viscous force also decreases, leading to opposing effects. When transitioning from 0 to 50 MWd/kgU burnup, the reduced buoyancy force causes a decrease in the mass flow rate. However, when burnup changes from 50 to 150 MWd/kgU, the mass flow rate remains similar due to the lower viscosity values, which generate reduced viscous resistance throughout the loop.

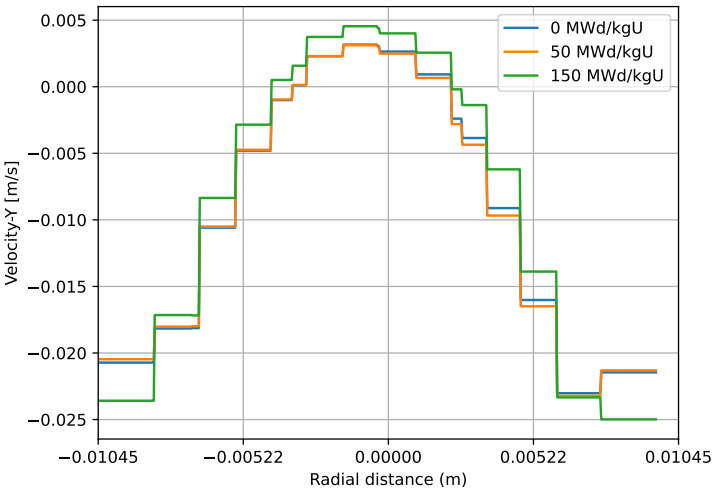

Figure 2.8: Vertical velocity at the exit of the cold leg at burnup values of 0, 50 and 150 MWd/kgU.

Table 2.3: Hot leg outlet temperature, cold leg outlet temperature and mass flow rates comparison between the three different salt burnup levels.

Burnup [MWd/kgU]	Hot Leg Temperature [K]	Cold Leg Temperature [K]	Mass Flow [kg/s]
0	904.0	896	1.62e-2
50	903.9	896.1	1.48e-2
150	903.5	896.5	1.51e-2

3 Verification, Validation, and Demonstration of Integrated Multi-scale Multi-physics MSR Modeling Capabilities

3.1 Improvements to the coupling schemes since FY24

This section provides a summary of advancements on the SAM-Pronghorn DO coupling accomplished in FY25. These developments are consolidated in a standalone document entitled "BlueCRAB Domain Overlapping Coupling: Theory & Verification" [16], which describes the theoretical approach, numerical formulation, and implementation of the DO coupling strategy within the Blue Comprehensive Reactor Analysis Bundle (BlueCRAB) code suite.

Section 3.1.1 provides a briefly describes the DO coupling method whereas Section 3.1.2 highlights the key advancements since its first version in FY23. Section 3.2 presents a summary of test cases that have been performed through FY25 for the implemented method, which includes verification, validation, and demonstration problems. Lastly, Section 3.4 details an additional validation case for the MSRE experiment.

3.1.1 SAM-Pronghorn Domain Overlapping Overview

This section provides a brief overview of the SAM-Pronghorn DO coupling. For a full description of the formulation and numerical scheme, the reader is refereed to the theory manual [16].

In the DO coupling, SAM provides Pronghorn with boundary conditions (BCs) that depend on the system-level simulation of the entire plant. In return, the overlapping coupled SAM components – termed "surrogate components" – receive friction factors and source terms computed dynamically based on the Pronghorn simulation. This method leads to consistent pressure drops and flow splits (in problems involving multiple outlets for the coupled domain), enthalpies, and scalar concentrations when comparing SAM and Pronghorn results.

SAM's surrogate components are governed by the same equations as standard one-dimensional components (i.e., `PBOneDFluidComponent`) [7]. What distinguishes DO surrogates is the use of specific parameters in their formulation to ensure consistent results between SAM and Pronghorn in coupled simulations. These parameters include friction factors to replicate pressure drops and flow splits, a coupled volumetric heat source (or sink) to capture enthalpy changes, and a coupled volumetric scalar source (or sink) to reproduce variations in scalar concentrations.

Figure 3.1 illustrates a simplified example of a coupled SAM-Pronghorn model using a pipe geometry. In this setup, two coupling interfaces – labeled Interface #1 and Interface #2 – define the boundaries of the DO region and are each connected to a corresponding surrogate SAM component. These surrogate components are connected through a single *branch* component, ensuring a continuous system-level model. On the Pronghorn side, a *reference plane* is defined to mimic the role of the SAM branch, establishing a one-to-one correspondence between each surrogate and its associated Pronghorn subdomain. For example, the region between Interface #1 and the reference plane maps to Surrogate #1, and similarly, the region between Interface #2 and the reference plane maps to Surrogate #2. Although this example uses a simple pipe geometry, the framework is generalizable to configurations with multiple inlets and outlets, as well as arbitrary geometries.

Figure 3.2 illustrates the execution scheme for the SAM-Pronghorn DO coupling for momentum, energy, and scalar concentration fields. The coupling relies on a fixed-point (Picard) iteration strategy to realize interdependent parameters between the two codes. In the case of momentum

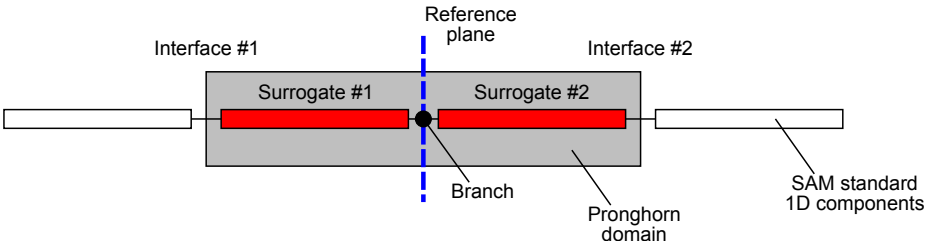

Figure 3.1: Schematics of a coupled SAM-Pronghorn model for a simple pipe setup.

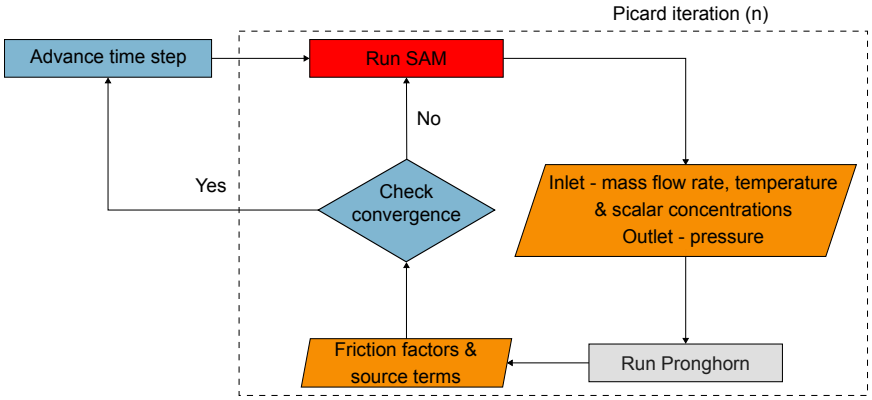

Figure 3.2: Execution scheme for coupling momentum, using fixed-point iterations.

coupling, SAM computes pressure drops and flow rates based on friction factors that are sensitive to local flow conditions. Since these friction factors are influenced by the flow rates provided by Pronghorn, Picard iterations are necessary to achieve convergence between the two solvers. Regarding the energy coupling, the system's thermal response modeled by SAM affects the temperature BCs sent to Pronghorn, in turn altering the coupled energy source term. The scheme proposes updating SAM's temperature BC based on the previous Pronghorn-informed energy source term, until the two codes finally converge. Similar to the energy coupling, the scalar transport coupling involves scalar boundary conditions provided to Pronghorn that depend on the concentration field computed by SAM, which is itself influenced by the scalar source term returned by Pronghorn. This necessitates an iterative update of the scalar BCs in SAM until the scalar exchange between the two codes stabilizes.

3.1.2 Improvements to the coupling schemes since FY23

Unlike the previous version, the present implementation of the DO coupling requires an explicit definition of a reference plane. Previously, the DO admitted arbitrary values for reference physical quantities, including pressure, enthalpy, and scalar concentrations [17]. The justification was that the overall balance between inlet and outlet boundaries – including pressure drops and variations in enthalpy and scalar concentrations – would remain invariant to the choice of reference values, since these are defined within the intermediate portion of the DO domain. However, it has been found that the location of the reference plane can affect the solution of coupled simulations if not correctly positioned, particularly in buoyancy-driven systems. In such cases, it is critical that the

reference plane and SAM's branch component are placed as closely as possible – ideally, the reference plane's center of mass should align with the branch location. This directive ensures that the surrogate components in SAM accurately retrieve the system's buoyancy head, which directly influences the overall flow and heat transfer behavior. A verification case involving a natural circulation loop with a known analytical solution was performed to demonstrate the application of this rule. The test is summarized in Section 3.2. Moreover, enforcing this requirement leads to more consistent behavior between the coupled Pronghorn and SAM models, which is generally preferable for ensuring alignment of physical fields and maintaining fidelity across the computational domains.

More targeted modifications were made to the formulations used for computing the coupling parameters, including both friction factors and source terms. For momentum coupling, a new term – referred to as the *flow split controller* – has been introduced. This term is specifically activated in cases involving multiple outlet surrogate components, i.e., when more than one component carries flow away from the DO coupled section. In such configurations, coupling only the hydraulic resistances is insufficient to ensure full consistency between Pronghorn and SAM. This is because, if the friction factors of the outlet surrogate components are adjusted solely based on their individual pressure drops, the resulting solution may achieve consistent momentum balances between the codes but may yield inconsistent mass flow distributions. In fact, the original implementation described in Ref. [17] accounted for this effect using a correction based directly on the mass flow rates computed by Pronghorn and SAM. In contrast, the current formulation adopts a more straightforward approach by directly comparing the flow splits computed between the codes.

Compared to the previous implementation, the current energy coupling formulation introduces two significant advancements that enhance both stability and convergence. First, the energy coupling formulation is no longer directly based on energy balance. Instead, the scheme is formulated for coupling enthalpy variations, thereby eliminating the need to explicitly constrain mass flow rates within the energy equation. This modification leverages the fact that mass flow is already addressed through momentum coupling, resulting in a more robust and decoupled solution strategy. Second, the earlier method relied on a Newton scheme that considered only the convective energy balance across inlet-outlet boundaries. This technique lacked physical reasoning since it did not consider thermal inertia and was prone to instabilities under small thermal perturbations – particularly in the case of natural circulation, where momentum and thermal solutions are tightly coupled. The new formulation eliminates the scheme derived from the Newton method and incorporates a thermal inertia term. This provides a more physically consistent representation of heat transport in the DO-coupled region, avoiding the deficiencies mentioned previously.

Similar to the previous energy coupling approach, the earlier scalar transport formulation relied on a Newton scheme that considered only the convective transport across inlet-outlet boundaries. While this method provided a basic coupling mechanism, it lacked physical reasoning due to the absence of an unsteady term. Unlike heat transport, scalar transport does not have a direct analogue to heat capacity, making the omission of the time-dependent term particularly problematic. As a result, the Newton-based solution was prone to instabilities, especially under small perturbations – such as when scalar quantities began advecting into the DO-coupled region or completed advecting out. The new formulation addresses these issues by eliminating the Newton-based scheme and explicitly incorporating an unsteady term. This addition provides a more physically consistent and numerically stable treatment of scalar transport, improving robustness in transient and tightly coupled scenarios. A mixing test in a double-T component was performed to assess the adequacy of the new formulation for coupling the transport of scalar quantities (see Section 3.2).

3.2 Summary of Test Cases Performed to Date (FY25)

Table 3.1 summarizes the test cases completed as of FY25, highlighting the diversity of flow regimes, thermal conditions, working fluids, and coupling scenarios evaluated. To evaluate the robustness and accuracy of the DO coupling implementation, a comprehensive suite of test cases was developed and categorized into three groups: **verification, validation, and demonstration** problems. Particular attention was given on the verification cases, as they provide the baseline to assess the effectiveness and applicability of the method.

These classifications and their corresponding test cases are discussed in the following sections. While the individual test cases are not detailed here, they comprise a collection of problems drawn from existing works or planned for inclusion in future publications; the sources of these cases will be indicated as applicable.

3.2.1 Summary of verification cases

Verification cases were constructed to admit analytical solutions, enabling direct comparison with theoretical expectations. These cases were specifically designed to assess pressure drops and energy balances under well-characterized conditions. In addition to the coupled SAM-Pronghorn simulations, standalone SAM and Pronghorn models were executed independently, each showing good agreement with the corresponding analytical benchmarks. This consistency confirms that the coupling method itself does not introduce numerical artifacts or alter the underlying physical results.

The majority of the verification cases are based on a simple pipe setup. The results were analyzed using two primary metrics: pressure drop and temperature rise. The pressure drop was computed using the Darcy–Weisbach equation, and the temperature rise was obtained using the steady-state energy balance for sensible heat, i.e., $\Delta T = Q/\dot{m}C_p$. The theory manual [16] details the setup and analysis using water as a reference case. Section 3.3 showcases the DO coupling using the Saline API. Verification cases using helium are planned for inclusion in the BlueCRAB test system.

The pipe loop verification case introduces buoyancy-driven flow and serves as a benchmark for natural circulation modeling. The analytical solution for this case is derived using the Boussinesq approximation, which assumes constant thermophysical properties and incorporates buoyancy effects in the momentum equation as a linear function of temperature. Under steady-state conditions, the mass flow rate and temperature distribution can be obtained from the analytical formulation presented in [18]. This solution is used to verify the accuracy of the coupling implementation in capturing natural circulation behavior and energy transport driven by buoyancy forces. The setup and analysis of this case are also documented in the theory manual [16].

3.2.2 Summary of validation cases

Validation cases involved comparison against experimental data, providing confidence in the physical fidelity of the models under more realistic operating conditions. These problems not only validate the coupling method but also the coupled codes themselves.

The case of pipe systems connected by a double-T junction is used to validate the consistent transport of scalar species concentrations between SAM and Pronghorn. A recent publication [19] demonstrated the accuracy of the DO approach using experimental data from a tracer mixing experiment involving two piping loops connected through a double-T junction [20]. The validation involves coupling the tracer transport across the double-T component, which features two inlets and

Table 3.1: Summary of test cases performed for DO coupling, including verification, validation, and demonstration.

Classification	Setup	Working Fluid	Flow Regime	Thermal Condition	Buoyancy-driven	Scalar Transport
Verification	Pipe	Water	Laminar	Isothermal	No	No
		Salt	Laminar	Isothermal	No	No
		Helium	Laminar	Isothermal	No	No
		Water	Turbulent	Isothermal	No	No
		Salt	Turbulent	Isothermal	No	No
		Helium	Turbulent	Isothermal	No	No
		Water	Turbulent	Heated	No	Yes
		Salt	Turbulent	Heated	No	No
		Helium	Turbulent	Heated	No	No
	Pipe loop	Helium	Turbulent	Heated	Yes	No
Validation	Pipe systems connected by double-T	Water	Turbulent	Isothermal	No	Yes
	Molten Salt Reactor Experiment (MSRE)	Salt	Turbulent	Heated	No	Yes
Demonstration	Flow split in a T-junction	Water	Turbulent	Isothermal	No	No
	Asymmetric flow in a tank with hydrostatic column	Water	Laminar	Isothermal	No	No
	Multiple junctions with asymmetric flow	Water	Turbulent	Isothermal	No	No
	Pebble Bed-Fluoride Salt Cooled High Temperature Reactor (PB-FHR)	Salt	Turbulent	Heated	No	No
	High-Temperature Reactor-Pebble-bed Module (HTR-PM)	Helium	Turbulent	Heated	No	No

two outlets, and requires accurate resolution of scalar mixing and flow partitioning. This case highlights the ability of the coupled framework to capture scalar transport phenomena in complex flow configurations.

The case involving the MSRE models the plant's primary system and its interaction with the secondary system through the heat exchanger. This validation case is documented in Section 3.4 of the present report.

3.2.3 Summary of demonstration cases

Demonstration cases focused on evaluating the coupling methodology through comparisons between SAM and Pronghorn during coupled simulations. Although some of these demonstration problems may admit analytical solutions or have corresponding experimental data, the test cases employed here were primarily designed to assess the coupling approach itself in a practical and targeted manner.

The flow split in a T-junction test case aims to demonstrate that the flow split controller introduced this year (see Section 3.1.2) ensures consistent outlet mass flow rates in coupled SAM and Pronghorn simulations. This case will be included in the test suite of BlueCRAB.

The setup of asymmetric flow in a tank with hydrostatic column is designed to test the robustness of the DO coupling in confined geometries with complex internal flow behavior. The tank geometry induces a non-uniform internal flow field characterized by expansion-contraction losses, asymmetric shear layers, and localized recirculation zones.

The multiple junctions with asymmetric flow case extends the complexity of the previous tank setup by introducing two independent, pump-driven loops connected through a single tank. This configuration introduces multiple inlets and outlets, resulting in intricate cross-flow patterns within the tank as the fluid redistributes in response to differing circulation rates in each loop. The case is intended to challenge the DO coupling's ability to handle dynamically evolving internal flow structures and maintain solution consistency across multiple boundaries. Both of these tank-based demonstration cases are described in greater detail in the theory manual [16].

Finally, preliminary tests were also conducted for the Pebble Bed–Fluoride Salt Cooled High Temperature Reactor (PB-FHR) and the High-Temperature Reactor–Pebble-bed Module (HTR-PM) demonstration cases. These simulations reflect that the capabilities demonstrated in the cases summarized here support analysis for reactors. Ongoing efforts are focused on extending these analyses to safety-relevant evaluations and advancing the applicability of the DO coupling.

3.3 Pronghorn-SAM-Saline coupled verification case

The enthalpy solvers in Pronghorn and SAM employing the `SalineMoltenSaltFluidProperties` user object in MOOSE is tested in a 2D axisymmetric pipe simulation. The domain overlapping coupling technique is applied to overlap the Pronghorn Multi-D domain with the SAM pipe components.

The flow enters the inlet domain with a fully developed laminar flow, and a constant inlet temperature. A constant heat flux is applied along the pipe wall, and the temperature boundary layer develops throughout the domain. Both SAM and Pronghorn employ the `SalineMoltenSaltFluidProperties` user object, querying the component FLiNaK with a composition of '0.465 0.115 0.42' for LiF, NaF and KF, respectively at a pressure of 1 atm.

Figure 3.3 shows the temperature contour predicted by both Pronghorn and the SAM overlapped domain. The enthalpy difference between the outlet and inlet in Pronghorn is used to compute a volumetric heat source which informs the 1D system code. This leads to the same energy conservation between both codes. The surface-averaged outlet temperature in the 2D domain and the temperature outlet value in the 1D domain are 892.4 K and 892.6 K, respectively. Figure 3.4 shows the laminar fully-developed velocity profile in Pronghorn and the 1D velocity value in SAM. The mass flow rates in both models are 0.0321 kg/s and 0.0322 kg/s, respectively. Figure 3.5 presents the distribution values of the temperature-dependent thermophysical properties as a function of temperature and space.

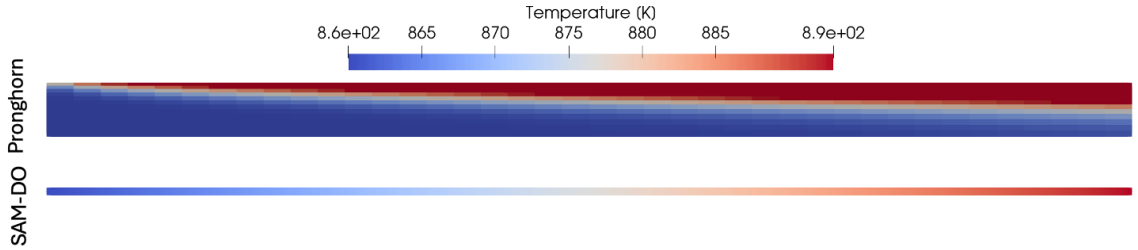

Figure 3.3: Temperature contour in the Pronghorn 2D domain (top). Temperature in the SAM domain.(bottom)

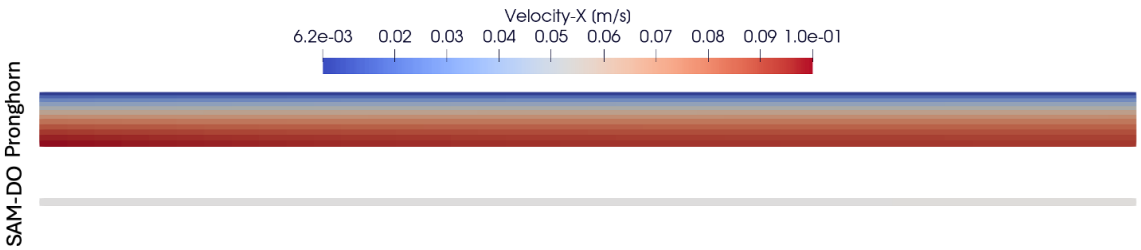

Figure 3.4: Laminar axial velocity contour plot in the Pronghorn 2D domain (top). Velocity in the SAM 1D domain. (bottom)

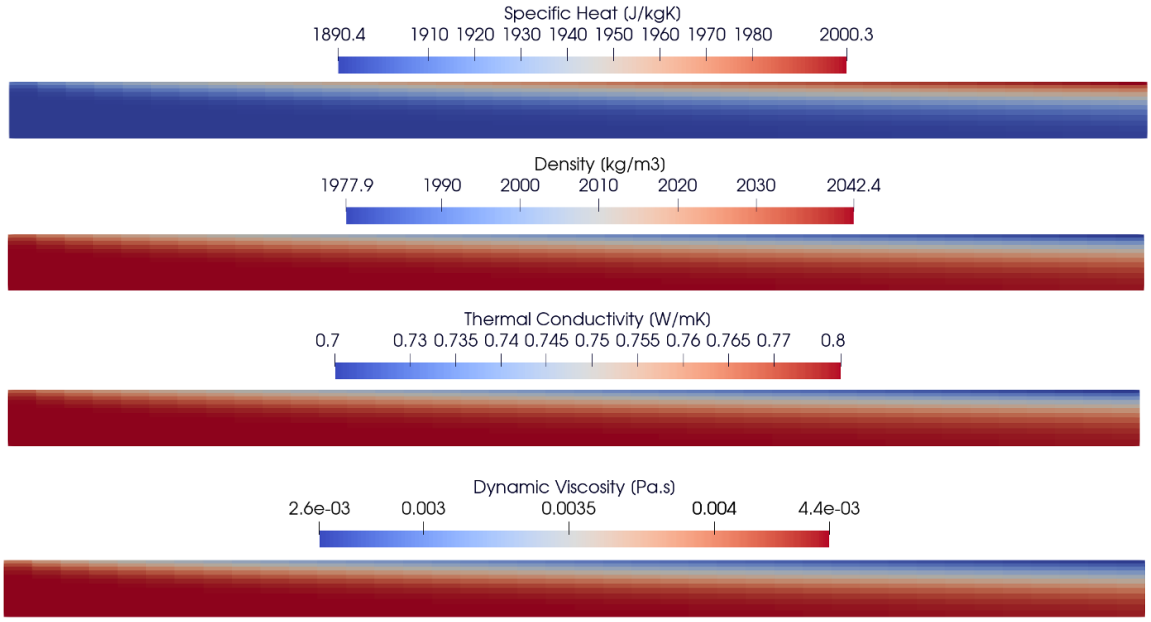

Figure 3.5: Temperature-dependent thermophysical properties for the Pronghorn domain using Saline MSTDB-TP database.

3.4 Pronghorn-SAM-Saline coupled demonstration case: Molten Salt Reactor Experiment

The MSRE was conducted by the Oak Ridge National Laboratory (ORNL) with the primary goal of demonstrating that the advantageous characteristics of the molten-salt reactor concept could be realized in a practical, operational reactor. The MSRE featured a fuel circulation system, where liquid fuel salt was continuously pumped through graphite moderator channels using electromagnetic pumps, where gaseous fission products were removed [21]. Graphite served as the moderator with a surrounding graphite reflector. The reactor utilized a shell-tube heat exchanger system to extract the nuclear heat. Designed with inherent safety features, such as highly negative reactivity feedback with respect to temperature, the MSRE allowed for safe execution of various experiments, including reactivity insertion transients. Constructed in 1964 at ORNL, the MSRE was the first reactor to operate with liquid fuel and graphite moderation, initially using U-235 fuel, which was later replaced with U-233 fuel. A schematic of the MSRE plant layout is shown in Figure 3.6.

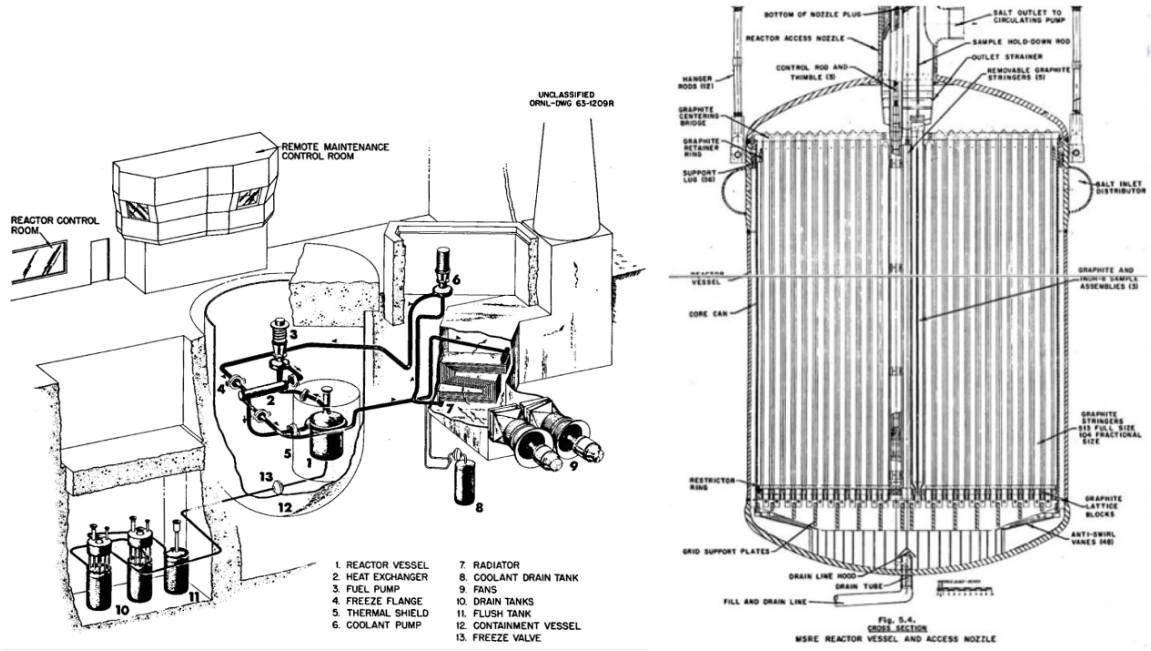

(a) MSRE loops

(b) MSRE core region

Figure 3.6: MSRE plant configuration, reproduced from [21]

To model the MSRE plant's primary system and its interaction with the secondary system through the heat exchanger, we employ the domain overlapping coupling approach. This method has been shown to provide consistent pressure, mass flow rates, enthalpy, and passive scalar distributions between the multi-domain coarse-mesh thermal-hydraulics code Pronghorn and the system thermal-hydraulics code SAM [17]. A sketch of the domain-overlapped model is shown in Figure 3.7.

Figure 3.7a presents the Pronghorn-Griffin model of the MSRE core region, represented as a 2D axisymmetric domain while preserving the original core dimensions specified in [21]. The core is modeled as a porous medium with a porosity of 0.223, defined by the ratio of the total volume of salt to the total volume, including the graphite moderator blocks. Additionally, the model incorporates a core bypass with a porosity value of 1.0 to represent the volume of fuel salt that bypasses the core through the outer region of the internal core barrel. The salt enters the core swirling through the downcomer region, which is separated from the core region through a solid core barrel region. Conjugate heat transfer is modeled between the core barrel and the fuel salt entering the downcomer and the fuel salt in the core region. The salt enters the lower plenum and flows through the core towards the upper plenum. Finally, it exits the core vessel through the riser outlet. Table 3.2. A weakly-compressible model with temperature-dependent thermophysical properties is employed, solving for the enthalpy of the salt. The reader is referred to [22] for the full model description including the equations for mass, momentum, enthalpy and delayed neutron precursor (DNP) conservation in a porous medium. The Churchill correlation is used to compute friction factors along the core porous region. In addition, to model the turbulent mixing in the

downcomer, lower and upper plenums, the zero-dimensional mixing length turbulence model is utilized. Inlet boundary conditions are imposed for velocity, enthalpy and passive scalars, with values transferred through the coupling with the overlapped systems code SAM. In addition, outlet boundary conditions for pressure are imposed by the SAM solution.

In the reactor core region, Pronghorn solves the velocities, the pressure, the enthalpy and six groups of delayed neutron precursors. The Griffin neutronics model transfers the normalized power source to Pronghorn in order to compute the production term for the neutron precursor groups and the volumetric heat source term for the enthalpy balance. The model details for the MSRE Griffin neutronics model can be found in [23].

Table 3.2: MSRE parameters for dimensions and the fuel salt.

Parameter	Values
Core radius	0.691 m
Core bypass thickness	0.011 m
Core height	1.660 m
Core barrel thickness	0.00635 m
Downcomer thickness	0.0254 m
Core vessel height	2.006 m
Fuel salt	LiF-BeF_2-ZrF_4-UF_4
Fuel composition	65%-29.1%-5.0%-0.9%
Fuel enrichment	33%

Figure 3.7c illustrates the SAM one-dimensional model of the MSRE primary circuit and its interaction with the secondary system. This model includes two pipe components that overlap with the multidimensional Pronghorn-Griffin model shown in Figure 3.7a. The first pipe component represents the downcomer volume, while the second pipe component encompasses the lower plenum, the core, the upper plenum, and the riser volumes. The exit of the overlapped core model undergoes a contraction before entering the core outlet pipe, which subsequently leads to the pump intake pipe. The pressure is increased at the pump component, directing the flow to the shell side of the heat exchanger. Here, heat is transferred through heat structures to the tube part of the secondary system. Finally, the cooled fuel salt re-enters the multidimensional domain at the downcomer inlet, undergoing a flow expansion. The SAM standalone model is documented in the Virtual Test Bed.[24]

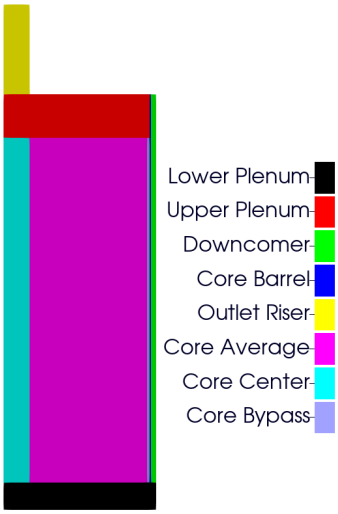

(a) MSRE core region (Pronghorn-Griffin)

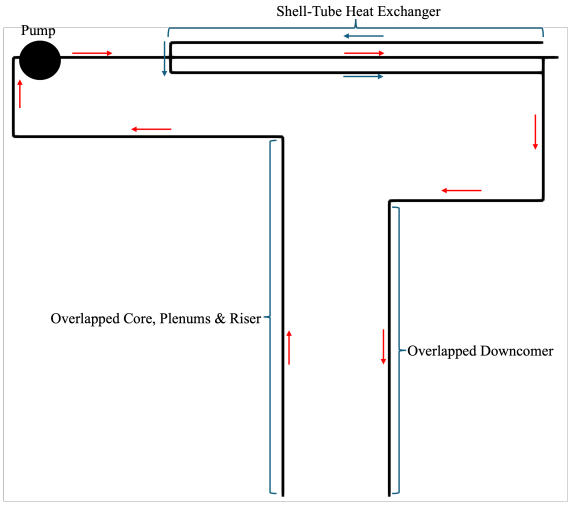

(b) MSRE circulation loop (SAM)

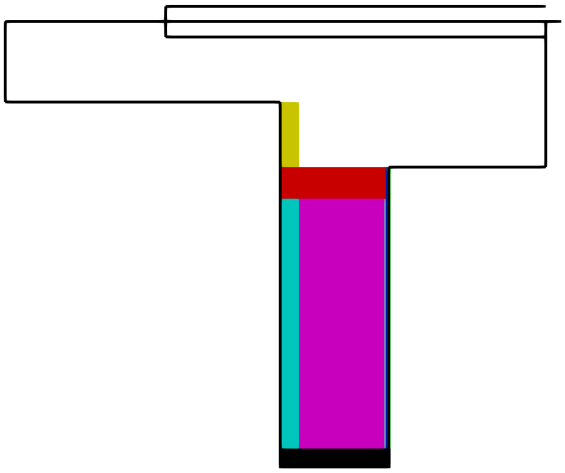

(c) MSRE full model

Figure 3.7: MSRE Domain overlapping model.

The thermophysical properties of the fuel salt LiF-BeF_2-ZrF_4-UF_4 corresponding for the corresponding composition are obtained via the molten salt thermophysical database [25]. The density temperature dependent function and the thermal conductivity were present in the database. The missing specific heat temperature-dependent data is added to the database by using the Calphad method in Thermochimica. The viscosity temperature function is obtained employing the Molten Salt Propnet, a machine learning framework which predicts thermophysical properties of molten salt mixtures, using MSTDB-TP and Janz compendium data [26]. The Saline interface, a submodule in the MOOSE framework, serves as the interface between the thermophysical properties database and the SAM/Pronghorn models. Table 3.3 details the functions used for the MSRE salt thermophysical properties as a function of temperature [K].

Table 3.3: MSRE fuel salt thermophysical properties. Temperature values are in Kelvin.

Property	Value
Molecular weight	40.05 g/mol
Density [kg/m^3]	2710 - 0.562*T
Viscosity [Pa.s]	1.24e^{-4} *exp(3.13e^4/(R*T))
Specific Heat [J/kg mol]	57.84 + 0.0259*T + 4.7441e^6*T^{-2} - 7.51e^{-6}*T^2
Thermal Conductivity [W/mK]	1.22

Figure 3.8 illustrates the heat capacity as a function of temperature and its distribution in the reactor core under steady-state 10 MW conditions. The operating temperature range of the MSRE encompasses the local minima observed in the function derived using the Calphad method in Thermochimica. This indicates that approximating the specific heat as a linear function of temperature could result in significant errors. Moreover, the temperature dependence of the specific heat is crucial for accurately computing the enthalpy balance within the domain. The Saline submodule in MOOSE introduces conversion functions between enthalpy and temperature through lookup tables for arbitrary temperature-dependent specific heat functions. This approach eliminates the need for the user to manually specify the conversion functions between enthalpy and temperature.

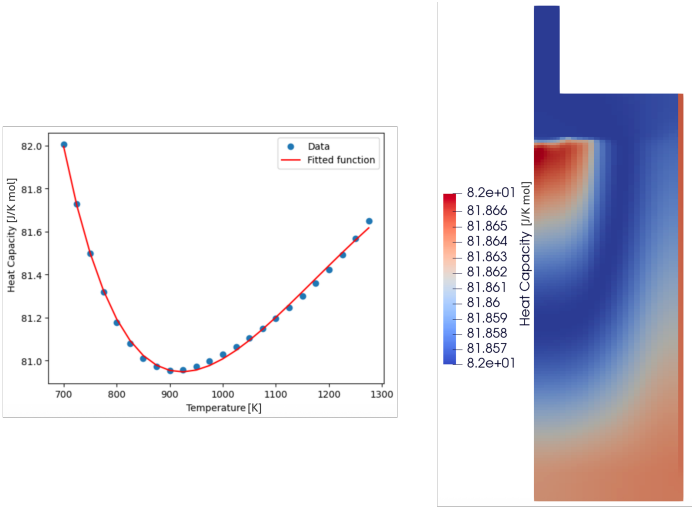

Figure 3.8: Heat Capacity for the MSRE fuel salt as a function of temperature and its distribution in the core under 10 MW power conditions.

3.4.1 MSRE 10 MW Steady state conditions

Steady-state conditions are achieved using a fully coupled multiphysics model. Pronghorn serves as the main application, solving for velocity, pressure, and liquid enthalpy for the salt, as well as solid enthalpy for the core graphite and core barrel, and delayed neutron precursors in the core region. SAM is coupled via the domain overlapping approach, solving for velocity, pressure, enthalpy, and delayed neutron precursor scalar advection, including decay for each group in the primary loop, and also accounting for heat exchange in the heat exchanger to the secondary system. Griffin solves the eigenvalue problem, obtaining the power distribution in the core region. A sketch

showing the coupling approach used for this validation exercise is given in Figure 3.10. The steady state parameters for a power of 10 MW correspond to the values in the MSRE report [21], and are summarized in Table 3.4.

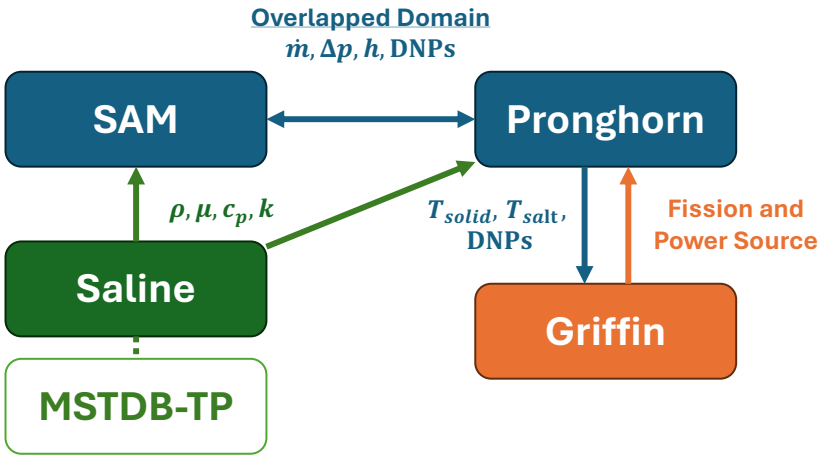

Figure 3.9: Coupling scheme used in the 10 MW steady state case.

Table 3.4: MSRE steady state operational values.

Parameter	Values
Power	10 MW
Mass flow rate	∼165 kg/s
Core Δ pressure	∼62 kPa
Core Δ temperature	∼27.8 K
Recirculation time	∼25 s

The velocity magnitude field is illustrated in Figure 3.10, depicting the SAM velocity in the primary loop and the Pronghorn velocity in the core, each with distinct scales for clarity. Velocity streamlines are also added in the core region for added description of the flow path within the reactor vessel. The pump head value in the SAM code is configured to achieve the nominal mass flow rate of 165 kg/s, as specified in Table 3.4, in order to overcome the system's total pressure drop. A deceleration is observed in the heat exchanger region of the loop, attributed to the expansion into the shell section of the heat exchanger. In the core, the flow enters the Pronghorn domain through the downcomer, bends and mixes in the lower plenum before entering the core, ascends in the core, splitting between the core and the core bypass, and finally contracts and mixes in the upper plenum before exiting towards the riser outlet pipe. The flow is predominantly one-dimensional in the core, due to significantly higher friction factors in the radial direction, which corresponds to the flow in the moderator channels observed in the MSRE. The velocity magnitude and the volume of the components in the model are utilized to compute a total recirculation time, which matches the 25-second recirculation time observed in the actual MSRE experiment.

The pressure field distribution in the MSRE model is presented in Figure 3.11. In the SAM loop, pressure increases as the flow is driven into the pump's outlet line. The pressure also rises in

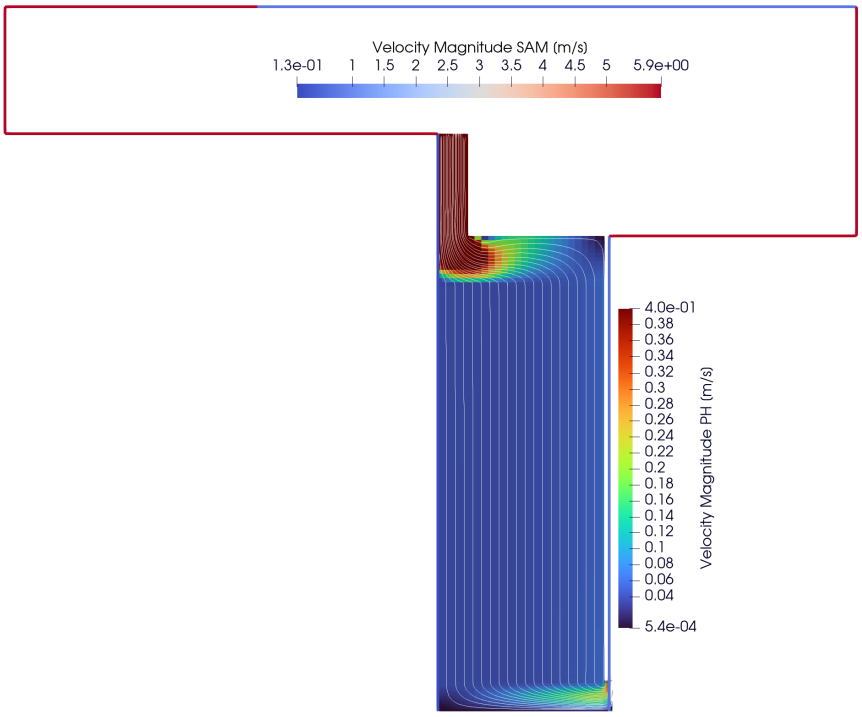

Figure 3.10: MSRE Domain overlapped velocity fields in Pronghorn and SAM. Velocity Streamlines are plotted in the Pronghorn core model.

the shell heat exchanger region due to the expansion in flow area. Additionally, there is an increase in pressure at the downcomer inlet as a result of flow expansion. The pressure difference in the core, measured between the downcomer inlet and the riser outlet, is 63.5 kPa, which is 1.5 kPa higher than the reference value of 62 kPa presented in Table 3.4.

The temperature field in the MSRE overlapped domain is shown in Figure 3.12. The fuel salt absorbs the heat generated in the reactor core, resulting in a temperature difference of 27.8 K between the inlet and outlet, which matches the temperature difference specified in Table 3.4. In the primary loop, the temperature remains constant until it reaches the heat exchanger, where it exits at 896 K due to the heat exchange with the secondary tube side. The power distribution in the core is displayed in Figure 3.13a.

The domain overlapping approach between SAM and Pronghorn-Griffin also incorporates the passive scalar advection and radioactive decay of the six groups of DNPs, which are crucial for the system's reactivity prediction. Figures 3.13b, 3.13c, and 3.13d illustrate the DNP distributions for groups 1, 3, and 6, representing the longest-lived precursor group, an intermediate-lived group, and the shortest-lived precursor group, respectively. The DNPs are produced following the fission source profile's spatial distribution, decay over time, and are advected by the velocity field. The domain overlapping approach ensures that at the core outlet, SAM matches the weighted mass flow average of each DNP group's distribution. SAM then advects these groups with the 1D velocity field and accounts for their decay in the primary loop, providing the inlet value of the DNPs when they return to the core downcomer.

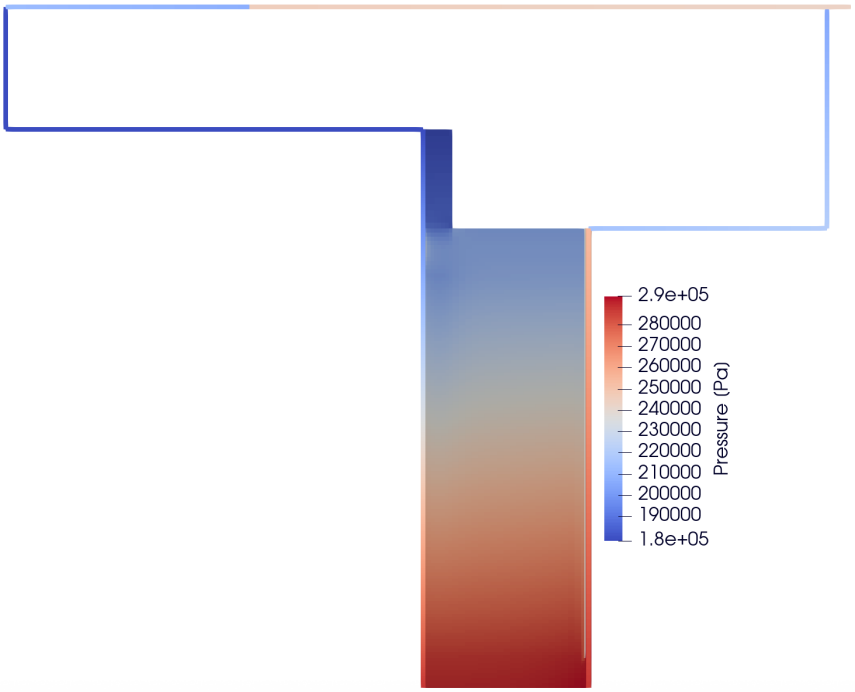

Figure 3.11: MSRE Domain overlapped pressure in Pronghorn and SAM.

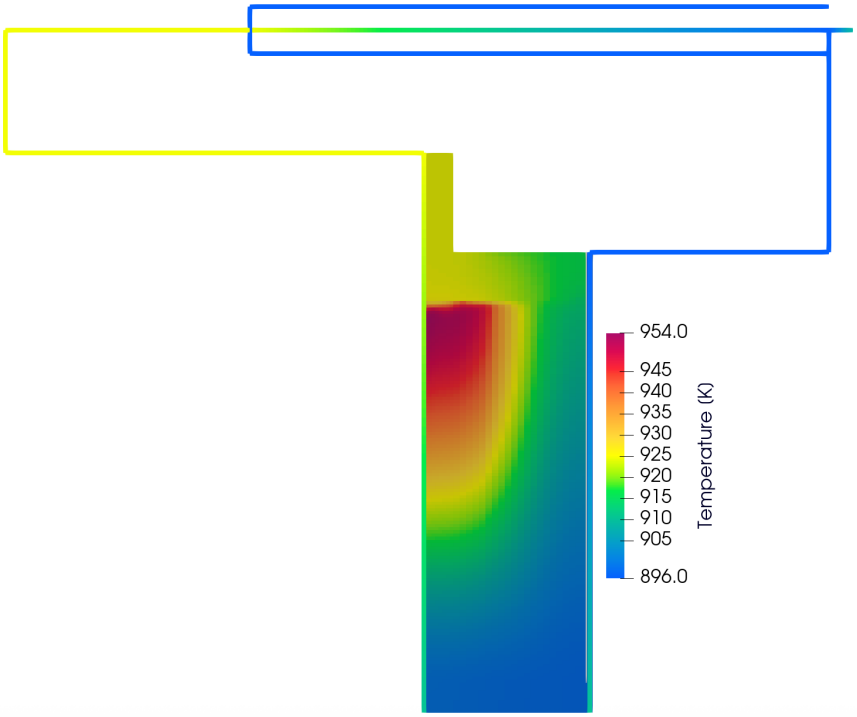

Figure 3.12: MSRE Domain overlapped temperature fields in Pronghorn and SAM.

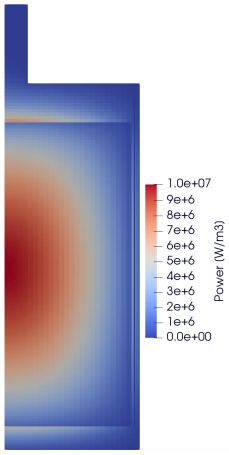

(a) MSRE core power density

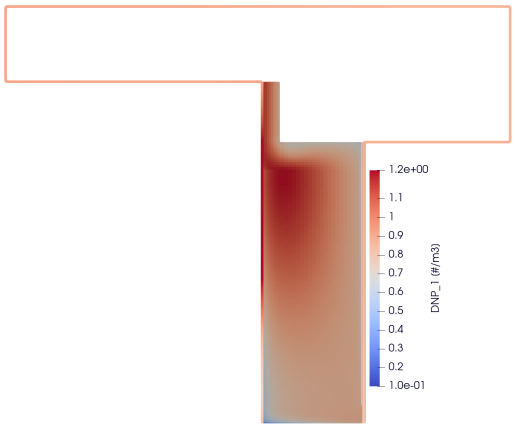

(b) DNP Group 1

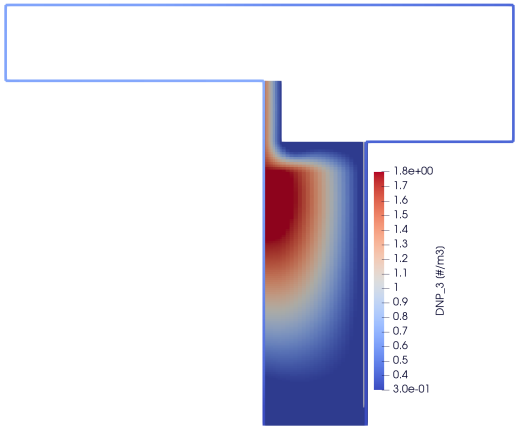

(c) DNP Group 3

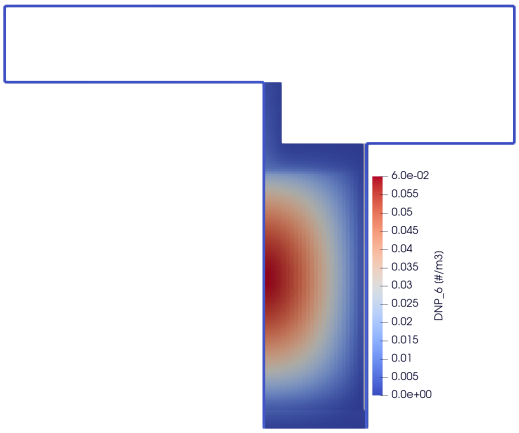

(d) DNP Group 6

Figure 3.13: MSRE core power distribution for steady state conditions at 10 MW and delayed neutron precursor distributions for groups 1, 3 and 6 in the primary loop (SAM) and in the core region (Pronghorn).

3.4.2 MSRE Zero-Power transients: Pump startup and Pump coastdown

Before the MSRE reactor was operated with significant nuclear heat generation, zero-power experiments were conducted and documented in [27]. These experiments aimed to measure critical neutronic characteristics of the MSRE under conditions of negligible nuclear heat generation. The program included several key assessments: initial critical loading with U-235, control rod calibration, determination of reactivity loss due to fuel circulation, “static” reactivity coefficients for excess U-235 concentration and isothermal core temperature, and the reactivity coefficient for fuel salt temperature. Transient flow-rate tests were conducted to determine the startup and coastdown characteristics for the fuel and coolant pump speeds and the coolant salt flow rate. Additionally, these tests aimed to assess the transient effects of changes in fuel flow rate on reactivity, isolating it

from any temperature feedback due to the low rated power.

The first transient involves a pump startup starting from critical and zero-power conditions. While the primary pump speed attains its maximum value within the first 1.5 seconds of the transient, the precise evolution of the fuel salt mass flow rate is not detailed in the analysis. A power level of 10 W is set in the MSRE Griffin model. Such a low power does not significantly alter the temperature of the fuel salt, effectively maintaining an isothermal condition. Griffin standalone is executed with static fuel to achieve the steady-state condition for the six groups of delayed neutron precursors. This state is reached when the production of DNPs from the critical fission source is balanced by the decay of the DNPs.

This is the initial condition for the startup transient, at a temperature of 908.15 K. The evolution of the pump head and the percentage of mass flow rate is illustrated in Figure 3.14 for both the pump startup and pump coastdown transients. The coupling scheme depicted in Figure 3.9 is employed for both startup and coastdown transients. In this scheme, Pronghorn functions as the primary application, while SAM and Griffin serve as sub-applications. SAM and Pronghorn are coupled using the domain overlapping coupling approach, with Picard iterations conducted at each timestep until the pressure drop, mass flow rates, enthalpy balance, and passive scalar balance are consistent between the codes. Griffin solves for an eigenvalue problem by solving the steady-state diffusion equation based on the DNP concentration distributions transferred from Pronghorn. Since a constant low power level was maintained, thermal feedback is disregarded, and changes in the eigenvalue are attributed only to variations in the DNP field.

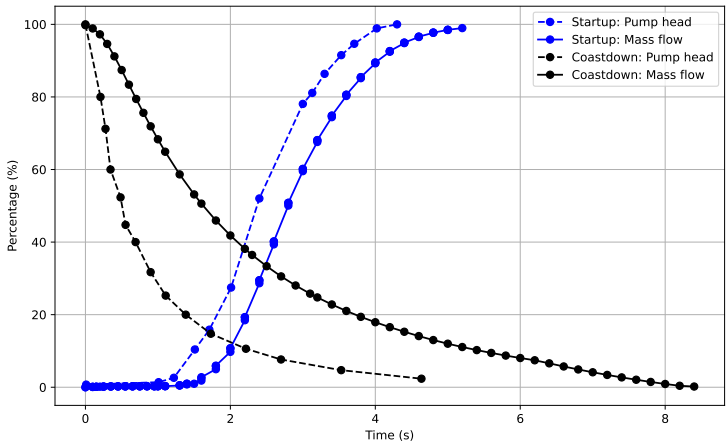

Figure 3.14: MSRE pump head and mass flow rate evolution during the zero-power pump transients

The reactivity loss evolution (negative reactivity) for the DO is presented in Figure 3.15 and compared with the experimental measurements in [27]. During the initial phase of the transient, the negative reactivity increases as the delayed neutron precursors are advected out of the core. At 14.5 seconds from the beginning of the transient, a peak in negative reactivity is observed as the DNPs start entering the core region. Although the timing of the peak matches the experimental value, the magnitude of the reactivity loss is not accurately captured. It is important to note that the reactivity on the y-axis of Figure 3.15 is derived from the reactivity rod worth calibration in the

report, as the actual experimental measurements were recorded in terms of rod extraction in inches. This leads to the hypothesis that the precision of the control rod servo controller, which maintained reactor criticality during the transient, is not fully understood and may have led to overshooting following a rapid reactivity change. The potential delayed effect of the servo controller is further examined in [28]. Although the peak is not accurately captured, the subsequent oscillations in reactivity are modeled successfully until a steady state is achieved. The model predicts a reactivity loss of 225 pcm relative to the static fuel critical condition. When extrapolating the average of the experimental measurements after the peak, the reactivity loss is determined to be 219 pcm, resulting in a difference of 6 pcm between the experimental data and the model.

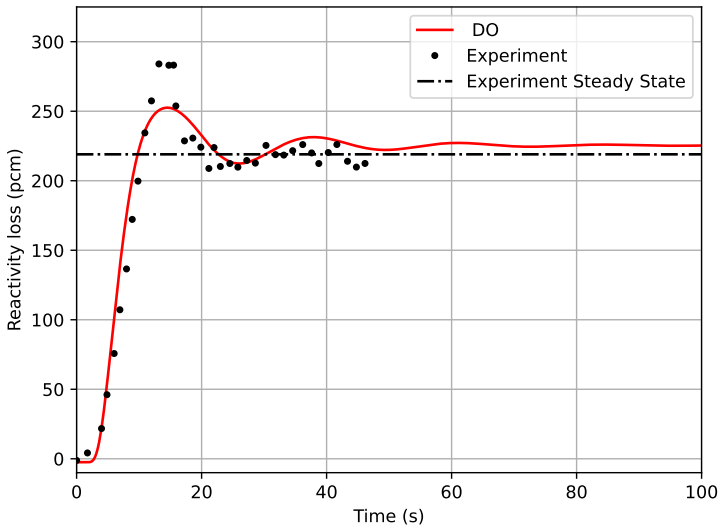

Figure 3.15: MSRE Domain overlapped reactivity loss evolution during the startup transient

From the critical steady-state condition achieved 200 seconds after the pump startup, a pump coastdown transient is initiated, following the pump speed head function depicted in Figure 3.14. The evolution of reactivity loss is presented in Figure 3.16. In contrast to the pump startup, the neutron contributions from the decay of the six DNP groups begin to increase as the flow rate decreases, thereby increasing core reactivity. The DO MSRE model shows good agreement with the experimental values of reactivity loss.

3.4.3 MSRE Reactivity insertion transient

A series of reactivity insertion transients at different power levels were performed in the MSRE during the later operation of the reactor fueled with U-233 [29], from which the 5 MW experiment data has been used in several previous efforts to validate SAM (with PKE) [30] and Griffin with Pronghorn standalone and the previous implementation of Pronghorn-SAM DO coupling [17]. In the integrated multiphysics model discussed in this section, the Griffin neutronics model was developed to model the zero-power transients which were performed early in the operation of MSRE using U-235 fuel. A Griffin model with U-233 fuel and updated cross sections has not yet been pre-

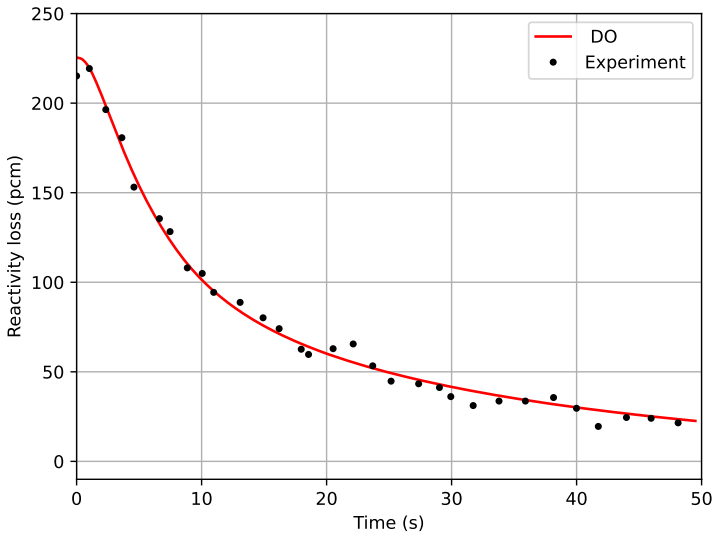

Figure 3.16: MSRE Domain overlapped reactivity loss evolution during the coastdown transient.

pared, so a brief demonstration of a postulated reactivity insertion will be presented in this section to illustrate the thermal fluid response in the context of the integrated multiphysics simulation.

The conditions of the 5 MW reactivity insertion case are adopted as the parameters for the simulation. The model is first initialized with a Griffin Eigenvalue calculation coupled to a 1000 sec null transient DO coupled Pronghorn-SAM-Saline model of the MSRE as discussed in Section 3.4.1, but reduced to an initial power of 5 MW. From this initial steady state, the model is restarted to perform an additional 1000 sec null transient in Griffin, Pronghorn, and SAM to confirm that the power and flow conditions are at a converged steady state before initiating the insertion transient. At $t = 0$ seconds, a 19 pcm insertion is introduced in the Griffin neutronics model, and the insertion transient is simulated over 400 sec until a new steady state power level is reached. As in previous exercises, the Griffin MSRE model does not currently include the control rods, so the 19 pcm insertion is achieved by manually adjusting the fuel fission cross section so that the k-eigenvalue is has a reactivity 19 pcm higher than at steady state.

The excess power and evolution of core fuel salt temperatures of the simulated transient are shown in Figures 3.17 and 3.18. As expected, the initial insertion results in a rapid increase of power with the fuel salt temperatures also following. The rise in fuel and moderator temperature results in negative density-Doppler feedback which arrests the power increase, which reduces until a new higher steady state power level is achieved (approximately 5.2 MW). The initial maximum power increase is lower than the measured experimental data for the 5 MW test conducted in the MSRE, most likely because the β_{eff} of U-235 is lower than for U-233. Future efforts will focus on updating the Griffin neutronics model to U-233 fuel for validation of the updated Griffin-Pronghorn-SAM-Saline multiphysics model.

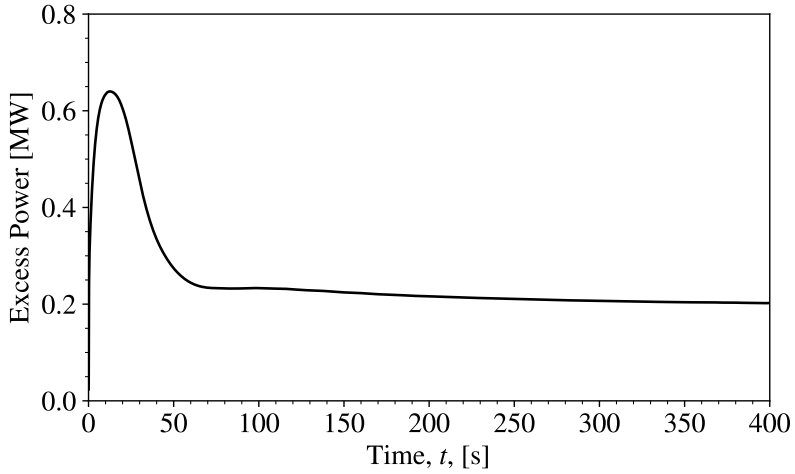

Figure 3.17: MSRE Domain overlapped excess power following 19 pcm insertion at 5 MW.

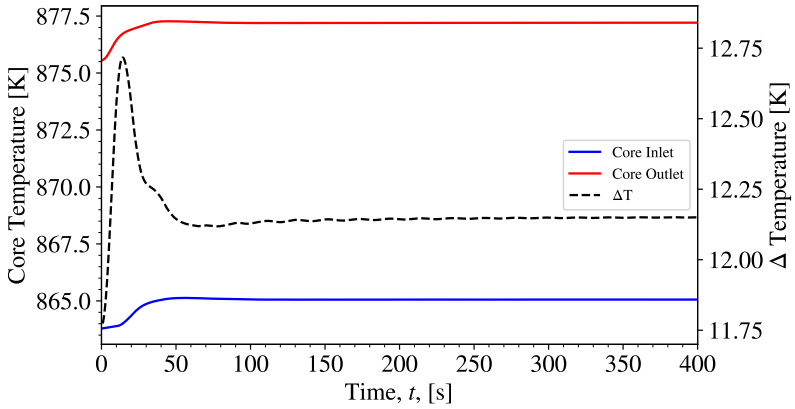

Figure 3.18: MSRE Domain overlapped core temperatures following 19 pcm insertion at 5 MW.

4 Improvements in Pronghorn for Corrosion and Plating Models for MSRs

4.1 Improving Noble-Metal Plating and Corrosion Wall-Flux via Enhanced Thermal-Hydraulics Model

We model an oxidized noble-metal species i (e.g., Ru, Pd) dissolved in the molten salt and allowed to plate onto, or corrode from, solid surfaces. The liquid-side state variable is the *molar concentration* $c \equiv c_i$ $[\mathrm{mol\,m^{-3}}]$. Transport in the bulk follows an advection–diffusion–reaction balance; at solid walls, an interfacial flux couples the liquid to the solid deposit. All fluxes are taken *positive from liquid to solid*.

The following symbols are introduced in this modeling framework:

- D (or D_{eff}) $[\mathrm{m^2\,s^{-1}}]$: (effective) diffusivity;
- k_m $[\mathrm{m\,s^{-1}}]$: mass-transfer coefficient across the wall film;
- k_0 $[\mathrm{m\,s^{-1}}]$: heterogeneous surface-rate coefficient at $\eta = 0$;
- J $[\mathrm{mol\,m^{-2}\,s^{-1}}]$: interfacial molar flux (plating $J > 0$, corrosion $J < 0$);
- $c_{\mathrm{eq}}(T,p)$ $[\mathrm{mol\,m^{-3}}]$: equilibrium dissolved concentration from Thermochimica at local temperature T and pressure p;
- $\eta = \phi - E$ [V]: overpotential (electrolyte potential minus reaction equilibrium potential);
- n (–): electrons transferred; F $[\mathrm{C\,mol^{-1}}]$: Faraday constant;
- α_a, α_c (–): anodic/cathodic transfer coefficients;
- M $[\mathrm{kg\,mol^{-1}}]$: metal molar mass; ρ_{dep}
- $[\mathrm{kg\,m^{-3}}]$: deposit density; h [m]: deposit thickness;
- T [K] is the temperature;
- p [Pa] is the pressure.

The solved models for interfacial mass balance and bulk transport reads as follows. In the liquid domain Ω_ℓ,

$$\partial_t(\rho c) + \nabla\cdot(\rho \mathbf{u}\, c) = \nabla\cdot\left(\rho D_{\mathrm{eff}} \nabla c\right) - R_{\mathrm{bulk}}, \tag{4.1}$$

with density ρ, velocity $\mathbf{u}$, and any homogeneous source R_{bulk} (e.g., redox buffering). On a wall Γ, the interfacial molar flux J satisfies the standard mass balance

$$-\boldsymbol{n}\cdot(D_{\mathrm{eff}}\nabla c)\Big|_{\Gamma} = J, \tag{4.2}$$

where $\boldsymbol{n}$ is the unit normal pointing out of the liquid (into the solid).

At each wall quadrature point, which for the finite volume formulation are the cell centers, Thermochimica is queried with local (T,p) and the phase composition to return the *equilibrium*

dissolved concentration $c_{\mathrm{eq}}(T,p)$ of species i in the liquid. This value defines the reversible state of the half-reaction $\mathrm{Ox}^{z+} + n\,e^- \rightleftharpoons \mathrm{M}(s)$ at $\eta = 0$.

Within a diffusion sublayer of thickness δ, the liquid-side concentration drops from a near-bulk value c_b to the interfacial fluid value c_w. The *film* model gives

$$J \;=\; k_m\,(c_b - c_w)\,, \qquad k_m \equiv \frac{D}{\delta}. \tag{4.3}$$

Correlations provide k_m via a Sherwood number $\mathrm{Sh} = k_m d_h/D$ (e.g., $\mathrm{Sh} = 1.86\,(\mathrm{Re}\,\mathrm{Sc}\,d_h/L)^{1/3}$ for developing laminar flow, or $\mathrm{Sh} = 0.023\,\mathrm{Re}^{0.83}\mathrm{Sc}^{0.33}$ for fully turbulent internal flow), or via the Chilton–Colburn analogy $j_D = \mathrm{Sh}/(\mathrm{Re}\,\mathrm{Sc}^{1/3}) \approx f/2$. However, these correlations are very approximated and mostly valid for pipes. **Hence, in this work, we intended to directly compute the friction factor f directly from coarse mesh CFD model in MOOSE**. This is detailed in the following section.

For the reduction of Ox to metal, a first-order heterogeneous law consistent with Butler–Volmer reads

$$J \;=\; k_0\Big[\,c_w\,e^{-\alpha_c nF\eta/(RT)} \;-\; c_{\mathrm{eq}}(T,p)\,e^{+\alpha_a nF\eta/(RT)}\Big]\,, \tag{4.4}$$

which recovers $J = 0$ at $c_w = c_{\mathrm{eq}}$ and $\eta = 0$. The *exchange current density* i_0 measured at equilibrium links to k_0 by

$$i_0 \;=\; nF\,k_0\,c_{\mathrm{eq}}(T,p) \quad\Rightarrow\quad k_0 \;=\; \frac{i_0}{nF\,c_{\mathrm{eq}}(T,p)}. \tag{4.5}$$

Equating (4.3) and (4.4) and eliminating c_w yields

$$\begin{aligned} J &= \frac{k_m k_0\,e^{-\alpha_c nF\eta/(RT)}}{k_m + k_0\,e^{-\alpha_c nF\eta/(RT)}}\;\Big[c_b - c_{\mathrm{eq}}(T,p)\,e^{+\alpha_a nF\eta/(RT)}\Big] \\ &\equiv k_{\mathrm{eff}}(\eta)\,\Big[c_b - c^*_{\mathrm{eq}}(\eta)\Big], \qquad c^*_{\mathrm{eq}}(\eta) = c_{\mathrm{eq}}\,e^{+\alpha_a nF\eta/(RT)}. \end{aligned} \tag{4.6}$$

Interpreting the boundary value $c|_\Gamma$ as c_b, the liquid equation imposes the *Robin* condition

$$-\boldsymbol{n}\cdot(D_{\mathrm{eff}}\nabla c)\Big|_\Gamma \;=\; k_{\mathrm{eff}}(\eta)\,\Big[c - c^*_{\mathrm{eq}}(\eta)\Big], \qquad k_{\mathrm{eff}}(\eta) = \frac{k_m k_0\,e^{-\alpha_c nF\eta/(RT)}}{k_m + k_0\,e^{-\alpha_c nF\eta/(RT)}}. \tag{4.7}$$

This form is *bidirectional*: if $c > c^*_{\mathrm{eq}}$ then $J > 0$ (plating); if $c < c^*_{\mathrm{eq}}$ then $J < 0$ (corrosion).

The deposit grow and corrosion law can then be directly computed form this interface transfer process. Let J be the net molar flux of metal to the solid. The interfacial areal mass flux and thickness rate follow

$$\dot m'' \;=\; M\,J, \qquad \dot h \;=\; \frac{\dot m''}{\rho_{\mathrm{dep}}} \;=\; \frac{M}{\rho_{\mathrm{dep}}}\,J \;=\; \frac{M}{\rho_{\mathrm{dep}}}\,k_{\mathrm{eff}}(\eta)\,\Big[c - c^*_{\mathrm{eq}}(\eta)\Big]. \tag{4.8}$$

Negative J decreases h (corrosion), positive J increases h (plating). In a volumetric solid balance, the same J enters with opposite sign to (4.2), ensuring conservation across the interface.

Equation (4.7) is a *series-resistance* law. The driving force is the interfacial supersaturation on a molar basis, $c - c^*_{\mathrm{eq}}(\eta)$. Two resistances act in series: (i) transport across the film, with conductance k_m; and (ii) surface reaction, with conductance $k^*_0(\eta) = k_0\,e^{-\alpha_c nF\eta/(RT)}$. Their combination is the harmonic mean $k_{\mathrm{eff}} = (k_m^{-1} + k_0^{*-1})^{-1}$, which automatically selects the controlling mechanism

without ad hoc switches. Thermochimica provides $c_{\mathrm{eq}}(T,p)$; the electrochemical state shifts the reversible target to $c^*_{\mathrm{eq}}(\eta)$ and rescales the intrinsic surface rate to $k_0^*(\eta)$.

It is convenient to define the *Damköhler number* under overpotential,

$$\mathrm{Da}(\eta) \;\equiv\; \frac{k_0^*(\eta)}{k_m} \;=\; \frac{k_0\, e^{-\alpha_c nF\eta/(RT)}}{k_m}. \tag{4.9}$$

Then $k_{\mathrm{eff}} = k_m\,\mathrm{Da}/(1+\mathrm{Da})$ and:

$$\mathrm{Da} \gg 1 \quad\Rightarrow\quad k_{\mathrm{eff}} \to k_m,\;\; J \to k_m\Big[c - c^*_{\mathrm{eq}}(\eta)\Big],\;\; c_w \to c^*_{\mathrm{eq}}(\eta) \qquad \text{(mass-transfer-limited)}, \tag{4.10}$$

$$\mathrm{Da} \ll 1 \quad\Rightarrow\quad k_{\mathrm{eff}} \to k_0^*(\eta),\;\; J \to k_0^*(\eta)\Big[c - c^*_{\mathrm{eq}}(\eta)\Big],\;\; c_w \to c \qquad \text{(reaction-limited)}. \tag{4.11}$$

At *equilibrium* ($\eta = 0$ and $c = c_{\mathrm{eq}}$), $J = 0$ and (4.7) reduces to the no-flux condition. For *strong cathodic polarization* ($\eta \ll 0$), k_0^* grows and c^*_{eq} decreases, pushing the system toward the mass-transfer limit (4.10) (plating-dominated). For *strong anodic polarization* ($\eta \gg 0$), k_0^* decreases and c^*_{eq} increases, favoring corrosion with the reaction-limited form (4.11). Near equilibrium ($|\eta| \ll 1$ and $|c - c_{\mathrm{eq}}| \ll c_{\mathrm{eq}}$), linearization of (4.4) and the canonical Butler–Volmer gives the consistent small-signal relations

$$i = i_0\left[e^{\alpha_a nF\eta/(RT)} - e^{-\alpha_c nF\eta/(RT)}\right] \tag{4.12}$$

$$i_0 = nF\,k_0\,c_{\mathrm{eq}}, \qquad J \approx \frac{k_m k_0}{k_m + k_0}\Big(c - c_{\mathrm{eq}}\Big), \tag{4.13}$$

validating the mixed-control form and the unit-consistent link between electrochemistry and molar transport.

From internal-flow correlations, $k_m = \mathrm{Sh}\,D/d_h$, with Sh from a geometry-appropriate correlation (e.g., developing laminar or fully turbulent forms noted above). From RANS fields, the Chilton–Colburn relation with the friction factor $f = 2\tau_w/(\rho u_b^2)$ gives $k_m = \dfrac{D}{d_h}\dfrac{f}{2}\,\mathrm{Re}\,\mathrm{Sc}^{1/3}$. Clip k_m against the first-cell height Δy_1 via $D/(10\Delta y_1) \le k_m \le D/\Delta y_1$ for numerical robustness.

Use (4.5) directly from measured i_0 and Thermochimica's $c_{\mathrm{eq}}(T,p)$. At operating overpotential η, use $k_0^*(\eta) = k_0 \exp(-\alpha_c nF\eta/(RT))$.

In the liquid species equation, impose (4.7) as a boundary flux. On the solid side (e.g., a surface areal density or a near-wall volumetric accumulator), add the same interfacial molar rate J with opposite sign to preserve conservation.

At each wall quadrature point, query Thermochimica for $c_{\mathrm{eq}}(T,p)$, form $c^*_{\mathrm{eq}}(\eta)$ and $k_0^*(\eta)$, evaluate k_m, then assemble $k_{\mathrm{eff}}(\eta)$ and J via (4.6). Thickness evolves by (4.8); hydraulic feedback may be modeled by increasing roughness $k_s \propto h$ or by geometric update if h/d_h ceases to be small.

All concentrations are in $\mathrm{mol\,m^{-3}}$; diffusivities in $\mathrm{m^2\,s^{-1}}$; k_m, k_0, and k_{eff} in $\mathrm{m\,s^{-1}}$; J in $\mathrm{mol\,m^{-2}\,s^{-1}}$; current density i in $\mathrm{A\,m^{-2}}$ with $J = i/(nF)$ when needed; $\dot{m}''$ in $\mathrm{kg\,m^{-2}\,s^{-1}}$; and $\dot{h}$ in $\mathrm{m\,s^{-1}}$. This guarantees that the interfacial mass balance (4.2) and the growth law (4.8) are dimensionally consistent.

4.2 Friction Factor Modeling with Improved $k-\varepsilon$ Models

As observed in the previous section, the mass transport in the plating and corrosion processes are highly dependent on the friction factor computed at the wall. For internal, fully developed flow of

bulk (section-mean) speed U_b, the wall shear stress τ_w defines the *shear velocity* $u_\star$ and the friction factors

$$u_\star \;=\; \sqrt{C_\mu^{0.5} k} \;\approx\; \sqrt{\tau_w/\rho}, \qquad C_f \;\equiv\; \frac{2\,\tau_w}{\rho U_b^2}, \qquad f_D \;\equiv\; \frac{8\,\tau_w}{\rho U_b^2} \;=\; 4C_f, \tag{4.14}$$

where C_f is the (skin) friction coefficient and f_D is the Darcy–Weisbach friction factor used in corrosion model. Note that these model hinges upon the computed turbulent kinetic energy k and bulk velocity for the cell near the wall U_b, which are computed by the RANS model. In RANS with an eddy viscosity closure, the mean wall-parallel stress is

$$\tau \;=\; (\mu+\mu_t)\,\frac{\partial U_\parallel}{\partial n}, \quad \Rightarrow \quad \tau_w \;=\; \mu\,\left.\frac{\partial U_\parallel}{\partial n}\right|_w, \tag{4.15}$$

because $\mu_t \to 0$ at the wall within the viscous sublayer. Equations (4.14)–(4.15) provide a consistent route to $u_\star$, C_f, and f_D directly from the resolved near-wall gradient or, when using wall functions, via the log law.

As the baseline RANS model, we use the standard two-equation $k-\varepsilon$ model with a Boussinesq stress relation

$$-\rho\,\overline{u_i' u_j'} \;=\; 2\mu_t S_{ij} - \tfrac{2}{3}\rho k\,\delta_{ij}, \qquad S_{ij} \equiv \tfrac{1}{2}(\partial_i U_j + \partial_j U_i)\,, \qquad \mu_t \;=\; \rho\,C_\mu\,\frac{k^2}{\varepsilon},$$

and transport equations

$$\partial_t(\rho k) + \nabla\cdot(\rho \mathbf{U} k) = \nabla\cdot\left[\left(\mu + \frac{\mu_t}{\sigma_k}\right)\nabla k\right] + P_k + G_b - \rho\varepsilon, \tag{4.16}$$

$$\partial_t(\rho \varepsilon) + \nabla\cdot(\rho \mathbf{U}\,\varepsilon) = \nabla\cdot\left[\left(\mu + \frac{\mu_t}{\sigma_\varepsilon}\right)\nabla \varepsilon\right] + C_{\varepsilon 1}\,\frac{\varepsilon}{k}\,(P_k + C_3\,G_b) - C_{\varepsilon 2}\,\rho\,\frac{\varepsilon^2}{k}. \tag{4.17}$$

Here $P_k \equiv 2\mu_t S_{ij} S_{ij}$ is shear production and G_b is buoyancy production. Default constants are $C_\mu = 0.09$, $C_{\varepsilon 1} = 1.44$, $C_{\varepsilon 2} = 1.92$, $\sigma_k = 1.0$, $\sigma_\varepsilon = 1.3$. For molten salts we take a turbulent Schmidt and Prandtl number $Sc_t \simeq 0.9$ and $Pr_t \simeq 0.9$. This number can be futher improved in the future with DNS data and utilizing Pronghorn's HOLO framework.

Two practical regimes are used for near-wall treatment in this extended $k-\varepsilon$ treatment: (i) *Wall-resolved* (small y^+), where τ_w follows (4.15) from the viscous sublayer and no empirical wall law is needed; note that this modeling approach requires non-equilibrium wall treatment. (ii) *High-Re wall functions* (first node in the logarithmic layer), where the mean velocity satisfies

$$U^+ \;=\; \frac{1}{\kappa}\ln y^+ + B - \Delta U_R^+ - \Delta U_B^+, \qquad U^+ \equiv \frac{U_\parallel}{u_\star},\; y^+ \equiv \frac{y\,u_\star}{\nu}, \tag{4.18}$$

with von Kármán constant $\kappa \approx 0.41$, smooth-wall intercept $B \approx 5.2$, and optional corrections ΔU_R^+ (equivalent sand-roughness) and ΔU_B^+.

Consistent wall-function values for the turbulence variables at the first off-wall point are

$$k_p \;=\; \frac{u_\star^2}{\sqrt{C_\mu}}, \qquad \varepsilon_p \;=\; \frac{u_\star^3}{\kappa\, y_p}, \tag{4.19}$$

which tie the closure to the inferred $\tau_w = \rho u_\star^2$. Equations (4.18)–(4.19) determine $u_\star$ and thus $f_D = 8(u_\star/U_b)^2$.

Thermal stratification and natural-convection-driven acceleration modifies turbulence through buoyancy. Under the Boussinesq approximation with thermal expansion β, gravity $\mathbf{g}$, and temperature T,

$$G_b \;=\; \beta\,\frac{\mu_t}{\mathrm{Pr}_t}\,\mathbf{g}\cdot\nabla T, \tag{4.20}$$

so that unstable (heating from below; $\mathbf{g}\cdot\nabla T<0$) gives $G_b>0$ (turbulence production), while stable stratification yields $G_b<0$ (damping).

The ε-equation uses a buoyancy-weighting C_3 to modulate how G_b feeds the dissipation:

$$\partial_t(\rho\varepsilon)+\ldots \supset C_{\varepsilon 1}\,\frac{\varepsilon}{k}\,\underbrace{(P_k+C_3\,G_b)}_{\text{net production}}. \tag{4.21}$$

A robust choice that preserves neutrality and avoids discontinuities is

$$C_3 \;=\; \tfrac{1}{2}\left[1+\tanh\!\left(\frac{G_b}{\delta\,|P_k|+\varepsilon_{\mathrm{m}}}\right)\right], \tag{4.22}$$

with $\delta\sim 0.1$ and a small ε_{m} to prevent division by zero.

Equation (4.22) makes $C_3\to 1$ for strongly destabilizing buoyancy ($G_b\gg 0$, aiding turbulence) and $C_3\to 0$ for stabilizing buoyancy ($G_b<0$), recovering the standard shear-dominated form when $G_b\approx 0$.

For log-law wall functions, buoyancy also alters the mean profile; ΔU_B^+ can be accounted for by integrating the Monin–Obukhov similarity correction or by local blending of (4.18) with a buoyant wall function using the Obukhov length L (not shown for brevity). In all cases, friction factors computed via $u_\star$ will increase (decrease) for destabilizing (stabilizing) stratification at fixed U_b.

The re-laminarization and turbulence damping are introduced via functional damping. Turbulence weakens in near-wall viscous regions, in accelerating streams, and at low Reynolds numbers. To enforce the correct *viscous sublayer* limit and obtain physically consistent friction at moderate Re, we use a low-Re $k-\varepsilon$ formulation

$$\mu_t \;=\; \rho\,C_\mu\,f_\mu\,\frac{k^2}{\varepsilon}, \qquad \partial_t(\rho\varepsilon)+\ldots \supset C_{\varepsilon 1}\,f_1\,\frac{\varepsilon}{k}\,P_k + C_{\varepsilon 2}\,f_2\,\rho\,\frac{\varepsilon^2}{k}, \tag{4.23}$$

with damping functions f_μ, f_1, f_2.

The re-laminatization implemented is a hybrid between the generally used Lam–Bremhorst type, which are able to recover the high-Re number model for the bulk of the flow, and the Chien type, which are able to better recover the linear law of the near wall behavior by dampening the turbulent viscosity with the distance to the wall. The re-laminarization model reads as follows:

$$f_\mu \;=\; 1-\exp\!\Big[-\Big(0.091\sqrt{Re_d}+0.0042Re_d+0.00011Re_d^2\Big)\Big], \tag{4.24}$$

$$f_2 \;=\; 1-0.3\,\exp(-Re_t^2), \tag{4.25}$$

$$f_1 \;=\; 1, \tag{4.26}$$

where $Re_t=\frac{k^2}{\nu\varepsilon}$ and $Re_d=\frac{\sqrt{k}}{\nu d}$, where d is the distance to the nearest wall. These choices guarantee $\mu_t\to 0$ at the wall, recover the linear law $U^+\approx y^+$ in the viscous sublayer, and collapse to the standard high-Re model for $Re_t\gg 1$. Also, this form dampens μ_t based on wall distance and similarly restores the correct viscous limit.

With this formulation, $\mu_t \to 0$ as $Re_d \to 0$, so τ_w is governed by the molecular term $\mu\,\partial U_\parallel/\partial n$ in (4.15), yielding the correct laminar scalings $C_f \to 2\times 16/Re$ (pipe: $f_D \to 64/Re$) as Re decreases or the flow rapidly accelerates (re-laminarization). At high Re_t, $f_\mu \to 1$, $f_2 \to 1$, and the closure reverts to the standard high-Re $k-\varepsilon$, reproducing the log law and canonical turbulent friction.

The solution algorithm is implemented in the linear solver of Pronghorn and goes as follows:

1. Solve (4.16)–(4.17) with μ_t from either the standard or low-Re form (4.23), with G_b from (4.20) and C_3 from (4.22).
2. Evaluate $\tau_w = \mu\,(\partial U_\parallel/\partial n)_w$ and compute $u_\star = \sqrt{\tau_w/\rho}$ and $f_D = 8(u_\star/U_b)^2$ via (4.14)(wall-resolved) or infer $u_\star$ from (4.18)–(4.19).
3. (Optional) For scalar mass transfer, use the Chilton–Colburn analogy $j_D \equiv \mathrm{Sh}/(\mathrm{Re}\,\mathrm{Sc}^{1/3}) \approx C_f/2 = f_D/8$ to obtain Sh and thus $k_m = \mathrm{Sh}D/d_h$. Improved f_D from buoyancy and low-Re corrections therefore feeds directly into interfacial mass-transfer modeling.

The asymptotic behavior of the model is as follows:

- **Neutral stratification** $(G_b = 0)$: $C_3 \to 1/2$ in (4.22) and the net production reduces to the shear term. Friction recovers the canonical turbulent correlations in the high-Re limit.
- **Unstable stratification** $(G_b > 0)$: $C_3 \to 1$, buoyancy augments production, increasing μ_t, $u_\star$, and f_D at fixed U_b.
- **Stable stratification** $(G_b < 0)$: $C_3 \to 0$, buoyancy subtracts from production in (4.21) and weakens turbulence, decreasing f_D.
- **Low-Re/relaminarization** $(Re_t \to 0)$: $f_\mu \to 0$, $f_2 \to 0.7$ (Lam–Bremhorst) or remains bounded (Chien), $\mu_t \to 0$, and the near-wall solution tends to $U^+ \approx y^+$ with $f_D \to 64/Re$ in a pipe.
- **Rough-wall at High-Re**: with $\Delta U_R^+ > 0$ in (4.18), the inferred $u_\star$ increases for a given U_b, giving a larger f_D as expected.

The combined buoyancy and low-Re corrections thus deliver a closure that preserves the correct viscous and turbulent limits, improves friction predictions across regimes encountered in molten-salt systems, and remains consistent with interfacial mass-transfer estimates used in the plating/corrosion model.

4.3 Verification cases

This section defines verification problems that isolate and test the contributions of (i) buoyancy production G_b with its C_3 weighting, and (ii) low–Re re-laminarization damping in the $k-\varepsilon$ model, as they affect the predicted wall shear and friction factor

$$u_\star = \sqrt{\tau_w/\rho}, \qquad C_f = \frac{2\tau_w}{\rho U_b^2}, \qquad f_D = 4C_f = \frac{8\tau_w}{\rho U_b^2}.$$

For all cases we:

1. Compute the section-mean bulk speed U_b and wall shear $\tau_w = \mu(\partial U_\parallel/\partial n)_w$.

2. Report $f_D = 8\tau_w/(\rho U_b^2)$.

3. Convergence is demonstrated when mesh refinement (wall-resolved: $\max y^+ \lesssim 1$; wall-function: $30 \lesssim y^+ \lesssim 100$) changes f_D by less than 0.5%.

4. Unless otherwise specified, accept a verification tolerance of $\pm 2\%$ to analytic/benchmark values for isothermal cases, and $\pm 5\%$ for buoyant cases (owing to property- and profile-sensitivity).

4.3.1 Case A: Isothermal Baseline (No Buoyancy, No Damping)

The purpose of the test is to establish the code path from wall gradient to f_D without buoyancy or low-Re damping.

The geometry is a 2D pipe, height $D = 0.05$ m, length $L = 25D$, incompressible liquid ($\rho = 2400\ \mathrm{kg\,m^{-3}}$, $\mu = 3.0 \times 10^{-3}$ Pa s). Isothermal walls and inlet; fully developed outlet (zero-gradient). The descriptions of the tests and status are summarized in Table 4.1. The pass criteria for A1 within 1% of $64/Re$; A3 within 2% the Churchill correlation. Both tests are passing.

Table 4.1: Results for Tests A.

Run	Regime	Target	Comment	Error	Status
A1	Laminar $Re = 50$	$f_D = 64/Re$	Exact Poiseuille	$\leq 0.01\%$	PASS
A2	Transitional $Re = 3000$	$\uparrow f_D$ vs A3	Damping off	NA	PASS
A3	Turbulent $Re = 10^5$	Canonical $k-\varepsilon$	Match Churchill Correlation	0.2%	PASS

4.3.2 Case B: Low-Re Re-Laminarization (Damping Functions On)

The purpose is to verify that the low-Re damping recovers laminar friction as Re decreases or under acceleration.

The geometry and boundary conditions are the as Case A. We enable the low-Re f_μ, f_1, f_2 damping explained in Section 4.2. We define two subcases:

B1: Quasi-steady low Re.

We run a sequence $Re = \{500, 1000, 2000, 3000\}$ with flat inlet profile. We expect

$$\mu_t \to 0 \text{ as } Re \downarrow, \quad f_D \to 64/Re.$$

The criteria for passing is that each point within 3% of $64/Re$; monotone transition across $Re \approx 2300$.

Table 4.2: Results for Tests B1.

Run	Re	f_D	Error	Average μ_t/μ	Status
B1.1	$Re = 500$	$f_D = 0.128$	$\leq 0.01\%$	$\leq 10^{-10}$	PASS
B1.2	$Re = 1,000$	$f_D = 0.064$	$\leq 0.01\%$	$\leq 10^{-10}$	PASS
B1.3	$Re = 2,000$	$f_D = 0.033$	3%	$\leq 6.2 \times 10^{-3}$	PASS
B1.4	$Re = 3,000$	$\downarrow f_D$ vs B1.3	NA	$\leq 1.4 \times 10^{-2}$	PASS

B2: Favorable pressure-gradient acceleration.

We impose an axial pressure drop that linearly decreases along x: $\mathrm{d}p/\mathrm{d}x = \text{const} \times (1 - x/L)$. We keep inlet $Re \approx 6,000$ (turbulent) and outlet $Re \approx 1,000$ (laminar). We expect re-laminarization: $Re_t \to 0$ downstream, $\mu_t \to 0$, and f_D smoothly approaching $64/Re(x)$. The passing criteria is that for the end of the channel, when the flow re-laminarizes, the local $f_D(x)$ within 5% of $64/Re(x)$ for the last $5D$. The results are depicted in Figure 4.1. The status of the test is PASS.

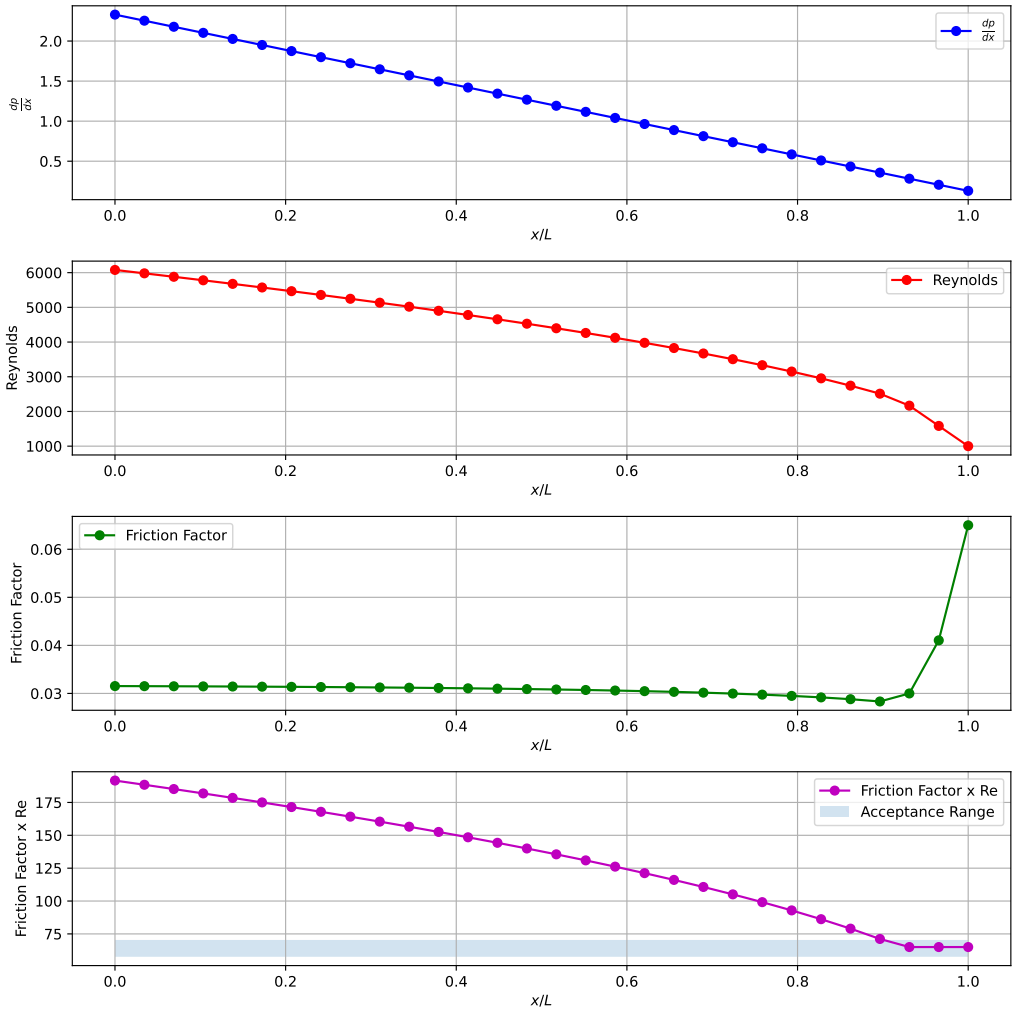

Figure 4.1: Results for test B2. The status of the test is PASS.

4.3.3 Case C: Pure Buoyancy Effect in Vertical Channels with Aiding vs. Opposing buoyancy

The purpose of the test is to isolate G_b and the C_3 weighting in the ε equation. The geometry consist of a vertical 2D plane channel (gap $H = 0.02$ m, width $W = 0.2$ m, length $L = 60H$), uniform inlet mass flow specifying $Re = 20{,}000$ (turbulent). Constant wall heat flux q'' on both walls; constant fluid properties with thermal expansion $\beta = 1 \times 10^{-4}$ K^{-1}. Gravity $\mathbf{g} = (0, 0, -g)$.

Two orientations are analyzed:

- Aiding buoyancy (heated upward flow): inlet at bottom, flow upward, walls heated: $\mathbf{g}\cdot\nabla T < 0 \Rightarrow G_b > 0$.
- Opposing buoyancy (heated downward flow): inlet at top, flow downward, walls heated: $\mathbf{g}\cdot\nabla T > 0 \Rightarrow G_b < 0$.

We define a friction-scaled Richardson number

$$\mathrm{Ri}_\tau \equiv \frac{-G_b}{P_k} = -\frac{\beta(\mathbf{g}\cdot\nabla T)}{2S_{ij}S_{ij}}\,\frac{\mu_t}{\mathrm{Pr}_t}\,\frac{1}{\mu_t},$$

which reduces numerically to $|\mathrm{Ri}_\tau| \approx \beta g H \Delta T/(U_b^2)$ for order-of-magnitude planning. Vary Ri_τ by sweeping q'' to obtain $\mathrm{Ri}_\tau = \pm\{0, 0.05, 0.1, 0.2\}$.

With the C_3 model in Section 4.2 the following behavior is expected:

$$C_3 \to 1 \text{ (aiding)} \quad \Rightarrow \quad f_D \uparrow, \qquad C_3 \to 0 \text{ (opposing)} \quad \Rightarrow \quad f_D \downarrow,$$

at fixed Re. Quantify $\Delta f_D/f_D|_{\mathrm{iso}}$ vs Ri_τ.

For the passing criteria, we expect monotonic increase with aiding buoyancy and monotonic decrease with opposing of f_D with Ri_τ and symmetry at $\mathrm{Ri}_\tau \to 0$. For verifying monotonicity and symmetric, a linear fitting is performing on the friction factors. The results obtained are presented in Table 4.3.

Table 4.3: Results for Tests C.

Run	Re	Ri	Buoyancy Type	f_D	Expected f_D	Status
C1	$Re = 20,000$	$Ri = -0.2$	Adding	0.023347	0.0233	PASS
C2	$Re = 20,000$	$Ri = -0.1$	Adding	0.024615	0.0246	PASS
C3	$Re = 20,000$	$Ri = -0.05$	Adding	0.025249	0.0252	PASS
C4	$Re = 20,000$	$Ri = 0.0$	NA	0.025883	NA	NA
C5	$Re = 20,000$	$Ri = 0.05$	Opposing	0.026517	0.0265	PASS
C6	$Re = 20,000$	$Ri = 0.1$	Opposing	0.027151	0.0271	PASS
C7	$Re = 20,000$	$Ri = 0.2$	Opposing	0.028420	0.0284	PASS

4.3.4 Case D: Horizontal Pipe with Thermal Stratification

The purpose of the test is to assess buoyancy effects when ∇T is primarily vertical while the mean shear is streamwise. The geometry is the same horizontal pipe then Case A. Apply a liner volumetric heating $Q'''/(\rho C_p) = cyK/s$, where c is a constant and y is the coordinate across the height of the channel, such that the cross-section develops a stable vertical temperature gradient (∇T colder at bottom). We set $Re = 50{,}000$ and use uniform thermophysical properties throughout.

As comparison metric, we compare the wall shear at top and bottom, f_D^{top} vs f_D^{bot}, and the section-averaged f_D. We expect $f_D^{\mathrm{bot}} < f_D^{\mathrm{top}}$ under stable stratification, i.e., reduced turbulence near the colder wall. Additionally, we expect the f_D decreases vs isothermal baseline. The results foe these tests are presented in Table 4.4.

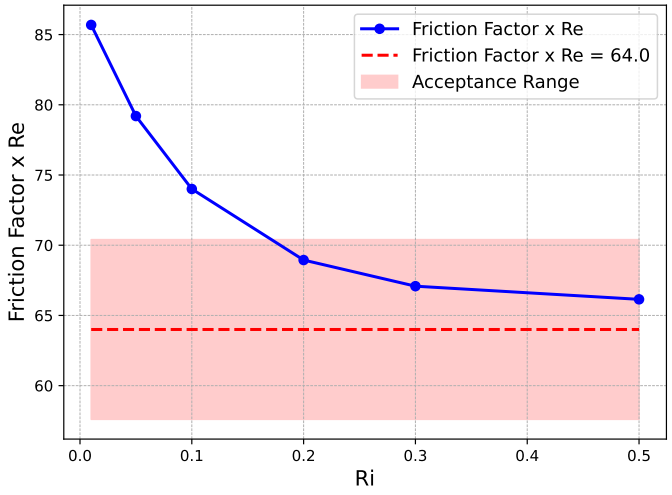

Figure 4.2: Results for Test E.

Table 4.4: Results for Tests D.

Run	Re	c	f_D^{top}	f_D^{bot}	Average f_D	Status
D1	$Re = 50,000$	0.0	0.020891	0.020891	0.020891	NA
D2	$Re = 50,000$	1.0	0.021623	0.020055	0.020839	PASS
D3	$Re = 50,000$	5.0	0.022535	0.019013	0.020774	PASS
D4	$Re = 50,000$	10.0	0.023227	0.018222	0.020725	PASS

4.3.5 Case E: Coupled Buoyancy with Re-Laminarization at Moderate Reynolds Number

The purpose of the test is verify the interplay of negative G_b (stabilizing) and low-Re damping. The geometry of the test consists of a vertical channel, $Re = 4{,}000$, which is weakly turbulent, opposing-buoyancy setup as in Case C. Then, we sweep the heat flux at the wall q'' to achieve $\text{Ri}_\tau = \{0, 0.05, 0.1\}$.

As Ri_τ increases, turbulence weakens, Re_t near the wall drops, damping functions further reduce μ_t, and the near-wall mean approaches the viscous sublayer. The predicted f_D transitions toward the laminar trend $64/Re$ even though the nominal $Re = 4000$. For the passing criteria f_D decreases with Ri_τ and approaches within 10% of $64/Re$ at the highest forcing. The results of the test are presented in Figure 4.2. As the re-laminarization of appropriately modeled causing the friction factors to fall within the acceptability range, the status of this test is PASS.

4.3.6 Case F (MMS): Manufactured Source to Verify G_b and Damping Implementation

The purpose of this test is to isolate code-level correctness of the buoyancy and damping terms by comparing to an *exact* manufactured solution.

The geometry consists of a 3D channel $y \in [-H, H]$, streamwise x, wall-normal y, spanwise z. The walls are at $y = \{-H, H\}$; the symmetry plane is at $y = 0$. Gravity is $\boldsymbol{g} = g_y \boldsymbol{e}_y$ (positive

downward; we choose $g_y < 0$ for upward buoyancy-aiding flows, $g_y > 0$ for opposing).

The manufactures solution is for a steady state 1-D in y. We prescribe smooth profiles for the mean velocity, temperature, turbulent kinetic energy, and dissipation:

$$U_{\parallel}(y) = U_0\left[1-\left(\frac{y}{H}\right)^2\right], \qquad T(y) = T_0 + \Delta T\,\frac{y}{H}, \tag{4.27}$$

$$k(y) = k_0\left(\frac{y}{H}\right)^2, \qquad \varepsilon(y) = \varepsilon_0\left(\frac{y}{H}\right)^2, \tag{4.28}$$

with constants $U_0, T_0, \Delta T, k_0, \varepsilon_0 > 0$. These fields satisfy the physical symmetry conditions $U_{\parallel}(H) = 0$, $(\partial_y U_{\parallel})(0) = 0$, T linear, and $k, \varepsilon \to 0$ at the centerline ($y \to 0$).

The eddy viscosity and the k–ε production/consumption terms follow the low-Re form (Sec. 4.2):

$$\mu_t(y) = \rho\, C_\mu\, f_\mu(y)\,\frac{k^2}{\varepsilon}, \qquad P_k(y) = 2\mu_t S_{ij}S_{ij}, \qquad G_b(y) = \beta\,\frac{\mu_t}{\mathrm{Pr}_t}\,\boldsymbol{g}\cdot\nabla T,$$

with damping functions f_μ, f_1, f_2 and optional E_ε; buoyancy enters the ε equation via C_3.

For $U_i = (U_{\parallel}(y), 0, 0)$, the only nonzero gradients are $\partial_y U_{\parallel}$; the symmetric strain-rate tensor is

$$S_{xy} = S_{yx} = \tfrac{1}{2}\,\partial_y U_{\parallel}, \qquad S_{ij} = 0 \text{ otherwise.}$$

From (4.27),

$$\partial_y U_{\parallel} = -\frac{2U_0}{H^2}\,y, \qquad S_{xy} = S_{yx} = -\frac{U_0}{H^2}\,y.$$

The invariant needed in P_k is

$$2S_{ij}S_{ij} = (\partial_y U_{\parallel})^2 = \frac{4U_0^2}{H^4}\,y^2, \qquad \Rightarrow \qquad P_k(y) = \mu_t(y)\,\frac{4U_0^2}{H^4}\,y^2.$$

From (4.27),

$$\nabla T = (0,\ \partial_y T,\ 0) = (0,\ \Delta T/H,\ 0), \qquad \boldsymbol{g}\cdot\nabla T = g_y\,\frac{\Delta T}{H}\ \ \text{(constant)}.$$

With (4.28),

$$\frac{k^2}{\varepsilon} = \frac{k_0^2}{\varepsilon_0}\,\frac{y^2}{H^2}, \qquad \Rightarrow \quad \mu_t(y) = \underbrace{\rho C_\mu\,\frac{k_0^2}{\varepsilon_0}}_{A_\mu}\,f_\mu(y)\,\frac{y^2}{H^2}.$$

Its y-derivative (needed in diffusive terms) is

$$\mu_t'(y) = A_\mu\left[\frac{2y}{H^2}\,f_\mu(y) + \frac{y^2}{H^2}\,f_\mu'(y)\right],$$

with chain rule

$$f_\mu'(y) = \frac{\mathrm{d}f_\mu}{\mathrm{d}Re_t}\,\frac{\mathrm{d}Re_t}{\mathrm{d}y}, \qquad \frac{\mathrm{d}Re_t}{\mathrm{d}y} = \frac{2\,Re_{t0}}{H^2}\,y, \quad Re_{t0} \equiv \frac{\rho\,k_0^2}{\mu\,\varepsilon_0}.$$

We use for the damping functions the Lam–Bremhorst profile as follows:

$$\frac{\mathrm{d}f_\mu}{\mathrm{d}Re_t} = f_\mu\,\frac{6.8}{50}\,\frac{1}{\left(1+Re_t/50\right)^3}, \qquad \Rightarrow\ f_\mu'(y) = f_\mu\,\frac{6.8}{50}\,\frac{1}{\left(1+Re_t/50\right)^3}\,\frac{2Re_{t0}}{H^2}\,y.$$

Because $\boldsymbol{g}\cdot\nabla T$ is constant,

$$G_b(y) = \beta\,\frac{\mu_t(y)}{\mathrm{Pr}_t}\,\boldsymbol{g}\cdot\nabla T = \beta\,\frac{A_\mu}{\mathrm{Pr}_t}\,\frac{y^2}{H^2}\,f_\mu(y)\left(g_y\,\frac{\Delta T}{H}\right).$$

With (4.28),

$$Re_t(y) = \frac{\rho\,k^2}{\mu\,\varepsilon} = \frac{\rho\,k_0^2}{\mu\,\varepsilon_0}\,\frac{y^2}{H^2} \equiv Re_{t0}\,\frac{y^2}{H^2}.$$

Once these quantities derived the forcing functions to add as sources to the turbulent model formulation can be derived. We write the *steady*, *1-D* balances (no streamwise derivatives, no advection of k,ε) and add manufactured sources so that the prescribed fields are exact solutions.

With pressure gradient $\partial_x p$ and a body-force/source $S_m(y)$,

$$0 = -\partial_x p + \frac{\mathrm{d}}{\mathrm{d}y}\left[\big(\mu+\mu_t(y)\big)\,\frac{\mathrm{d}U_\parallel}{\mathrm{d}y}\right] + S_m(y). \tag{4.29}$$

Using $\frac{\mathrm{d}U_\parallel}{\mathrm{d}y} = -\frac{2U_0}{H^2}y$ and $\mu_t'(y)$ above,

$$\frac{\mathrm{d}}{\mathrm{d}y}\Big[(\mu+\mu_t)U_\parallel'\Big] = \mu_t'(y)\,\Big(-\frac{2U_0}{H^2}y\Big) + \big(\mu+\mu_t(y)\big)\,\Big(-\frac{2U_0}{H^2}\Big).$$

Therefore the *manufactured momentum forcing* that makes (4.29) hold is:

$$\boxed{\,S_m(y) = \partial_x p + \frac{2U_0}{H^2}\,\Big[\;\mu+\mu_t(y)+y\,\mu_t'(y)\;\Big]\,}. \tag{4.30}$$

Two convenient choices are: (a) set $\partial_x p = 0$ and use (4.30) as-is; or (b) choose a constant $\partial_x p$ to remove the section-average of S_m.

The steady 1-D k-equation with source $S_k(y)$ reads as follows:

$$0 = \frac{\mathrm{d}}{\mathrm{d}y}\left[\Big(\mu+\frac{\mu_t}{\sigma_k}\Big)\frac{\mathrm{d}k}{\mathrm{d}y}\right] + P_k(y) + G_b(y) - \rho\,\varepsilon(y) + S_k(y). \tag{4.31}$$

From (4.28), $\mathrm{d}k/\mathrm{d}y = 2k_0\,y/H^2$ and $\mathrm{d}^2k/\mathrm{d}y^2 = 2k_0/H^2$. Hence,

$$\frac{\mathrm{d}}{\mathrm{d}y}\left[\Big(\mu+\frac{\mu_t}{\sigma_k}\Big)\frac{\mathrm{d}k}{\mathrm{d}y}\right] = \Big(\mu+\frac{\mu_t}{\sigma_k}\Big)\frac{2k_0}{H^2} + \frac{\mu_t'}{\sigma_k}\,\frac{2k_0\,y}{H^2}.$$

Using $P_k(y) = \mu_t(4U_0^2/H^4)y^2$ and $G_b(y)$ from above, the *manufactured k-forcing* is

$$\boxed{\begin{aligned} S_k(y) = &-\Big(\mu+\frac{\mu_t}{\sigma_k}\Big)\frac{2k_0}{H^2} - \frac{\mu_t'}{\sigma_k}\,\frac{2k_0\,y}{H^2} \\ &- \mu_t\,\frac{4U_0^2}{H^4}\,y^2\beta\,\frac{\mu_t}{\mathrm{Pr}_t}\left(g_y\,\frac{\Delta T}{H}\right) + \rho\,\varepsilon_0\left(\frac{y}{H}\right)^2. \end{aligned}} \tag{4.32}$$

The steady 1-D ε-equation with low-Re coefficients, buoyancy weighting C_3, and source $S_\varepsilon(y)$ is

$$0 = \frac{\mathrm{d}}{\mathrm{d}y}\left[\Big(\mu+\frac{\mu_t}{\sigma_\varepsilon}\Big)\frac{\mathrm{d}\varepsilon}{\mathrm{d}y}\right] + C_{\varepsilon 1}\,f_1\,\frac{\varepsilon}{k}\,P_k + C_{\varepsilon 1}\,\frac{\varepsilon}{k}\,C_3\,G_b C_{\varepsilon 2}\,f_2\,\rho\,\frac{\varepsilon^2}{k} + E_\varepsilon + S_\varepsilon(y). \tag{4.33}$$

From (4.28), $\mathrm{d}\varepsilon/\mathrm{d}y = 2\varepsilon_0\, y/H^2$ and $\mathrm{d}^2\varepsilon/\mathrm{d}y^2 = 2\varepsilon_0/H^2$. Therefore

$$\frac{\mathrm{d}}{\mathrm{d}y}\left[\left(\mu + \frac{\mu_t}{\sigma_\varepsilon}\right)\frac{\mathrm{d}\varepsilon}{\mathrm{d}y}\right] = \left(\mu + \frac{\mu_t}{\sigma_\varepsilon}\right)\frac{2\varepsilon_0}{H^2} + \frac{\mu_t'}{\sigma_\varepsilon}\,\frac{2\varepsilon_0\, y}{H^2}.$$

Using P_k and G_b from above, and the manufactured ratio

$$\frac{\varepsilon}{k} = \frac{\varepsilon_0}{k_0} \quad \text{(constant in } y\text{)},$$

the *manufactured ε-forcing* that closes (4.33) is

$$\boxed{\begin{aligned} S_\varepsilon(y) = &-\left(\mu + \frac{\mu_t}{\sigma_\varepsilon}\right)\frac{2\varepsilon_0}{H^2} - \frac{\mu_t'}{\sigma_\varepsilon}\,\frac{2\varepsilon_0\, y}{H^2} \\ &- C_{\varepsilon 1}\, f_1\, \frac{\varepsilon_0}{k_0}\,\mu_t\,\frac{4U_0^2}{H^4}\, y^2 C_{\varepsilon 1}\,\frac{\varepsilon_0}{k_0}\, C_3\,\beta\,\frac{\mu_t}{\mathrm{Pr}_t}\left(g_y\,\frac{\Delta T}{H}\right) \\ &+ C_{\varepsilon 2}\, f_2\,\rho\,\frac{\varepsilon_0^2}{k_0} \;-\; E_\varepsilon(y). \end{aligned}} \tag{4.34}$$

A common low-Re choice for the viscous term is

$$E_\varepsilon(y) = 2\nu\left(\partial_y\sqrt{k}\right)^2 = \frac{\nu}{2k}\left(\partial_y k\right)^2 = \frac{\nu}{2\,k_0(y/H)^2}\left(\frac{2k_0\, y}{H^2}\right)^2 = \frac{2\nu\, k_0}{H^2},$$

which is constant for the manufactured $k(y)$.

If you also verify the temperature equation, write a steady 1-D advection–diffusion balance with source $S_T(y)$:

$$0 = \frac{\mathrm{d}}{\mathrm{d}y}\left[k_{\mathrm{eff}}(y)\,\frac{\mathrm{d}T}{\mathrm{d}y}\right] + S_T(y), \quad k_{\mathrm{eff}} = \lambda + \rho c_p\,\frac{\mu_t}{\mathrm{Pr}_t},$$

with $\mathrm{d}T/\mathrm{d}y = \Delta T/H$ and $\mathrm{d}^2T/\mathrm{d}y^2 = 0$, giving

$$\boxed{S_T(y) = -\frac{\mathrm{d}}{\mathrm{d}y}\left[k_{\mathrm{eff}}(y)\,\frac{\Delta T}{H}\right] = -\frac{\Delta T}{H}\,k_{\mathrm{eff}}'(y) = -\frac{\Delta T}{H}\,\rho c_p\,\frac{\mu_t'(y)}{\mathrm{Pr}_t}}. \tag{4.35}$$

The manufactured fields (4.27)–(4.28) together with the analytic derivatives above produce *exact* steady solutions of the 1-D RANS–k–ε system when the sources $\{S_m, S_k, S_\varepsilon, S_T\}$ in (4.30), (4.32), (4.34), (4.35) are applied. Buoyancy enters *both* k and ε equations via $G_b(y)$, and the C_3 weighting is explicitly present in (4.34). Low-Re effects are embedded through f_μ, f_1, f_2 in μ_t and the modeled production/sink terms; only f_μ requires a derivative (through μ_t'). For Lam–Bremhorst, f_μ' is given explicitly; for other forms (e.g., Chien), substitute the corresponding $\mathrm{d}f_\mu/\mathrm{d}Re_t$. All terms are smooth polynomials in y multiplied by bounded damping factors, so the MMS is well-conditioned and grid-convergent. Near $y = 0$, $k, \varepsilon \sim y^2$ ensure $Re_t \sim y^2$ and $\mu_t \sim y^2$, recovering the viscous limit.

The summary of the tests performed with the manufactured solution is provided below:

- (F1) Pointwise residuals below 10^{-10} when comparing velocity, temperature, turbulent kinetic energy, and turbulent kinetic energy dissipation rate against manufactured solutions. Status: PASS.

- (F2) Recovered wall shear from $U_{\parallel}$ matches the analytic $\tau_w = \mu U_0(2/H)$ at $y = 0$ to machine precision. Status: PASS.
- (F3) Switching off G_b or setting $C_3 = 0$ changes only the analytic source terms, not the recovered gradients, thereby confirming the algebraic placement/sign of G_b and C_3. Status: PASS.
- (F4) With k, ε scaled so $Re_t \to 0$, verify $\mu_t \to 0$ numerically. Status: PASS.

4.3.7 Summary of the verification suite

Passing the verification suite entials that the following hold:

1. Case A: f_D within stated tolerances vs analytic/correlation targets.
2. Case B1/B2: $f_D \to 64/Re$ in the appropriate limits; $\mu_t \to 0$.
3. Case C/D: monotone trends of f_D with Ri_τ (increase for aiding; decrease for opposing/stable); symmetry at $\mathrm{Ri}_\tau \to 0$.
4. Case E: approach toward laminar f_D at high opposing buoyancy.
5. Case F (MMS): residual and gradient checks at machine precision; toggling G_b and C_3 rebalances sources without changing manufactured gradients.

Together, these cases verify the correct asymptotic behavior, algebraic placement, and numerical impact of buoyancy and low-Re corrections on the friction factor used by the interfacial mass-transfer model.

4.4 Demonstration cases

4.4.1 Evaluating the Effect of Re-Laminarization and Buoyancy Corrections on the Steady-State Operation of the L - MSR

The L-MSR is developed as an open-source version of the Molten Chloride Reactor Experiment (MCRE) following TerraPower's specifications for external model development [31]. This subsection examines how low–Reynolds-number (re-laminarization) correction and the buoyancy correction to the $k-\varepsilon$ closure reshape the steady thermal–hydraulic state of the L - MSR. For clarity, we refer to the streamlines in Fig. 4.3, the baseline thermohydraulic fields in Fig. 4.4, and the incremental field changes caused by the two corrections in Figs. 4.5 and 4.6. Throughout, three local diagnostics organize the discussion: the turbulent Reynolds number $Re_t = \rho k^2/(\mu\varepsilon)$, the buoyancy production term $G_b = \beta\,\mu_t(\boldsymbol{g}\cdot\nabla T)/\mathrm{Pr}_t$, and the skin-friction measure $C_f = 2(u_\star/U_b)^2$ with $u_\star = \sqrt{\tau_w/\rho}$. The re-laminarization model acts primarily through a damping function $f_\mu(Re_t)$ that depresses $\mu_t = \rho C_\mu f_\mu k^2/\varepsilon$ as Re_t falls, whereas the buoyancy correction modifies the k and ε budgets via G_b and its weighting C_3.

The baseline $k-\varepsilon$ solution (Fig. 4.3a and Fig. 4.4) exhibits the familiar recirculation of a high-eddy-viscosity closure: streamlines show broad cross–stream leakage and persistent weak recirculation, the bulk velocity is overly diffused in regions of rapid acceleration, and the turbulent quantities k and ε remain appreciable well beyond the near-wall shear layers. Because $k_{\mathrm{eff}} = \lambda + \rho c_p \mu_t/\mathrm{Pr}_t$ is

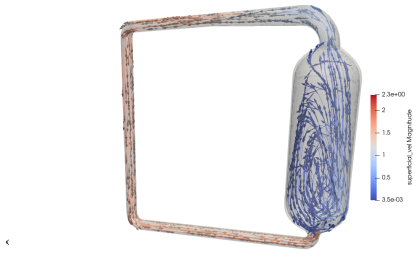

(a) Baseline $k-\varepsilon$ model.

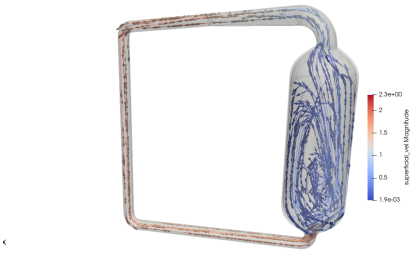

(b) Re-laminarization correction.

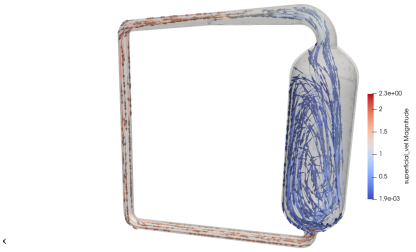

(c) Re-laminarization and buoyancy correction.

Figure 4.3: Streamlines for baseline and corrected models.

dominated by the turbulent contribution, the temperature field lacks sharp stratification and lateral gradients are flattened. The associated pressure field balances both molecular and turbulent stresses; its cross-stream structure mirrors the secondary motions implied by the streamlines.

Activating the re-laminarization correction (Fig. 4.3b) suppresses μ_t wherever Re_t is small—typically along accelerating streamlines, in viscous-dominated pockets, and in portions of the core where production cannot sustain the baseline turbulence levels. Because $P_k = 2\mu_t S_{ij} S_{ij}$, reducing μ_t immediately curtails production, which in turn reduces ε, thins the region of finite k, and further depresses Re_t. The resulting flow is more axially aligned and less permeated by weak cross-stream cells. The difference maps in Fig. 4.5 quantify these signatures: velocity magnitude decreases in shear layers where secondary motion had been artificially maintained, while it increases or remains unchanged along axial cores that now carry a larger fraction of the throughflow; both k and ε are reduced over wide areas; the turbulent viscosity drops almost everywhere except in narrow bands of peak mean strain; and the temperature field develops noticeably steeper gradients because the effective conductivity diminishes with μ_t. These changes have a direct hydraulic consequence. In regions where the baseline over-predicted eddy viscosity, the section-mean friction inferred from $u_\star$ decreases because the turbulent contribution to the streamwise stress is smaller; conversely, in truly viscous near-wall zones the correction restores the proper $U^+ \sim y^+$ behavior, which can slightly increase the resolved wall gradient and local τ_w when the baseline wall treatment had been too diffusive. The net pressure-drop impact therefore depends on the competition between these two tendencies, but in the present configuration the dominant effect is the reduction of spurious bulk mixing and concomitant decrease in turbulent shear.

When buoyancy is included together with the re-laminarization model (Fig. 4.3c), the mean fields reflect the sign of $\boldsymbol{g}\cdot\nabla T$. In regions of unstable stratification (aiding buoyancy) the term $G_b > 0$ injects energy into the turbulence, counteracting part of the re-laminarization damping,

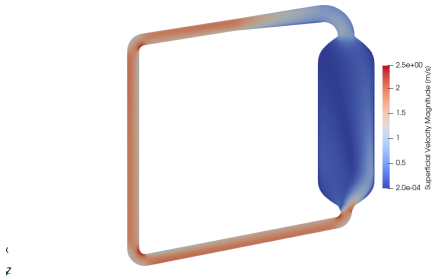

(a) Velocity magnitude.

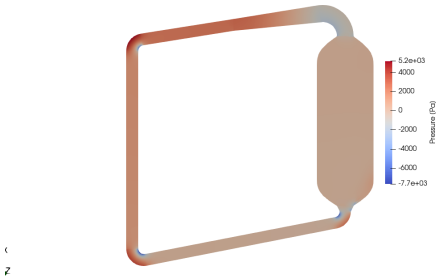

(b) Pressure.

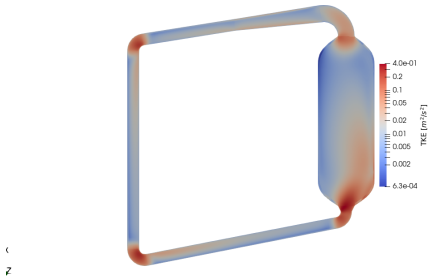

(c) Turbulent kinetic energy.

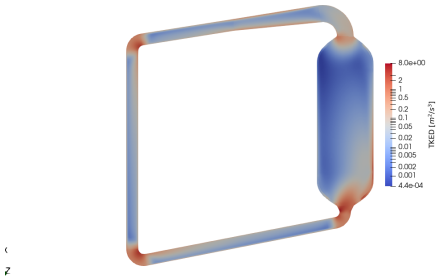

(d) Turbulent kinetic energy dissipation rate.

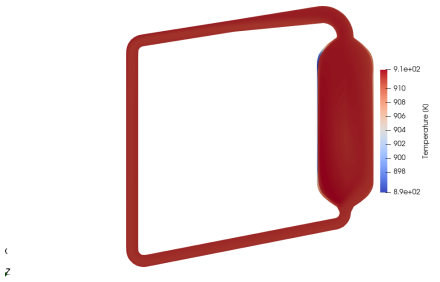

(e) Temperature.

Figure 4.4: Main thermal-hydraulics field predicted by the $k-\varepsilon$ model for the operation of the L-MSR.

strengthening plumes, and bending streamlines toward rising hot pathways. In stably stratified regions (opposing buoyancy), $G_b < 0$ removes energy from the turbulence budgets, reinforcing the low-Re damping and producing more quiescent, axially aligned flow with suppressed cross–stream exchange. The corresponding difference fields in Fig. 4.6 are spatially asymmetric for this reason: k and ε increase where unstable layers form and decrease where stable blanketing develops; μ_t follows suit; velocity differences concentrate around plume cores and stable interfaces; and temperature gradients steepen appreciably in the stable zones while relaxing in unstable ones. Because the dissipation equation employs $C_3 G_b$, the magnitude of the buoyant feedback is further modulated by the local flow state: values of C_3 near unity allow the full effect of G_b in strongly unstable patches, whereas values near zero quickly extinguish turbulence in stable patches once production falls below the threshold needed to sustain k.

The two corrections therefore act through distinct physical pathways and may either compete or reinforce each other depending on location. In accelerating, unstable regions the baseline closure typically overestimates mixing; the re-laminarization term pushes back by lowering μ_t, while the buoyancy term re-energizes production. The combined outcome is an intermediate mixing level in which coherent plumes persist but remain sharper and less laterally smeared than in the baseline. In accelerating, stable regions both corrections depress μ_t and the flow tends toward a laminar-like state with strong thermal stratification, reduced secondary motion, and diminished cross-stream transport. This partitioning is precisely what the streamline panels show: a transition from broadly diffusive trajectories (baseline) to axially aligned paths (re-laminarization only) and, finally, to a physically asymmetric pattern in which hot plumes preferentially rise and cold layers inhibit vertical exchange (both corrections).

These structural changes carry clear system-level implications. First, the streamwise momentum balance $\partial_x p \approx \partial_y[(\mu + \mu_t)\,\partial_y U]$ indicates that, for a prescribed bulk flow, any reduction of μ_t over significant portions of the cross section lowers the required pressure gradient; only if near-wall viscous recovery dominates would the total pressure drop increase, which is not the case here. Second, the effective thermal conductivity $k_{\text{eff}} = \lambda + \rho c_p \mu_t / \mathrm{Pr}_t$ decreases in stably stratified regions and increases in unstable plumes, so the corrected solution restores the expected coexistence of thermal blankets and plume-enhanced exchange that the baseline diffused away. Third, by the Chilton–Colburn analogy $j_D \simeq C_f/2$ at fixed Re and Sc, the modified skin friction maps directly into mass-transfer coefficients, lowering wall exchange where turbulence is suppressed and raising it along buoyant plumes. This mechanistic link explains the corrosion and noble-metal plating differences discussed later: interfacial fluxes proportional to $k_m(c - c^*_{\text{eq}})$ inherit the spatial redistribution of k_m implied by the corrected C_f.

Finally, it is worth remarking on quantitative consistency checks suggested by these maps. Cross-sectional budgets of production $P_k = 2\mu_t S_{ij} S_{ij}$, buoyancy G_b, and dissipation ε should show a global reduction of P_k when only re-laminarization is active, and a signed redistribution when buoyancy is added—positive in unstable zones, negative in stable ones—without spurious sources in neutral regions. Likewise, profiles of $u_\star$ and the derived C_f should decrease where the baseline solution had artificially high μ_t, increase only where viscous recovery demands it, and map consistently to Sherwood numbers through j_D. The combined evidence across Figs. 4.3–4.6 indicates that the corrected closure eliminates baseline over-mixing, reinstates the asymmetric physics of mixed convection, and produces friction and scalar-transfer levels in line with the local turbulence state Re_t and the sign of G_b. These are precisely the features required to obtain credible predictions of pressure drop, temperature stratification, and wall mass exchange in the L - MSR's steady operation.

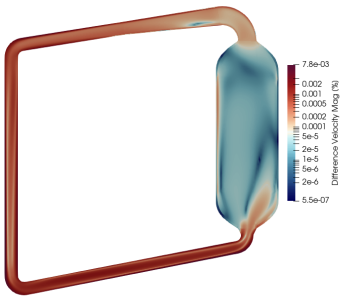

(a) Velocity magnitude.

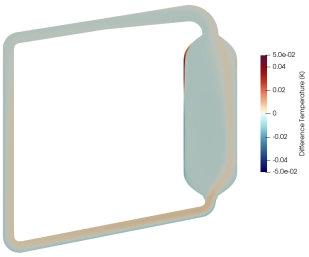

(b) Temperature.

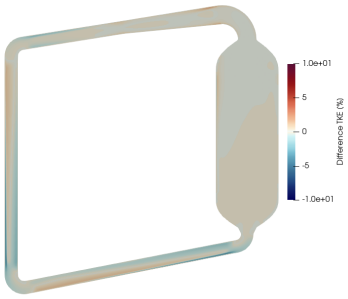

(c) Turbulent kinetic energy

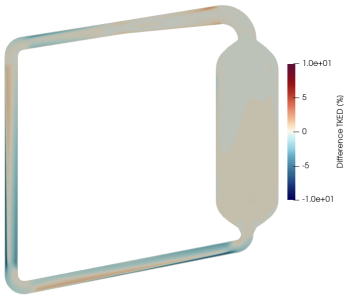

(d) Turbulent kinetic energy dissipation rate.

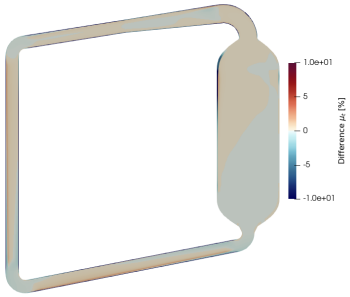

(e) Turbulent dynamic viscosity.

Figure 4.5: Difference in the thermal hydraulics fields by introducing re-laminarization correction.

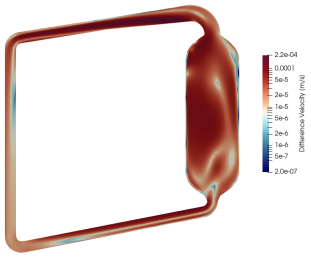

(a) Velocity magnitude.

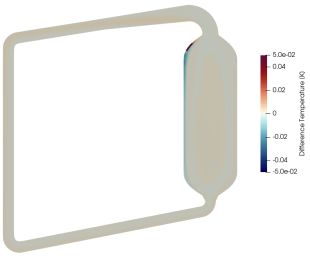

(b) Temperature.

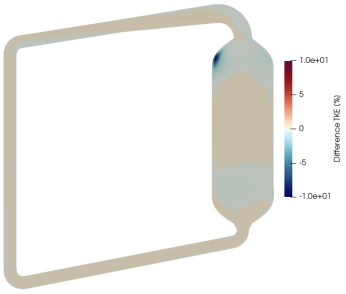

(c) Turbulent kinetic energy

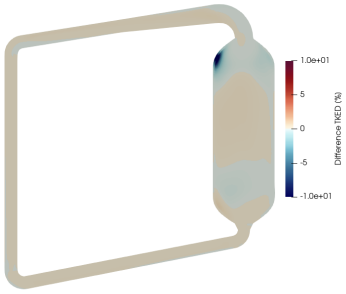

(d) Turbulent kinetic energy dissipation rate.

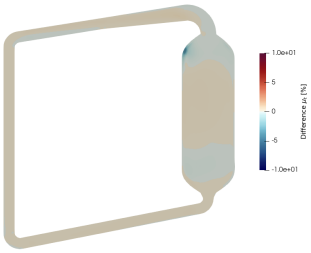

(e) Turbulent dynamic viscosity.

Figure 4.6: Difference in the thermal hydraulics fields by introducing buoyancy correction.

4.4.2 Impact of Re-Laminarization and Buoyancy Corrections on Corrosion Modeling in the L - MSR

We interpret the chromium, iron, and nickel depletion patterns in Fig. 4.7 together with the differential maps obtained when re-laminarization and buoyancy corrections are enabled (Figs. 4.8–4.10) through the interfacial model developed earlier. In the molar framework, the wall flux of a dissolving alloying element $i \in \{\mathrm{Cr}, \mathrm{Fe}, \mathrm{Ni}\}$ is

$$J_i \;=\; k_{\mathrm{eff},i}(\eta)\left[c_i - c^{*}_{i,\mathrm{eq}}(\eta)\right], \qquad k_{\mathrm{eff},i}(\eta) \;=\; \frac{k_{m,i}\,k^{*}_{0,i}(\eta)}{k_{m,i}+k^{*}_{0,i}(\eta)}, \qquad k^{*}_{0,i}(\eta) = k_{0,i}\,e^{-\alpha_{c,i}n_iF\eta/(RT)}, \tag{4.36}$$

with c_i the liquid concentration at the wall, $c^*_{i,\mathrm{eq}}(\eta) = c_{i,\mathrm{eq}}(T,\xi)\, e^{+\alpha_{a,i} n_i F \eta/(RT)}$ the electrochemically shifted equilibrium concentration returned by Thermochimica, and $k_{m,i}$ the liquid-side mass-transfer coefficient. In steady dissolution, $J_i < 0$ depletes the solid according to $\partial_t(\rho_s w_i) = -J_i$, where w_i is the solid mass fraction of element i. Thus, for fixed thermodynamic driving $\Delta c_i \equiv c_i - c^*_{i,\mathrm{eq}}(\eta)$, the rate is controlled by the series conductance $k_{\mathrm{eff},i}$, which interpolates between a reaction-limited ($k^*_{0,i}$) and a mass-transfer-limited ($k_{m,i}$) regime through the Damköhler number $\mathrm{Da}_i = k^*_{0,i}/k_{m,i}$.

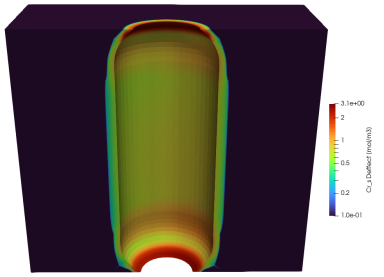

(a) Chromium defect.

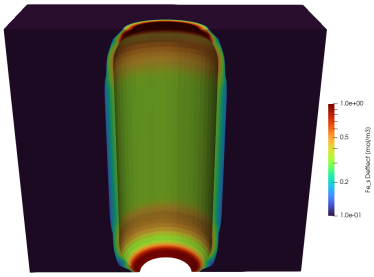

(b) Iron defect.

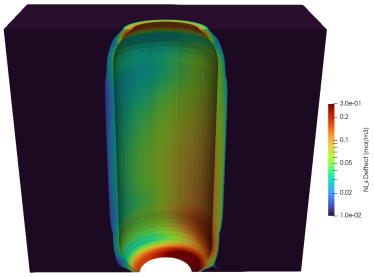

(c) Nickel defect.

Figure 4.7: Defect in the concentration of the main stainless steel components as predicted by the baseline $k-\varepsilon$ model due to flow-accelerated corrosion.

The turbulence corrections act on J_i through two tightly coupled channels. First, they change the hydrodynamic conductance $k_{m,i}$. In the near-wall limit appropriate for internal flows, the Chilton–Colburn analogy implies $j_{D,i} \equiv \mathrm{Sh}_i/(\mathrm{Re}\,\mathrm{Sc}_i^{1/3}) \approx C_f/2$, so that $k_{m,i} = \mathrm{Sh}_i D_i/d_h \propto C_f\,\mathrm{Re}\,\mathrm{Sc}_i^{1/3} D_i/d_h$. Any reduction in the skin friction $C_f = 2(u_\star/U_b)^2$ therefore depresses $k_{m,i}$ almost linearly at fixed Re and Sc_i; conversely, a local increase of $u_\star$ near buoyant plumes raises $k_{m,i}$. Second, the corrections reshape the scalar fields T and c_i themselves. Buoyancy shifts the partitioning between unstable plumes and stable blankets, altering T and hence $c_{i,\mathrm{eq}}(T,\xi)$ and the sign/magnitude of Δc_i; re-laminarization reduces turbulent diffusion and cross-stream advection, steepening temperature and concentration boundary layers and increasing the sensitivity of c_i to local sources and sinks. The net effect on J_i is therefore the product of a modified conductance and a modified driving force. This coupling is precisely why the patterns in Figs. 4.8–4.10 are not mere scaled copies of the friction or temperature maps.

The difference fields with re-laminarization alone quantify the response when $k_{m,i}$ is selectively suppressed in low-Re_t regions and the core becomes more axially aligned. In zones where the baseline model maintained artificially large eddy viscosity, C_f decreases, $k_{m,i}$ decreases, and a mass-

transfer-controlled process ($\mathrm{Da}_i \gg 1$) exhibits a nearly proportional reduction in $|J_i|$. This explains the broad attenuation of chromium dissolution seen in Fig. 4.8 (left): among the three elements, chromium typically has the largest $k_{0,i}$ and the highest chemical driving under oxidizing redox states, making it the most mass-transfer-limited of the trio. The sensitivity $\partial J_i/\partial k_{m,i} = \left(k^*_{0,i}/(k_{m,i} + k^*_{0,i})\right)^2 \Delta c_i$ approaches Δc_i in that limit. Iron follows the same trend but with a smaller amplitude, consistent with more mixed control ($\mathrm{Da}_{\mathrm{Fe}} \sim \mathscr{O}(1)$), while nickel shows the smallest change because its kinetics are slower and the dissolution is more reaction-limited ($\mathrm{Da}_{\mathrm{Ni}} \ll 1$), so that $k_{\mathrm{eff,Ni}} \approx k^*_{0,\mathrm{Ni}}$ is relatively insensitive to k_m. Where re-laminarization steepens the near-wall temperature gradient and reduces cross-stream entrainment, $c_{i,\mathrm{eq}}(T,\xi)$ and c_i both shift, but these contributions are second order compared with the dominant, friction-mediated change in $k_{m,i}$ for the more reactive species. Taken together, the maps in Figs. 4.8–4.10 under re-laminarization alone convey a uniform physical message: by removing spurious turbulent transport, the model damps flow-accelerated corrosion where it had been artificially sustained, and it leaves reaction-limited dissolution largely unchanged.

When buoyancy is added to the re-laminarization model, the response becomes intrinsically asymmetric because $G_b = \beta \mu_t (\boldsymbol{g}\cdot\nabla T)/\mathrm{Pr}_t$ is signed. In unstable, plume-dominated sectors, turbulence production increases, $u_\star$ and C_f rise, and hence $k_{m,i}$ increases. Simultaneously the local temperature tends to be higher, which—depending on the dissolution thermochemistry returned by Thermochimica—often raises $c_{i,\mathrm{eq}}(T,\xi)$ for endothermic dissolution, reducing Δc_i in magnitude. The first effect strengthens the conductance; the second weakens the driving force. In mass-transfer-limited dissolution the conductance dominates and $|J_i|$ increases, recovering part of the attenuation produced by re-laminarization alone, with the largest rebound for chromium, smaller for iron, and minimal for nickel. In stably stratified blankets, turbulence is damped, $u_\star$ and C_f drop, $k_{m,i}$ decreases, and temperatures are lower; if $c_{i,\mathrm{eq}}(T,\xi)$ decreases with T in the relevant interval, the driving force Δc_i may increase in magnitude. Here the conductance and the driving force shift in opposite directions; for chromium and iron the conductance effect wins, sharpening patches of reduced dissolution that align with the stable layers in Fig. 4.8 and Fig. 4.9 (right). For nickel, the reaction-limited character again buffers the change. The emerging picture in the full correction is therefore topologically consistent with the hydrodynamics: hot, rising plumes amplify mass transfer and corrosion where the thermodynamic driving remains significant, while cold, stable blankets suppress cross-stream exchange and reduce corrosion even if local supersaturation grows.

These mechanistic trends are echoed by the baseline defect maps in Fig. 4.7. The regions of chromium depletion are the most extensive and deepest because the combination of fast surface kinetics ($k_{0,\mathrm{Cr}}$) and high chemical driving makes chromium dissolution the most sensitive to k_m. Iron shows a milder, spatially similar pattern, while nickel's depletion is weakest and more localized, often tied to geometrical features where the local overpotential or redox state transiently elevate Δc_{Ni}. The differential maps then clarify that a turbulence model which overestimates eddy viscosity will exaggerate flow-accelerated corrosion of the more reactive constituents by inflating k_m in large swaths of the domain. By contrast, the re-laminarization correction restores laminar-like transport where appropriate, reducing apparent susceptibility to flow-accelerated corrosion without altering the underlying thermodynamic preference for chromium dissolution. The buoyancy correction adds the missing directional physics, intensifying corrosion along buoyant upwellings and shielding stably stratified surfaces, exactly as one expects in a mixed-convection molten-salt system.

It is useful to frame these observations in terms of the Damköhler number. Wherever the corrections push Da_i below unity, the process transitions toward reaction control and becomes insensitive to further reductions in C_f or k_m; the signature in the Δ-maps is a collapse of sensitivity, most evi-

dent for nickel. Conversely, when Da_i remains large even after re-laminarization, corrosion remains mass-transfer controlled and mirrors the spatial pattern of $u_\star$ and the sign of G_b; this is the regime where buoyancy leaves a strong imprint, and where chromium's depletion responds most. Because the sign of J_i is set by Δc_i, changes in T induced by buoyancy can, in principle, flip the interfacial behavior from dissolution to precipitation in localized pockets if c_i crosses $c^*_{i,\mathrm{eq}}$. Although the present section focuses on dissolution, those same transitions explain the plating maps discussed later for noble metals.

Finally, we note the implications for integral corrosion metrics. The spatial redistribution of k_m and Δc_i lowers the domain-averaged chromium corrosion current when re-laminarization is added, primarily by extinguishing artificial high-k_m corridors. Adding buoyancy then introduces a net bias: if the unstable volume fraction is modest, the shielded area in stable blankets dominates and the average corrosion rate remains below the baseline; if large coherent plumes occupy a significant fraction of the wetted perimeter, the global attenuation can be partially offset by localized intensification along the plume paths. These tendencies are already visible in Figs. 4.8–4.9 and are consistent with the friction and temperature reorganizations documented in the previous subsection. In short, the turbulence corrections do not simply rescale corrosion uniformly; they recover the physically required sensitivity of wall dissolution to the local turbulence state (Re_t) and stratification (G_b), sharpen material selectivity through Da_i, and thereby deliver corrosion maps whose topology follows the actual mixed-convection physics of the L - MSR rather than the artifacts of an over-diffusive closure.

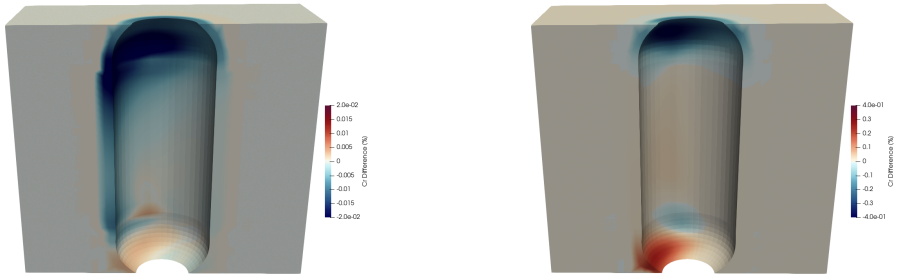

(a) Re-laminarization correction.

(b) Buoyancy correction.

Figure 4.8: Changes in chromium corrosion profiles due corrections in the turbulence model.

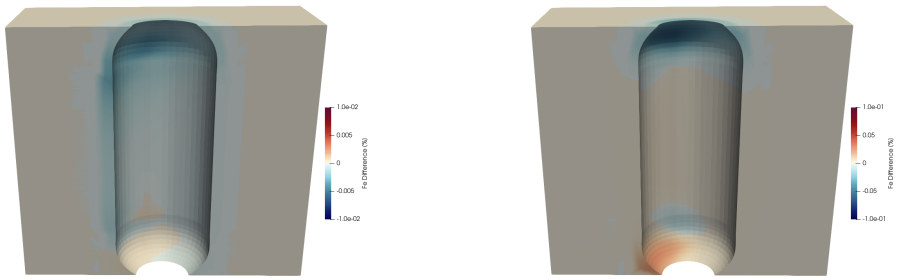

(a) Re-laminarization correction.

(b) Buoyancy correction.

Figure 4.9: Changes in iron corrosion profiles due corrections in the turbulence model.

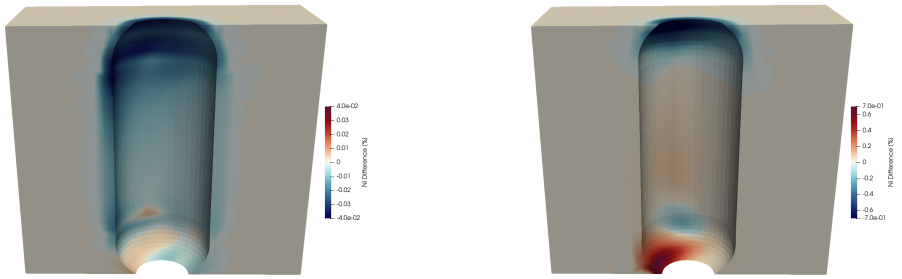

(a) Re-laminarization correction.

(b) Buoyancy correction.

Figure 4.10: Changes in nickel corrosion profiles due corrections in the turbulence model.

4.4.3 Impact of Re - Laminarization and Buoyancy Corrections on Noble Metal Plating in the L - MSR

We interpret the Ru, Rh, Pd, and Ag deposition maps in Fig. 4.11 and the corresponding difference fields with and without the turbulence corrections in Fig. 4.12 using the mixed film–kinetics wall law established earlier. For each ionic noble metal i, the interfacial molar deposition flux (positive for plating) is

$$J_i \;=\; k_{\mathrm{eff},i}(\eta)\left[c_i - c^{*}_{i,\mathrm{eq}}(\eta)\right], \qquad k_{\mathrm{eff},i}(\eta) \;=\; \frac{k_{m,i}\,k^{*}_{0,i}(\eta)}{k_{m,i}+k^{*}_{0,i}(\eta)}, \qquad k^{*}_{0,i}(\eta) = k_{0,i}\,e^{-\alpha_{c,i}n_iF\eta/(RT)}. \tag{4.37}$$

Here c_i is the liquid-side interfacial concentration, and $c^{*}_{i,\mathrm{eq}}(\eta) = c_{i,\mathrm{eq}}(T,\xi)\,e^{+\alpha_{a,i}n_iF\eta/(RT)}$ is the electrochemically shifted equilibrium concentration provided by Thermochimica at the local temperature and redox state. The liquid-side conductance $k_{m,i} = \mathrm{Sh}_i D_i/d_h$ follows the Chilton–Colburn relation $\mathrm{Sh}_i \approx \frac{1}{2}C_f\,\mathrm{Re}\,\mathrm{Sc}_i^{1/3}$ at fixed geometry, linking the skin friction $C_f = 2(u_\star/U_b)^2$ to mass transfer. The surface kinetics enter through $k^{*}_{0,i}$ (or, equivalently, $i_{0,i} = n_iFk_{0,i}c_{i,\mathrm{eq}}$). Whether plating is mass-transfer limited or reaction limited is governed by $\mathrm{Da}_i = k^{*}_{0,i}/k_{m,i}$, with $k_{\mathrm{eff},i} \to k_{m,i}$ when $\mathrm{Da}_i \gg 1$ and $k_{\mathrm{eff},i} \to k^{*}_{0,i}$ when $\mathrm{Da}_i \ll 1$.

In the baseline solution, the high eddy viscosity broadens regions of elevated $u_\star$ and, therefore, of large $k_{m,i}$. Because noble metals in fluoride salts typically have low dissolved equilibrium concentrations $c_{i,\mathrm{eq}}$ under reactor redox conditions, the driving force $\Delta c_i = c_i - c^{*}_{i,\mathrm{eq}}$ is positive across much of the wetted perimeter and the deposition rate is set primarily by the liquid-side conductance; the resulting plate-out fields in Fig. 4.11 track hydrodynamic features with high shear and strong cross–stream exchange (impingement zones, turning regions, and buoyant pathways). The species-to-species variation mainly reflects differences in D_i, $k_{0,i}$, and the Thermochimica-predicted $c_{i,\mathrm{eq}}$: for otherwise similar flow, a larger D_i and larger $k_{0,i}$ push Da_i upward and amplify the sensitivity to C_f, whereas a larger $c_{i,\mathrm{eq}}$ diminishes Δc_i and attenuates deposition.

The re-laminarization correction reduces the turbulent viscosity where the local turbulent Reynolds number $Re_t = \rho k^2/(\mu\varepsilon)$ falls, collapses spurious secondary motions, and narrows the energetic shear layers. Through $\mathrm{Sh}_i \propto C_f$, this drives a systematic decrease of $k_{m,i}$ across significant fractions of the perimeter. In the mass-transfer-dominated regime ($\mathrm{Da}_i \gg 1$), the sensitivity

$$\frac{\partial J_i}{\partial k_{m,i}} = \left(\frac{k^{*}_{0,i}}{k_{m,i}+k^{*}_{0,i}}\right)^2 \Delta c_i \;\xrightarrow[\mathrm{Da}_i\gg 1]{}\; \Delta c_i, \tag{4.38}$$

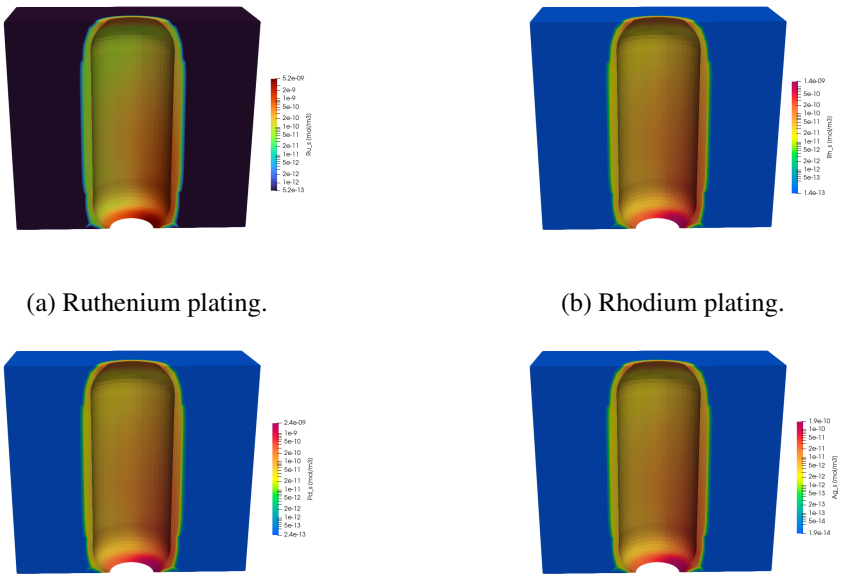

(a) Ruthenium plating.

(b) Rhodium plating.

(c) Palladium plating.

(d) Silver plating.

Figure 4.11: Plating profiles for noble metals.

implies a nearly one-to-one reduction in J_i with $k_{m,i}$. This is precisely what the difference plot "Re-laminarization correction" in Fig. 4.12 shows: broad swaths of negative ΔJ_i (less deposition) aligned with the corridors where the baseline model had maintained excessive shear and mixing. Because Da_i and D_i are species dependent, the attenuation is strongest for the metals that are most mass-transfer limited under the prevailing redox and temperature (typically those with smaller $c_{i,\mathrm{eq}}$ and larger $k_{0,i}$), and weakest for the more reaction-limited species. A secondary consequence of the damping is a slight rise of c_i in the bulk, because reduced wall uptake relaxes the sink; however, for steady operation this back-reaction is modest and does not overcome the dominant conductance effect on J_i.

When buoyancy is activated together with re-laminarization, the sign of $\boldsymbol{g}\cdot\nabla T$ partitions the perimeter into unstable plume-facing sectors and stably blanketed sectors. In unstable regions $G_b > 0$ raises k, ε, and $u_\star$, thereby increasing C_f and $k_{m,i}$; in stable regions $G_b < 0$ does the opposite. The difference plot "Buoyancy correction" in Fig. 4.12 therefore exhibits an inherently asymmetric pattern: deposition intensifies on surfaces swept by rising hot plumes and weakens under cold, stratified blankets. Temperature changes reinforce this anisotropy by altering $c_{i,\mathrm{eq}}(T,\xi)$ and thus the driving force Δc_i; if the solubility of the reduced metal increases with T in the local interval, $c_{i,\mathrm{eq}}$ grows within the plume and partially offsets the increase in $k_{m,i}$, while the opposite occurs in stable blankets. In mass-transfer control the conductance change dominates and the net effect is an increase of J_i along plume paths and a decrease elsewhere; in mixed control the two contributions are comparable and the sign of ΔJ_i follows the local balance between $k_{m,i}$ and Δc_i. Because Sh_i scales with C_f only weakly through $\mathrm{Sc}_i^{1/3}$, species-to-species differences in the buoyancy response are governed more by kinetic parameters than by D_i; metals with larger $k_{0,i}$ exhibit a more pronounced buoyant modulation.

These mechanisms explain the hierarchy and topology visible across the panels. Regions that plate aggressively in the baseline but are shear driven rather than truly buoyant shrink markedly once re-laminarization removes artificial eddy viscosity; where the hydrodynamics are genuinely governed by thermal plumes, buoyancy restores and focuses deposition on the plume-facing surfaces. Conversely, surfaces shielded by stable stratification show diminished $u_\star$, reduced $k_{m,i}$, steeper near-wall thermal and concentration gradients, and therefore weaker plate-out, even if the local supersaturation Δc_i increases. The net, domain-averaged effect of the two corrections is a reduction in total noble-metal deposition relative to baseline, with localization of the remaining deposition onto physically identifiable upwelling pathways rather than a broad, closure-induced smear.

Two practical consequences follow for reactor assessment. First, because plate-out thickness evolves as $\dot{h}_i = \frac{M_i}{\rho_{\mathrm{dep},i}} J_i$, the corrected hydrodynamics slow uniform fouling and redistribute deposition toward discrete zones; this reduces the probability of diffuse performance degradation while increasing the need to monitor specific surfaces where plumes impinge. Second, the corrected C_f maps feed the Chilton–Colburn link to species transport, so the same turbulence modeling choices that improve pressure-drop and temperature predictions directly condition the fidelity of the plate-out forecast. In design or mitigation studies the logical workflow is therefore to (i) calibrate $k_{0,i}$ (or $i_{0,i}$) and validate $c_{i,\mathrm{eq}}(T,\xi)$ with Thermochimica, (ii) include re-laminarization to avoid spurious mass-transfer control, and (iii) include buoyancy to recover the asymmetric mixed-convection physics that determine where noble metals will actually plate in the L - MSR.

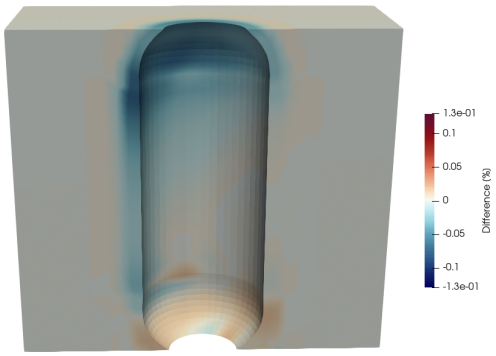

(a) Re-laminarization correction.

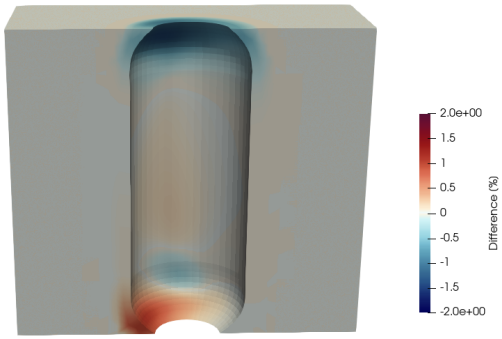

(b) Buoyancy correction.

Figure 4.12: Changes in noble metal corrosion profiles due corrections in the turbulence model.

5 Two-Phase Euler-Euler Modeling in Pronghorn

5.1 Description and derivation of the multi-phase Euler-Euler model implemented in Pronghorn

The nomenclature and principal symbols used in this section are the following:

- α_q (—) volume fraction
- ρ_q (kg m^{-3}) density
- $\boldsymbol{u}_q$ (m s^{-1}) velocity
- p (Pa) pressure
- μ_q (Pa s) laminar viscosity
- $\mu_{t,q}$ (Pa s) eddy viscosity
- k_q (m^2 s^{-2}) TKE
- ε_q (m^2 s^{-3}) dissipation
- h_q (J kg^{-1}) specific enthalpy
- T_q (K) temperature
- k_q (W m^{-1} K^{-1}) thermal conductivity
- $c_{p,q}$ (J kg^{-1} K^{-1}) specific heat
- $\boldsymbol{g}$ (m s^{-2}) gravity
- σ_{qp} (N m^{-1}) surface tension
- a_{qp} (m^2 m^{-3}) interfacial area density
- d_{qp} (m) interfacial length
- C_D, C_L, C_{VM}, C_{td} (—) closure coefficients
- $\mathrm{Pr}_{t,q}$ (—) turbulent Prandtl
- κ (—) von Kármán constant
- E, A^+ (—) wall–function constants
- overdot sources $\dot{m}_{pq}$, $\dot{Q}_{pq}$ are interphase mass and heat transfer rates

We consider N_p interpenetrating phases indexed by $q \in \{1,\dots,N_p\}$ occupying the same control volume with volume fractions $\alpha_q(\boldsymbol{x},t)$ such that

$$\sum_{q=1}^{N_p} \alpha_q = 1, \qquad 0 \le \alpha_q \le 1. \tag{5.1}$$

Each phase q is characterized by density $\rho_q(p,T_q)$, velocity $\boldsymbol{u}_q$, specific enthalpy h_q, temperature T_q, laminar viscosity $\mu_q(T_q)$, and thermal conductivity $k_q(T_q)$. A single thermodynamic pressure field $p(\boldsymbol{x},t)$ couples the phases. Gravity $\boldsymbol{g}$ acts as a body force. Weak compressibility is retained via $\rho_q(p,T_q)$ and pressure–work terms in the energy equations while velocities remain subsonic (low–Mach).

The transport of each volume fraction α_q is written with a boundedness–preserving compression flux to sharpen interfaces:

$$\frac{\partial \alpha_q}{\partial t} + \boldsymbol{\nabla}\cdot(\alpha_q \boldsymbol{u}_q) + \boldsymbol{\nabla}\cdot[\alpha_q(1-\alpha_q)\,\boldsymbol{u}_c] = \sum_{p\neq q} \frac{\dot{m}_{pq}}{\rho_q}. \tag{5.2}$$

Here $\dot{m}_{pq}$ (kg m^{-3} s^{-1}) is the volumetric mass transfer rate from phase p to phase q (with $\sum_q \sum_{p\neq q} \dot{m}_{pq} = 0$), and $\boldsymbol{u}_c$ is a compression velocity aligned with the interface normal that does not contribute to net mass transport. We use

$$\boldsymbol{u}_c = c_\alpha\, u_c^\star\, \hat{\boldsymbol{n}}, \qquad \hat{\boldsymbol{n}} = \frac{\boldsymbol{\nabla}\alpha_q}{\left\|\boldsymbol{\nabla}\alpha_q\right\| + \varepsilon}, \qquad u_c^\star = \min(\lambda_c\, \|\boldsymbol{u}_r\|, u_{\max}), \tag{5.3}$$

with compression coefficient $c_\alpha \in [0,1]$, limiter $\lambda_c > 0$, regularization $\varepsilon \ll 1$, interphase slip $\boldsymbol{u}_r = \boldsymbol{u}_p - \boldsymbol{u}_q$, and optional cap $u_{\max}$.

For each phase, the mass conservation (implied by (5.2) and solved in conservative form) is

$$\frac{\partial(\alpha_q \rho_q)}{\partial t} + \boldsymbol{\nabla}\cdot(\alpha_q \rho_q \boldsymbol{u}_q) = \sum_{p\neq q} \dot{m}_{pq}. \tag{5.4}$$

The RANS–filtered momentum equation for phase q including buoyancy, viscous and turbulent stresses, interfacial momentum exchange (drag, lift, virtual mass, turbulent dispersion), and capillary force reads

$$\begin{aligned}\frac{\partial(\alpha_q \rho_q \boldsymbol{u}_q)}{\partial t} + \boldsymbol{\nabla}\cdot(\alpha_q \rho_q \boldsymbol{u}_q \otimes \boldsymbol{u}_q) = &-\alpha_q \boldsymbol{\nabla} p + \boldsymbol{\nabla}\cdot\left[\alpha_q \boldsymbol{\tau}_q^{\mathrm{eff}}\right] + \alpha_q \rho_q \boldsymbol{g} \\ &+ \sum_{p\neq q} \left(\boldsymbol{M}_{qp}^{\mathrm{drag}} + \boldsymbol{M}_{qp}^{\mathrm{lift}} + \boldsymbol{M}_{qp}^{\mathrm{vm}} + \boldsymbol{M}_{qp}^{\mathrm{td}}\right) + \boldsymbol{f}_{\sigma,q} + \boldsymbol{S}_q^{(m)}.\end{aligned} \tag{5.5}$$

The effective stress uses a Boussinesq eddy viscosity:

$$\boldsymbol{\tau}_q^{\mathrm{eff}} = \mu_q^{\mathrm{eff}} \left[\boldsymbol{\nabla}\boldsymbol{u}_q + (\boldsymbol{\nabla}\boldsymbol{u}_q)^\top\right] - \frac{2}{3}\mu_q^{\mathrm{eff}} (\boldsymbol{\nabla}\cdot\boldsymbol{u}_q)\boldsymbol{I} - \frac{2}{3}\alpha_q \rho_q k_q \boldsymbol{I}, \qquad \mu_q^{\mathrm{eff}} = \mu_q + \mu_{t,q}, \tag{5.6}$$

with k_q the turbulent kinetic energy of phase q and $\mu_{t,q}$ its eddy viscosity.

The interfacial momentum closures are:

$$\text{Drag:}\quad \boldsymbol{M}_{qp}^{\text{drag}} = K_{qp}^{\text{drag}}\,(\boldsymbol{u}_p - \boldsymbol{u}_q), \qquad K_{qp}^{\text{drag}} = \frac{1}{2} C_D\,\rho_m\,\frac{a_{qp}}{4}\,\left\|\boldsymbol{u}_p - \boldsymbol{u}_q\right\|, \tag{5.7}$$

$$\text{(alternative particulate form: } K_{qp}^{\text{drag}} = \tfrac{3}{4} C_D\,\rho_m\,\frac{\alpha_q \alpha_p}{d_{qp}}\,\left\|\boldsymbol{u}_p - \boldsymbol{u}_q\right\|\text{);}$$

$$\text{Lift:}\quad \boldsymbol{M}_{qp}^{\text{lift}} = C_L\,\rho_m\,\alpha_q\,(\boldsymbol{u}_p - \boldsymbol{u}_q) \times \boldsymbol{\omega}_m, \qquad \boldsymbol{\omega}_m = \boldsymbol{\nabla} \times \boldsymbol{u}_m; \tag{5.8}$$

$$\text{Virtual mass:}\quad \boldsymbol{M}_{qp}^{\text{vm}} = C_{VM}\,\rho_m\,\alpha_q \left(\frac{D\boldsymbol{u}_p}{Dt} - \frac{D\boldsymbol{u}_q}{Dt} \right); \tag{5.9}$$

$$\text{Turbulent dispersion:}\quad \boldsymbol{M}_{qp}^{\text{td}} = -\,C_{td}\,\rho_m\,k_m\,\boldsymbol{\nabla}\alpha_q; \tag{5.10}$$

where C_D is a drag coefficient (function of Re_{qp}, Eo, Mo as appropriate), a_{qp} is the interfacial area density between phases q and p, d_{qp} a characteristic interphase length (e.g. Sauter mean diameter), $\rho_m = \sum_r \alpha_r \rho_r$ is the mixture density, $\boldsymbol{u}_m = \sum_r \alpha_r \rho_r \boldsymbol{u}_r / \rho_m$ the mass–weighted mixture velocity, $k_m = \sum_r \alpha_r \rho_r k_r / \rho_m$, and $D(\cdot)/Dt = \partial(\cdot)/\partial t + \boldsymbol{u}_m \cdot \boldsymbol{\nabla}(\cdot)$ is the material derivative along $\boldsymbol{u}_m$. Typical constants are $C_{VM} \approx 0.5$ and $C_{td} = \mathcal{O}(0.1\text{–}1)$. The surface tension force is modeled in continuum–surface–force (CSF) form:

$$\boldsymbol{f}_{\sigma,q} = \sum_{p \neq q} \sigma_{qp}\,\kappa_{qp}\,\alpha_q \alpha_p\,\hat{\boldsymbol{n}}_{qp}\,\delta_\Gamma \;\approx\; \sum_{p \neq q} \sigma_{qp}\,\kappa_{qp}\,\boldsymbol{\nabla}\alpha_q, \qquad \kappa_{qp} = -\boldsymbol{\nabla}\cdot\hat{\boldsymbol{n}}_{qp},\;\; \hat{\boldsymbol{n}}_{qp} = \frac{\boldsymbol{\nabla}\alpha_q}{\|\boldsymbol{\nabla}\alpha_q\| + \varepsilon}, \tag{5.11}$$

with σ_{qp} the pairwise surface tension, κ_{qp} the interface curvature, and δ_Γ a smeared interface indicator. The term $\boldsymbol{S}_q^{(m)}$ collects any additional body forces (e.g. porous resistance).

The weakly–compressible enthalpy equation for phase q is

$$\begin{aligned} \frac{\partial(\alpha_q \rho_q h_q)}{\partial t} + \boldsymbol{\nabla}\cdot(\alpha_q \rho_q h_q \boldsymbol{u}_q) = \alpha_q \frac{Dp}{Dt} - \boldsymbol{\nabla}\cdot\boldsymbol{q}_q^{\text{eff}} + \Phi_q + S_q^{(h)} \\ + \sum_{p \neq q} \left(\dot{m}_{pq}\,h_{pq} + \dot{Q}_{pq} \right). \end{aligned} \tag{5.12}$$

Here $\boldsymbol{q}_q^{\text{eff}} = -\,\alpha_q\,(k_q + k_{t,q})\,\boldsymbol{\nabla} T_q$ is the sum of laminar and turbulent heat fluxes with $k_{t,q} = \mu_{t,q} c_{p,q} / \mathrm{Pr}_{t,q}$, $\mathrm{Pr}_{t,q}$ the turbulent Prandtl number, $c_{p,q}$ the specific heat at constant pressure, Φ_q the viscous dissipation (often negligible at low Mach), $S_q^{(h)}$ a volumetric source (e.g. nuclear heating), $\dot{Q}_{pq}$ the interfacial heat transfer from p to q, and h_{pq} the specific enthalpy carried by mass transfer $\dot{m}_{pq}$.

Each phase carries its own turbulent kinetic energy k_q and dissipation rate ε_q:

$$\begin{aligned} \frac{\partial(\alpha_q \rho_q k_q)}{\partial t} + \boldsymbol{\nabla}\cdot(\alpha_q \rho_q k_q \boldsymbol{u}_q) = \boldsymbol{\nabla}\cdot\left[\alpha_q \left(\mu_q + \frac{\mu_{t,q}}{\sigma_k} \right) \boldsymbol{\nabla} k_q \right] + \alpha_q \left(P_{k,q} + P_{k,q}^{(b)} - \rho_q \varepsilon_q \right) \\ + S_q^{(k)} + S_{q,\text{int}}^{(k)}, \end{aligned} \tag{5.13}$$

$$\begin{aligned} \frac{\partial(\alpha_q \rho_q \varepsilon_q)}{\partial t} + \boldsymbol{\nabla}\cdot(\alpha_q \rho_q \varepsilon_q \boldsymbol{u}_q) = \boldsymbol{\nabla}\cdot\left[\alpha_q \left(\mu_q + \frac{\mu_{t,q}}{\sigma_\varepsilon} \right) \boldsymbol{\nabla} \varepsilon_q \right] + \alpha_q \left(C_{\varepsilon 1} \frac{\varepsilon_q}{k_q} P_{k,q} - C_{\varepsilon 2}\,\rho_q \frac{\varepsilon_q^2}{k_q} \right) \\ + S_q^{(\varepsilon)} + S_{q,\text{int}}^{(\varepsilon)}. \end{aligned} \tag{5.14}$$

The eddy viscosity is

$$\mu_{t,q} = C_\mu\, f_\mu\, \rho_q\, \frac{k_q^2}{\varepsilon_q}, \qquad P_{k,q} = 2\,\mu_{t,q}\,\boldsymbol{S}_q : \boldsymbol{S}_q - \frac{2}{3}\,\mu_{t,q}\,(\boldsymbol{\nabla}\cdot\boldsymbol{u}_q)^2, \qquad \boldsymbol{S}_q = \tfrac{1}{2}\Big[\boldsymbol{\nabla}\boldsymbol{u}_q + (\boldsymbol{\nabla}\boldsymbol{u}_q)^{\top}\Big], \tag{5.15}$$

and $P_{k,q}^{(b)}$ is the buoyant production/destruction (e.g. $P_{k,q}^{(b)} = -\mu_{t,q}\,\boldsymbol{g}\cdot\boldsymbol{\nabla}\rho_q/\rho_q$ for weak stratification). The interfacial turbulence exchanges $S_{q,\mathrm{int}}^{(k)}$ and $S_{q,\mathrm{int}}^{(\varepsilon)}$ model bubble/wake–induced turbulence and may be related to interfacial drag power, e.g.

$$S_{q,\mathrm{int}}^{(k)} = \sum_{p\neq q} C_{k,\mathrm{int}}\, \frac{\big\|\boldsymbol{M}_{qp}^{\mathrm{drag}}\big\|\,\big\|\boldsymbol{u}_p - \boldsymbol{u}_q\big\|}{\rho_m}, \qquad S_{q,\mathrm{int}}^{(\varepsilon)} = C_{\varepsilon,\mathrm{int}}\,\frac{\varepsilon_q}{k_q}\,S_{q,\mathrm{int}}^{(k)}. \tag{5.16}$$

A two–region near–wall treatment is used: in the logarithmic layer ($y^+ \gtrsim 30$), wall functions prescribe the normal fluxes of k_q and ε_q and the wall eddy viscosity via

$$U^+ = \frac{1}{\kappa}\ln\!\big(E\,y^+\big), \qquad \mu_{t,q}^{\mathrm{wall}} = \rho_q\,\kappa\,y\,u_\tau\left(1-\exp\!\left[-\frac{y^+}{A^+}\right]\right)^2, \qquad k_{q,w} = \frac{u_\tau^2}{\sqrt{C_\mu}}, \quad \varepsilon_{q,w} = \frac{u_\tau^3}{\kappa\,y}, \tag{5.17}$$

with $u_\tau = \sqrt{\tau_w/\rho_q}$ the friction velocity, y the wall–normal distance, $y^+ = \rho_q u_\tau y/\mu_q$, von Kármán constant $\kappa = 0.41$, $E \simeq 9.8$, and $A^+ \simeq 26$. In the viscous–buffer region ($y^+ \lesssim 30$), low–Re damping f_μ or equivalent blending to the wall function is applied. Default constants are $C_\mu = 0.09$, $\sigma_k = 1.0$, $\sigma_\varepsilon = 1.3$, $C_{\varepsilon 1} = 1.44$, $C_{\varepsilon 2} = 1.92$, with phase–specific turbulent Prandtl numbers $\mathrm{Pr}_{t,q} \in [0.7, 1.0]$. In future, we will introduce bubbly turbulent boundary layer[32] to better capture the existence of bubble on the near wall region.

The density $\rho_q(p, T_q)$ may be provided by a weakly–compressible equation of state (linearized or tabulated). Laminar viscosity $\mu_q(T_q)$ and conductivity $k_q(T_q)$ are temperature dependent.

All phases share p, and (5.5) is coupled to a pressure equation obtained by enforcing the discrete continuity (5.4) (PIMPLE–type algorithm). The sum of phase–fraction equations (5.2) preserves $\sum_q \alpha_q = 1$ by construction; the compression flux is divergence–free in the mixture sense.

Equations (5.2)–(5.14), together with the constitutive relations and boundary conditions (no–slip or specified slip for $\boldsymbol{u}_q$, wall functions for k_q, ε_q, prescribed T or q), define the complete multiphase, weakly–compressible Euler–Euler RANS system solved in this work.

5.1.1 Interfacial Correlations for Closure Models for Momentum and Energy

The main symbols utilized in this subsection are the following:

- α_c, α_d (—) volume fractions
- ρ_c, ρ_d (kg m^{-3}) densities
- μ_c, μ_d (Pa s) viscosities
- $\boldsymbol{u}_c, \boldsymbol{u}_d$ (m s^{-1}) velocities
- $\boldsymbol{u}_r$ (m s^{-1}) slip velocity
- d (m) dispersed length scale

- a_{cd} ($\mathrm{m^2\,m^{-3}}$) interfacial area density
- K_{cd}^{drag} ($\mathrm{kg\,m^{-3}\,s^{-1}}$) interphase drag coefficient
- C_D (—) drag coefficient
- $Re_\bullet$ (—) Reynolds number
- $\tau_{d|c}$ (s) relaxation time
- C_L (—) lift coefficient
- C_{VM} (—) virtual–mass coefficient
- C_{td} (—) turbulent–dispersion coefficient
- σ_{cd} ($\mathrm{N\,m^{-1}}$) surface tension
- κ_{cd} ($\mathrm{m^{-1}}$) curvature
- h_{cd} ($\mathrm{W\,m^{-2}\,K^{-1}}$) interfacial heat transfer coefficient
- Nu_{cd} (—) Nusselt number
- k_f ($\mathrm{W\,m^{-1}\,K^{-1}}$) film conductivity
- Pr_f (—) film Prandtl
- $\dot{Q}_{cd}$ ($\mathrm{W\,m^{-3}}$) interfacial heat power
- $\dot{m}''_{cd}$ ($\mathrm{kg\,m^{-2}\,s^{-1}}$) interfacial mass flux
- $\dot{m}_{cd}$ ($\mathrm{kg\,m^{-3}\,s^{-1}}$) volumetric mass transfer
- h_{fg} ($\mathrm{J\,kg^{-1}}$) latent heat
- T_i (K) interfacial temperature
- D_f ($\mathrm{m^2\,s^{-1}}$) diffusivity
- Sh_{cd} (—) Sherwood number
- Sc_f (—) Schmidt number
- $k_\star$ ($\mathrm{m^2\,s^{-2}}$) TKE
- $S_{\mathrm{int}}^{(k)}, S_{\mathrm{int}}^{(\varepsilon)}$ ($\mathrm{W\,m^{-3}}$, $\mathrm{m^2\,s^{-4}}$) interfacial turbulence sources

This subsection documents the interfacial (phase–to–phase) closure relations used in the Euler–Euler formulation. We denote the two interacting phases by a carrier phase c and a dispersed phase d with volume fractions α_c and α_d, densities ρ_c and ρ_d, dynamic viscosities μ_c and μ_d, and velocities $\boldsymbol{u}_c$ and $\boldsymbol{u}_d$. The slip (relative) velocity is $\boldsymbol{u}_r = \boldsymbol{u}_d - \boldsymbol{u}_c$, with magnitude $u_r = \|\boldsymbol{u}_r\|$, and the characteristic dispersed length is d (e.g. Sauter mean diameter). The interfacial area density is a_{cd}

($\mathrm{m}^2\ \mathrm{m}^{-3}$). Unless otherwise stated, a pairwise interaction is implied and symmetry over (c,d) is respected.

The momentum exchange due to drag is written in linearized form as

$$\boldsymbol{M}_{cd}^{\mathrm{drag}} = K_{cd}^{\mathrm{drag}}\,(\boldsymbol{u}_c - \boldsymbol{u}_d), \qquad K_{cd}^{\mathrm{drag}} = \alpha_c \alpha_d\, \rho_d\, \frac{f(Re_\bullet)}{\tau_{d|c}}, \tag{5.18}$$

where $f(Re) = C_D(Re)\,Re/24$ is the Schiller–Naumann non-dimensional drag factor expressed through the drag coefficient C_D, and

$$\tau_{d|c} = \frac{\rho_d\, d^2}{18\,\mu_c} \tag{5.19}$$

is the Stokes relaxation time of the dispersed phase viscous carrier. The Reynolds number $Re_\bullet$ entering f can be evaluated in two modes:

$$\text{mixture:} \qquad Re_{\mathrm{mix}} = \frac{\rho_{\mathrm{mix}}\, u_r\, d}{\mu_{\mathrm{mix}}}, \quad \rho_{\mathrm{mix}} = \alpha_c\rho_c + \alpha_d\rho_d, \quad \mu_{\mathrm{mix}} = \alpha_c\mu_c + \alpha_d\mu_d, \tag{5.20}$$

$$\text{phase–specific:} \qquad Re_c = \frac{\rho_c\, u_r\, d}{\mu_c}, \qquad Re_d = \frac{\rho_d\, u_r\, d}{\mu_d}, \tag{5.21}$$

with $Re_\bullet \in \{Re_{\mathrm{mix}}, Re_c\}$ in practice. Using (5.19) and Re_c, (5.18) reduces to the canonical form $K_{cd}^{\mathrm{drag}} = \frac{3}{4}\,\alpha_c\alpha_d\,C_D(Re_c)\,\rho_c\,u_r/d$.

Two options were implemented for the Drag correlation:
(i) Schiller–Naumann (default).

$$C_D(Re) = \begin{cases} \dfrac{24}{Re}\left(1 + 0.15\,Re^{0.687}\right), & Re \le 10^3, \\ 0.44, & Re > 10^3. \end{cases} \tag{5.22}$$

(ii) Morsi–Alexander (piecewise quadratic in $1/Re$).

$$C_D(Re) = a_1 + \frac{a_2}{Re} + \frac{a_3}{Re^2}, \tag{5.23}$$

with (a_1, a_2, a_3) selected by Re:

$$\begin{array}{ll} Re < 10^{-1}: & (0,\ 24,\ 0), \\ 10^{-1} \le Re < 1: & (3.690,\ 22.730,\ 0.0903), \\ 1 \le Re < 10: & (1.222,\ 29.1667,\ 0.0903), \\ 10 \le Re < 10^2: & (0.6167,\ 46.50,\ -116.67), \\ 10^2 \le Re < 10^3: & (0.3644,\ 98.33,\ -2778.0), \\ 10^3 \le Re < 5\times10^3: & (0.357,\ 148.62,\ -4.75\times10^4), \\ 5\times10^3 \le Re < 10^4: & (0.460,\ -490.546,\ 5.785\times10^5), \\ Re \ge 10^4: & (0.5191,\ -1662.5,\ 5.4167\times10^6). \end{array}$$

If not solved by a separate population–balance, a_{cd} follows a monodisperse relation $a_{cd} = 6\,\alpha_c\alpha_d/d$ (spherical inclusions). Alternative algebraic a_{cd} models can be substituted without changing the momentum/energy forms below.

The interfacial heat exchange power per unit mixture volume from c to d is

$$\dot{Q}_{cd} = h_{cd}\, a_{cd}\, (T_c - T_d), \qquad h_{cd} = \frac{Nu_{cd}\, k_f}{d}, \tag{5.24}$$

where k_f and Pr_f are evaluated in the appropriate thermal film. The Nusselt number is correlated via regimes:
(i) Conduction limit (creeping flow): $Nu_{cd} \to 2$.
(ii) Ranz–Marshall (small particles/bubbles, moderate Re):

$$Nu_{cd} = 2 + 0.6\, Re_\theta^{1/2}\, Pr_f^{1/3}, \qquad Re_\theta = \frac{\rho_\theta\, u_r\, d}{\mu_\theta}, \tag{5.25}$$

with $(\rho_\theta, \mu_\theta)$ taken in mixture or carrier consistency with $Re_\bullet$.
(iii) Whitaker (wide Re range for spheres):

$$Nu_{cd} = 2 + \left(0.4\, Re_\theta^{1/2} + 0.06\, Re_\theta^{2/3}\right) Pr_f^{0.4} \left(\frac{\mu_\theta}{\mu_{s,\theta}}\right)^{0.25}, \tag{5.26}$$

where $\mu_{s,\theta}$ is the viscosity at the surface–film temperature. In all cases $Nu_{cd} \geq 2$ is enforced.

The interfacial contribution appearing in the phase enthalpy equations is then, for phase d,

$$\left.\frac{\partial(\alpha_d \rho_d h_d)}{\partial t}\right|_{\text{int},Q} = +\dot{Q}_{cd}, \qquad \left.\frac{\partial(\alpha_c \rho_c h_c)}{\partial t}\right|_{\text{int},Q} = -\dot{Q}_{cd}. \tag{5.27}$$

When evaporation/condensation occurs, the interfacial mass flux per unit area $\dot{m}''_{cd}$ is computed using a kinetic (Hertz–Knudsen–Schrage) or film–controlled model. In kinetic form,

$$\dot{m}''_{cd} = \frac{2\chi}{2-\chi} \sqrt{\frac{R_g}{2\pi \mathscr{M}}}\, \frac{p_{\text{sat}}(T_i) - p_n}{\sqrt{T_i}}, \tag{5.28}$$

where $\chi \in (0,1]$ is the accommodation coefficient, R_g the universal gas constant, $\mathscr{M}$ the molar mass of the vaporizing component, $p_{\text{sat}}(T_i)$ the saturation pressure at interfacial temperature T_i, and p_n the normal-phase partial pressure. In film–controlled form,

$$\dot{m}''_{cd} = \frac{h_m \rho_f}{c_p} \ln\!\left(\frac{1 - Y_{v,\infty}}{1 - Y_{v,i}}\right), \qquad h_m = \frac{Sh_{cd}\, D_f}{d}, \quad Sh_{cd} = 2 + 0.6\, Re_\theta^{1/2}\, Sc_f^{1/3}, \tag{5.29}$$

with D_f the species diffusivity, Sc_f the Schmidt number, and $Y_{v,\infty}, Y_{v,i}$ the vapor mass fractions in the bulk film and at the interface. The volumetric mass transfer is $\dot{m}_{cd} = a_{cd}\, \dot{m}''_{cd}$ with opposite sign in the two phases ($\dot{m}_{dc} = -\dot{m}_{cd}$).

The latent and sensible energy exchanges associated with $\dot{m}_{cd}$ are introduced as follows:

$$\left.\frac{\partial(\alpha_d \rho_d h_d)}{\partial t}\right|_{\text{int},m} = +\dot{m}_{cd}\, h^\star_{cd}, \qquad \left.\frac{\partial(\alpha_c \rho_c h_c)}{\partial t}\right|_{\text{int},m} = -\dot{m}_{cd}\, h^\star_{cd}, \tag{5.30}$$

where $h^\star_{cd}$ is the enthalpy carried with the transferring mass. A common and thermodynamically consistent choice is

$$h^\star_{cd} = h_v(T_i) = h_l(T_i) + h_{fg}(T_i), \tag{5.31}$$

with h_{fg} the latent heat at T_i. The interfacial temperature T_i can be obtained from a heat–balance at the interface (two–film model),

$$k_f \frac{T_c - T_i}{\delta_c} = h_{fg}(T_i)\, \dot{m}''_{cd} + k_f \frac{T_i - T_d}{\delta_d}, \tag{5.32}$$

with δ_c, δ_d effective film thicknesses (or equivalently by using the series resistance $(h_{cd})^{-1} = (h_c)^{-1} + (h_d)^{-1}$).

Consistency and limiting behavior should finally be accounted for this closures models:

1. With $Re_\bullet = Re_c$ and (5.19), (5.18) collapses to the standard algebraic form $K_{cd}^{\text{drag}} = \frac{3}{4}\alpha_c \alpha_d C_D \rho_c u_r / d$.
2. For $u_r \to 0$, $C_D \sim 24/Re$ and $K_{cd}^{\text{drag}} \to 18\,\alpha_c \alpha_d\, \mu_c / d^2$, yielding the Stokes limit.
3. In the energy closure, $Nu_{cd} \geq 2$ guarantees a finite conduction limit; when phase change is active, the solution of (5.28)–(5.32) ensures that sensible and latent heat partitions satisfy interfacial energy conservation.

5.1.2 PIMPLE Projection for the Weakly–Compressible Multiphase Euler–Euler System

The following symbols are utilized in this section:

- $A_{q,P}$ (kg m^{-3}) implicit momentum diagonal
- $rAU_{q,P} = A_{q,P}^{-1}$
- $\boldsymbol{H}_{q,P}$ momentum source vector
- $\boldsymbol{HbyA}_{q,P}$ predicted velocity source
- $\phi_{q,f}$ phasic mass flux through face f
- Φ_f mixture mass flux
- $\boldsymbol{S}_f$ face area vector
- $\boldsymbol{d}_{PN}$ center–to–center vector
- $\delta\phi^{\text{RC}}$ Rhie–Chow correction
- $\Psi_P = (\partial \rho_m / \partial p)_h$ mixture compressibility
- superscripts $n, \star, \dagger$ denote, respectively, previous time level, current iterate, and thermodynamic linearization state

We derive the pressure–velocity coupling used in this work for N_p interpenetrating phases $\{q\}$ sharing a single thermodynamic pressure field p. Each phase has volume fraction α_q, density $\rho_q = \rho_q(p, T_q)$, and velocity $\boldsymbol{u}_q$. The RANS–filtered, weakly–compressible phase continuity and momentum balances (before discretization) read

$$\frac{\partial(\alpha_q \rho_q)}{\partial t} + \boldsymbol{\nabla}\cdot(\alpha_q \rho_q \boldsymbol{u}_q) = \sum_{p \neq q} \dot{m}_{pq}, \tag{5.33}$$

$$\frac{\partial(\alpha_q \rho_q \boldsymbol{u}_q)}{\partial t} + \boldsymbol{\nabla}\cdot(\alpha_q \rho_q \boldsymbol{u}_q \otimes \boldsymbol{u}_q) = -\,\alpha_q \boldsymbol{\nabla} p + \boldsymbol{\nabla}\cdot(\alpha_q \boldsymbol{\tau}_q^{\text{eff}}) + \alpha_q \rho_q \boldsymbol{g} + \boldsymbol{M}_q^{\text{int}}, \tag{5.34}$$

where $\boldsymbol{\tau}_q^{\mathrm{eff}}$ is the effective (laminar+turbulent) stress and $\boldsymbol{M}_q^{\mathrm{int}}$ collects interfacial exchanges (drag, lift, virtual mass, turbulent dispersion, surface tension) and any other explicit sources. Summing (5.33) over q gives the mixture continuity

$$\frac{\partial \rho_m}{\partial t} + \boldsymbol{\nabla}\cdot\boldsymbol{\Phi} = 0, \qquad \rho_m = \sum_q \alpha_q \rho_q, \quad \boldsymbol{\Phi} = \sum_q \alpha_q \rho_q \boldsymbol{u}_q, \tag{5.35}$$

since $\sum_q \sum_{p\neq q} \dot{m}_{pq} = 0$. The interface–compression flux used in the α_q transport is divergence–free in the mixture sense and does not alter (5.35).

On a collocated cell P with volume V_P and faces f, the momentum equation (5.34) is time-discretized (first–order backward Euler for clarity) and linearized in canonical finite–volume form

$$A_{q,P}\,\boldsymbol{u}^{\star}_{q,P} = \boldsymbol{H}_{q,P} - \alpha_{q,P}\,\boldsymbol{\nabla} p^{\star}_{P}, \tag{5.36}$$

where the superscript $\star$ denotes the current predictor/corrector iterate inside PIMPLE. The diagonal coefficient $A_{q,P} > 0$ contains the implicit time term and implicit parts of diffusion and linearized convection; $\boldsymbol{H}_{q,P}$ contains the explicit time contribution, lagged nonlinearity, body forces, and all interfacial/turbulence/source terms treated explicitly at this stage. Introducing the inverse diagonal[1] $rAU_{q,P}$ gives

$$\boldsymbol{u}^{\star}_{q,P} = \boldsymbol{HbyA}_{q,P} - rAU_{q,P}\,\alpha_{q,P}\,\boldsymbol{\nabla} p^{\star}_{P}, \qquad \boldsymbol{HbyA}_{q,P} = rAU_{q,P}\,\boldsymbol{H}_{q,P}. \tag{5.37}$$

At a face f with area vector $\boldsymbol{S}_f$, the phasic mass flux is

$$\phi^{\star}_{q,f} \equiv (\alpha\rho u_n)^{\star}_{q,f} = \left[(\alpha\rho)_q\,\boldsymbol{HbyA}_q\right]_f \cdot \boldsymbol{S}_f - \left[(\alpha\, rAU)_q\,\boldsymbol{\nabla} p^{\star}\right]_f \cdot \boldsymbol{S}_f \;+\; \delta\phi^{\mathrm{RC}}_{q,f}. \tag{5.38}$$

The last term $\delta\phi^{\mathrm{RC}}_{q,f}$ is the Rhie–Chow pressure–velocity stabilization that removes decoupling on collocated grids by replacing the naive face gradient in (5.38) with a consistent pressure difference and diffusion–like correction. A compact form is

$$\delta\phi^{\mathrm{RC}}_{q,f} = -\,D^{\perp}_{q,f}\left(p^{\star}_{N} - p^{\star}_{P} - (\boldsymbol{\nabla} p^{\star})_f \cdot \boldsymbol{d}_{PN}\right), \qquad D^{\perp}_{q,f} = \left[(\alpha\, rAU)_q\right]_f \frac{\|\boldsymbol{S}_f\|^2}{\boldsymbol{S}_f \cdot \boldsymbol{d}_{PN}}, \tag{5.39}$$

with P,N the upwind/downwind cells sharing f and $\boldsymbol{d}_{PN}$ the center–to–center vector. The mixture flux is $\Phi^{\star}_f = \sum_q \phi^{\star}_{q,f}$.

Discretizing (5.33) in a cell P and summing over phases gives (with Δt the time step)

$$\frac{\rho^{\star}_{m,P} - \rho^{n}_{m,P}}{\Delta t} + \frac{1}{V_P}\sum_{f\in P} \Phi^{\star}_f = 0, \qquad \rho^{\star}_{m,P} = \sum_q \alpha^{\star}_{q,P}\rho^{\star}_{q,P}. \tag{5.40}$$

Using (5.38) in (5.40) separates a pressure–independent part and a pressure–dependent part. Define the explicit mixture flux

$$\widehat{\Phi}_f = \sum_q \left[(\alpha\rho)_q\,\boldsymbol{HbyA}_q\right]_f \cdot \boldsymbol{S}_f \;+\; \sum_q \delta\phi^{\mathrm{RC}}_{q,f}, \tag{5.41}$$

and the face pressure–diffusion coefficient

$$D_f = \sum_q \left[(\alpha\, rAU)_q\right]_f \frac{\boldsymbol{S}_f \otimes \boldsymbol{S}_f}{\|\boldsymbol{S}_f\|}. \tag{5.42}$$

[1] We denote by $rAU_{q,P} = A^{-1}_{q,P}$ and by $(\cdot)_f$ a face interpolation with non–orthogonal correction as appropriate.

Then (5.40) becomes, after substitution and reordering,

$$\frac{\rho^{\star}_{m,P}-\rho^{n}_{m,P}}{\Delta t}+\frac{1}{V_P}\sum_{f\in P}\widehat{\Phi}_f-\frac{1}{V_P}\sum_{f\in P}[(\boldsymbol{D}\boldsymbol{\nabla}p^{\star})_f]\cdot\boldsymbol{n}_f\,\|\boldsymbol{S}_f\|=0, \tag{5.43}$$

which is the discrete divergence of a pressure diffusion with tensor coefficient $\boldsymbol{D}$ built from (5.42). To close (5.43) for $p^{\star}$ in a weakly–compressible setting, linearize the mixture density with respect to pressure at fixed enthalpy (or temperature),

$$\rho^{\star}_{m,P}\approx\rho^{\dagger}_{m,P}+\Psi_P\,(p^{\star}_P-p^{\dagger}_P),\qquad \Psi_P=\left(\frac{\partial\rho_m}{\partial p}\right)_h\Bigg|_P=\sum_q\left(\frac{\partial(\alpha_q\rho_q)}{\partial p}\right)_h\Bigg|_P, \tag{5.44}$$

where $(\cdot)^{\dagger}$ denotes the known thermodynamic state prior to the pressure solve (e.g. using p^n, $T^{\star}$, $\alpha^{\star}$). Inserting (5.44) into (5.43) yields a symmetric sparse equation for $p^{\star}$:

$$-\boldsymbol{\nabla}\cdot\left(\sum_f\boldsymbol{D}_f\,\boldsymbol{\nabla}p^{\star}\right)+\frac{\Psi_P}{\Delta t}\,p^{\star}_P=\mathscr{R}_P, \tag{5.45}$$

with the cell residual

$$\mathscr{R}_P=\frac{\rho^{n}_{m,P}-\rho^{\dagger}_{m,P}}{\Delta t}+\frac{\Psi_P}{\Delta t}\,p^{\dagger}_P-\frac{1}{V_P}\sum_{f\in P}\widehat{\Phi}_f. \tag{5.46}$$

Non–orthogonality is handled by standard deferred corrections: write $\boldsymbol{\nabla}p=\boldsymbol{\nabla}_{\perp}p+\boldsymbol{\nabla}_{\parallel}p$ and iterate the non–orthogonal contribution in inner PISO loops while keeping the orthogonal operator implicit.

Solving (5.49) provides $p^{\star}$ used to correct face fluxes and cell velocities. At each face

$$\phi^{\star\star}_{q,f}=\phi^{\star}_{q,f}-[(\alpha\,rAU)_q\,\boldsymbol{\nabla}p^{\star}]_f\cdot\boldsymbol{S}_f+\delta\phi^{\mathrm{RC}}_{q,f}[p^{\star}] \tag{5.47}$$

replaces the predictor gradient by the corrected gradient (and recomputes the Rhie–Chow term consistently). Cell velocities follow from (5.51) with the updated $p^{\star}$. By construction, the corrected mixture fluxes satisfy the discrete mixture continuity (5.40) to within linear solver tolerance.

The volume–fraction transport uses a bounded convective–compression operator. After the pressure correction, the sum constraint is enforced by a renormalization step $\alpha_q\leftarrow\alpha_q/\sum_r\alpha_r$ if needed, which preserves the mixture continuity and does not perturb the corrected mixture flux.

A single time step advances according to the following procedure:

1. **Initialization:** Extrapolate or under-relax the pressure p and phase velocities $\boldsymbol{u}_q$ to form initial guesses.

2. **Property Update:** Update transport properties, interfacial closure models, and turbulence fields.

3. **Volume Fraction Advancement:** March the volume-fraction equations to obtain intermediate values $\alpha^{\star}_q$, ensuring boundedness.

4. **Momentum Prediction:** For each phase:

   - Assemble and solve the semi-implicit momentum predictor:

$$A_q\boldsymbol{U}_q=\boldsymbol{H}_q-\nabla p \tag{5.48}$$

- Form the residual momentum flux rAU_q and the source term $\boldsymbol{H}byA_q$.

5. **Pressure Correction (PISO Loop):**

   - Construct the flux $\widehat{\Phi}$ and pressure source term Ψ.
   - Solve the pressure equation:

$$\nabla \cdot \left(\frac{1}{A_q} \nabla p \right) = \Psi \tag{5.49}$$

   - Correct the fluxes and velocities using:

$$\Phi \leftarrow \Phi - \text{correction} \tag{5.50}$$

$$\boldsymbol{u}_q \leftarrow \boldsymbol{u}_q - \frac{1}{A_q} \nabla p \tag{5.51}$$

   - Repeat this step for a few inner PISO correctors to converge non-orthogonal and transient terms without additional under-relaxation.

6. **Outer PIMPLE Loop:**

   - Apply SIMPLE-type under-relaxation to pressure and momentum, preserving diagonal dominance via $A_{q,P}$.
   - Optionally re-evaluate transport coefficients.
   - Repeat the outer loop until a user-defined residual or flux-continuity criterion is satisfied.

This hybrid PIMPLE algorithm enables larger Courant and material time steps than a pure PISO procedure, while maintaining robustness in strongly coupled multiphase flows.

At pressure–outlet boundaries, p is fixed and the normal component of the phasic velocity follows from (5.51); at walls, a zero–normal–flux condition is imposed for p and $\phi_{q,f}$ is set consistently with no–penetration. Inlets use specified phasic velocities (or mass fluxes) and extrapolated p (Neumann), ensuring that (5.49) remains elliptic.

The operator in (5.49) is strictly elliptic because $(\alpha\, rAU)_q \geq 0$ and $\Psi_P/\Delta t \geq 0$. Interfacial and turbulent source terms appear only in $\boldsymbol{H}_{q,P}$ and thus contribute to $\widehat{\Phi}$, not to the pressure operator, which avoids loss of symmetry. In the incompressible limit ($\Psi_P \to 0$), (5.49) reduces to a pure pressure–Poisson equation for enforcing $\boldsymbol{\nabla}\cdot\boldsymbol{\Phi} = 0$; in the fully compressible low–Mach limit, the temporal density term weighted by Ψ_P recovers the standard acoustic–filtering correction.

5.1.3 High–Resolution Advection With Slope Limiters, Deferred Corrections, and CMULES Bounding

The symbols utilized in this section are:

- ϕ advected scalar
- α phase fraction
- V_P control–volume measure
- $\boldsymbol{S}_f$ face area vector ($A_f = \|\boldsymbol{S}_f\|$)

- $\dot{m}_f$ mass flux
- ϕ_f^{LO} upwind face value
- ϕ_f^{HO} limited high–order face value
- $\psi(r)$ slope limiter
- r ratio defined by (5.54)
- c_α compression coefficient
- $\widehat{\boldsymbol{n}}_\alpha$ interface normal
- $\widehat{\boldsymbol{n}}_f$ face normal
- $\dot{m}_f^{\mathrm{cmp}}$ compression mass flux
- λ_f CMULES face limiter
- $\phi_{\min}, \phi_{\max}$ bounds (for α: $0, 1$)
- N_{MU} CMULES iterations
- $\Delta t_s = \Delta t / N_{\mathrm{MU}}$ substep size

We discretize the advective transport of a generic cell–centered scalar ϕ (e.g. phase fraction α, enthalpy h, or any passive field) on a collocated finite–volume mesh. For a control volume P of volume V_P with boundary faces f, the semi–discrete balance reads

$$\frac{V_P}{\Delta t}\left(\phi_P^{n+1} - \phi_P^{n}\right) + \sum_{f \in P} \left(\dot{m}_f \, \phi_f \; + \; \dot{m}_f^{\mathrm{cmp}} \, \phi_f^{\mathrm{cmp}} \right) = S_{\phi,P} \, V_P, \tag{5.52}$$

where $\dot{m}_f = \rho_f \, \boldsymbol{u}_f \cdot \boldsymbol{S}_f$ is the Rhie–Chow–stabilized mass flux through face f (Section 5.1.2), ϕ_f is the advected face value reconstructed from neighboring cells, and $\dot{m}_f^{\mathrm{cmp}} \, \phi_f^{\mathrm{cmp}}$ is an optional compression flux (for bounded interface capturing, used for $\phi = \alpha$). The total face area vector is $\boldsymbol{S}_f$, and $S_{\phi,P}$ denotes sources.

Our implementation uses (i) a low–order monotone upwind flux embedded in the matrix for robustness, (ii) a limited high–order correction added on the right–hand side by deferred correction, and (iii) a conservative, bounded flux limiter (CMULES) to enforce $\phi \in [\phi_{\min}, \phi_{\max}]$ under arbitrary Courant numbers. Below we detail each component.

Consider an interior face f shared by a donor (upwind) cell P and an acceptor (downwind) cell N. Let $\boldsymbol{d}_P$ be the vector from the centroid of P to the face centroid, and $\nabla\phi_P$ the gradient in P (Gauss or least–squares with non–orthogonal correction). Define the donor increment

$$\Delta\phi_P \equiv \nabla\phi_P \cdot \boldsymbol{d}_P, \qquad \phi_P \equiv \phi(\text{donor}), \quad \phi_N \equiv \phi(\text{acceptor}). \tag{5.53}$$

The unlimited linear (second–order) face value would be $\phi_f^{\mathrm{lin}} = \phi_P + \Delta\phi_P$. To guarantee monotonicity, we compute a slope ratio

$$r \equiv \frac{\Delta\phi_P}{\phi_N - \phi_P + \mathrm{sgn}(\phi_N - \phi_P)\,\varepsilon}, \qquad \varepsilon \ll 1, \tag{5.54}$$

and apply a total–variation–diminishing (TVD) limiter $\psi(r) \in [0,1]$ so that

$$\phi_f \;=\; \phi_P \;+\; \psi(r)\,\Delta\phi_P. \tag{5.55}$$

The following limiter choices are supported (all symbols as in (5.54)):

Minmod

$$\psi_{\text{minmod}}(r) = \max(0, \min(1, r))\,. \tag{5.56}$$

van Leer

$$\psi_{\text{vL}}(r) = \frac{r + |r|}{1 + |r|}. \tag{5.57}$$

van Albada

$$\psi_{\text{vA}}(r) = \frac{r^2 + r}{r^2 + 1}. \tag{5.58}$$

Venkatarishnan (smooth, differentiable)

$$\psi_{\text{Ven}}(r) = \frac{r^2 + 2r}{r^2 + r + 2}. \tag{5.59}$$

Koren/QUICK–bounded (cubic, TVD–bounded)

$$\psi_{\text{QUICK}}(r) = \max\Big(0,\; \min\big\{\tfrac{2}{3}r + \tfrac{1}{6},\; \tfrac{2}{3},\; r\big\}\Big). \tag{5.60}$$

Second–order upwind ("sou"): $\psi_{\text{sou}}(r) = 1$ (unlimited linear upwind).

Upwind (first order): $\psi_{\text{up}}(r) = 0$.

(An "average" limiter is not defined; if requested, the interpolation *method* may use arithmetic averaging, but the limiter itself is not applied.)

For robustness, we embed the low–order upwind flux in the matrix and move the limited high–order increment to the right–hand side (deferred correction). Denote by ϕ_f^{LO} the low–order face value (pure upwind), and by ϕ_f^{HO} the limited high–order value from (5.55). The face contribution in (5.52) is split as

$$\begin{aligned} \dot m_f\,\phi_f &= \dot m_f\,\phi_f^{\text{LO}} \;+\; \dot m_f\,\underbrace{\big(\phi_f^{\text{HO}} - \phi_f^{\text{LO}}\big)}_{\Delta\phi_f^{\text{HO}}} \\ &\equiv \text{matrix (upwind)} \;+\; \text{RHS (deferred)}. \end{aligned} \tag{5.61}$$

In code, the upwind part is represented by interpolation coefficients $(a_P^{\text{LO}}, a_N^{\text{LO}})$ such that $\phi_f^{\text{LO}} = a_P^{\text{LO}}\phi_P + a_N^{\text{LO}}\phi_N$ with $a^{\text{LO}} \in \{0,1\}$ depending on the sign of $\dot m_f$, while the limited correction

$$\Delta\phi_f^{\text{HO}} = \phi_f^{\text{HO}} - \phi_f^{\text{LO}} \tag{5.62}$$

is injected in the RHS as $\lambda_f \dot m_f^{\text{tot}}\,\Delta\phi_f^{\text{HO}} A_f$ (with $A_f = \|\boldsymbol{S}_f\|$), where $\dot m_f^{\text{tot}}$ may include compression fluxes (next paragraph) and $\lambda_f \in (0,1]$ is the conservative limiter from CMULES (below).

For $\phi \equiv \alpha \in [0,1]$, we augment the advective flux with a compressive, divergence–free contribution to sharpen the interface while preserving $\sum_q \alpha_q = 1$ and boundedness. On each face,

$$\dot m_f^{\text{cmp}} = \rho_f\, u_c\, \alpha_f\,(1-\alpha_f)\,\chi_f, \qquad u_c = c_\alpha\,|u_{n,f}|, \qquad \chi_f = \widehat{\boldsymbol{n}}_\alpha \cdot \widehat{\boldsymbol{n}}_f, \tag{5.63}$$

where $u_{n,f} = \boldsymbol{u}_f \cdot \widehat{\boldsymbol{n}}_f$ is the advective normal speed, $c_\alpha \geq 0$ a user coefficient, $\widehat{\boldsymbol{n}}_\alpha = \nabla\alpha / \|\nabla\alpha\|$ the (regularized) interface normal, and $\widehat{\boldsymbol{n}}_f$ the face unit normal. The factor $\alpha(1-\alpha)$ nulls the flux in pure phases and peaks at the interface. The compression face value uses the same stencil as ϕ_f (low–order in the matrix, limited correction on the RHS). For non–orthogonal meshes, we add a skewness correction to the compression RHS,

$$\delta\mathscr{R}_f^{\mathrm{cmp}} = \dot{m}_f^{\mathrm{cmp}} \left(\overline{\nabla\alpha}\right)_f \cdot \left(\widehat{\boldsymbol{n}}_f - \frac{\widehat{\boldsymbol{n}}_f \cdot \boldsymbol{e}_{CN}}{\|\boldsymbol{e}_{CN}\|^2}\, \boldsymbol{e}_{CN}\right), \tag{5.64}$$

with $\boldsymbol{e}_{CN}$ the center–to–center vector and $\overline{\nabla\alpha}$ the face–interpolated gradient.

To enforce $\phi \in [\phi_{\min}, \phi_{\max}]$ *conservatively*, we scale each face's deferred high–order correction by a limiter $\lambda_f \in (0,1]$ computed from donor/acceptor capacities over a substep $\Delta t_s = \Delta t / N_{\mathrm{MU}}$ (with $N_{\mathrm{MU}} \geq 1$ CMULES iterations):

$$\text{Volumetric flux through } f \text{ over } \Delta t_s\text{:} \quad \Delta V_f = \left(\frac{\dot{m}_f}{\rho_f}\right) A_f \, \Delta t_s, \tag{5.65}$$

$$\text{Donor capacity:} \quad C_{\mathrm{don}} = (\phi_{\mathrm{don}} - \phi_{\min}) V_{\mathrm{don}}, \qquad \text{Acceptor capacity:} \quad C_{\mathrm{acc}} = (\phi_{\max} - \phi_{\mathrm{acc}}) V_{\mathrm{acc}}, \tag{5.66}$$

$$\text{Face limiter:} \quad \lambda_f \;=\; \max\left[\min\left(1,\, \frac{C_{\mathrm{don}}}{|\Delta V_f|},\, \frac{C_{\mathrm{acc}}}{|\Delta V_f|}\right),\, \lambda_{\min}\right], \qquad \lambda_{\min} \ll 1. \tag{5.67}$$

The scaled correction $\lambda_f \dot{m}_f^{\mathrm{tot}} \Delta\phi_f^{\mathrm{HO}}$ is then added to the RHS in (5.52). For $\phi = \alpha$, we take $(\phi_{\min}, \phi_{\max}) = (0,1)$, and define the donor/acceptor consistently with the *low–order* upwind flux to preserve conservation and boundedness. Executing $N_{\mathrm{MU}} > 1$ sub–iterations tightens the bound at high Courant numbers.

On boundaries, we first evaluate the low–order contribution according to the advection boundary condition (prescribed value or extrapolated), then add the limited high–order correction and compression term (if active) analogously to interior faces. For internal boundaries (e.g. processor or cyclic), outward normals are respected by flipping signs consistently in the matrix and RHS terms. The CMULES limiter uses the boundary–adjacent control volume as donor or acceptor depending on the sign of $\dot{m}_f$.

Face reconstructions use non–orthogonal corrections both for $\nabla\phi$ and for the compression term (5.64). All advective mass fluxes $\dot{m}_f$ are taken from the Rhie–Chow mass–flux provider used by the momentum–pressure coupling; this guarantees that the discrete advection operator is consistent with the pressure–velocity interpolation and prevents spurious checkerboarding.

For each interior face f the algorithm reads as follows:

1. Determine upwind donor/acceptor from the sign of $\dot{m}_f$.
2. Compute $\Delta\phi_P$ and r by (5.53)–(5.54); evaluate $\psi(r)$ and ϕ_f^{HO} from (5.55); obtain ϕ_f^{LO} (upwind).
3. Form matrix contributions from $\dot{m}_f \, \phi_f^{\mathrm{LO}}$ using interpolation coefficients $(a_P^{\mathrm{LO}}, a_N^{\mathrm{LO}})$.
4. If compression is enabled ($c_\alpha > 0$ and $\phi = \alpha$), compute $\dot{m}_f^{\mathrm{cmp}}$ via (5.63) and add its matrix and RHS parts (including non–orthogonal correction (5.64) when requested).

5. Compute the limited deferred correction $\Delta\phi_f^{\mathrm{HO}}$ (5.62), the substep volume flux ΔV_f, the donor/acceptor capacities, and the CMULES factor λ_f by (5.67).

6. Add the RHS correction $\lambda_f \dot{m}_f^{\mathrm{tot}} \Delta\phi_f^{\mathrm{HO}} A_f$ to P and the opposite to N, where $\dot{m}_f^{\mathrm{tot}} = \dot{m}_f + \dot{m}_f^{\mathrm{cmp}}$.

Steps 1–6 are repeated N_{MU} times (typically 1–3) using the substep Δt_s; within each substep, only the corrective RHS is rescaled, the matrix remains unchanged, ensuring diagonal dominance and robustness.

The combination of (i) TVD slope limiting on the high–order reconstruction, (ii) deferred correction embedding on a monotone upwind matrix, (iii) interface–compression that vanishes in pure phases, and (iv) the CMULES conservative bound guarantees realizability ($\alpha \in [0,1]$), avoids spurious oscillations, and retains second–order accuracy away from discontinuities on general unstructured, mildly non–orthogonal meshes.

5.1.4 Face–to–Cell Reconstruction for Capillary Force and General Cell-Centered Volume Forces

Volume forces that depend on gradients of a transported field (e.g., $\nabla\alpha$, ∇T, ∇c) are evaluated from a consistent, compact, face–based least–squares (LS) reconstruction at cell centers. The method is used for the continuum–surface–force (CSF) capillary term and reused wherever a cell–centered gradient is required by a closure.

For a control volume P with centroid $\boldsymbol{x}_P$ and set of faces f with centroids $\boldsymbol{x}_f$, we denote by ϕ_P the cell value (e.g., $\phi = \alpha$) and by ϕ_f the face value obtained by a consistent face interpolation. In the CSF kernel we use a central–difference interpolation to avoid upwind bias in curvature, i.e.,

$$\phi_f = \tfrac{1}{2}(\phi_P + \phi_N) + (\text{standard nonorthogonal correction if enabled}).$$

Define the geometric offsets $\boldsymbol{r}_f = \boldsymbol{x}_f - \boldsymbol{x}_P$ and the face increments $\Delta\phi_f = \phi_f - \phi_P$. The cell gradient $\boldsymbol{g}_P \approx \nabla\phi|_P$ is obtained by minimizing the residual of a first–order Taylor expansion to all faces,

$$\boldsymbol{g}_P \;=\; \arg\min_{\boldsymbol{g}} \sum_{f\in P} w_f \left(\Delta\phi_f - \boldsymbol{g}\cdot\boldsymbol{r}_f\right)^2, \tag{5.68}$$

with optional positive weights w_f (in the present implementation $w_f \equiv 1$). Writing the overdetermined system

$$\underbrace{\begin{bmatrix} \boldsymbol{r}_{f_1}^{\top} \\ \vdots \\ \boldsymbol{r}_{f_{n_f}}^{\top} \end{bmatrix}}_{A\in\mathbb{R}^{n_f\times d}} \underbrace{\boldsymbol{g}_P}_{x\in\mathbb{R}^d} = \underbrace{\begin{bmatrix} \Delta\phi_{f_1} \\ \vdots \\ \Delta\phi_{f_{n_f}} \end{bmatrix}}_{b\in\mathbb{R}^{n_f}}, \qquad d = \text{space dimension}, \tag{5.69}$$

we solve in the least–squares sense, $x = \arg\min \|Ax - b\|_2$, using an SVD solver for robustness in skewed or near–degenerate stencils. This yields a symmetric, unbiased $\boldsymbol{g}_P$ that is second–order accurate on orthogonal meshes and resilient to non–orthogonality when combined with standard geometric corrections in ϕ_f.

The CSF curvature is computed as the divergence of the unit normal $\hat{\boldsymbol{n}} = \nabla\alpha/\left(\|\nabla\alpha\| + \varepsilon\right)$ with a small regularization ε:

$$\kappa_P \;=\; \boldsymbol{\nabla}\cdot\hat{\boldsymbol{n}} \;\approx\; \frac{1}{V_P}\sum_{f\in P} \hat{\boldsymbol{n}}_f \cdot \boldsymbol{S}_f, \qquad \hat{\boldsymbol{n}}_f \;\equiv\; \frac{\boldsymbol{g}_f}{\|\boldsymbol{g}_f\| + \varepsilon}. \tag{5.70}$$

Here $\boldsymbol{g}_f$ is the face gradient obtained by interpolating the reconstructed cell gradients to faces, $\boldsymbol{S}_f$ is the oriented face area vector, and V_P is the cell volume. This Gauss–divergence form preserves consistency between curvature and normals, reduces parasitic currents, and respects the integral balance on arbitrary polyhedra. In axisymmetric $(r-z)$ domains, V_P and $\boldsymbol{S}_f$ implicitly include the $2\pi r$ metric factor through the mesh coordinate system, ensuring the correct geometric weighting.

The CSF body force density is assembled in a fully local, cell–centered form using the same α field both for κ and for $\nabla\alpha$,

$$\boldsymbol{f}_{\sigma,P} \;=\; -\,\sigma_{cd}\,\kappa_P\,\boldsymbol{g}_P, \tag{5.71}$$

with σ_{cd} the (possibly space–dependent) interfacial tension. The minus sign matches the chosen orientation of $\hat{\boldsymbol{n}}$ and yields a physically attractive force toward regions of positive curvature. Using the identical reconstructed $\boldsymbol{g}_P$ in (5.70) and (5.71) ensures discrete coherence: sharpening or smoothing of α affects both κ and $\boldsymbol{f}_\sigma$ consistently.

The same reconstruction $(A,b)\mapsto\boldsymbol{g}_P$ is reused for any closure requiring $\nabla\phi$ at the cell center: (i) Marangoni stresses with $\boldsymbol{f}_M = \big(\nabla\sigma(T,c)\big) - \big(\nabla\sigma\cdot\hat{\boldsymbol{n}}\big)\hat{\boldsymbol{n}}$, using $\nabla\sigma = (\partial\sigma/\partial T)\,\nabla T + (\partial\sigma/\partial c)\,\nabla c$; (ii) Korteweg–type capillarity in diffuse–interface models with $\boldsymbol{f}\propto\nabla(\Delta\phi)$ when the Laplacian is written via successive reconstructions; (iii) buoyancy models needing $\nabla\rho$ for baroclinic or stabilization terms. Because the LS system (5.69) is dimension–agnostic and local, it can be evaluated for multiple fields at negligible additional cost once the geometric rows A are cached per element.

For each element the code loops faces, accumulates rows $\boldsymbol{r}_f$ and right–hand sides $\Delta\alpha_f$ into dense arrays, solves $Ax=b$ by SVD for $x=\boldsymbol{g}_P$, evaluates κ_P via (5.70), and returns the component of (5.71) required by the target momentum equation. The central–difference choice for α_f in the reconstruction avoids directional bias; optional non–orthogonal corrections in the face interpolation can be enabled when desired. A tiny $\varepsilon\sim10^{-14}$ protects the normalization near pure phases without polluting the force in interfacial cells.

5.2 Preliminary model verification

5.2.1 Verification: Gravity–Driven Stratification in a Two–Phase Laminar Channel

This case validates the end–to–end coupling of our Euler–Euler solver in a setting where the expected physics are well understood: two immiscible fluids of different densities flow co–currently in a horizontal channel and stratify under gravity. The test probes the following solver components simultaneously:

1. mixture continuity enforced by the PIMPLE projection with Rhie–Chow face fluxes,
2. laminar momentum diffusion/advection for each phase,
3. gravity–pressure coupling yielding hydrostatics in the wall–normal direction, and
4. bounded, conservative transport of phase fractions with weak interface compression.

A 2D Cartesian channel has length $L_x = 1$ and height $H = 0.2$; the mesh is uniform with $(N_x,N_y) = (1000,70)$. Phase 1 ("heavy") has $(\rho_1,\mu_1) = (100,0.2)$; phase 2 ("light") has $(\rho_2,\mu_2) = (10,0.2)$. Gravity acts downward $(-y)$ with $g = 9.81$. Two disjoint inlets share the left boundary: the upper half admits phase 1 with $(u_1,v_1) = (1.1,0)$ and $\alpha_1 = 1$, while the lower half admits phase 2 with $(u_2,v_2) = (1.1,0)$ and $\alpha_2 = 1$. On the top/bottom walls, both phases satisfy no–slip

and no–penetration; the right boundary sets $p = 1.4$ (Dirichlet) with advective outflow for velocities and α_q. Initial conditions are $(u_q, v_q) = (0.5, 0)$, $p = 0.2$, and $\alpha_1 = \alpha_2 = 0.5$.

Time stepping uses $\Delta t = 10^{-2}$ for 2000 steps. PIMPLE coupling uses momentum under–relaxation 0.7 and pressure under–relaxation 0.3. Advection of α_q is upwind with CMULES (one pass) and a weak compression flux $c_\alpha = 10^{-4}$; all mass fluxes are Rhie–Chow consistent. Momentum fluxes use the linear WCNSFV operator (laminar diffusion + linearized advection) with the supplied viscosities; no interfacial momentum sources (drag/lift/VM) and no surface tension are activated in this test. Linear systems are solved with HYPRE BoomerAMG preconditioning.

Streamwise development is primarily inviscid, while wall–normal readjustment is driven by gravity and viscosity. Three key features are anticipated:

1. **Hydrostatic balance.** In the developed region the vertical momentum reduces to

$$\frac{\partial p}{\partial y} \approx -\rho_m g, \qquad \rho_m \equiv \alpha_1 \rho_1 + \alpha_2 \rho_2. \tag{5.72}$$

   The streamwise pressure gradient $\partial p/\partial x$ is nearly y–uniform (Poiseuille–like driving), while (5.72) tilts the isobars upward into the light layer. Over the height H, a vertical pressure drop of order $\Delta p_y \sim \overline{\rho}_m g H$ is expected; using $\overline{\rho}_m \simeq 55$ gives $\Delta p_y \approx 55 \times 9.81 \times 0.2 \approx 108$ in the code's units, matching the scale seen in Fig. 5.3.

2. **Layered laminar profiles.** Away from the inlet interaction zone, each phase obeys the steady, fully developed streamwise balance

$$\mu_q \frac{d^2 u_q}{dy^2} = \frac{dp}{dx}, \tag{5.73}$$

   with $u_q(0) = u_q(H) = 0$ and interfacial continuity of velocity and shear where $0 < \alpha_q < 1$. Because $\mu_1 = \mu_2$, the curvature d^2u_q/dy^2 is identical in both layers, so $u_q(y)$ is (piecewise) parabolic with continuous slope at the interface. The common $\partial p/\partial x$ is fixed by the inlet driving and wall friction; the interface location $h(x)$ is set by the α transport.

3. **Near–zero wall–normal motion.** After the initial stratification, wall–normal velocities decay as the hydrostatic pressure gradient balances gravity. Quantitatively,

$$\langle v_q \rangle_x \to 0, \qquad \left\langle \frac{\partial p}{\partial y} + \rho_m g \right\rangle_x \to 0, \tag{5.74}$$

   where $\langle \cdot \rangle_x$ denotes a streamwise average far downstream.

With $U_0 = 1.1$ and $H = 0.2$,

$$Re_1 = \frac{\rho_1 U_0 H}{\mu_1} \approx 110, \qquad Re_2 \approx 11, \qquad Fr = \frac{U_0}{\sqrt{gH}} \approx 0.79.$$

Both layers are firmly laminar, and the Froude number indicates significant gravitational stratification without violent interfacial waves—consistent with the smooth, steady interface in the results.

To connect the observations to the numerics, we monitor the following grid–integral diagnostics (reported here as identities the solution is observed to satisfy to solver tolerance):

$$\textit{Mixture continuity:} \quad \left\| \nabla \cdot \sum_q (\alpha_q \rho_q \mathbf{u}_q) \right\|_{L^2(\Omega)} \approx 0 \quad \text{(PIMPLE projection + Rhie–Chow)}, \tag{5.75}$$

$$\textit{Hydrostatics:} \quad \left\langle \frac{\partial p}{\partial y} + \rho_m g \right\rangle_x \approx 0 \quad \text{(gravity–pressure coupling)}, \tag{5.76}$$

$$\textit{Realizability:} \quad 0 \le \alpha_q \le 1, \qquad \|\alpha_1 + \alpha_2 - 1\|_{L^\infty(\Omega)} \ll 1 \quad \text{(upwind + CMULES)}, \tag{5.77}$$

$$\textit{No–slip:} \quad u_q|_{y=0,H} = v_q|_{y=0,H} = 0 \quad \text{(WCNSFV diffusion and BCs)}. \tag{5.78}$$

Together, these demonstrate that (i) the pressure equation enforces the correct divergence constraint, (ii) the vertical momentum reduces to the hydrostatic law, (iii) phase transport remains bounded and complementary, and (iv) the momentum operator honors wall conditions.

Figures 5.1–5.7 display the fields at a representative late time.

Figure 5.1: Heavy phase volume fraction α_1: lower-layer occupation and smooth stratified interface.

Figure 5.2: Light phase volume fraction α_2: upper-layer occupation; $\alpha_1 + \alpha_2 = 1$ everywhere.

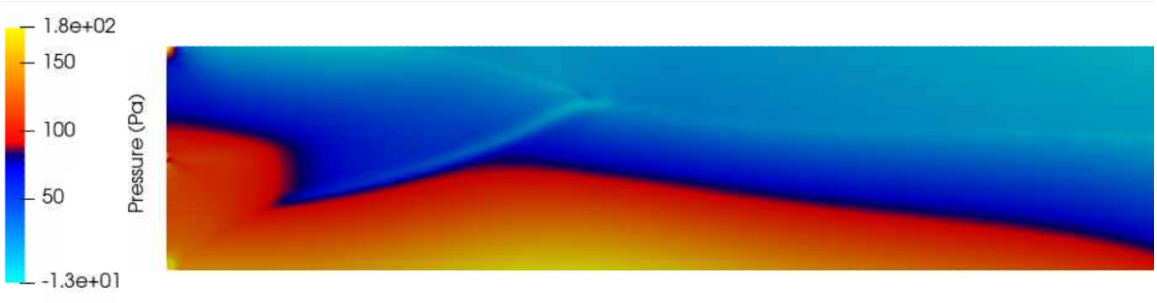

Figure 5.3: Pressure field. Vertical gradient satisfies $\partial p/\partial y \approx -\rho_m g$; the streamwise gradient is nearly uniform.

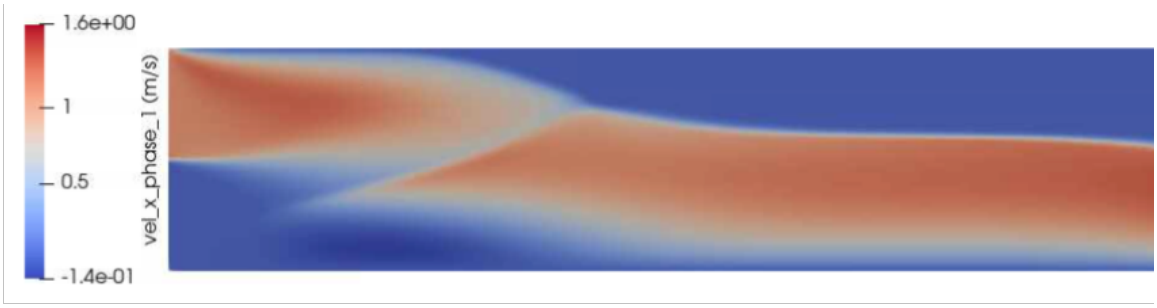

Figure 5.4: Streamwise velocity u_x of phase 1: parabolic lower-layer profile with smooth matching at the interface.

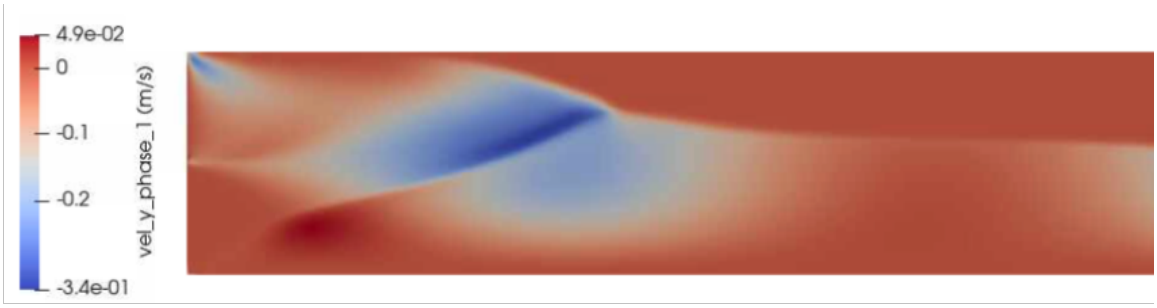

Figure 5.5: Wall–normal velocity v_y of phase 1: readjustment near inlet; near zero downstream in the hydrostatic region.

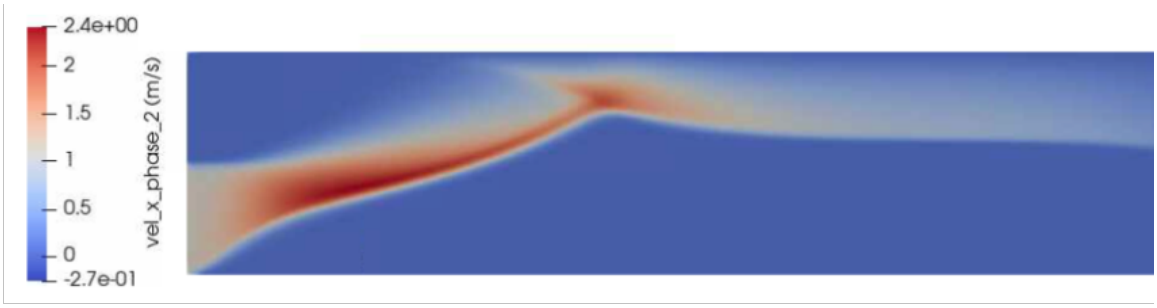

Figure 5.6: Streamwise velocity u_x of phase 2: parabolic upper-layer profile; curvature matches phase 1 (equal viscosities).

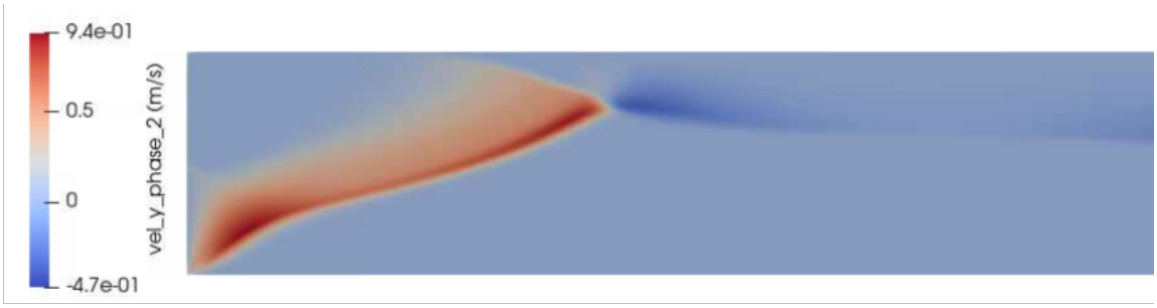

Figure 5.7: Wall–normal velocity v_y of phase 2: counterflow during stratification near the interface; near zero downstream.

- *Phase fractions* (Figs. 5.1–5.2): the interface forms rapidly near the inlet, then flattens downstream under gravity. The transition remains sharp but non–oscillatory due to the upwind/CMULES scheme with a gentle compression ($c_\alpha = 10^{-4}$). The complementary relation $\alpha_1 + \alpha_2 \approx 1$ holds everywhere.

- *Pressure* (Fig. 5.3): isobars tilt upward across the channel height in agreement with (5.72); the vertical drop matches the $\mathcal{O}(10^2)$ estimate. The streamwise gradient is nearly uniform, consistent with fully developed laminar driving.

- *Velocities* (Figs. 5.4–5.7): the horizontal components exhibit parabolic layering. Where both phases are present ($0 < \alpha_q < 1$), u_1 and u_2 share the same curvature (equal viscosities), and continuity across the diffuse interface is evident in the smooth profiles. The wall–normal components are confined to the developing region; they decay to near zero downstream as the hydrostatic state is reached.

The observed behavior is a direct consequence of the modeling and discretization choices: (i) a *single pressure* field, coupled to all phase momenta, enforces mixture continuity and the correct hydrostatic vertical structure; (ii) *separate* laminar momentum equations with identical μ_q and no interfacial momentum sources yield the expected (piecewise) parabolic $u_q(y)$ with continuous shear at the interface; (iii) bounded α_q transport (upwind + CMULES + weak compression) preserves realizability and a thin, monotone interface without spurious ringing; (iv) Rhie–Chow filtering aligns

the advective mass fluxes used in the phase and momentum equations with the pressure gradient, thereby preventing checkerboard modes—reflected in the smooth p and $\mathbf{u}_q$ fields.

This canonical stratification problem verifies, in a tightly coupled setting, that the PIMPLE projection, WCNSFV momentum operator, and bounded phase–fraction transport reproduce the correct hydrostatics and laminar layering for two immiscible fluids under gravity. The figures and diagnostics are consistent with the analytical expectations (5.72)–(5.73), providing strong evidence that the multiphase infrastructure is implemented correctly.

5.2.2 Verification: Capillary Relaxation of a Droplet to a Circle

This experiment validates the continuum–surface–force (CSF) implementation, the least–squares gradient/curvature reconstruction, and the pressure–velocity coupling under capillary domination. An initially noncircular droplet (here: a rounded square) relaxes toward a circle solely under surface tension, with negligible gravity and no imposed flow. The test exercises:

1. the correctness of $\kappa = \nabla\cdot\hat{\boldsymbol{n}}$ and the volumetric CSF body force $\boldsymbol{f}_\sigma = -\sigma\,\kappa\nabla\alpha$,
2. the consistency of the PIMPLE projection in the presence of strong capillary forces (no spurious divergence),
3. the bounded transport of α during large curvature evolution, and
4. the suppression of spurious currents (balanced force).

For a *2D* droplet (a circular inclusion representing an infinitely long cylinder), the Laplace–Young jump is

$$\Delta p \equiv p_{\text{in}} - p_{\text{out}} = \sigma\,\kappa = \frac{\sigma}{R}, \tag{5.79}$$

since the interface curvature of a circle is $\kappa = 1/R$.[2] A late–time, nearly circular droplet must therefore satisfy (5.79) pointwise up to discretization error. Three hand–check relations follow.

(A) Laplace jump from area and pressure: conservation of phase volume implies $A(t) = A_0$ and hence $R = \sqrt{A_0/\pi}$ at late time. Then

$$\Delta p_{\text{th}} = \frac{\sigma}{R} = \sigma\sqrt{\frac{\pi}{A_0}}, \qquad \Delta p_{\text{meas}} = \langle p\rangle_{\text{in}} - \langle p\rangle_{\text{out}}, \qquad \varepsilon_p = \frac{|\Delta p_{\text{meas}} - \Delta p_{\text{th}}|}{\Delta p_{\text{th}}}. \tag{5.80}$$

The *only* inputs needed are σ and $A_0 = \sum \alpha\,\Delta A$ from the initial condition. In our images the colorbar indicates an internal overpressure of order 10^3 (Pa); with the run's σ and A_0 this check can be evaluated directly.

(B) Energy balance: surface energy decreases as the interface length L shortens from its initial value L_0 to $L = 2\pi R$,

$$\Delta\mathscr{E}_\sigma \;=\; \sigma\,(L_0 - 2\pi R) \tag{5.81}$$

[2] For a *3D* sphere, $\kappa = 2/R$ and $\Delta p = 2\sigma/R$. Our solver uses $\kappa = \nabla\cdot\hat{\boldsymbol{n}}$; in a 2D computation this returns $1/R$ for a circle and in a 3D computation $2/R$ for a sphere.

(and $\Delta\mathscr{E}_\sigma = \sigma(4\pi R^2 - S_0)$ in 3D). The drop in $\mathscr{E}_\sigma$ is converted into kinetic energy that is ultimately dissipated by viscosity. Integrating the discrete kinetic energy balance over the transient gives

$$\Delta\mathscr{E}_\sigma \;\approx\; \int_0^{t_f} \sum_q \int_\Omega 2\mu_q \boldsymbol{S}_q : \boldsymbol{S}_q \,\mathrm{d}\Omega\,\mathrm{d}t \quad \text{(capillary–viscous relaxation).} \tag{5.82}$$

This equality holds up to temporal/spatial error and provides a robust, integral check of sign and magnitude of the CSF forcing.

(C) Capillary timescales and regime: define the Ohnesorge number

$$\mathrm{Oh} = \frac{\mu_\star}{\sqrt{\rho_\star \sigma R}}, \tag{5.83}$$

with $\rho_\star, \mu_\star$ representative properties (e.g. inside the droplet). For $\mathrm{Oh} \gg 1$, the viscous–capillary time

$$t_\mu \sim \frac{\mu_\star R}{\sigma} \tag{5.84}$$

sets the shape–relaxation rate; for $\mathrm{Oh} \ll 1$, the inertial–capillary time

$$t_c \sim \sqrt{\frac{\rho_\star R^3}{\sigma}} \tag{5.85}$$

governs the underdamped Rayleigh–Lamb oscillation frequency. The observed relaxation between $t = 0$, 4×10^{-4}, and 10^{-3} s can be compared to t_μ or t_c once $(\rho_\star, \mu_\star, \sigma, R)$ are specified.

- **Balanced force and reconstruction:** curvature κ_P is built from a face–consistent LS gradient (Section *Reconstruction*), and the CSF source uses *the same* gradient in both κ and $\boldsymbol{f}_\sigma$, minimizing parasitic currents. The quadrupolar transient flow seen in the velocity maps is physical and decays rapidly.

- **Projection with capillarity:** the PIMPLE projection handles the large, highly localized CSF forcing without producing checkerboard pressure/velocity artifacts; the pressure field is smooth and the velocity becomes divergence–free to solver tolerance.

- **Realizability and mass conservation:** bounded advection with weak compression preserves $0 \le \alpha \le 1$ and the droplet area $A(t)$ to within the truncation error; circularization occurs without voids/overlaps.

Figures 5.8–5.10 depict the evolution. Initially ($t = 0$) the droplet has a square footprint with uniform pressure. As curvature concentrates at the corners, the internal pressure rises and a quadrupolar flow develops that rounds the corners (panels at $t = 4 \times 10^{-4}$ s); by $t = 10^{-3}$ s the interface is nearly circular and the flow has largely decayed.

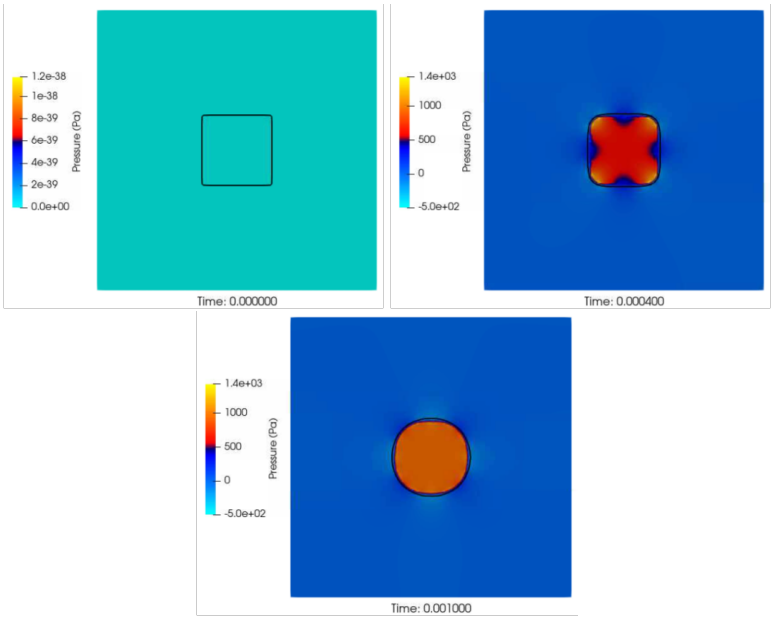

Figure 5.8: Pressure at $t = 0$: nearly uniform inside/outside; the interface (black contour) marks the initial rounded square. Pressure at $t = 4 \times 10^{-4}$ s: curvature–induced overpressure forms, strongest near former corners. Pressure at $t = 10^{-3}$ s: nearly uniform interior overpressure consistent with $\Delta p = \sigma / R$.

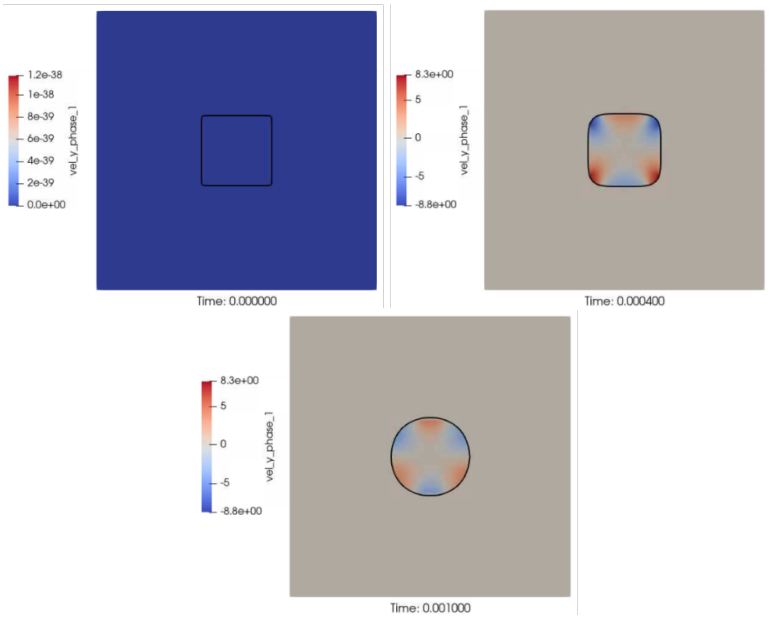

Figure 5.9: Phase–1 vertical velocity at $t = 0$: zero everywhere (quiescent initial state). Phase–1 vertical velocity at $t = 4 \times 10^{-4}$ s: quadrupolar pattern as the droplet rounds its corners. Phase–1 vertical velocity at $t = 10^{-3}$ s: strong decay toward rest; negligible spurious currents remain.

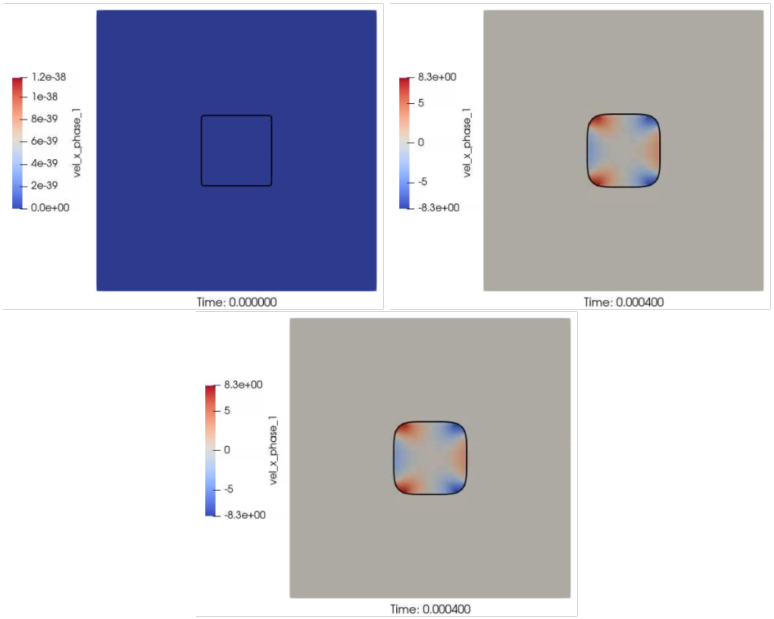

Figure 5.10: Phase–1 horizontal velocity at $t = 0$: zero everywhere. Phase–1 horizontal velocity at $t = 4 \times 10^{-4}$ s: complementary quadrupole to Fig. 5.9. Phase–1 horizontal velocity at $t = 10^{-3}$ s: decay toward rest consistent with viscous dissipation of surface energy.

- *Pressure (Fig. 5.8):* the overpressure inside the droplet grows toward a nearly uniform value, with a narrow collar where κ is largest; the late–time uniform interior level matches the Laplace prediction (5.79) within the discretization error.

- *Velocity (Figs. 5.9–5.10):* the transient quadrupole is characteristic of curvature–driven relaxation of a square toward a circle. Its amplitude decays in time, evidencing viscous dissipation of the surface–energy drop; no persistent spurious currents are visible after circularization.

The following post-processing operation are then performed to compare the obtained results against the hand calculations:

1. Compute the initial droplet area $A_0 = \sum_\Omega \alpha(\boldsymbol{x}, 0)\,\Delta A$ and the late–time area A_f; verify $|A_f - A_0|/A_0 \ll 1$.

2. Infer $R = \sqrt{A_f/\pi}$ and evaluate $\Delta p_{\text{th}} = \sigma/R$ (2D) or $2\sigma/R$ (3D).

3. From the late–time fields, average p in a small disk just inside the interface and just outside to get Δp_{meas}; compute ε_p.

4. Estimate $\max|\mathbf{u}|$ at late time and ensure it is $\ll \Delta p_{\text{th}}\,(\Delta x/\mu_\star)$; on balanced CSF schemes, $\max|\mathbf{u}| \propto (\Delta x/R)^2$ under refinement.

5. Compare the elapsed time to circularize against t_μ or t_c using the case's $(\rho_\star, \mu_\star, \sigma, R)$ to confirm the expected regime (Oh).

The droplet test demonstrates that (i) the CSF force computed from the reconstructed curvature yields the correct Laplace overpressure; (ii) the PIMPLE projection remains stable and conservative with strong localized capillarity; (iii) bounded phase transport preserves droplet mass and produces a monotone interface; and (iv) spurious currents decay to negligible levels. Together with the stratified–channel case, this provides complementary verification for gravity– and capillarity–dominated limits of the solver.

5.3 Plan for further verification cases

This section lays out a suite of verification problems purpose-built to evaluate the numerical performance of Euler–Euler multiphase models, focusing on advection schemes, interface capturing fidelity, and the dynamics of free-surface flows.

5.3.1 Zalesak's problem

Zalesak's slotted-disk test is a widely used benchmark in computational fluid dynamics, designed to evaluate the accuracy of numerical advection schemes. The setup consists of a slotted circular disk placed in a prescribed rotating velocity field. Under ideal conditions, the disk should return to its original configuration after completing one full revolution, making the case a stringent test of a method's ability to conserve both shape and volume during rigid-body rotation. Accuracy is assessed by comparing the final interface against the initial one, typically through the L_1 and L_2 error norms, which quantify numerical diffusion and dispersion.

In the present study, we employ the square computational domain used by Yue et al[33]. with a resolution of 100×100 (non-dimensional units). The disk has a radius of $r = 15$ and a slot width of $s = 6$, and is initially positioned at $(x,z) = (50, 75)$. The domain center is at $(x_c, z_c) = (50, 50)$, about which the disk rotates with a constant angular velocity of $\omega = 0.01$. The velocity field is defined to enforce solid-body rotation, with $u(x,z) = -\omega(z - z_c)$ and $w(x,z) = \omega(x - x_c)$. One complete revolution requires a time of $T = 2\pi/\omega \approx 628$, after which the interface should ideally coincide with its initial state. In our Euler–Euler formulation, the interface is tracked by the phase fraction field α, advected using a finite–volume volume of fraction scheme with high–resolution slope–limited fluxes and CMULES bounding. The interface thickness is maintained by compression fluxes proportional to $\alpha(1-\alpha)$, ensuring boundedness $\alpha \in [0,1]$. Since the velocity is prescribed and the disk remains away from the boundaries, Neumann conditions are imposed on α at the outer edges. Performance is evaluated by comparing α fields before and after rotation, using L_1/L_2 error norms to assess shape preservation and volume conservation.

5.3.2 Stretching of a circular fluid element

This verification case examines the model's competence in handling deformation and reversibility. A circular fluid element undergoes stretching under a custom velocity field—commonly a simple shear or sine-based gradient—and is subsequently reversed. In the ideal outcome, the element would fully recover its original circular form. Key quantities of interest include the degree of deformation achieved at mid-process and the recovery accuracy upon reversal, evaluated through area conservation and shape congruity metrics, typically via normalized L_1 and L_2 errors between the reconstructed and initial interfaces.

We will follow the swirling shear flow setup in Yue et al.[33] on the same 100×100 domain. A circular interface of radius $r = 15$ initially centered at $(50, 75)$ is advected by a divergence-free velocity field derived from a stream function that vanishes at the boundaries, yielding zero velocity on all walls and thereby avoiding boundary-driven artifacts. In the scaled coordinates of the 100×100 domain, the imposed velocity is

$$u(x,z) = -\sin^2\Big(\frac{\pi x}{100}\Big)\sin\Big(\frac{\pi z}{50}\Big), \qquad w(x,z) = \sin^2\Big(\frac{\pi z}{100}\Big)\sin\Big(\frac{\pi x}{50}\Big).$$

This field stretches the element into a thin filament and, for a time-reversed cycle, allows recovery toward the initial circle. The volume of fraction implementation advects the volume fraction field α with slope–limited reconstruction and interface compression to minimize smearing. Verification is based on recovery accuracy and global volume conservation, measured by comparing the final and initial α distributions via normalized error norms.

5.3.3 Travelling Solitary Wave

To verify the capability of capturing free-surface dynamics, a solitary wave is generated in a numerical tank and allowed to propagate without distortion or breaking. The test evaluates whether the Euler–Euler model accurately predicts wave celerity and surface elevation profiles. Comparison is made against analytical solutions and reference experiment data[34], and the discrepancy is quantified using metrics such as root mean square error (RMSE) between simulated and reference free-surface elevations. This case is especially valuable in assessing the advection and surface tracking accuracy in long-distance propagation scenarios.

We consider a numerical wave tank of length $20h$ and height $2h$ containing air above water (density ratio $\rho_a/\rho_w = 1.2 \times 10^{-3}$, viscosity ratio $\nu_a/\nu_w = 15$). The still-water depth is h, and the reference wave celerity is set to $C_w = \sqrt{gh} = 1\,\mathrm{m/s}$, giving a Reynolds number $Re = C_w h/\nu_w = 5 \times 10^4$. A Cartesian grid of 200×120 is used, uniform in x, and clustered in z between 0 and the initial amplitude to resolve the interface; the interfacial half-thickness is two Δz. A solitary wave is generated by releasing an initially still free surface with a Boussinesq-type profile at the left wall in hydrostatic balance, e.g.

$$A(x,0) = \frac{A_0}{\cosh^2\Big(\sqrt{\frac{3A_0}{2}}\,x\Big)},$$

and, after a short adjustment (about $t = 6\,\mathrm{s}$), the wave propagates as an essentially solitary pulse toward the right wall. Initial conditions are quiescent velocity and hydrostatic pressure in both phases with the level set defining the air–water interface. Boundary conditions are no-slip at the bottom and both vertical walls; the top boundary is also treated with a no-slip condition (its influence is negligible because of the large density contrast). Verification is achieved by comparing the simulated free–surface profiles, celerity, damping, and wall run-up against analytical and experimental references.

Table 5.1: Summary of verification cases

Run	Quantities of Interest	Target	Comment
V1	Interface preservation, volume error	Minimal L_1/L_2 deviation	Zalesak's problem
V2	Shape recovery, area conservation	Return to initial circle, area errors	Stretching test
V3	Wave elevation, propagation speed	Damping rate, wave run-up	Travelling solitary wave

5.3.4 Error norms and conservation metrics

Verification of the advection tests (Zalesak's disk, circular stretching, solitary wave) is carried out using error norms defined on the phase fraction field α. Let $\alpha^n(\boldsymbol{x})$ denote the numerical phase fraction after advection and $\alpha^e(\boldsymbol{x})$ the exact or reference solution. Over a computational domain Ω discretized into control volumes V_i, the following norms are employed:

- **Discrete L_1 error norm**:

$$L_1 = \frac{\sum_i V_i \left| \alpha_i^n - \alpha_i^e \right|}{\sum_i V_i}. \tag{5.86}$$

- **Discrete L_2 error norm**:

$$L_2 = \left(\frac{\sum_i V_i \left(\alpha_i^n - \alpha_i^e \right)^2}{\sum_i V_i} \right)^{1/2}. \tag{5.87}$$

- **Volume conservation error**:

$$E_V(t) = \frac{\left| \sum_i V_i \, \alpha_i^n(t) - \sum_i V_i \, \alpha_i^n(0) \right|}{\sum_i V_i \, \alpha_i^n(0)}. \tag{5.88}$$

  Here, $E_V(t)$ represents the relative error in the total volume of the $\alpha = 1$ phase at time t, normalized by the initial volume.

The L_1 norm measures absolute shape distortion, while the L_2 norm highlights localized smearing or overshoots at the interface. The conservation error E_V detects any loss or gain of the total transported phase, ensuring that the VOF implementation remains conservative and bounded ($\alpha \in [0,1]$) under the action of the slope limiter, deferred correction, compression, and CMULES bounding procedure.

For the traveling solitary wave, we also quantify the viscous damping characteristics of the wave and compare the results with those predicted by Mei's perturbation theory[35]:

- **Damping characteristics of the wave**:

$$A_{\max}^{-1/4} = A_{0\max}^{-1/4} + 0.08356 \left(\frac{\nu_w}{C_w^{1/2} h^{3/2}} \right)^{1/2} \frac{C_w t}{h} \tag{5.89}$$

The wave run-up which defined as the highest point at the right vertical wall will also be computed and compared with reference data from literature [34].

5.4 Plan for validation cases

Validation cases serve to benchmark the Euler–Euler two-fluid model against experimental data, highlighting its practical viability in real-world multiphase systems.

5.4.1 Dam-break

Dam-break experiments are fundamental free-surface benchmarks characterized by rapid transient flows with complex air–water interface evolution and pressure dynamics. They provide time-resolved data on front propagation and impact pressures on downstream structures. Simulating such a scenario allows a rigorous test of the Euler–Euler model's temporal accuracy, interface resolution, and ability to capture fluid–structure interaction effects.

The dam-break benchmark tests robustness for violent free-surface dynamics. The computational domain is $5a \times 1.25a$, with an initial water column $\alpha = 1$ of side a in the lower-left corner, adjacent to the bottom and left walls, and air $\alpha = 0$ elsewhere. At $t = 0$, the column is released under gravity. Boundary conditions are no-slip on all walls, consistent with a closed tank. The collapse produces rapid interface evolution, splashing, and wall impacts. The volume of fluid method advects α with slope-limited high-order fluxes and CMULES bounding, with compression fluxes $\propto \alpha(1-\alpha)$ to prevent excessive smearing. Validation is performed by comparing surge-front positions and remaining column height against Martin & Moyce (1952)[36], along with qualitative agreement in free-surface breakup and air entrainment.

5.4.2 Hosokawa and Tomiyama (2013)

Hosokawa and Tomiyama [37] investigated bubble-induced pseudo-turbulence in upward laminar bubbly flows using a vertical pipe of 20 mm diameter and 2 m height, operated at a bulk liquid Reynolds number as low as 900. Water and air at ambient conditions were introduced through an optimized injector to ensure nearly uniform bubble sizes. The experiments varied superficial liquid and gas velocities to achieve void fractions between 0.18% and 1.56% with bubble diameters of about 2.6–3.6 mm. Measurements were taken at an axial distance of 1.7 m, where the flow could be regarded as quasi-fully developed. Recorded quantities included radial distributions of void fraction, mean liquid velocity, mean bubble velocity, turbulent kinetic energy, and Reynolds shear stresses. These data provide a demanding benchmark for testing whether the Euler–Euler baseline model can reproduce core-peaking or wall-peaking void profiles. Validation will compare radial profiles of gas distribution, velocities, and turbulence quantities, with particular attention to the role of lift and wall forces in shaping void distributions.

5.4.3 Kim et al. (2016)

Kim and colleagues [38] performed complementary experiments in a larger vertical pipe of 40 mm diameter and 1.75 m height at a bulk Reynolds number of about 750. Using two-phase PIV, they measured radial profiles of void fraction, mean liquid velocity, mean bubble velocity, and root-mean-square velocity fluctuations at three axial positions, $z/D = 4.5$, 21, and 42, capturing both developing and fully-developed regimes. For validation purposes, we focus on the fully-developed regime at $z/D = 42$, where the flow is within fully-developed regime. Cases covered void fractions between 0.05% and 0.64% with bubble diameters of 2.2–3.7 mm, corresponding to increasing gas

fluxes. Compared with Hosokawa and Tomiyama (2013), these experiments in a larger diameter pipe tend to exhibit flatter void profiles and stronger influence of turbulent dispersion. Validation will therefore focus on the model's ability to capture the differences in bubble distribution and turbulence structure between narrow and wide pipes, highlighting the effect of pipe-to-bubble size ratio on laminar-to-turbulent transition.

Table 5.2: Summary of validation cases

Run	Quantities of Interest	Target	Comment
VAL1	Void fraction, velocity profiles, fluctuations	Hosokawa & Tomiyama data	Vertical narrow pipe
VAL2	Void fraction, velocity profiles, fluctuations	Kim et al. (2016) data	Vertical wide pipe
VAL3	Free-surface evolution, pressure effects	Dam-break experimental data	Transient wave/impact validation

5.4.4 Fluid properties and quantities for comparison

All validation simulations are performed with air–water systems at room temperature and atmospheric pressure. The fluid properties used are summarized in Table 3 of [39], in accordance with Hosokawa and Tomiyama (2013) [37] and Kim et al. (2016) [38].

The experimental cases selected for comparison are listed in Table 1 of [39]. The Hosokawa and Tomiyama (H-series) cases correspond to a 20 mm diameter pipe with liquid Reynolds number $\mathrm{Re} \approx 900$, with void fractions ranging from 0.18-1.27 %, bubble diameters ranging from 3.48-2.62 mm, and superficial gas velocities ranging from 0.0 to 3.0 mm/s. The Kim et al. (K-series) cases correspond to a 40 mm diameter pipe with $\mathrm{Re} \approx 750$, with void fractions ranging from 0.05-0.64 %, bubble diameters ranging from 2.2 - 3.7 mm, and superficial gas velocities ranging from 0.0 to 2.44 mm/s. Both datasets report radial distributions of void fraction, liquid velocity, bubble velocity, and turbulence statistics, and are therefore highly suited for validation of Euler–Euler model.

5.5 Model demonstration for MSRE pump bowl

The following section models the operation of the MSRE pump. The pump operation, computational model, and results obtained for the pump priming with two phase flow are explained in this section.

5.5.1 MSRE Pump Bowl: Operating Principle

The MSRE pump (Fig. 5.11) performs (i) *circulation* of the dense fuel salt and (ii) *centrifugal gas disengagement*. Dense molten salt (phase 1, ρ_1=2200 kg/m^3, μ_1=4×10^{-3} Pa s) is drawn upward through the *suction* riser into the impeller eye. Rotation at rpm=1000 ($\Omega = 2\pi\mathrm{rpm}/60 \approx 1.047\times10^2$ rad/s) imparts swirl and pressure rise, expelling the salt radially into the shallow *bowl*. There, the bowl's free surface and residence volume allow entrained/produced gas (phase 2, $\rho_2 \approx 1$ kg/m^3, μ_2=1.48×10^{-5} Pa s) to separate and migrate to the center/top, where it is withdrawn through the *off–gas* line. The liquid is then collected by the outer *volute* and delivered to the *discharge* nozzle.

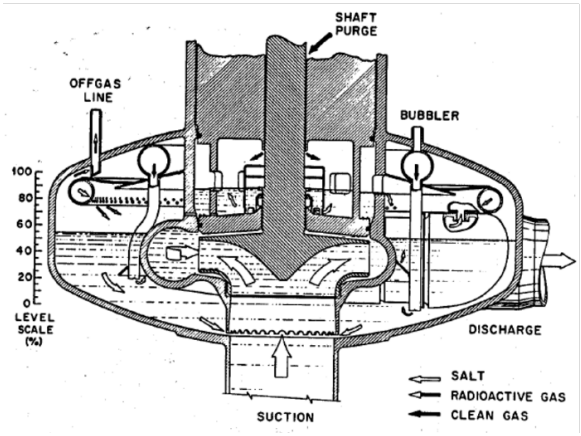

Figure 5.11: Schematic of the MSRE pump bowl, adapted from [21]). Principal features: central *suction* riser feeding the impeller eye; rotating *impeller* beneath a shallow *bowl* that provides a free surface and disengagement volume; annular *ring*/weir guiding the swirling liquid; outer *volute* collecting the discharge; top *off–gas* line removing separated gas; *bubbler*/level instrumentation immersed in the bowl; and a *shaft purge* to protect the drive penetration.

Within the bowl the bulk flow is close to solid–body rotation. In cylindrical coordinates, the pressure in a frame rotating at Ω satisfies

$$\frac{\partial p}{\partial r} = \rho\,\Omega^2 r, \qquad \frac{\partial p}{\partial z} = -\rho g, \qquad \Rightarrow \qquad p(r,z) = p_0 + \tfrac{1}{2}\rho\Omega^2 r^2 - \rho g z. \tag{5.90}$$

At the gas–liquid interface, $p = p_{\text{gas}}$ is (nearly) uniform, so the free surface follows a paraboloid

$$z_s(r) = z_0 + \frac{\Omega^2}{2g}\, r^2. \tag{5.91}$$

Rather than a literal height change inside the shallow bowl, (5.91) is best interpreted as an *equivalent centrifugal head*

$$H_c = \frac{\Omega^2 R^2}{2g}, \qquad \Delta p_c = \rho_1 g H_c = \tfrac{1}{2}\rho_1 \Omega^2 R^2, \tag{5.92}$$

which quantifies the pump's ability to lift and separate phases. Using the geometric bowl scale in the model ($R\approx 0.4$ m), one finds a tip speed $U_t = \Omega R \approx 41.9$ m/s, an equivalent head $H_c \approx 89$ m, and characteristic pressure rise $\Delta p_c \approx 1.93$ MPa. The ratio of centrifugal to gravitational acceleration is

$$\frac{a_c}{g} = \frac{\Omega^2 R}{g} \approx 4.5\times 10^2, \tag{5.93}$$

explaining the pump bowl's efficacy as a *centrifugal separator*: dense salt is driven outward; the light gas collects near the axis/top and is skimmed by the off–gas line.

1. **Suction and impeller.** Salt enters axially through the suction riser, is accelerated by the impeller, and discharged radially into the bowl. For the salt properties above, $Re = \rho_1 U_t (2R)/\mu_1 \sim 1.8\times 10^7$, justifying the use of the two–equation k–ε closure in the simulation.

2. **Bowl and ring/weir.** The annular ring shapes the swirling layer and suppresses large–scale recirculation; the shallow bowl provides residence volume for gas disengagement and sets the free surface where instrumentation (bubbler) measures level.

3. **Gas handling.** Separated gas accumulates at the bowl's top and exits through the off–gas line. A small *bubbler* injection (modeled in the input by a vertical velocity at "walls-bubbler") supports level sensing and promotes additional de–gassing when required.

4. **Volute and discharge.** The volute recovers part of the swirl into static head and guides the flow to the discharge nozzle feeding the external loop.

5. **Shaft purge.** A clean–gas purge protects the drive penetration from salt ingress; in the simulation this region is treated as a no–penetration wall with pressure extrapolation.

The input mirrors these functions: (i) rotation is imposed kinematically on the wetted walls via the functions `vel_x_impeller`, `vel_y_impeller` using the specified `rpm`; (ii) the bowl's gas–liquid environment is represented by the Euler–Euler phases (`alpha_1`, `alpha_2`) with bounded upwind transport and gentle compression ($c_\alpha = 0.1$); (iii) turbulent mixing is captured by the two–region k–ε terms for each phase; (iv) interphase momentum coupling uses a Schiller–Naumann drag law with a representative bubble diameter (`particle_diameter` $= 5$ mm), consistent with centrifugal separation in the bowl; and (v) specialized inlets emulate the *spray ring* and *bubbler* through time–dependent auxiliary fields (`spray_vel_*`) confined to the physical locations (`z_min_spray`, `z_max_spray`, $r<r_{\text{spray}}$).

Equations (5.90)–(5.92) summarize the physics that the simulation must reproduce in the bowl: a rigid–body–like swirl setting a strong radial pressure gradient (high H_c), robust phase separation due to $a_c \gg g$, and turbulent yet well–directed discharge through the volute. The model configuration provided in the following sections operationalizes these mechanisms for the MSRE geometry.

5.5.2 Computational Model: Geometry, Mesh, and Problem Setup

Figure 5.12 shows the pump bowl model used for the simulations. The solid comprises the *suction* riser feeding the impeller eye, the rotating *impeller* shroud, the shallow *bowl* with an inner ring/weir, the outer *volute* leading to the *discharge*, as well as the *off–gas* and *bubbler* ports. The computational domain includes all wetted passages that participate in circulation and gas disengagement; small mechanical clearances are modeled implicitly by no–penetration walls.

The domain is discretized with an unstructured, body–fitted tetrahedral mesh imported via `FileMeshGenerator` from `pump_wall_distance_out.e`. Cells are graded to resolve the bowl, the volute cross–section, the suction riser, and the spray/bubbler regions (Fig. 5.13). No explicit prism layers are used; instead, a precomputed wall–distance field $d(\mathbf{x})$ (stored in the mesh and read as an auxiliary variable) supplies the *two–layer* k–ε wall treatment, enabling robust near–wall modeling without resolving viscous sublayers everywhere.

The simulation solves the weakly–compressible Euler–Euler system for two phases (molten salt, gas), with a common pressure field advanced by a PIMPLE projection and Rhie–Chow–consistent mass fluxes. Turbulence in each phase uses a two–region k–ε model with the constants in Table 5.3. Phase fractions are advected with upwind reconstruction, a van–Leer limiter (when high–order is activated), and CMULES bounding with interface compression. Interphase momentum exchange uses the Schiller–Naumann drag with a representative bubble diameter.

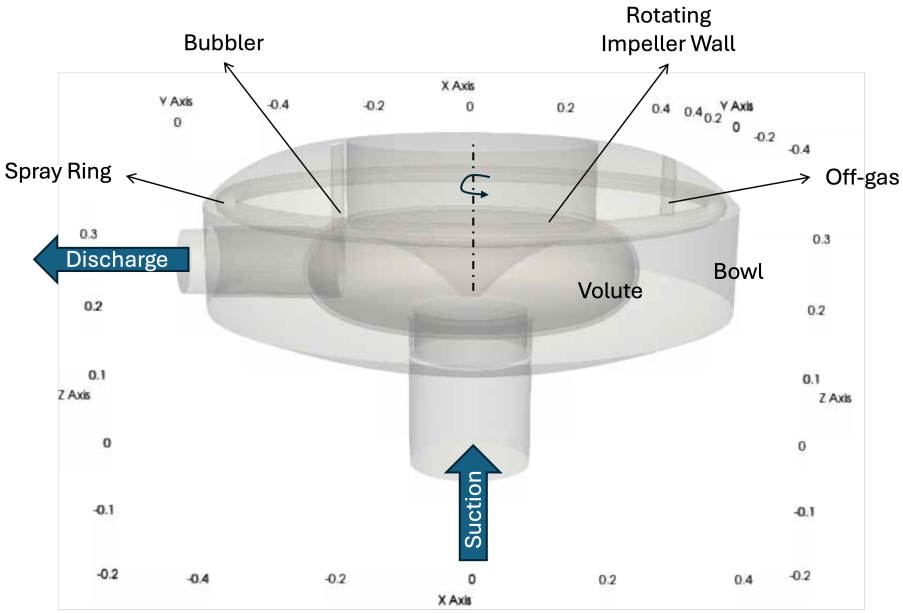

Figure 5.12: CAD of the MSRE pump bowl used to generate the fluid domain. Major components are labeled for reference.

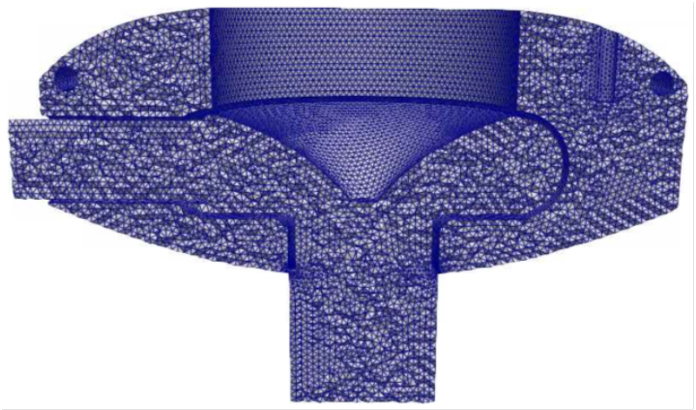

Figure 5.13: Unstructured tetrahedral mesh with local refinement in the bowl/volute and through the suction riser. The auxiliary field $d(\mathbf{x})$ (not shown) provides the wall distance for the two–layer turbulence closures.

Table 5.3 lists the material properties, operating point, turbulence constants, and numerical settings taken directly from the input.

Table 5.3: Operational parameters, model constants, and key numerics.

Quantity	**Symbol / Setting**	**Value**
Liquid density	ρ_1	2200 $\mathrm{kg\,m^{-3}}$
Liquid viscosity	μ_1	4.0×10^{-3} Pa s
Gas density	ρ_2	1.0 $\mathrm{kg\,m^{-3}}$
Gas viscosity	μ_2	1.48×10^{-5} Pa s
Gravity	g	9.81 $\mathrm{m\,s^{-2}}$ (downward)
Impeller speed	rpm	1000 ($\Omega = 2\pi\mathrm{rpm}/60$)
Interphase drag	Model, d_p	Schiller–Naumann, 5 mm, mixture-*Re* formulation
k–ε constants	C_μ, $C_{1\varepsilon}$, $C_{2\varepsilon}$	0.09, 1.44, 1.92
k/ε turbulent Prandtl	σ_k, σ_ε	1.0, 1.3
Wall treatment		two–layer (uses wall distance d, $Re_y^* = 60$ in ε terms)
Initial phase fractions	α_1, α_2	0.99, 0.01 in the bowl
Spray ring (active region)	$z \in [z_{\min}, z_{\max}]$, $r < r_{\text{spray}}$	$[0.264, 0.280]$ m, $r_{\text{spray}} = 0.40$ m
Spray composition	$\alpha_{2,\text{spray}}$	0.5 (50/50 gas–liquid)
Bubbler composition	$\alpha_{2,\text{bubbler}}$	1.0 (pure gas)
Bubbler vertical speed	w_{bub}	0.1 $\mathrm{m\,s^{-1}}$ upward (applied; liquid $\alpha_1 = 0$ there)
Advection method (phases)		Upwind + CMULES, limiter = van–Leer, $c_\alpha = 0.1$
Time step / horizon	dt, $t_{\max}$	0.01 s, 50 s
Coupling	PIMPLE	relaxation: $u/p/k/\varepsilon/\alpha$ = 0.7/0.3/0.25/0.25/0.5
Linear solvers (all systems)	PC	HYPRE BoomerAMG (settings as in input)

All boundary groups and variables are summarized in Table 5.4. Tangential rotation is imposed kinematically by the analytic wall functions

$$u_\theta(\mathbf{x},t) = \Omega(t)\, r, \qquad \Omega(t) = \frac{2\pi}{60}\,\mathtt{rpm} \times \mathtt{pump\_mass\_flow\_fraction}(t),$$

applied in Cartesian components through `vel_x_impeller`, `vel_y_impeller`; the ramp function rises from 0 to 1 over ~ 10 s. The *spray ring* uses local, inward–radial and downward velocities $\propto$ `pump_mass_flow_fraction` scaled by the `spray_fraction` (=0.07), active only for $z \in [z_{\min}, z_{\max}]$ and $r < r_{\text{spray}}$.

The impeller speed is ramped from rest to the target rotation using the provided piecewise–linear function `pump_mass_flow_fraction`(t).

The above setup directly implements the operating principle summarized earlier: (i) rotating walls generate the centrifugal pressure field that drives outward transport and gas disengagement;

Table 5.4: Boundary conditions by boundary group. Where a phase index is omitted, the same condition applies to both phases.

Boundary group	**Field**	**Condition (value / expression)**
`walls-off-gas`	$\mathbf{u}_1$ (salt)	No–slip: $u = v = w = 0$
	$\mathbf{u}_2$ (gas)	Rotating wall: $(u,v) = (\texttt{vel\_x\_impeller}, \texttt{vel\_y\_impeller})$, $w = 0$
	p	Extrapolated pressure (Neumann)
	k, ε	Two–layer wall treatment via $d(\mathbf{x})$
`walls-impeller`	$\mathbf{u}_{1,2}$	Rotating wall: $(u,v) = (\texttt{vel\_x\_impeller}, \texttt{vel\_y\_impeller})$, $w = 0$
	p	Extrapolated pressure (Neumann)
	k, ε	Two–layer wall treatment via $d(\mathbf{x})$
	$\alpha_{1,2}$	Zero normal flux (implicit)
`walls-spray`	$\mathbf{u}_{1,2}$	$(u,v,w) = (\texttt{spray\_vel\_x}, \texttt{spray\_vel\_y}, \texttt{spray\_vel\_z})$, active for $z \in [z_{\min}, z_{\max}]$, $r < r_{\text{spray}}$
	α_1, α_2	Dirichlet: $\alpha_2 = 0.5$, $\alpha_1 = 0.5$
	k, ε	Dirichlet: $k = \varepsilon = 0.1$ (code units)
	p	Extrapolated pressure (Neumann)
`walls-bubbler`	$\mathbf{u}_{1,2}$	Vertical injection: $w = +0.1$ m/s (applied; liquid flux negligible since α_1=0)
	α_1, α_2	Dirichlet: $\alpha_2 = 1.0$, $\alpha_1 = 0$ (pure gas)
	k, ε	Dirichlet: $k = \varepsilon = 0.1$
	p	Extrapolated pressure (Neumann)
`inlet`	$\mathbf{u}_{1,2}$	Advective outflow (zero–gradient)
	α_1, α_2	Dirichlet: $\alpha_1 = 0.99$, $\alpha_2 = 0.01$
	k, ε	Dirichlet: $k = \varepsilon = 0.1$
	p	Extrapolated pressure (Neumann)
`outlet`	$\mathbf{u}_{1,2}$	Advective outflow (zero–gradient)
	α_1, α_2	Advective outflow (zero–gradient)
	k, ε	Advective outflow (zero–gradient)
	p	Dirichlet: $p = 1.4$ (code units)

(ii) gravity and the two–layer wall model establish realistic recirculation within the shallow bowl and volute; (iii) the spray ring and bubbler are represented as localized momentum and composition inlets in their physical locations; and (iv) the Euler–Euler plus interphase drag model captures salt–gas slip in regions of high swirl and separated gas near the axis/top.

5.5.3 Pump Priming Transient: Formation of the Bowl Atmosphere and Onset of Entrainment

Figure 5.14 summarizes the priming run. The impeller accelerates from rest following the ramp function `pump_mass_flow_fraction`(t). In parallel, the *spray ring* injects a short, inward/downward jet of mixed gas–liquid and the *bubbler* issues a weak vertical gas plume. These sources seed a low–density atmosphere in the bowl headspace; part of this gas is skimmed by the off–gas port, while the remainder accumulates near the axis/top due to buoyancy and the centrifugal field. As the atmosphere strengthens, a central gas core forms above the impeller eye; when it intersects the suction streamline topology, gas begins to be ingested into the main circulation line.

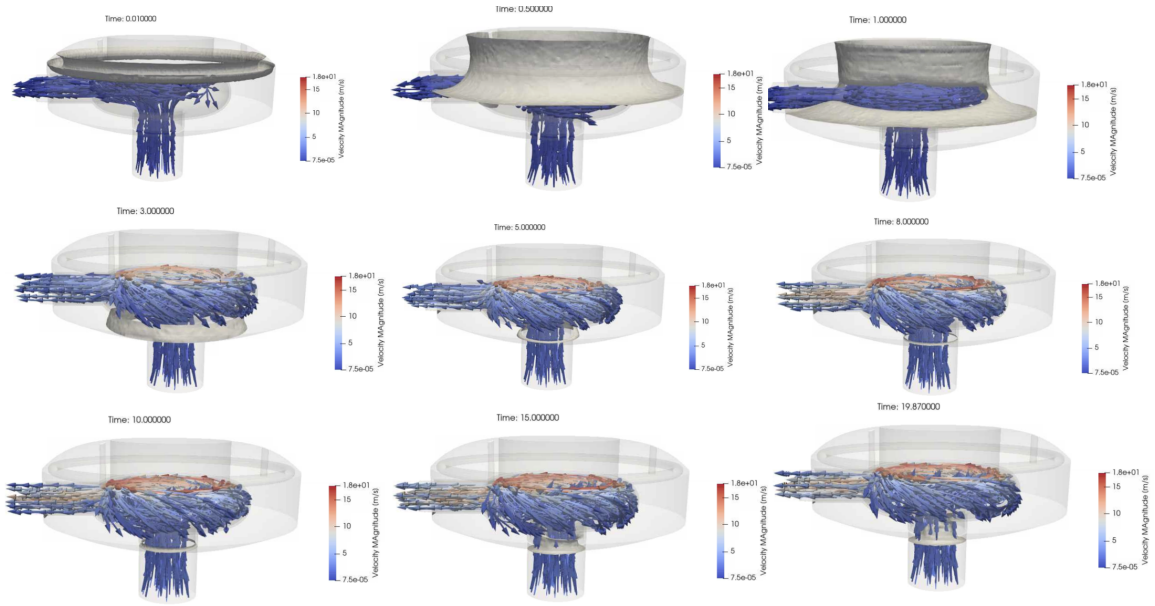

Figure 5.14: Velocity magnitude and arrows during the priming transient (times annotated). Early acceleration produces a rigid–body–like swirl in the bowl; the spray and bubbler establish a gas atmosphere near the top/axis, which later couples to the suction and initiates gas ingestion.

The accelerating impeller quickly establishes a quasi solid–body swirl in the bowl. In a rotating frame with angular speed $\Omega(t) = 2\pi \mathrm{rpm}(t)/60$, the mean pressure follows

$$\frac{\partial p}{\partial r} = \rho\,\Omega^2 r, \qquad \frac{\partial p}{\partial z} = -\rho g, \qquad \Rightarrow \qquad p(r,z,t) = p_0(t) + \tfrac{1}{2}\rho\,\Omega^2(t)\,r^2 - \rho g z. \tag{5.94}$$

The free surface satisfies $p_\ell = p_g$; thus its shape is a paraboloid $z_s(r,t) = z_0(t) + \Omega^2(t) r^2/(2g)$ and the corresponding centrifugal head is $H_c(t) = \Omega^2(t) R^2/(2g)$. With rpm $= 1000$, $\Omega \approx 1.05 \times 10^2$ rad/s, $R \approx 0.4$ m, one obtains $U_t = \Omega R \approx 42$ m/s and $H_c \approx 89$ m, i.e. $a_c/g = \Omega^2 R/g \approx 4.5 \times$

$10^2 \gg 1$. This enormous centrifugal dominance drives dense salt outward and leaves the light phase near the axis/top, exactly as seen in the snapshots.

The *spray ring* applies an inward radial momentum and a small downward component over $z \in [z_{\min}, z_{\max}]$, $r < r_{\text{spray}}$, with gas mass fraction $\alpha_{2,\text{spray}} = 0.5$. Simultaneously the *bubbler* introduces a gentle upward gas jet ($w = +0.1\,\text{m/s}$) at the center. Because $\rho_2 \ll \rho_1$, centrifugal forcing $F_c = \rho\Omega^2 r$ is much weaker on the gas: gas parcels stay close to the axis while salt is flung outward. The developing overpressure at the wall (from (5.94)) sweeps liquid into the volute and leaves a growing, low–density cap under the bowl lid. Part of this cap is immediately removed through the off–gas line, while the remainder thickens the headspace.

As $\Omega(t)$ reaches its plateau, the bowl assumes a rigid–body–like swirl. The turbulence fields (k–ε per phase) grow along the shear layers at the ring and bowl top and then saturate. Interphase drag rapidly equilibrates the slip (bubble relaxation time $\tau_p = \rho_2 d_p^2/(18\mu_1) \approx 3.5 \times 10^{-4}\,\text{s}$ for $d_p = 5\,\text{mm}$); the *Stokes number* $St = \tau_p\Omega \approx 0.036 \ll 1$ explains why the gas velocity adapts quickly to local liquid motion while still drifting toward the axis/top under the centrifugal/buoyant imbalance.

With sustained spray/bubbler injection and continued centrifugal segregation, the interface described by $z_s(r,t)$ approaches the plane of the impeller eye. A practical criterion for ingestion is when the free-surface paraboloid first intersects the suction plane at radius $r = r_e$:

$$z_s(r_e, t^\star) \;\le\; z_{\text{eye}} \quad\Longleftrightarrow\quad r_e \;\gtrsim\; \sqrt{\frac{2g\,(z_{\text{eye}} - z_0)}{\Omega^2(t^\star)}}. \tag{5.95}$$

At that time $t^\star$ a continuous gas pathway forms from the head space into the impeller eye; the snapshots at $t = 10, 15, 19.9$ s display the emergence of a low–density *core* aligned with the axis and suction streamlines, consistent with (5.95). From then on, two competing sinks balance the injected gas: (i) skimming through the off–gas line and (ii) ingestion into the circulation line.

To quantify the transient, we evaluate (or define, for future postprocessing) the following integral measures:

$$M_g^{\text{bowl}}(t) = \int_{\Omega_{\text{bowl}}} \rho_2\,\alpha_2(\mathbf{x},t)\,\mathrm{d}V, \qquad \text{(headspace gas inventory)} \tag{5.96}$$

$$\dot m_g^{\text{spray}}(t) = \int_{\Gamma_{\text{spray}}} \rho_2\,\alpha_2\,(\mathbf{u}\cdot\mathbf{n})\,\mathrm{d}A, \qquad \dot m_g^{\text{bub}}(t) = \int_{\Gamma_{\text{bubbler}}} \rho_2\,(\mathbf{u}\cdot\mathbf{n})\,\mathrm{d}A, \tag{5.97}$$

$$\dot m_g^{\text{off}}(t) = \int_{\Gamma_{\text{off}}} \rho_2\,\alpha_2\,(\mathbf{u}\cdot\mathbf{n})\,\mathrm{d}A, \qquad \dot m_g^{\text{ing}}(t) = \int_{\Gamma_{\text{suction}}} \rho_2\,\alpha_2\,(\mathbf{u}\cdot\mathbf{n})\,\mathrm{d}A, \tag{5.98}$$

with the global balance

$$\frac{\mathrm{d}}{\mathrm{d}t} M_g^{\text{bowl}}(t) = \dot m_g^{\text{spray}}(t) + \dot m_g^{\text{bub}}(t) - \dot m_g^{\text{off}}(t) - \dot m_g^{\text{ing}}(t).$$

During early times $\dot m_g^{\text{ing}} \approx 0$ and M_g^{bowl} grows; once the central core forms (criterion (5.95)), $\dot m_g^{\text{ing}}$ increases until a quasi-steady balance is reached. A second, operationally useful metric is the *eye void fraction*

$$\overline{\alpha_2}^{\text{eye}}(t) = \frac{1}{A_{\text{eye}}} \int_{\Gamma_{\text{suction}}} \alpha_2\,\mathrm{d}A,$$

which signals ingestion onset when it departs from zero.

All observed features are consistent with the implemented physics: (i) the PIMPLE projection and Rhie–Chow fluxing admit a strong, localized centrifugal body force without spurious modes; (ii) the k–ε model supplies the correct shear production and mixing along the swirling layers, matching the progressive smoothing of the velocity field seen in Fig. 5.14; (iii) the Euler–Euler transport with Schiller–Naumann drag yields the expected segregation (salt outward, gas axis/top) and a rapid gas response (small St); (iv) the headspace *paraboloid* implied by (5.94) provides a clear geometrical criterion (5.95) that aligns with the time at which ingestion is first visualized in the snapshots.

The priming transient proceeds through three reproducible stages:

1. *spin-up and seeding*—impeller acceleration, spray/bubbler establish a nascent gas cap;
2. *atmosphere growth*—centrifugal segregation concentrates gas at the axis/top while off–gas skims excess;
3. *ingestion onset and balance*—a central gas core connects to the suction and a dynamic equilibrium is set between the spray and bubbler injection and the off–gas removal and ingestion.

These results demonstrate, in a single transient, the interaction of our rotating-wall forcing, two-phase transport/drag, turbulence, and pressure projection in an industrial geometry of interest to the MSR industry.

6 SAM Capability Enhancements for MSR Material Transport and Reactivity Modeling

The use of liquid fuel in MSR concepts requires tools that capture the unique system thermal hydraulic response of an internally heated fluid, as well as system-level mass transport phenomena that pose both reactor kinetic and source term considerations. Noble gases such as xenon and krypton radioisotopes are formed as fission products during normal operation of a nuclear reactor. Although noble gases are chemically inert and contained in solid fueled reactors, they present a unique challenge in liquid-fueled molten salt reactors as they can transport throughout the reactor. Work began in FY24 to leverage the species and gas transport frameworks in SAM to provide a system-level capability for modeling noble gas transport in MSRs by allowing for species decay chain tracking and for species to transport in the liquid or gas phase and transfer mass by convection between phases [40].

In FY25, the species transport framework was expanded to model diffusion of species in porous solid materials and convective mass transfer from bulk liquids to porous solids to simulate the migration of noble gases into graphite moderators in thermal-spectrum MSRs. Several updates have also been made to the gas-species transport framework to model the fission products themselves as the dominant gas phase. With a complete noble gas transport model in place, a general purpose capability was added in FY25 to account for reactivity feedback due to changes in species concentrations, such as Xe-135, and has been integrated with the point kinetics capability in SAM. To improve the fidelity of current and future mass transport modeling capability, new multi-scale and multi-phase mass transfer closure (Sherwood number) correlations have been added to SAM based on selections from literature as well as developments from the high-fidelity CFD MOSCATO/NekRS code. Lastly, a redox corrosion model developed from companion efforts [41] has been incorporated into SAM and are all discussed in this section.

6.1 Noble gas migration into porous materials

Noble gases can readily transport throughout a liquid-fueled reactor system, either dissolved in the liquid fuel (molten salt) or transferred and transported in a mobile gas phase, thus providing a potential means of removal from the system. In thermal-spectrum MSRs, graphite is typically used as a moderating material, and due to its porous structure these noble gases can potentially transfer and be retained in the core graphite. Xe-135 is a particularly important fission product since it is a significant neutron poison and has low solubility in the salt and can therefore migrate to the graphite pore space, impacting the reactivity balance [42]. The transport processes of Xe-135 have been extensively studied for the MSRE [42, 43], and the recent work by Price and Chvala [44] provides a helpful survey of the previous work and a summary model of the transport mechanisms for Xe-135 into MSR graphite. Within the graphite, noble gases can migrate throughout the open (connected) pore space through diffusion, which can be described by Fick's law for porous diffusion. Radionuclide noble gases will also decay or be absorbed over time. The governing equation for noble gas transport inside porous structures (graphite) is thus described as:

$$\frac{\partial c_{gr}}{\partial t} - \frac{D}{\varepsilon}\left(\nabla^2 c_{gr}\right) + \lambda c_{gr} + \phi \sigma_a c_{gr} = 0 \tag{6.1}$$

Here c_{gr} is the concentration of the species in the graphite (pore and solid matrix volume) [mol/m^3], D is the diffusivity of the species within the pore [m^2/s], ε is the porosity, λ is the decay constant of the species [s^{-1}], and ϕ and σ_a are the flux and absorption cross section to account for burn-up. The diffusivity within the pore space can be primarily characterized as Knudsen diffusion as the mean free path of particles is larger than the typically small pore size of nuclear grade graphite [45], and is calculated as:

$$D_{Xe,gr} \approx D_{\text{Knudsen}} = \frac{d_{\text{pore}}}{3}\sqrt{\frac{8RT}{\pi M_{Xe}}} \tag{6.2}$$

Here d_{pore} is the pore diameter [m], T is the temperature in the graphite, and M_{Xe} is the molar mass of the noble gas (xenon) [kg/mol].

At the salt-graphite interface, noble gases can transport into the graphite through various mechanisms. As discussed by Price [44], Xe-135 can transfer directly from its dissolved state in the fuel salt, from xenon in bubbles interacting with the graphite, or from micro-bubbles attached to the graphite surface. Under typical turbulent flow regimes, is assumed that most micro-bubbles will detach and conglomerate with the larger bubbles in the salt. The interaction of bubbles with graphite is not as well understood but could occur as a direct gas exchange from the bubble to the pore space [46, 47]. In the present model, this graphite-bubble interaction is not modeled but may be considered in future work. For the transfer of xenon dissolved in the salt to the graphite gas pore space, the two-film model is adopted to describe the mass transfer kinetics at the salt-graphite interface, as depicted in Figure 6.1.

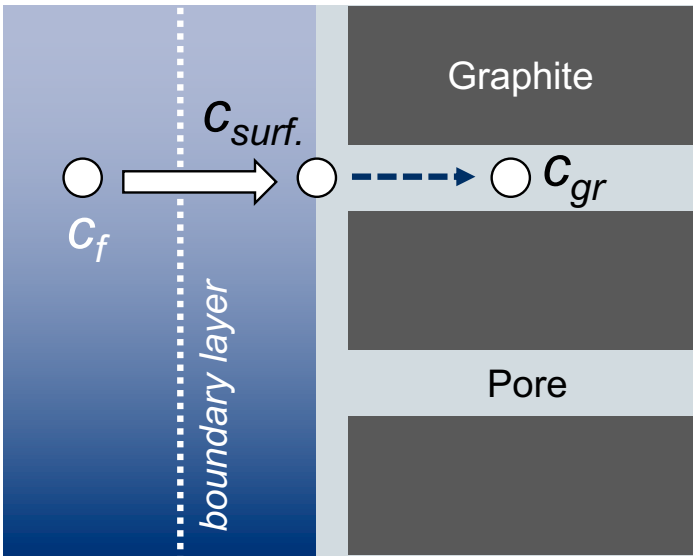

Figure 6.1: Convective mass transfer of xenon from bulk fluid c_f through boundary layer to surface thin film gas layer c_{surf} and diffusion through graphite pore space c_s.

It is assumed that the surface area for mass transfer is equal to the macroscopic graphite structure surface area (and not the surface area inside the pore space), as a thin film layer of gas will exist between the salt and the surface of the graphite porous structure. Thus, the noble gas will transport by convective mass transfer through the fluid boundary layer to the fluid-gas film layer where the

interface concentration is defined by Henry's law for solubility of xenon in the salt [44]. Therefore, the flux at the salt-graphite interface can be described as:

$$J_{xe} = k_m \left(c_f - HRT\varepsilon^{-1} c_{gr,\text{surf.}} \right) \tag{6.3}$$

Here k_m is the convective mass transfer coefficient from the bulk fluid to the solid [m/s], c_f is the concentration of the species dissolved in the bulk fluid [mol/m^3], H is Henry's solubility constant [mol/m^{3}Pa], R is the gas constant, T is the near-wall fluid temperature [K], and $c_{gr,\text{surf.}}$ is the species concentration at the surface of the graphite [mol/m^3]. The mass transfer coefficient k_m is determined by a library of correlations for different flow geometries, which was expanded in FY25 and discussed in Section 6.4. The diffusivity of xenon in the fuel salt (FLiBe), which defines the Schmidt number in most k_m correlations, can be determined from the Stokes-Einstein equation [48]:

$$D_{Xe,FLiBe} = \frac{k_b T}{6\pi\mu r_{xe}} \tag{6.4}$$

Here k_b is Boltzmann's constant, T is the bulk fluid temperature [K], μ is the fluid viscosity [Pa-s], and r_{xe} is the noble gas (xenon) atomic radius [Å]. The Henry's solubility of Xenon in FLiBe can be determined from the equation derived by Watson et al. [49] from their measurements of various noble gases in FLiBe and FLiNaK:

$$H_{Xe,FLiBe} = \exp\left(-\frac{18.08 r_{xe}^2 \gamma}{RT} \right) \tag{6.5}$$

$$\gamma_{FLibe} = 235.5 - 0.09(T - 273.15) \tag{6.6}$$

Here the Henry's solubility H is given as the ratio of the noble gas concentration in liquid to gas phase, r_{xe} is the noble gas (xenon) atomic radius [Å], γ is the surface tension of FLiBe [ergs/cm^2], and T is the bulk fluid temperature [K].

6.2 Reactivity feedback integrated with species transport

The SAM reactivity feedback model has been extended such that a change in a species concentration within a component, either fluid or structure, can result in a change in the overall reactivity. The species feedback model was developed to be flexible such that any number of species could be considered with respect to reactivity feedback. Of primary interest for the MSR, is the contribution of Xenon, whether it be in the gas or liquid phase within the coolant, or trapped within the graphite moderator.

The species reactivity feedback is integrated over the coolant or structure mesh and the difference between the initial and transient values is provided to the Point Kinetics model for the calculation of fission power. Considering the mesh of a component is split into N volumes,

$$R_S(t) = \sum_n^N \alpha_n s_n(t) V_n \tag{6.7}$$

$$\Delta R_S(t) = R_S(t) - R_S^{ss} \tag{6.8}$$

where $\Delta R_S(t)$ is the change in species reactivity (R_S at time t minus the steady state R_S^{ss}), in the unit of Δk/k; α_n is the species reactivity coefficient of n-th volume in unit of Δk/k per unit of species; $s_n(t)$ is the species concentration of n-th volume at the time of t; V_n is the volume of n-th volume.

6.3 Updates to SAM gas transport model

6.3.1 Model update for gas mixtures

The previous form of the gas transport model, as presented in Mui [40], was designed with the intention of modeling a sparge gas. This means it was implicitly assumed that a single gas dominates the gas system in terms of quantity (e.g., the overwhelming amount of gas is helium with a relatively small amount of fission gas products such as xenon and krypton). As the fission gas presence was assumed to be insignificant, they were assumed to have no impact on gas properties or quantity in the system as phase transfer occurred. This is not a suitable assumption for a system that does not include a dominant sparge gas, but rather, generates gas species from fission gas generation and salt release only. To remedy this, the model was reformulated to allow for gas mixtures.

The formulation of the governing equation is slightly modified from the previous form of the model. The species transport equation for any given gas species is as follows:

$$\frac{\partial \alpha_s c_s}{\partial t} + \frac{\partial \alpha_s c_s v_k}{\partial x} = S \tag{6.9}$$

Here s is the species identifier (e.g., xenon, krypton, etc.). Therefore, α_s is the gas void fraction of the individual gas species and c_s is the concentration of the pure species. Here, this is interpreted as units of $\mathrm{mol\,m^{-3}}$, but amount per volume could also be used. Only one velocity is calculated for all gas species using the drift flux model, as it is assumed that the gas mixture is well mixed and all gas species travel at the same speed. The product of α_s and c_s is the total volume concentration of the species. By dividing by the pure species concentration, c_s, the volume fraction of the species can be determined. The pure species concentration can be determined using the Ideal Gas Law in combination with the local pressure and temperature. After the individual species volume fraction is known for all species, the total gas void fraction can be determined as the sum of all gas species void fractions in the system.

$$\alpha_{\mathrm{tot}} = \Sigma_{s=1}^{N} \alpha_s \tag{6.10}$$

The gas mixture density, which is needed for the drift flux model calculation, is calculated as a void weighted sum of the individual species densities.

6.3.2 Bubble efflux model

Most MSR designs require some way of removing high volatile fission gasses that continuously escape from the salt. One method of removal is to simply allow the gas to form bubbles, which then rise to a free surface due to buoyancy forces. To allow for modeling this phenomenon, a bubble efflux feature was added for the `PBLiquidVolume` component in SAM, which is a 0D volume component that defines a free surface of the liquid. This component can be placed at the top of the flow loop, where it will provide a pressure boundary condition and will allow any gas that exists in the volume to escape due to buoyancy.

The bubble rise is determined by one of two ways: the user can specify a constant rise velocity or the buoyancy term of the drift flux model can be used. If the modeling option is not explicitly set, the code will default to the drift flux approach. Otherwise, the user can define which approach to use with the `bubble_rise_model` input in the `PBLiquidVolume` component definition in the input file. Options include `harmathy`, which refers to the buoyancy portion of the drift flux model, or

`constant`. If `constant` is selected, then the user must also provide the `vgj` input, which accepts a scalar real value.

The method for calculating the efflux rate depends on the species volatility and phase. First, the species will not leave the system if it exists in the liquid phase. If the species volatility is high, then the efflux rate will be calculated as follows:

$$\dot{m} = \max\left(c_T v_{gj} A, 0\right) \tag{6.11}$$

The c_T term is the total volume concentration of the species in the `PBLiquidVolume` component. The bubble rise velocity is v_{gj} and the surface area of the free surface is A. This term is applied as a sink in the species mass equation, so it will act to deplete the species in the volume over time.

The efflux rate for a low volatile gas is defined in the same way; however, as low volatile gasses do not include a mass equation and are instead defined in relation to the local liquid concentration of the low volatile (see Section 6.3.3), the efflux rate does not serve as a sink term that depletes the low volatile species. The efflux rate is only provided as an estimate of the release rate of the species. It is incorrect to assume that removal of the species will not impact the species amount in the system; however, it is assumed that since the species is low volatile and will thus be low concentration in the gas compared to its presence in the liquid. Therefore, the low gas concentration will translate to a low efflux rate in relation to the liquid concentration and thus a negligible sink.

6.3.3 Low volatile option

The default approach for modeling phase transfer is to model gases as high-volatile. In this approach, the phase transfer is calculated using the Henry coefficient H as follows:

$$\Phi = k_\ell A_i \left(c_g HRT - c_\ell\right) \tag{6.12}$$

The phase transfer source term is denoted by Φ. This will be a source in the gas phase and a sink in the liquid phase. Modeling the gas as a high-volatile requires that the species exists in both the liquid and gas phases in the SAM model.

A low-volatile gas makes the assumption that the quantity of species leaving the liquid for the gas space is so small that it can simply be assumed that the gas concentration of the species is at its equilibrium value and that no mass transfer term is needed. The species mass conservation can be solved in the liquid phase only. The mass transfer rate will be so low that it will remove an insignificant amount from the liquid space and can therefore be ignored. However, it may still be important to know the amount of species in the gas phase (e.g., the amount of cesium in the gas space may be needed for source term analysis).

The Henry coefficient must still be provided. Currently it is obtained from user input. Assuming equilibrium conditions, the relationship between liquid and gas concentration can be determined from Eq. 6.12.

$$c_\ell = c_g HRT \tag{6.13}$$

Therefore, the gas phase concentration of the low-volatile will be a function of the local liquid concentration and temperature in addition to the Henry coefficient of the species. While it is technically possible to model a low-volatile gas using the high-volatile model, convergence can be more difficult due to the vastly different phase transfer rates between the high- and low-volatile species and it also adds more to the runtime due to additional species transport equations being required.

6.3.4 Summary of model changes

After the model updates, there are two options for modeling gas in the system.

1. Four-equation drift flux model
2. Passive species transport with one or more species existing in the gas phase

The two models are separate from one another. In the first model, a true four equation drift flux model is implemented. This is the model that was defined and implemented as covered in Salko [50]. The governing equations solved by SAM are for a two-phase mixture and a fourth drift flux equation is used to determine the gas phase slip and volume fraction. The user must specify the EOS to use for the gas phase and, as such, only a single gas can be modeled in the system. A mixture of gases can be modeled if an EOS is defined for that mixture. This model is valid to use if the gas content in the system becomes more significant (e.g., greater than 10 or 20%). As of now, this modeling option cannot be used if any passive species exist in the model.

The second modeling option is the one that has been added for this milestone. The user can define any number of species in the model and they can also define any number of those to exist in the gas phase. The user can also define a phase-change linkage between species that exist in the liquid and gas phases. As a species leaves liquid and enters the gas, it will cause the total gas in the system to increase. This model option supports modeling of mixtures of gases and the property of the gas mixture will be defined based on the mole fraction of the individual species. This option passively transports all species (either gas or liquid), so it is only suitable to use if the total void fraction remains low (e.g., 1% or less). The same drift-flux model that is used for the first model is used to determine the gas mixture velocity in this model. The void will be implicitly determined based on the phase slip calculated by the drift flux model.

The following new inputs were added for utilizing the new model. Note that the SAM User Manual is the final authority for input options that are available. This list is merely given to give the reader an idea of what new options are available as of now using the model in its current state. Final implementation of the model may result in differences in the actual model available to the user.

- `passive_scalar_efflux`—Enables the bubble release model in the `PBLiquidVolume` component. The input type is a vector of Boolean (one entry per species in the model). The input shall be false for liquid species. The default is false for all species if not provided.
- `passive_scalar_volatility`—Defines whether the species is high or low volatile. Valid inputs are `high, low, none`, with `none` being used if the species does not leave the liquid. The input type is a vector of string values (one entry per species in the model). The default is `none` if input is not provided.
- `passive_scalar_molar_mass`—Specifies the molar mass of the species. Only required for gas species, but may be entered for all species. This is used in the Ideal Gas Law to determine the density of gas species. The input type is a vector of real values with units of $\mathrm{kg\,mol^{-1}}$ (one entry per species in the model). There is no default if this is omitted and it is required if there are any gas species in the model.
- `ps_input_as_moles`—This specifies that initial conditions and boundary conditions will be entered in units of moles instead of amount. The input type is a scalar Boolean value. The

default, if not provided, is false. Note that when using the passive scalar gas transport model, it is required that this option is True and that all boundary and initial conditions are given in moles instead of amount.

- `global_constant_gas_bubble_diameter`—This allows the user to set a fixed, specified bubble diameter for the gas model instead of allowing SAM to calculate it using either the interfacial area transport model or the Weber based criteria. The input type is a scalar real value in units of meters.

- `bubble_rise_model`—This input may be set in the input block for the `PBLiquidVolume` component, if one exists in the model. This will set the option to use for bubble efflux out of the system, if that option was enabled. This input type is a string value of either `constant` or `harmathy`.

- `vgj`—This input may be set in the input block for the `PBLiquidVolume` component, if one exists in the model. This input is only valid if the `bubble_rise_model` input was set to `constant`. This input accepts the constant rise velocity that will be applied for determining the bubble efflux rate from the system. The input type is a real scalar value and it has units of $\mathrm{m\,s^{-1}}$.

6.4 Multi-scale and multi-phase mass transfer closure models

In various mass transfer processes, the convective mass transfer of species from one phase to another (liquid-solid or liquid-gas) is particularly important to model accurately as it can be the limiting transport step. For 1-D system codes, Sherwood number correlations are adopted as closure models for this process, which are are typically derived from fitting to measured experimental data. Prior to FY25, the Chilton-Colburn heat-mass transfer analogy [51] was used to calculate the Sherwood number based on the local Nusselt number and the species diffusivity, since there is already an extensive library of heat transfer closure models built into SAM [14]. However, this analogy is typically only valid for highly turbulent flow in pipe geometry, so a set of *Sh* correlations has been selected to be incorporated into SAM and is discussed in this section.

Three correlations for fluid-solid mass transfer in different flow geometries have been adopted from work by Yuan & Hoyt [52, 53] using high-fidelity CFD modeling in MOSCATO/NekRS. The Schmidt numbers encountered in molten salts can be as high as O(1000), two orders of magnitude higher than the Prandtl number, requiring a high degree of near wall mesh refinement to accurately capture high-Sc number transport of species. Although Schmidt numbers on the order of O(1000) can be modeled using Artificial Viscosity Method (AVM), the present correlations were developed up to a maximum of O(100) to refrain from using AVM. Still, these correlations are a significant improvement over their analagous reference correlations from literature and are an example of "multi-length scale" coupling between the two thermal fluid tools developed for advanced reactors. Two correlations for fluid-gas (bubble) mass transfer are selected from literature [54, 55] as these were developed specifically for this phase transfer mode from measured data and improve on the previous implementation that only supported a constant user-provided value.

An additional parameter, `SC_MTC` is also added to allow for a user input Function multiplicative sensitivity coefficient to perturb the calculated K_m value for sensitivity and uncertainty quantification study. The `SC_MTC` and `MTC_user_option` parameters can be specified for individual SAM

Components or for the entire system in the `GlobalParams` block. Additional correlations from literature have also been identified and summarized in recent work [56], and may be considered for future inclusion in SAM.

6.4.1 Yuan-Hoyt (2021) for pipe flow

This correlation [52] was developed for flow in a straight tubular section (pipe) and is the default geometry in SAM and a majority of flow paths. A tubular section was simulated in MOSCATO/NekRS with a mesh using 88,200 elements with a high degree of refinement near the wall and over 30 million Degrees of Freedom (DOFs). The model was simulated at two Reynolds numbers (3000 and 10^4) and three Schmidt numbers (10, 50, and 100) to capture a range of flow conditions. The Pinczewski and Sidemann (1974) [57] correlation for pipe flow was selected as as the literature reference, which was developed over a wide range of measured heat and mass transfer data. A new correlation was fitted using data generated from the NekRS simulations, following the reference correlation model form:

$$\mathrm{Sh} = 0.00308\ \mathrm{Re}^{1.045}\ \mathrm{Sc}^{0.327} \tag{6.14}$$

With a valid range of Re: [3000, 10^4], Sc: [10, 100]. The literature correlation performs fairly well with a mean relative error of 9.5% compared to the high fidelity NekRS data and the fitted correlation has a mean error of only 3.3%. This correlation is adopted as the default model for `Pipe` geometry type flow components, and can also be specified as the `YuanHoytPipe` user option.

6.4.2 Yuan-Hoyt (2021) for bundle flow

This correlation [52] was developed for in-line subchannel flow in a rod bundle, which is a common geometry in both light-water reactor (LWR) and advanced non-LWR core and heat exchanger designs. A square-pitch subchannel section with a pitch-diameter (P/D) ratio of 1.33 was simulated in NeKRS with a mesh using 102,400 elements and over 35 million DOFs. The model was simulated at two Reynolds numbers (3750 and 12500) and three Schmidt numbers (10, 50, and 100) to capture a range of flow conditions. The Inayatov (1975) [58] correlation for rod bundle heat transfer was selected as as the literature reference and translated to a mass transfer correlation by direct analogy. A new correlation was fitted using data generated from the NekRS simulations and following the reference correlation model form:

$$\mathrm{Sh} = 0.023 \left(\frac{P}{D}\right)\ \mathrm{Re}^{1.10}\ \mathrm{Sc}^{0.36} \tag{6.15}$$

With a valid range of Re: [3750, 12500], Sc: [10, 100]. The literature correlation did not perform as well, having a mean relative error of 42% compared to the high fidelity NekRS data. The updated fitted correlation has a mean error of only 3%, which is a significant improvement. This correlation is adopted as the default model for `Bundle` geometry type flow components, and can also be specified as the `YuanHoytBundle` user option.

6.4.3 Yuan-Hoyt (2021) for pebble bed flow

This correlation [53] was developed for flow in randomly packed beds of spherical pebbles, which is relevant to core modeling in the Pebble Bed-Fluoride Salt Cooled High Temperature Re-

actor (PB-FHR) and pebble-bed High-Temperature Gas-Cooled Reactor (HTGR) concepts. The Voronoi cell method was used to simulate a randomly packed bed of 1568 pebbles in NeKRS with a mesh using 2,567,456 elements and approximately 0.88 billion DOFs. The model was simulated with an upward flow configuration (corresponding to the PB-FHR concept) at three Reynolds numbers (100, 500, and 1000), where the Re_p characteristic length is based on the pebble diameter, and three Schmidt numbers (10, 50, and 100) to capture a range of flow conditions. The mesh and concentration profile at Re = 100 is shown in Figures 6.2 and 6.3:

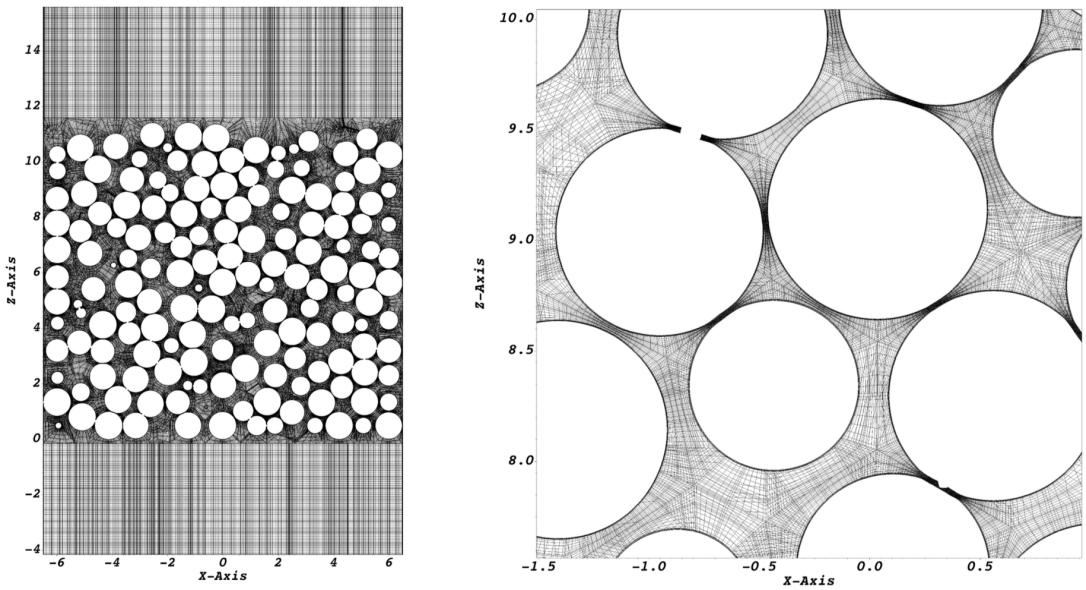

Figure 6.2: NekRS mesh in a randomly packed bed of 1568 pebbles. Reproduced from [53].

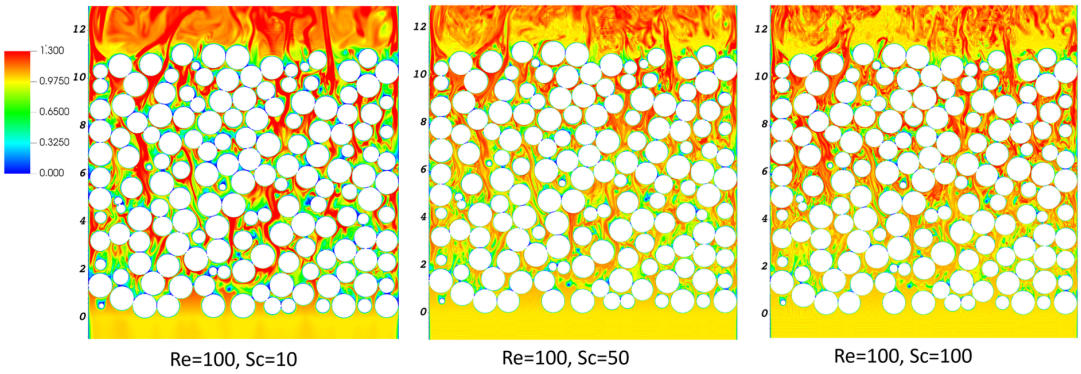

Figure 6.3: NekRS instantaneous concentration profile in random pebble bed at Re = 100. Reproduced from [53].

The Wakao (1979) [59] correlation for pebble bed heat transfer was selected as as the literature reference and translated to a mass transfer correlation by direct analogy. A new correlation was

fitted using data generated from the NekRS simulations and following the reference correlation model form:

$$\mathrm{Sh} = 2 + 0.50275\ \mathrm{Re}_p^{\,0.64123}\ \mathrm{Sc}^{1/3} \tag{6.16}$$

With a valid range of Re_p: [100, 1000], Sc: [10, 100]. The literature correlation significantly deviated from the simulation, over-predicting Sh by as much as $\sim 80\%$ in comparison to the high fidelity NekRS data. The updated fitted correlation has a much closer agreement to the data well within an error of 20%. This correlation is adopted as the default model for `PebbleBed` geometry type flow components, and can also be specified as the `YuanHoytPebbleBed` user option.

6.4.4 Calderbank & Moo-Young (1961) for bubbly flow

This correlation [54] is one of the first efforts to measure gas-liquid mass transfer coefficient using a novel light-reflection and gamma-ray transmission methods to measure interfacial area. Vessels filled with various fluids including aqueous glycol-glycerol mixtures, water, and polyacrylamide solutions were saturated with oxygen and carbon dioxide then agitated at varying rates to measure mass transfer rates at different bubble sizes.

$$\mathrm{Sh} = 0.082\ \mathrm{Re}^{0.69}\ \mathrm{Sc}^{1/3} \tag{6.17}$$

This correlation is useful as it does not have a dependence on bubble diameter in its model formulation and can be used in instances where the bubble size is not available, and can be specified in the SAM input as the `CalderbankMooYoung` user option.

6.4.5 Kress (1972) for bubbly flow

This correlation [55] was originally developed in support of analysis of the MSRE and from finding that the correlation developed by Calderbank & Moo-Young was insufficient to describe the mass transfer found in turbulent bubbly flow in the MSRE primary loop. Kress developed the Sh correlation from measured data collected in a pumped surrogate fluid loop of varying glycerine-water mixtures at different flow velocities to simulate a range of Re and Sc flow conditions. In the experiment, the loop was initially saturated with oxygen until a steady concentration was measured, then a 0.3% void of helium bubbles was sparged into the system and the decrease in oxygen concentration was measured to determine the overall mass transfer rate. Bubble probes and pictures taken through viewing ports allowed for measurement of the average bubble diameters to determine the interfacial area and fit a Sh correlation to the data including the characteristic diameter ratio of bubble diameter d_b to conduit (hydraulic) diameter D_h:

$$\mathrm{Sh} = 0.335\ \mathrm{Re}^{0.94}\ \mathrm{Sc}^{1/2} \left(\frac{d_b}{D_h} \right) \tag{6.18}$$

With a valid range of Re: $[10^4, 2 \times 10^5]$, Sc: [370, 2013], with a $\sim 20\%$ mean relative error to the measured data. This correlation is adopted as the default model for fluid-gas interphase mass transfer, and can also be specified as the `Kress` user option.

6.5 System-level redox corrosion modeling

Corrosion of structural materials in molten salt due to redox reactions, such as the depletion of Cr from Fe-Cr-Ni-based alloys has been observed in the MSRE and can vary depending on factors such as control of the redox potential or impurities in the salt coolant. Upon generation, those corrosion products transport with the molten salt at the advection effect of molten salt fluid. When the redox potential changes to a more reducing environment, either by adding some reductive agents or consuming the oxidizing species, the corrosion products are reduced back to their metallic state and precipitate from the molten salt, behave like the noble metals [60]. The corrosion products could deposit on structural surface or at the bubble interface, having the potential effects the same as noble metals to the molten salt operation system. Consequently, a theoretical framework has been developed in MOOSE [41] in FY23-24 and in FY25 has been incorporated into SAM. This redox corrostion model is structured around the foundations of species transport theory, interfacial redox reaction kinetics theory, and the implementation of mixed potential theory which couple the species transport with redox reaction kinetics.

Corrosion products arise from the reaction of different components in the structural alloy with an oxidizing agent, such as fluorine. These corrosion products are advected in the salt following the general species transport equation in SAM:

$$\frac{\partial c_i}{\partial t} + \nabla \cdot (u_k c_i) - \nabla \cdot (D_i \nabla c_i) + \lambda_i c_i + S_{\Phi,i} = S_i \tag{6.19}$$

where c_i is the species total volumetric concentration ($\#/m^3$); u_k is the velocity of the carrier phase (m/s); D_i is the diffusion coefficient for species i (m^2/s); S_i is the source term ($\#/m^3 s$); λ_i is the decay constant for species i (s^{-1}); and S_Φ is a term to account for phase transfer ($\#/m^3 s$). The local redox reaction rates will also vary with temperature throughout the molten salt system, resulting in consumption and production of these products, reflected as source/sink terms in the species transport equation for each corrosion product in the salt. The local redox reaction kinetics can be defined according to the Butler-Volmer equation:

$$j_k = j_0 \left[\exp\left(\frac{(1-\alpha)nF}{RT} \eta \right) - \exp\left(\frac{-\alpha nF}{RT} \eta \right) \right] \tag{6.20}$$

where j_k is the current density for reaction k, j_0 is the exchange current density, α is the charge transfer coefficient, and η is the overpotential, defined as $\eta = E_{electrode} - E_{eq}$. The equilibrium potential can be evaluated using Nernst's equation:

$$E_{eq} = E^0 + \frac{RT}{nF} \ln\left(\frac{c_{oxidized}}{c_{reduced}} \right) \tag{6.21}$$

where E^0 is the formal potential for the redox reaction, and $c_{oxidized}$ and $c_{reduced}$ are the concentration of oxidized and reduced ions at the salt-structure interface. To evaluate the electrode potential $E_{electrode}$, the mixed potential theory is applied to determine the shared potential. Adhering to the principle of charge conservation, it is assumed there is no net accumulation of electrons, implying that if one reactant receives a specified number of electrons, other reactants must lose the same number of electrons. Consequently, the current density calculated for different redox reactions should be in balance with one another, i.e. $\sum_k j_k = 0$. This constraint is evaluated according to Mixed Potential Theory to balance the multiple simultaneous redox reactions occurring, with the

current implementation supporting up to 3 reactants. From this constraint, the shared electrode potential can be determined and the current density used to calculate the source/sink term for each corrosion product based on mass transfer:

$$j_k = nFK_d \left(c_{o/r,int.} - c_{o/r,bulk} \right) \tag{6.22}$$

where K_d is the mass transfer coefficient determined from closure correlations (as discussed in Section 6.4, and $c_{o/r}$ represents the concentration of the oxidation/redox reaction ions at the solid-fluid interface and in the fluid bulk.

In the current SAM integration effort, the objects from the original MOOSE implementation of this model have been incorporated into SAM and updated to directly couple with the thermal hydraulics field variables (pressure, velocity, temperature), as well as the species concentration and mass transfer coefficient field variables. In this way, all of the model parameters will be directly coupled to and informed by the thermal fluid solution of the system, although the present model does not consider any feedback to the fluid flow or heat transfer. SAM will solve for the fluid flow and advection of ions throughout the system following Eq. 6.19. At each linear iteration, SAM will also evaluate the the local source term for each ion according to the local concentrations and redox potential according to Eq. 6.22. An inner iteration is also evaluated implicitly that the local net balance of all currents to Eq. 6.20 is zero such that charge is conserved. Note that this assumption differs from the implementation in other models that consider a global net balance (where the sum of currents over all surfaces is zero), such as in MOSCATO [52]. Future efforts will revisit this configuration to assess the correct methodology to evaluate this constraint and also with regards to compatibility for multi-length scale coupling between computational tools.

Another major assumption is that the diffusion kinetics inside the metal structure is not currently modeled, such that the advection and convective mass transfer processes are slower than the diffusion process of ions through the structure and the surface concentration of ions is constant. In reality, this assumption is likely invalid as it is readily observed that the composition near the surface will evolve as different ions deplete or deposit at different rates [61]. Future work will be needed to connect the SAM transport model for species diffusion in structures to the redox corrosion model. Lastly, the input syntax for species transport in SAM will be revisited to provide a more user-friendly interface for specifying individual species and their transport phenomena and material properties as the overall framework grows in complexity.

7 Verification and Demonstration of Integrated MSR Mass Transport Models in SAM

7.1 Verification of gas transport model updates

A variety of verification tests were added to SAM to ensure the proper functioning of the new model and features that have been added. Tests 7.1.1 and 7.1.2 are for the existing four-equation drift flux model. They test the ability to use that model with the new gas efflux and bubble constant diameter features that have been added. The remainder of the tests focus on the new pure species gas transport model that has been added. A test to verify the most basic functionality for simple pipe geometry is shown in Test 7.1.3. Basic checks such as mass conservation are used for this case. Branching geometry is checked in Test 7.1.4, again checking for mass conservation in the components. Then geometry is expanded to a full flow loop in Tests 7.1.5 and 7.1.6. These tests add heat input and a heat exchanger. The first one uses a `PBTDV` component to act as a pressurizer while the second one uses a `PBLiquidVolume` component to simulataneously act as a pressurizer and also allow for bubble efflux to be turned on. After this, a series of verification tests are run to compare the SAM solution against actual analytical solutions. Tests 7.1.7, 7.1.8, and 7.1.9 are all 0D tests representing a tank with no liquid flow. The first one shows that decay works for the new model for both gas and liquid species. The second one has two high-volatile species in solution and shows how they come out into the gas phase over time to form a gas mixture. The last one models a two-phase mixture and represents how a sparging gas can be modeled with the new model. Tests 7.1.10, 7.1.11, and 7.1.12 are all 1D pipe geometries with liquid and gas species injection. The first one shows that advection works for the new model and the second one shows that boundary conditions could be specified as a mass concentration. The third one shows that phase transfer can be modeled for flowing gases.

7.1.1 Offgas test

This model has a vertical pipe that connects to a `PBLiquidVolume` component above it. The fluid in the pipe and tank is stagnant. This model uses the four equation drift flux model. There is a gas injected into the pipe using a uniform volumetric source term. Due to buoyancy, the gas rises out of the pipe and into the tank and then out of the tank due to gas efflux. This test ensures that the flow out of the top of the pipe and out of the top of the tank is equal to the volumetric injection rate at steady state conditions. This test ensures the new gas efflux model is working with the four equation drift flux model.

7.1.2 Bubble constant diameter test

This test is a vertical pipe that has liquid and gas injection at the bottom. The four-equation drift flux model is used to determine the bubble velocity. A constant bubble diameter is specified. This test will ensure that the bubble diameter is always equal to the input value.

7.1.3 Pipe with fixed density

This is a vertical pipe with flowing liquid. A gas species is injected at the pipe inlet by specifying the volumetric concentration of the gas. A void of 1% is targetted when setting the inlet

concentration. The Ideal Gas Law can be used to determine the required concentration. The density of the pure species will be defined as $\frac{p}{RT}$ in units of $\mathrm{mol\,m^{-3}}$. To convert the species concentration to total volume concentration (the required input for SAM), it should be multiplied by the volume fraction. The test ensures that total volumetric concentration of the gas does not change along the axial direction of the pipe, which is true due to there being no sinks or sources. Additionally, the mass flow rate of the species is checked at inlet and oulet to confirm the mass balance and that the mass flow rate postprocessor is working.

A variation of this test called `simple_gas_specific` utilizes the specific concentration feature, where species concentration is specified per mass instead of per volume in both input and output values. This ensures this feature works with the new model and that species flow rates are still correctly calculated.

7.1.4 Branch tee test

This model has one vertical pipe that splits into two horizontal pipes at a `PBBranch` component. A two-phase flow is injected into the bottom vertical pipe. The area of the branch pipes are different and the pipes have different losses, so the volume fraction is different in the two outlet pipes. This test uses the new passive species gas transport model. It is ensured that mass conservation is maintained between inlet and outlet and that the void change is equivalent to the density change caused by the pressure variation from the bottom of the model to the top.

7.1.5 Flow loop with gas transport test

This is a model of a flow loop with a two phase mixture. The new passive species transport model is used. Two species exist; one in the liquid and one in the gas space. There are no sources or sinks for the species in the model. The slip ratio between the phases is set to a constant value. The flow area of all pipes in the loop are the same, which means the void change from one component to another will only be due to gas density changes due to pressure changes. This test ensures that the mass flow rate of liquid species and gas species do not change in different parts of the loop. Furthermore, it checks that the specific concentration of the liquid and gas species also do not change in different parts of the loop.

7.1.6 Flow loop with gas transport and efflux test

This is a simple flow loop with heating on one side. The new passive species gas transport model is used for this test. The model includes a high-volatile species that transfer between liquid and gas phases. It also includes a low-volatile species. Therefore, 3 species transport equations are solved in total. The case is a transient, but is run until steady state conditions are reached. The case has a source of the liquid species defined in the heater. A PBLiquidVolume is defined at the top of the model, which allows bubbles to rise and leave the system. The bubbles will carry both the high- and low-volatile gasses out of the system. The test ensures that the high-volatile species injection rate equals the offgas rate at the top of the model at steady state conditions.

7.1.7 Tank with decaying species

This model uses a 1-D pipe in SAM to represent a tank by setting inlet liquid and species flow to zero. The tank initially contains a two-phase mixture of a salt and gaseous iodine. The iodine

exists in both phases. The initial liquid concentration is $100\,\mathrm{mol\,m^{-3}}$. The initial total volume gas concentration is set so that the initial void fraction is 0.001. This volume can be determined using the initial pressure and temperature of 101 325 Pa and 628.15 K, respectively, along with the Ideal Gas Law. The decay constant is set to $0.293\,\mathrm{s^{-1}}$ for both the gas and liquid species. For this problem, the phase transfer is disabled. The liquid and gas iodine will both deplete as follows:

$$I = I_0 \exp(-\lambda t) \tag{7.1}$$

Here, I is the iodine concentration at time t, I_0 is the initial concentration, and λ is the decay constant. Note that the gas iodine simply disappears from the system as it decays because no daughter isotope was defined, so the system void will also decrease as time passes. The transient is run for 5 s and compared to the expected analytical solution. Fig. 7.1 shows that the decay of iodine in the gas and liquid phases matches expected analytical solutions and Fig. 7.2 shows that the void change also matches the expected solution.

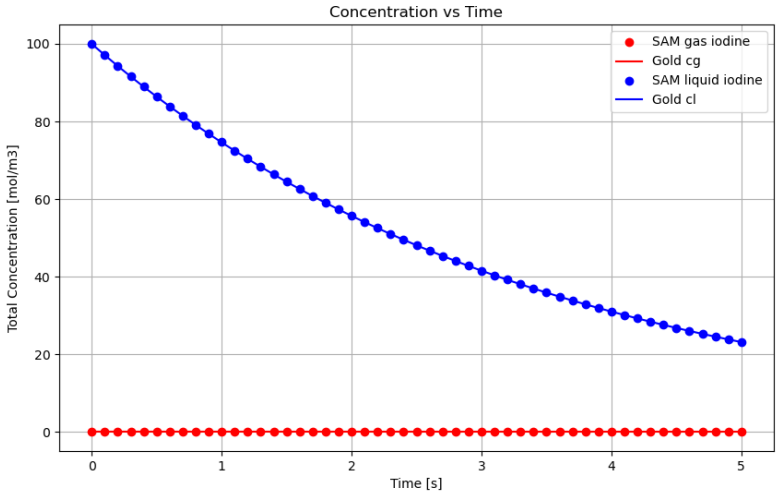

Figure 7.1: Comparison of SAM and analytical solution for decay of iodine in liquid and gas phases in a tank with no flow.

7.1.8 Tank with a system of species

This is a model of a tank with non-flowing salt that contains two high-volatile species dissolved in the salt initially. Because the species are highly volatile, they escape and form a gas mixture over time. The two species are xenon and krypton and their Henry coefficients are defined as constant values of $9.87 \times 10^{-6}\,\mathrm{mol\,m^{-3}\,Pa^{-1}}$ and $4.93 \times 10^{-6}\,\mathrm{mol\,m^{-3}\,Pa^{-1}}$, respectively. The xenon and krypton are initially in the salt only, meaning there is no gas space at the start of the transient. The initial xenon and krypton in the salt is $0.9\,\mathrm{mol\,m^{-3}}$ and $0.7\,\mathrm{mol\,m^{-3}}$, respectively. The mass transfer coefficient for both species is set to $0.1\,\mathrm{m\,s^{-1}}$. The analytical solution for the equilibrium condition of this system involves three sets of equations. First, the mass of the individual xenon and krypton species must be conserved as they migrate from liquid to gas:

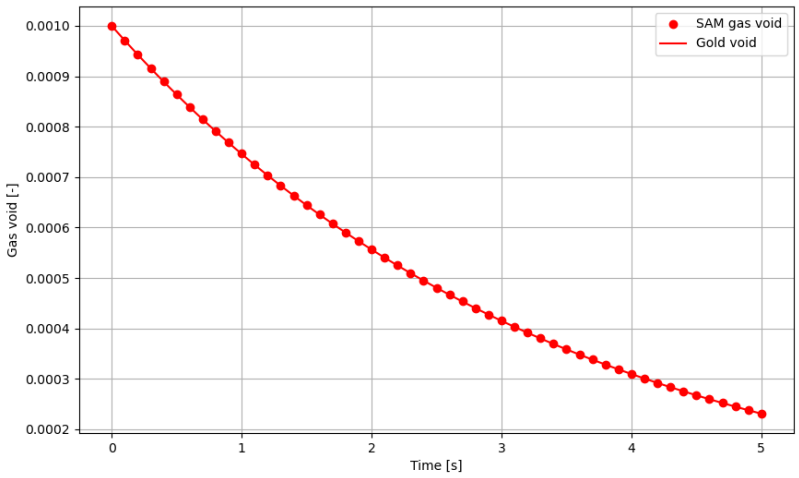

Figure 7.2: Comparison of SAM and analytical solution for change in void as gaseous iodine decays in tank.

$$c^0_{s,\ell} = c^N_{s,\ell}(1-\alpha^N) + c^N_{s,g}\alpha^N \tag{7.2}$$

Here, s is the species identifier. There is one equation for xenon and one for krypton. The species total volume concentration is denoted with c, the volume fraction is denoted with α, and the ℓ and g subscripts denote whether the species exists in the liquid or gas phase, respectively. The 0 and N superscripts denote that the value is either at the initial time in the transient or the final time in the transient, respectively. The final time is defined as the time when the system has reached equilibrium conditions. The second set of equations defines the ratio of gas-to-liquid concentration for each of the species using Henry's Law.

$$c^N_{s,g} H_s RT = c^N_{s,\ell} \tag{7.3}$$

Again, there is one equation per species. The Henry coefficient for the species is given by H_s, the universal gas constant is R, and the system temperature, which is constant throughout the transient, is T. Finally, the volume fraction at the equilibrium condition can be determined using the Ideal Gas Law assuming that both the pressure and temperature did not change over the transient.

$$c^N_{\mathrm{xe},g} + c^N_{\mathrm{kr},g} = p/R/T \tag{7.4}$$

Solution of this system of equations will provide the equilibrium values. The equilibrium void is compared to the transient SAM solution in Fig. 7.3 and it is shown that SAM correctly arrives at the analytical value.

7.1.9 Tank with sparging gas

This model uses a 1D pipe in SAM to represent a tank by setting inlet liquid and species flow to zero. The tank includes a system of three species: xenon in liquid and gas phases and helium.

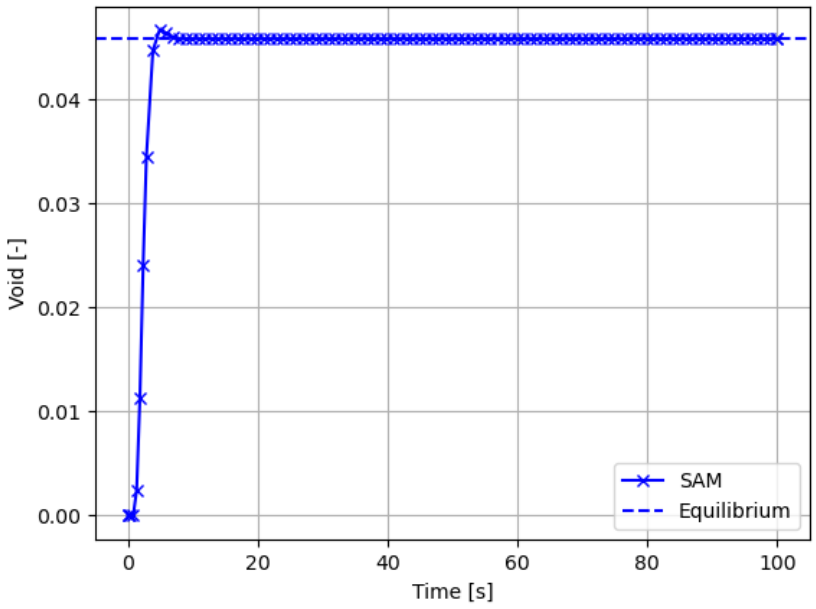

Figure 7.3: Comparison of SAM transient void and the analytical equilibrium value in a non-flowing tank where two dissolved species come out of solution to form a two gas mixture.

Initially, the gas phase is 100% helium and there is enough helium to create an initial void of 1%. The helium is non-volatile, meaning it will not transfer back into the liquid. The xenon, however, is high-volatile and has a constant Henry coefficient of $9.9 \times 10^{-7}\,\mathrm{mol\,m^{-3}\,Pa^{-1}}$ is set along with a mass transfer coefficient of $0.1\,\mathrm{m\,s^{-1}}$. The total volume concentration of xenon in the liquid is $0.05\,\mathrm{mol\,m^{-3}}$. A system of three equations is needed to solve the equilibrium system behavior for this case.

$$c^0_{\mathrm{Xe},\ell} = c^N_{\mathrm{Xe},\ell}\left(1-\alpha^N\right) + c^N_{\mathrm{Xe},g}\alpha^N \tag{7.5}$$

$$\alpha^e = \alpha^0 + \frac{c^N_{\mathrm{Xe},g}}{p/(RT)} \tag{7.6}$$

$$c^N_{\mathrm{Xe},\ell} = c^e_{\mathrm{Xe},g} HRT \tag{7.7}$$

The first equation denotes the fact that the total xenon mass does not change from its initial value. The concentration is represented with c and the subscripts ℓ and g declare whether the species is in the liquid or gas phase. The 0 and N superscripts declare whether the value is initial or final equilibrium. The second equation states that the final void will be the sum of the initial void plus the void occupied by the xenon at equilibrium conditions. Because the helium is non-volatile, its void does not change. Finally, the last equation relates the xenon concentration in liquid and gas phases using Henry's Law. Fig. 7.4 shows that the total void reaches the equilibrium value during the transient. Furthermore, the helium void (red) does not change over the transient, as expected.

The xenon void starts at zero and increases to an equilibrium value dictated by Henry's Law and its increase is fully responsible for the increase in total system void during the transient.

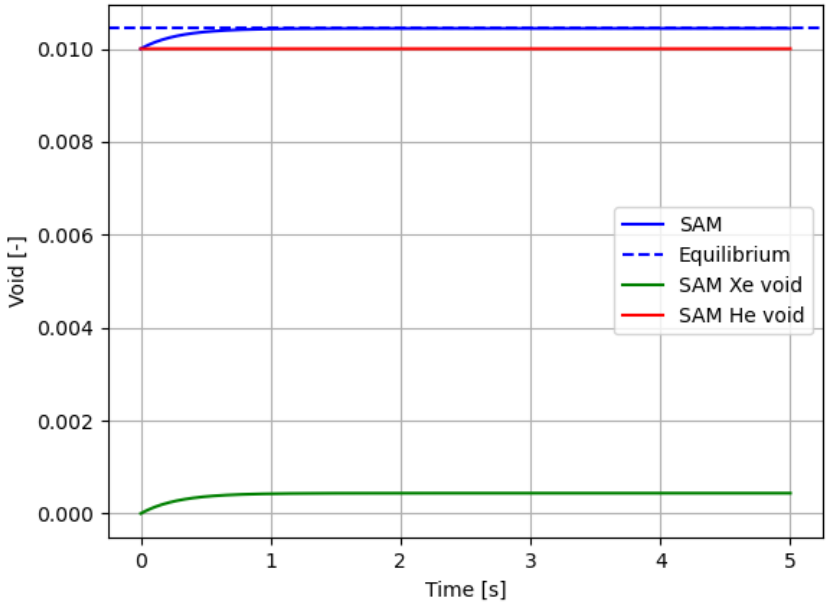

Figure 7.4: The SAM solution for helium, xenon, and total void over a transient where xenon leaves the liquid phase and enters the helium gas space.

7.1.10 Liquid and gas species injection into a pipe

Two passive species are injected into a vertical pipe. This test uses the new passive species gas transport model. The liquid inlet velocity is $1\,\mathrm{m\,s^{-1}}$. The gas moves at a constant slip ratio of 1.2, which is defined via input. The case is not heated, so gas and liquid velocities are fixed throughout the pipe. The inlet species concentration is $1\,\mathrm{mol\,kg^{-1}}$ for both the liquid and the gas species. Note that this test exercises the ability to specify the boundary condition as a specific mass concentration ($\mathrm{mol\,kg^{-1}}$) rather than a volumetric concentration ($\mathrm{mol\,m^{-3}}$). Both species experience decay with a decay constant of $2.11 \times 10^{-1}\,\mathrm{s^{-1}}$. Because the gas phase is moving faster than the liquid phase, a different species profile is obtained for the two species. Because there is no phase transfer or other sources or sinks, the solution to the 1D species transport equation with decay is:

$$s = s_0 \exp\left(-\lambda_s / v s\right) \tag{7.8}$$

The analytical solution is compared to the SAM solution in Fig. 7.5 for this problem, which shows excellent agreement for both phases. Note that the figure shows the concentration in $\mathrm{mol\,m^{-3}}$. When a specific mass concentration is used as a boundary condition, it is assumed that the two-phase mass is used. Given that void is low in this case, the mixture density is approximately $2000\,\mathrm{kg\,m^{-3}}$, which is the density of the liquid phase. Therefore, the $1\,\mathrm{mol\,kg^{-1}}$ concentration of both species are

multiplied by the mixture density to obtain the inlet pipe value of 2000 $\mathrm{mol\,m^{-3}}$. The liquid moves slower through the pipe, so it has more time to decay to a lower value, as shown in the figure.

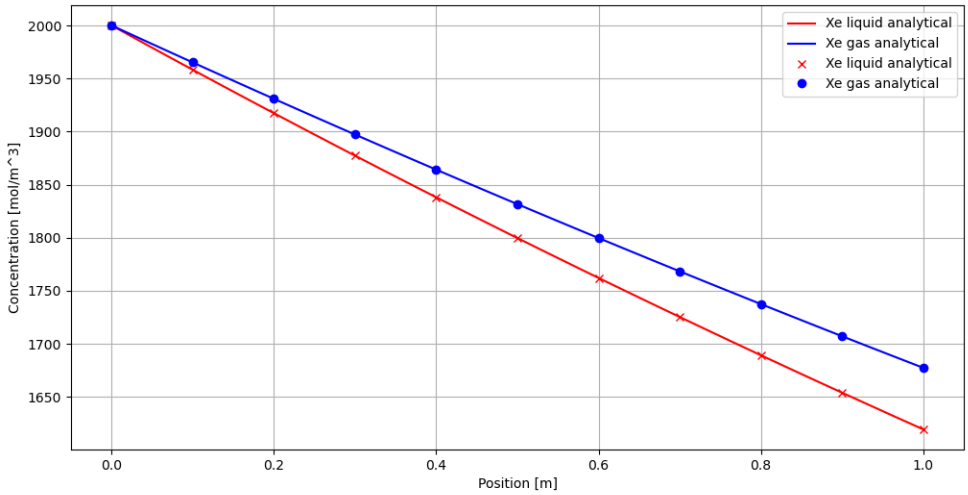

Figure 7.5: Comparison of SAM and analytical solution for convection and decay of liquid and gas species in a 1D pipe.

7.1.11 Liquid and gas species injection into a pipe with specific mass for boundary conditions

This case is essentially the same as the previously described test in Section 7.1.10. The primary difference is that the boundary condition is specified as a volumetric concentration instead of a specific mass concentration. The boundary condition is set to 1.2 $\mathrm{mol\,m^{-3}}$ for both the gas and liquid species. Note that this is a total volume concentration, not a phase concentration. The new SAM model does not accept a phase concentration as input as of now, but it can output the phase concentration of the species if requested. Like the previous test, this case also shows good agreement with the analytical solution, which is shown in Fig. 7.6.

7.1.12 Liquid and gas species injection into a pipe with phase change

In this case, a horizontal pipe is modeled with both liquid and gas species injection on the left side. The species are linked via phase transfer and a constant Henry coefficient of 1.826×10^{-9} $\mathrm{mol\,m^{-3}\,Pa^{-1}}$ is specified. The new gas passive gas transport model is used. The constant bubble diameter feature is activated and bubble size is set to 3 mm. The liquid total volume concentration at the inlet is 0.5 $\mathrm{mol\,m^{-3}}$. The gas total volume concentration is set to achieve an inlet volume fraction of 0.01% (using the approach defined in Section 7.1.3. The equation set for this problem is as follows:

$$\frac{\partial c_\ell}{\partial x} = \frac{kA_i}{v_\ell}\left(c_g HRT - c_\ell\right) \tag{7.9}$$

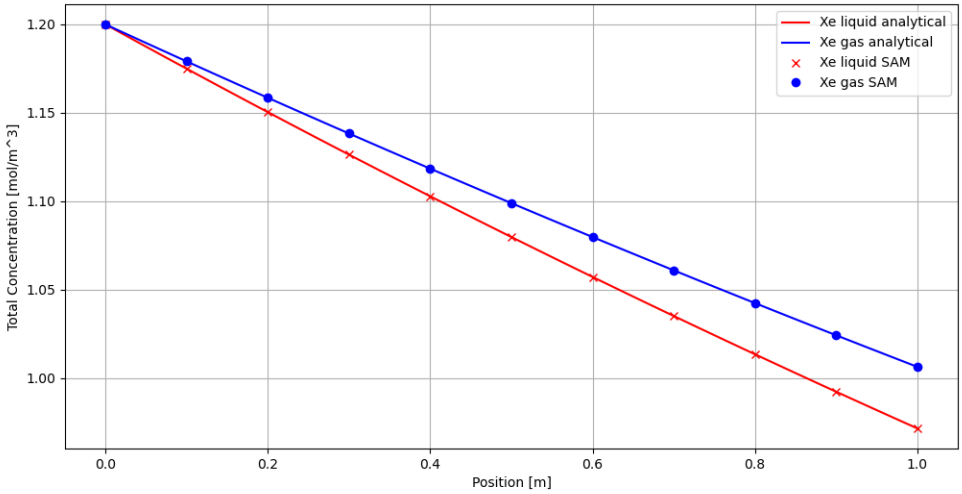

Figure 7.6: Comparison of SAM and analytical solution for convection and decay of liquid and gas species in a 1D pipe when the boundary condition is given as volumetric concentration.

$$\frac{\partial c_g}{\partial x} = \frac{kA_i}{v_g}\left(c_\ell - c_g HRT\right) \tag{7.10}$$

$$\frac{\partial \alpha}{\partial x} = \frac{kA_i}{v_g p/(RT)}\left(c_\ell - c_g HRT\right) \tag{7.11}$$

$$A_i = \frac{6\alpha}{d_b} \tag{7.12}$$

The first two equations are the species transport equations. The only source term is the the phase transfer term, which affects both species. The temperature and mass transfer coefficient values are set to fixed values via input: $628.15\,\mathrm{K}$ and $4.616 \times 10^{-2}\,\mathrm{m\,s^{-1}}$. The species travel at different velocities of $1\,\mathrm{m\,s^{-1}}$ for the liquid (v_ℓ) and $1.2\,\mathrm{m\,s^{-1}}$ for the gas (v_g). The void fraction is determined using a mass balance equation given by Eq. 7.11. Note that the $v_g p/(RT)$ in the denominator, when moved to the left-hand-side, results in the gas advection term. The source term for the gas is the phase transfer into the species, which is the remainder of terms on the right-hand-side. Finally, the interfacial area is determined from the definition of the Sauter mean diameter given in Eq. 7.12. These equations are solved simultaneously using Scipy and compared against the SAM solution. Fig. 7.7 shows the solution for the phase concentrations of the liquid and gas species. The gas concentration agrees well with the molar density predicted by the Ideal Gas Law. The change in phase concentration over the pipe length is small, which makes the solution look unchanging; however, Fig. 7.8 shows the void profile, which is clearly exponentially increasing. The SAM and analytical solutions are in good agreement.

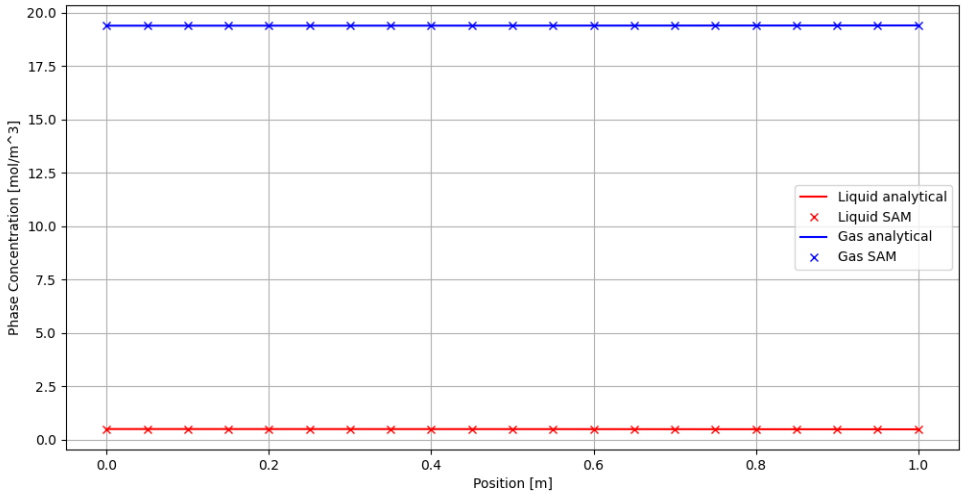

Figure 7.7: Comparison of SAM and analytical solution for liquid and gas species with phase transfer in a horizontal pipe.

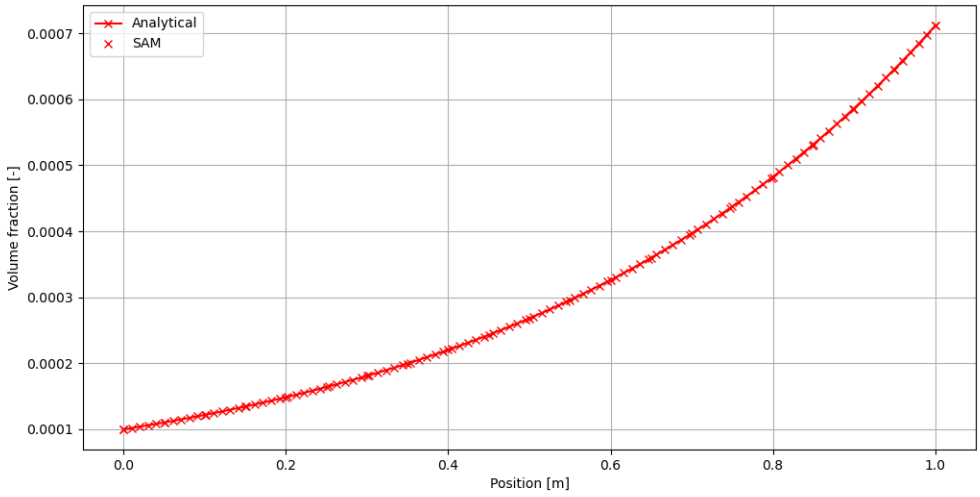

Figure 7.8: Comparison of SAM and analytical solution for void in a horizontal pipe with phase transfer between liquid and gas species.

7.2 Verification of ideal gas diffusion in porous structures

The integrated framework for species transport in fluid Components, diffusion in solid Components, and conjugate mass transfer has been verified and validated in previous efforts [62, 63]. Additional regression tests were developed to ensure the additional capabilities to model the physical phenomena for Xe migration into graphite discussed in Section 6.1. These regression tests verify several aspects of the model, including:

- Interface constraint for an ideal gas dissolved in liquid to porous solid , selected by interface type `porous-diffusion`, is verified against an analytical calculation of the solid wall surface flux when applied as ambient boundary conditions to a `HeatStructure`.
- Interface constraint for an ideal gas dissolved in liquid to porous solid, selected by interface type `porous-diffusion`, is verified against an analytical calculation of the solid wall surface flux when coupled between `HeatStructure` and `PBOneDFluidComponent`-type component.
- Decay and burnup reactions within `HeatStructure` are verified against analytical calculation of time-evolution of species concentration.
- Built-in material properties for Xe-135 in Flibe, and Xe-135 in IG11 graphite are correctly calculated by checking SAM-reported property values over a range of temperatures against a verified gold reference.
- Updated porous-diffusion conjugate mass transfer is accessible by composite components: `PBPipe`, `PBCoreChannel`, and `PBHeatExchanger`.

7.2.1 Analytical verification of FLiBe-Graphite Xe permeator extraction pipe

In addition, a tritium permeator/extraction pipe SAM model was adopted from previous work [63] and reformulated as a postulated Xenon extraction FLiBe-Graphite pipe permeator for additional verification as this configuration has a derived analytical solution for the steady species concentration profile throughout the domain [64]. For flow of a species with advection in a 1-D pipe and convective mass transfer to a 1-D or 2-D solid wall with diffusion and a vacuum (zero concentration) outer wall BC, the analytical solution for the steady concentration profile can be derived assuming constant properties. In configurations where both the liquid and solid regions are governed by Henry's (or Sievert's) law for solubility, the ratio of concentrations in the wall near the fluid $c_{w,l}$ and on the outer surface of the wall $c_{w,s}$ are proportional to the ratio of the solubility in liquid K_l and solubility in solid K_s:

$$\frac{c_{w,l}}{c_{w,s}} = \frac{K_l}{K_s} \tag{7.13}$$

which in this case, K_l is given by the Henry's law solubility for Xe in FLiBe (Eq. 6.5), and $K_s = \varepsilon/RT$ for an ideal gas in a porous structure.

Starting from a fixed boundary condition of $c_s(r_o) = 0$ on the outer wall, the concentration profile within a cylindrical shell has a well-known solution for constant diffusivity (disregarding any xenon decay reaction terms for simplicity). The flux constraint at the interface is balanced:

$$K_m\left(c_b - c_{w,l}\right) = \frac{2D_s c_{w,l}}{d_i \ln\left(d_o/d_i\right)} \frac{K_s}{K_l} \tag{7.14}$$

where K_m is the mass transfer coefficient, c_b is the concentration in the bulk liquid, D_s is the diffusivity in the wall, and d_i and d_o are the pipe inner/outer diameters. Conserving this flux balance with the transport flux of the bulk liquid species in the axial flow direction, an expression for $c_b(z)$ can be derived:

$$c_b(z) = c_0 \exp\left(-\frac{4K_t z}{v d_i} \frac{\zeta}{1+\zeta}\right) \tag{7.15}$$

$$\zeta = \frac{2D_s K_s}{K_t K_l d_i \ln\left(d_o/d_i\right)} \tag{7.16}$$

where c_0 is the inlet concentration and v is the 1-D flow velocity in the z direction. Further details on this derivation can be found in [64]. This configuration was modeled in SAM as a 1-D FLiBe-graphite pipe as a `PBPipe` using the built-in properties for Xe-135 in FLiBe and IG-11 graphite as shown in Figure 7.9.

Table 7.1: Parameters for SAM model of postulated Xe extraction Flibe-Graphite permeator pipe.

Parameter	Value	Parameter	Value
Inner Diameter	2.54 cm	K_m	0.164 mm/s
Wall thickness	2.5 mm	K_l	2.05E-05 mol/m^{3}Pa
Length	50 m	K_s	2.57E-05 mol/m^{3}Pa
Temperature	973.15 K	D_s	3.96E-05 m^2/s
Inlet Velocity	2.5 m/s	λ_{Xe}	0.0 s^{-1}
Inlet Xenon	1.0 mmol/m^3	Outer Wall BC	0.0 mol/m^3

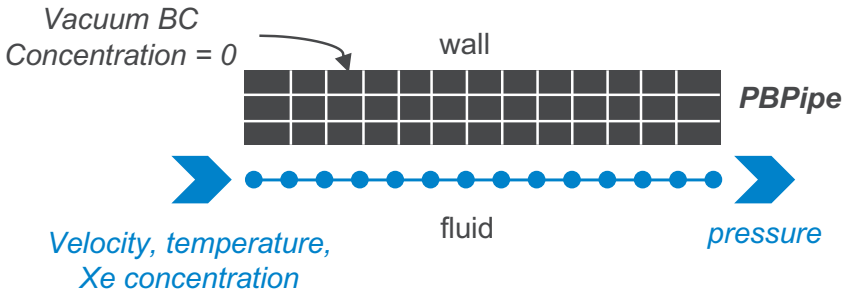

Figure 7.9: Diagram of a hypothetical xenon-graphite permeator verification model in SAM.

The SAM prediction is compared to the analytically derived concentrations in the bulk fluid, near the wall in the fluid, and at the outer wall surface to confirm that the model produces the correct solution, as depicted in Figure 7.10. This particular configuration has a 40.1% efficiency at extracting xenon out of the flowing FLiBe.

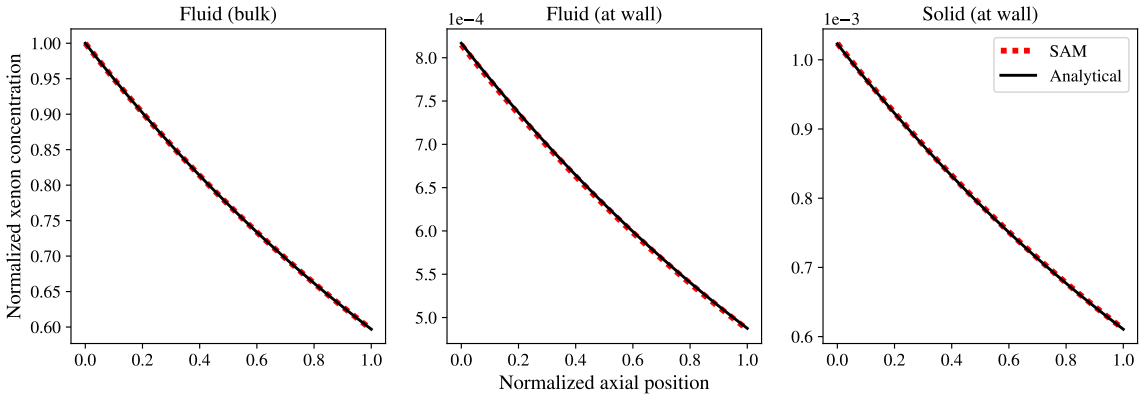

Figure 7.10: Verification of SAM with analytical solution of bulk fluid, near wall and outer wall surface xenon concentrations in a hypothetical xe-graphite permeator.

7.3 Verification of updated mass transfer closure models

Regression tests for the mass transfer closure models discussed in Section 6.4 were also added into SAM to verify that the code output Sh and K_m values match the hand-calculated verification values for all five model options. The pipe phase transfer regression test (see Section 7.1.12 was adopted for verification of the Calderbank & Moo-Young and Kress Sh correlations for liquid-bubble mass transfer, as shown in Figures 7.11 and 7.12. A regression test was also added to verify the correct implementation of the `SC_MTC` sensitivity coefficient parameter.

7.4 Verification of redox corrosion model

A demonstration problem based on modeling the corrosion of a beryllium sample rod inserted in the MSRE pump bowl modeled by the previous redox corrosion model development was used for code-to-code verification of the corrosion model incorporated into SAM [41]. In the MSRE, corrosion was observed over the lifetime of the reactor, and specifically during Run 15 a small beryllium rod in a nickel cage was inserted into the pump bowl and partially immersed during operation. An ïron-rich coatingẅas found when the rod was extracted, deposited from corrosion of structural materials elsewhere in the primary loop.

A small 1-D problem was used to demonstrate this phenomena in which a 4 cm diameter Be rod is assumed to be inserted at a depth of 10 cm into the pump bowl fuel salt. Assuming that the salt flows along the inserted length of the rod at a given velocity and temperature, the oxidation-reduction of the rod is simulated in the original RPI redox model in Moose and compared to the updated simulation using SAM. The current density profile along the axial length of the rod is compared between the two models at $t = 0.01s$ and $0.025s$ as shown in Fig. 7.13, at which point the corrosion has reached a constant rate. The corrosion can also be observed by the exchanging of Fe2+ ions in the salt with Be2+ ions from the inserted rod, where the comparing the predicted concentrations of both ions at the end of the rod as shown in Fig. 7.14. Both models are in close agreement, with some slight differences that may be attributed to differences in species advection models implemented in the `ConservativeAdvection` Kernel in Moose compared to the Streamline-Upwind Petrov-Galerkin (SUPG)-stabilized form for species advection implmeneted in SAM.

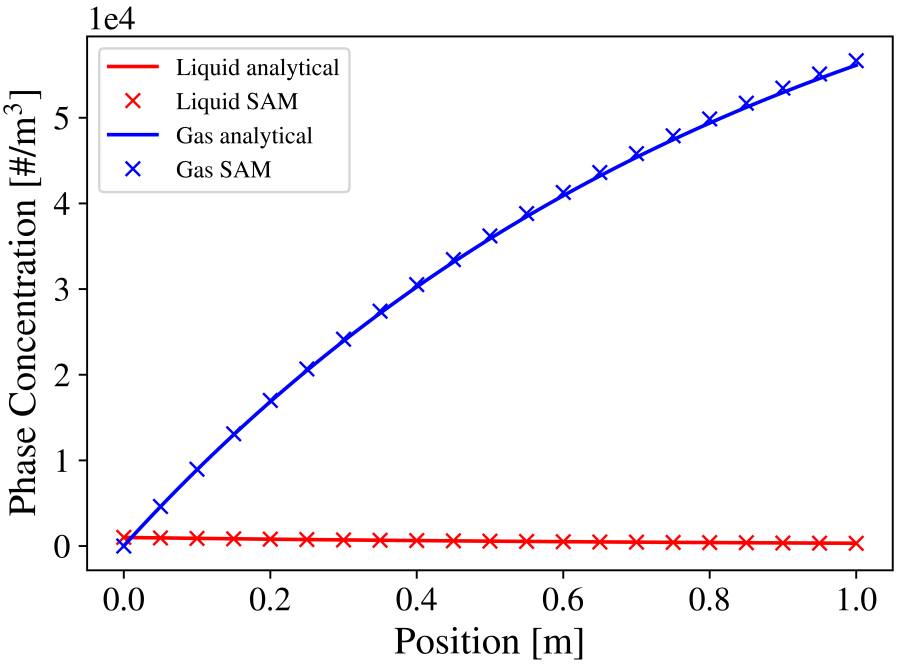

Figure 7.11: Comparison of SAM and analytical solution for liquid and gas species with phase transfer in a horizontal pipe using the Calderbank & Moo-Young mass transfer correlation

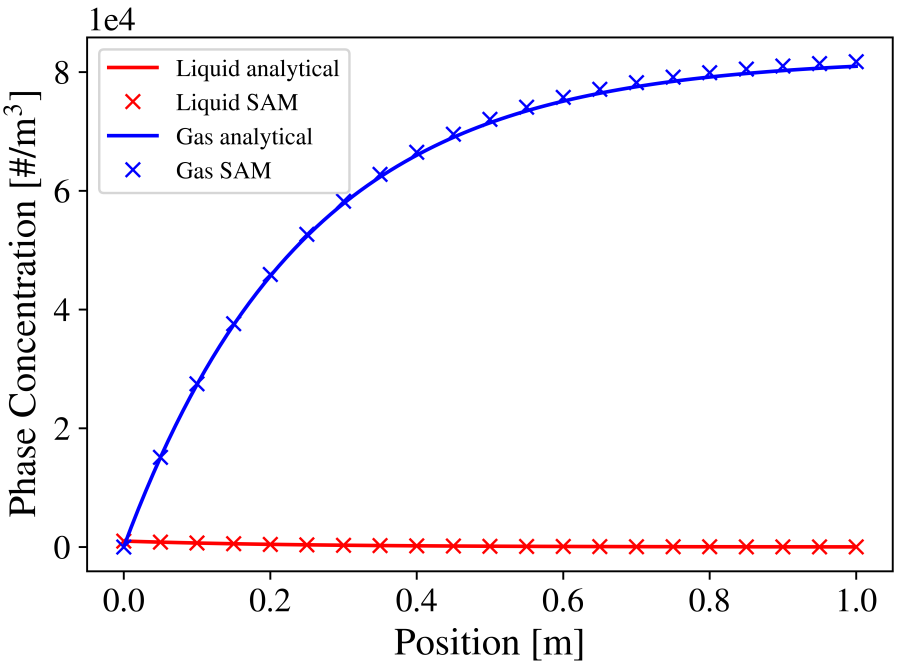

Figure 7.12: Comparison of SAM and analytical solution for liquid and gas species with phase transfer in a horizontal pipe using the Kress mass transfer correlation

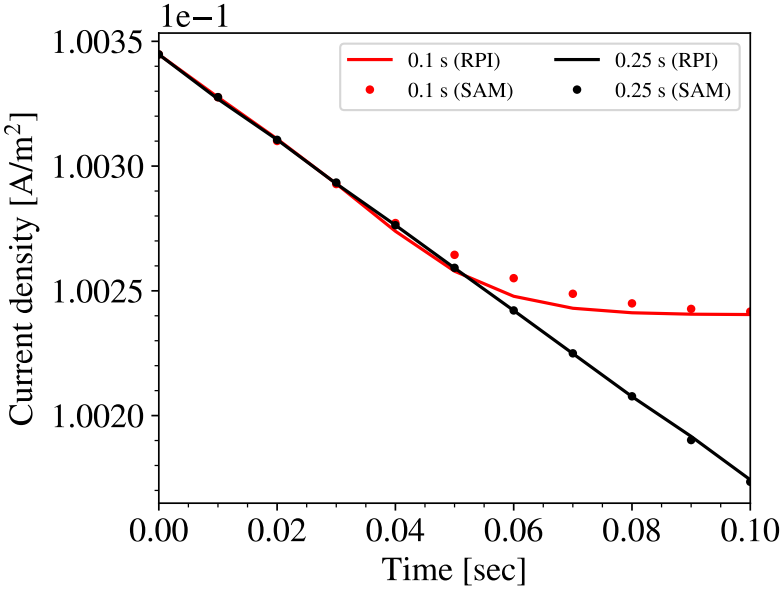

Figure 7.13: Verification of SAM calculated current density with original RPI redox model at $t = 0.1s$ and $0.25s$ along axial length of a Be rod corrosion demonstration [41].

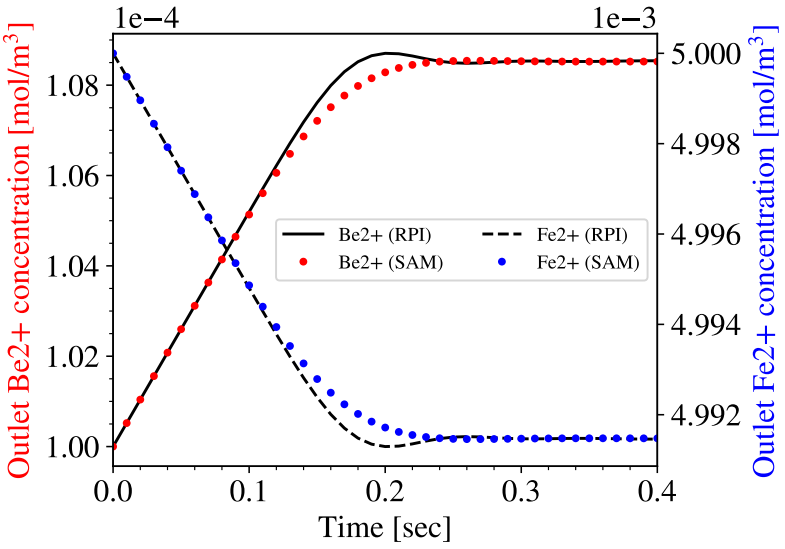

Figure 7.14: Verification of SAM calculated ion concentrations at the end of a Be rod with original RPI redox model calculation [41].

7.5 Integrated demonstration of Xe-135 transport and reactivity in the MSRE

7.5.1 Equilibrium Xe-135 distribution at nominal steady state

The noble gas migration model in graphite is demonstrated in a SAM model of the MSRE primary loop, which has been used in previous demonstrations of the drift flux model [13] and the interphase transport capability [40]. Building upon previous models, the simulation has been updated to incorporate additional Xe-related transport phenomena and has been extended to a simulation time of 72 hours to estimate the equilibrium distribution of I-135 and Xe-135 in the core. The MSRE core is represented by a single average fuel salt channel coupled with a single average graphite moderator heat structure that is 2.54 cm thick to represent the half-width of a graphite stringer while preserving the total moderator volume and surface area. Please refer to Figure 3.6 for a diagram of the plant configuration and Figure 7.15 for a schematic of the SAM model layout.

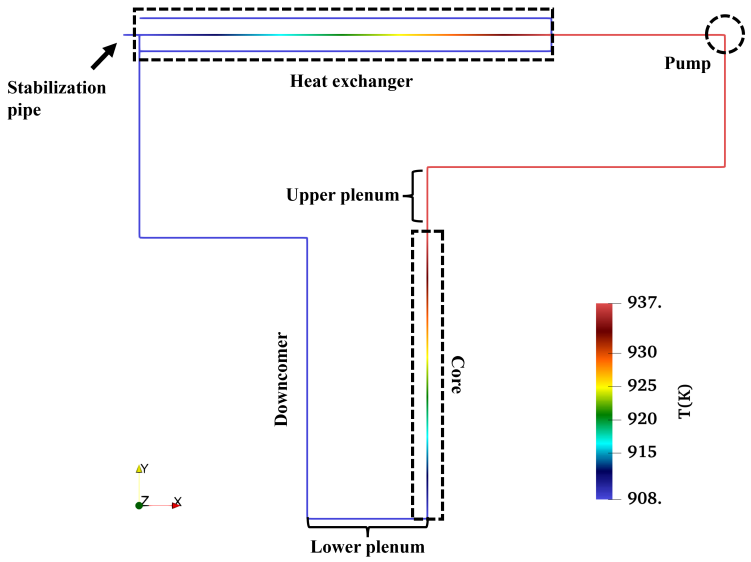

Figure 7.15: SAM 1-D model of the MSRE and fuel salt temperatures at 10 MW, reproduced from [65]. Note the graphite moderator is adjacent to the core fuel salt channel but is not shown in this figure.

To approximate the cover gas that is entrained as bubbles and broken up through a stripping process in the pump bowl, the SAM model is initiated with a uniform 0.5% helium void throughout the system with no gas phase sources or sinks and allowed to reach a steady state distribution that is primarily determined by the local slip ratio and the pressure and temperature distribution in the primary loop [13]. At steady state nominal full power (7.4 MWth), due to the high slip ratio in the core and the opposite effect in the downcomer (due to low bulk velocity and buoyancy effects), the void in the core region is roughly 0.2% whereas it is much higher at 0.9% in the downcomer. A diagram of the SAM MSRE model and the steady void distribution is shown in Figure 7.16.

Iodine and xenon are added to the system, such that I-135 is generated with a 2.66% yield and Xe-135 with a 3.2% yield from fission dissolved in the fuel salt core channels (liquid phase). The dissolved Xe-135 is allowed to transfer to the helium bubbles (gas phase) throughout the primary

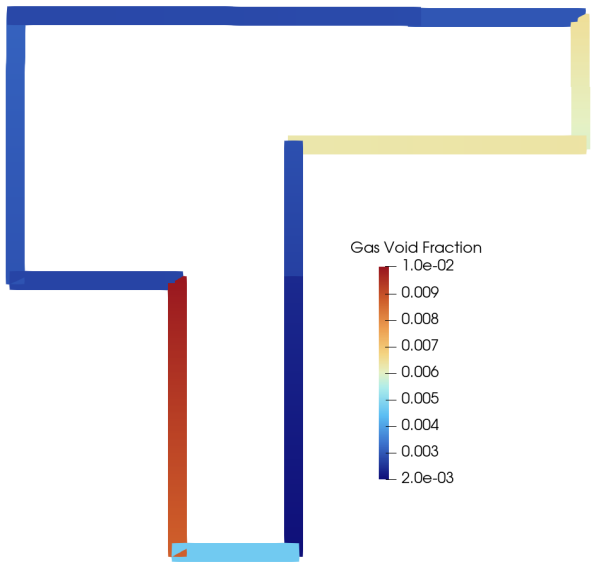

Figure 7.16: MSRE SAM model void distribution at nominal full power.

loop with the liquid-gas convective mass transfer coefficient determined by the Kress (1972) correlation [55]. These species will be advected by the liquid and gas phases, with I-135 decaying to Xe-135 (dissolved) and Xe-135 decaying out of the system (daughter products not tracked). The absorption burn-up of these species are also captured with estimated burn-up rates that are assumed to directly scale with total power [56]. In the pump bowl, the MSRE incorporated a stripping mechanism in which roughly 10% of the salt was diverted to a spray ring in an effort to release Xe-135 from entrained sparging gas. For the current demonstration, we assume that the stripping efficiency is 1% for the Xe-135 gas phase in the pump bowl. For transfer of Xe-135 to the graphite, the convective liquid-solid mass transfer coefficient is calculated using the Yuan-Hoyt (2021) correlation for pipe flow [52]. The effective diffusivity of Xe in the MSRE graphite is assumed to be 1.32×10^{-8} m^2/s with a porosity of 10%, as calculated by [45]. The average thermal fluid and mass transport properties are summarized in 7.2, and the I-135/Xe-135 transport parameters in specific phases and regions are summarized 7.3.

Table 7.2: SAM MSRE model core thermal-fluid and mass transfer parameters at steady state.

Parameter	Units	Value
Total Power	MW	7.4
Total Flow	kg/s	169
Average temperature	K	893
Average void	%	0.2
Avg. Liquid-Wall K_m	m/s	8.3×10^{-6}
Avg. Liquid-Bubble K_m	m/s	3.4×10^{-4}
Avg. Graphite Diffusivity D_{eff}	m^2/s	1.32×10^{-8}

Table 7.3: SAM MSRE model iodine and xenon transport parameters.

Parameter	Units	I-135 (salt)	Xe-135 (salt)	Xe-135 (gas)	Xe-135 (graphite)
Yield per fission	%	2.66	3.2	0.0	0.0
Decay constant	s^{-1}	2.93e-05	2.11e-05	2.11e-05	2.11e-05
Burn-up rate	s^{-1}	4.162e-10	2.791e-05	2.791e-05	5.01e-05
Pump bowl stripping	%	0.0	0.0	1.0	–

The SAM MSRE model is simulated for 72 hours to observe the system reaching an equilibrium distribution of Xe-135, as shown in Figures 7.17 and 7.18. It should be noted that the assumed values and helium void parameters used in this demonstration are not exact and may not represent the actual operation of the MSRE. After 3 days of operation, the system reaches an equilibirum distribution in the core with I-135 having the highest concentration due to its low burn-up compared to Xe-135. Out of the total Xe-135 content in the core, about half of the Xe-135 is in the helium bubbles, which is quickly and continuously carried out of the core and stripped in the pump bowl. About 30% of the Xe-135 diffuses into and accumulates in the graphite moderator, with the remaining 20% dissolved in the fuel salt. A majority of the Xe-135 is no longer retained in the fuel salt due to its low solubility in FLiBe, with more xenon being picked up by the helium sparging gas, which has a higher mass transfer rate and considerable surface area in comparison to the transfer rates into graphite.

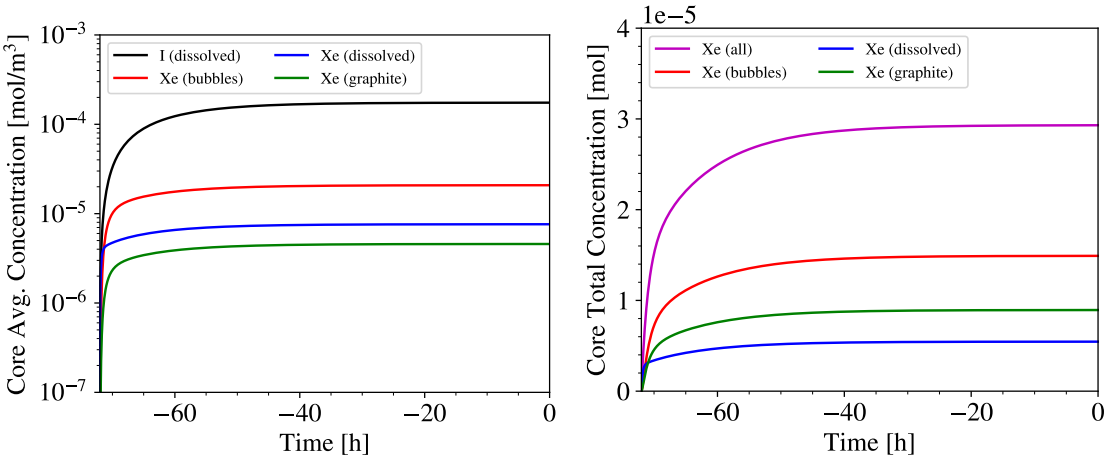

(a) Average

(b) Total

Figure 7.17: Steady state 72 hour simulation of I-135 and Xe-135 concentrations in the SAM MSRE model core region to estimate equilibrium distributions.

7.5.2 Xe-135 transport phenomena during shutdown

From this equilibrium state, the dynamics of xenon transport in the system is observed by simulating a ”shutdown” scenario in which the power is immediately dropped to 0 MW and the primary and secondary pumps are reduced to half of their nominal flow rate. Once the core power is reduced, the system will reach an equilibrium temperature and there is no longer any production or burn-up of I-135 or Xe-135. Both isotopes will continue to decay out of the system and Xe-135 in

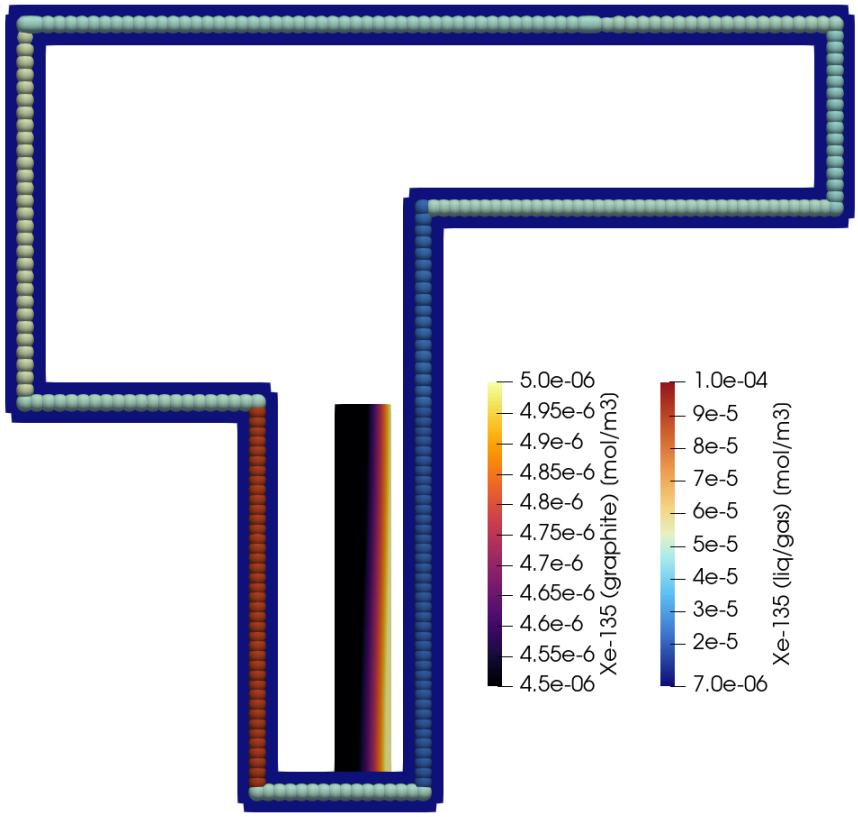

Figure 7.18: MSRE SAM model Xe-135 distribution in the primary fuel salt liquid (background blue line) and gas phases (overlaid dots) and in the graphite moderator (dark block in the middle of lower loop section). Note that object widths have been exaggerated for visibility.

bubbles will be removed from the pump bowl. The pump stripping efficiency is also estimated to reduce from 0.1% to 0.05% due to the reduced pump flow, with a sensitivity study performed on this parameter. This shutdown scenario is simulated for 40 hours to observe the evolution of Xe-135 concentrations in the core region and are shown in Figures 7.19 and 7.20.

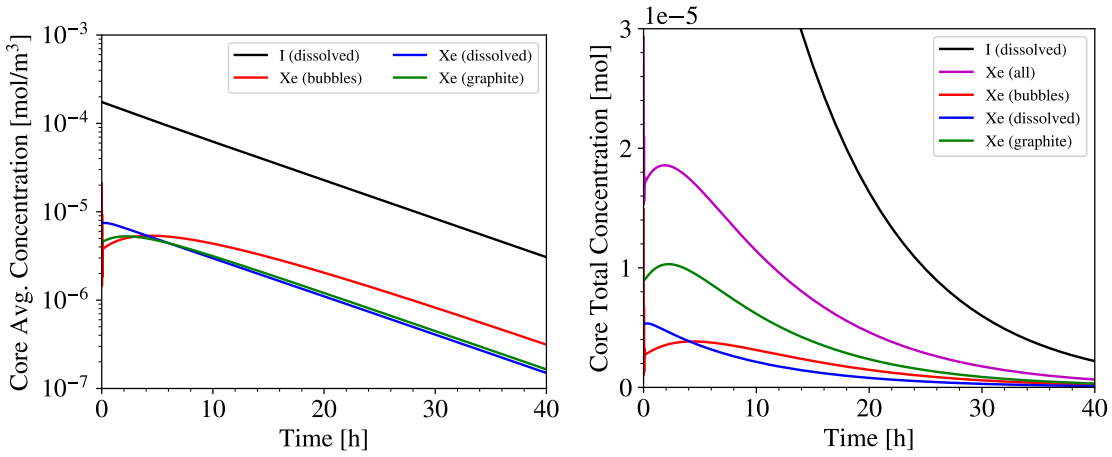

(a) Average (b) Total

Figure 7.19: Shutdown 40 hour simulation of I-135 and Xe-135 concentrations in the SAM MSRE model core region from full to zero power and 50% nominal flow.

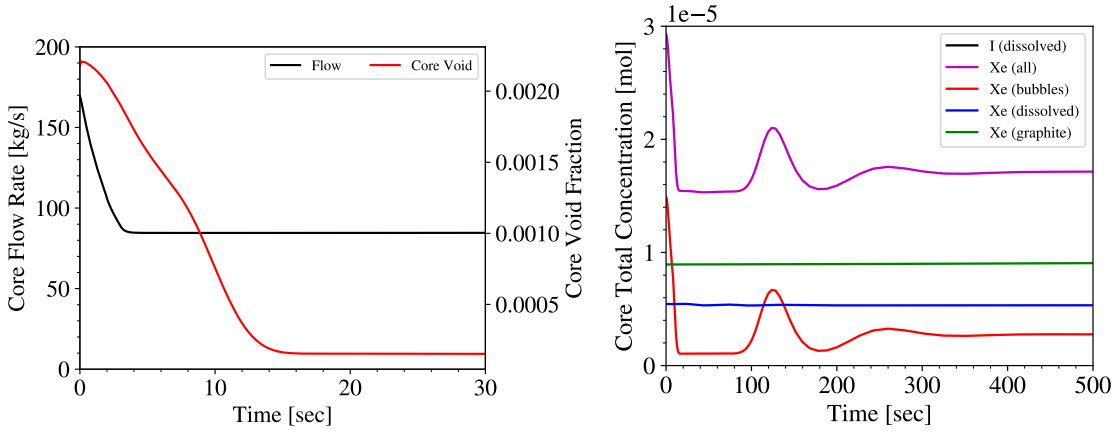

(a) Flow and void reduction (b) Xe at initial stages

Figure 7.20: Shutdown 40 hour simulation of I-135 and Xe-135 concentrations in the SAM MSRE model core region from full to zero power and 50% nominal flow.

In the shutdown scenario, it is observed that the reduction in flow has a significant influence on the core void fraction. As the flow reduces to 50% within a few seconds, the He sparging gas void quickly drops from 0.2% down to 0.01% (and later recovers back to about 0.04%). The reduction in flow velocity results in an increase of slip velocity in the core fuel salt channels and decrease of slip

and hold-up of void in the downcomer region. As previously discussed, the total He void content is constant in the current model (without sinks or sources), whereas during a shutdown the total void should also decrease as the pump speed ramps down and less gas is entrained into the primary loop, and may be more realistically modeled in future efforts. This reduction in gas void also results in an initial 90% decrease of Xe-135 gas phase concentration in the core, while the Xe-135 dissolved concentration is relatively uniform throughout the primary loop and does not change significantly during the initial flow reduction. I-135 dissolved in the salt will continue to decay to dissolved Xe-135, although the dissolved Xe-135 will still preferably transfer out to the remaining sparging gas and graphite. The xenon concentrations in graphite and the gas phase will have slight increases in the first 10 hours as there is no longer any burn-up, but will eventually decay out of the system as well.

To further investigate the impact of pump stripping, the shutdown scenario was simulated without any reduction in stripping efficiency (1%) and with a complete reduction in stripping (0%) to compare the evolution of Xe-135 in the core, as shown in Figure 7.21. As anticipated, the reduction in core void still has the most significant impact on the Xe-135 core concentration (since half of the initial xenon content is in the gas phase), but the stripping efficiency does have an impact on how much the xenon will recover before decaying out of the system. An improved model could directly account for the reduction in flow and void production/removal in the pump bowl to more accurately estimate the change in stripping efficiency.

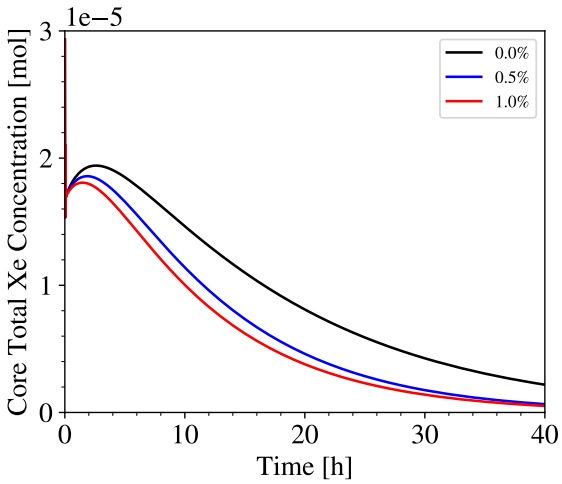

Figure 7.21: Comparison of pump stripping efficiency effect on evolution of total Xe-135 in the core during shutdown.

7.5.3 Integrated model of Xe-135 reactivity feedback during load follow

In order to demonstrate the impact a change in the Xenon concentration has on the reactivity of the core, a simple transient case was developed using the updated MSRE model, described in Section 7.5. In the core channel a uniform worth of -21.6792 and -63.231 $(\Delta k/k)/(mol/m^3)$ are assumed for the Xenon in the coolant and reflector, respectively [56]. In addition to the reactivity coefficients for the Xenon, a simple control system was developed for the MSRE model. The control

system takes a target power as the input and manipulates the external reactivity to change the reactor power.

In the transient, the reactor power is dropped from 100 % to a target 75 % power over the course of 10 minutes. After holding at 75 % power for 10 minutes, the power is returned to 100 %. Throughout the transient, the control system attempts to maintain the outlet temperature and inlet temperature at a constant value by changing the primary pump head and the intermediate flow rate boundary condition, respectively. The normalized power profile, as well as the normalized primary pump head and normalized intermediate flow rate, are shown in Figure 7.22. The core inlet and outlet temperature are shown in Figure 7.23.

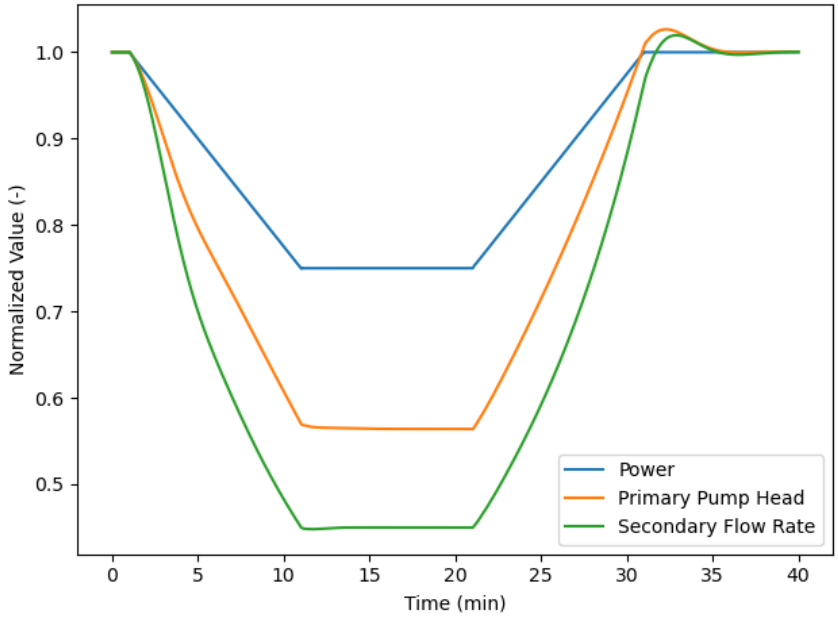

Figure 7.22: Normalized power, primary pump head, and intermediate flow rate as a function of time.

As shown in Figure 7.24, the control system must compensate for changing temperatures and changing Xe levels within the core. Further refinement of the control system can reduce the reactivity feedback caused by changing temperatures. However, the Xenon levels within the core are observed to be a strong function of the core void fraction. Figure 7.25 shows the total core void fraction as a function of time. As the primary pump head decreases to maintain to power to flow ratio at lower power levels, the void fraction within the system redistributes and accumulates within the downcomer. While this redistribution is physical, its magnitude is likely being over-predicted due to the modeling approximations that are being made at the pump bowl. In addition to the dependency on the flow rate, the Xenon feedback is observed to be a strong function of the pump bowl removal efficiency. As shown in Figure 7.26, without stripping of Xenon (dashed lines), the reactivity feedback caused by redistribution of the void fraction is approximately an order of magnitude larger than when 1 % of the Xenon in gas is stripped at the pump bowl (solid line). Further model refinement is needed to better represent the response of the void as a function of flow rate.

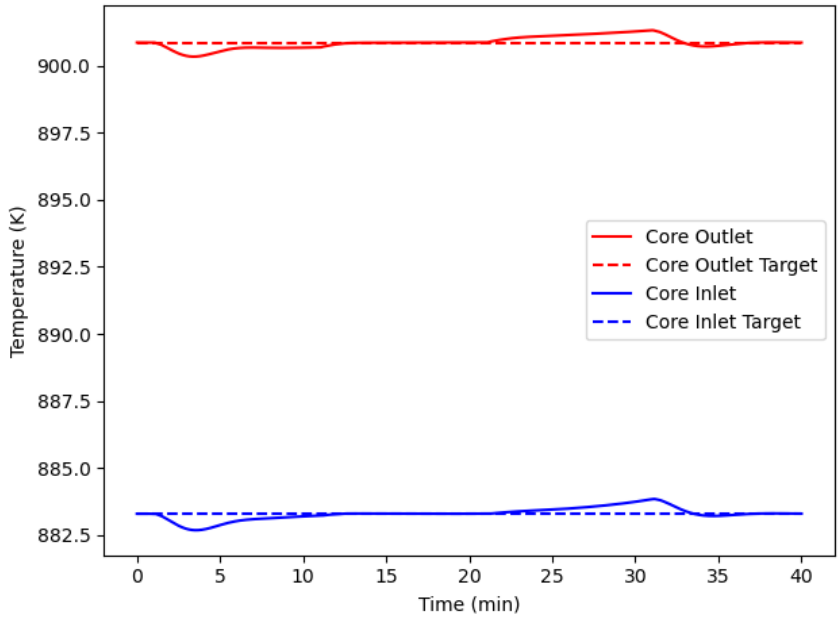

Figure 7.23: Core inlet and outlet temperature (solid), along with their target values (dashed), as a function of time.

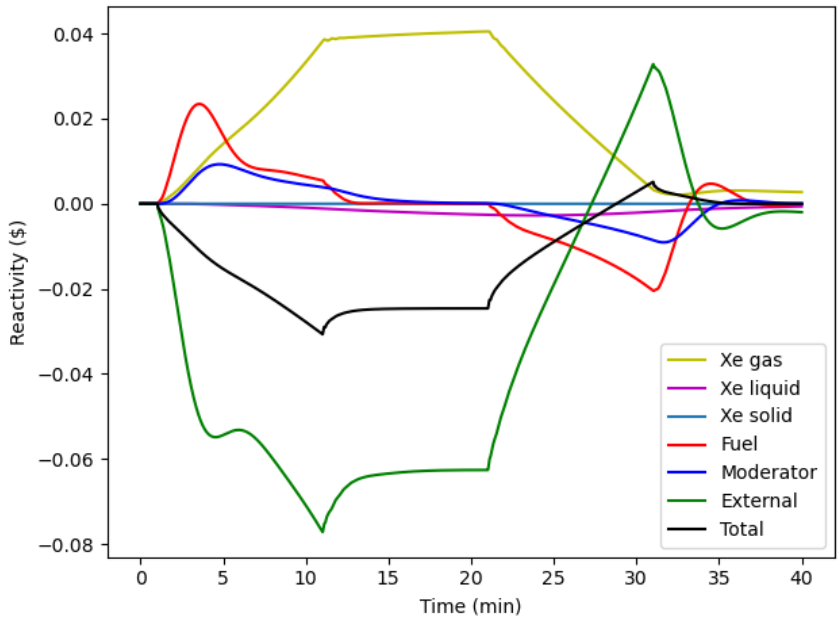

Figure 7.24: Reactivity feedback required for changing power levels.

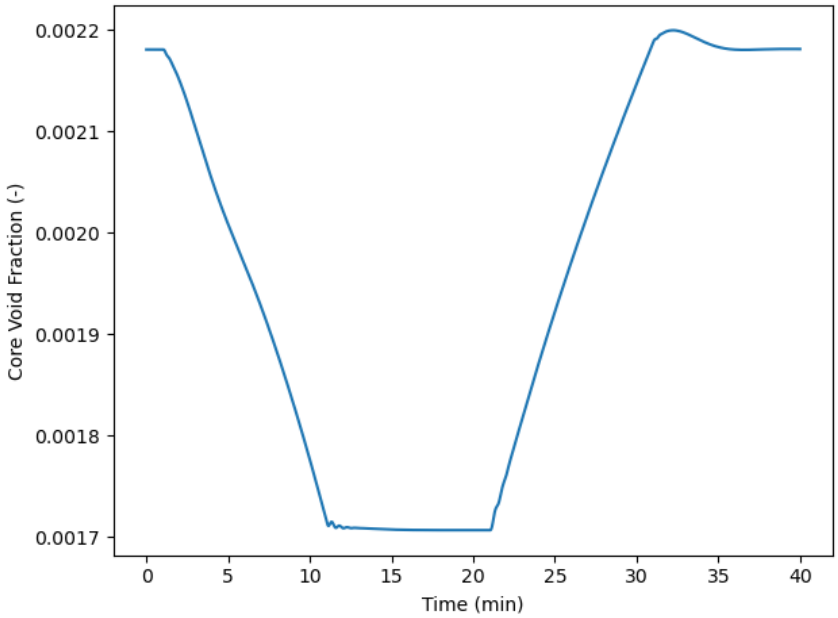

Figure 7.25: Total void within the core channel as a function of time.

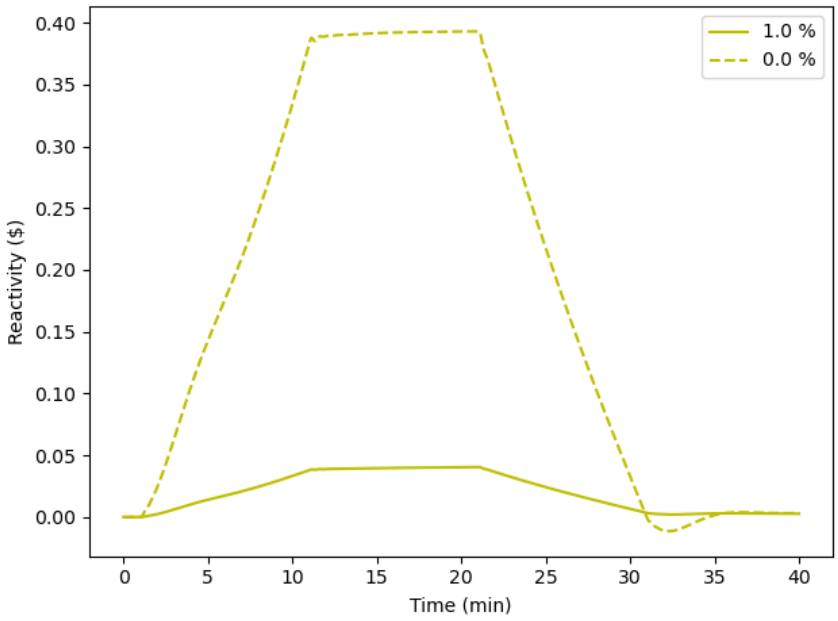

Figure 7.26: Impact of pump bowl stripping efficiency at nominal on the reactivity feedback from Xenon due to changing power and flow.

8 Summary

This report documents significant advancements in integrated multi-scale thermal-hydraulics modeling for MSRs through the coupling of the system-level SAM code with the engineering-scale Pronghorn solver via the Saline thermophysical property interface. These developments have notably enhanced the stability, robustness, and physical fidelity of coupled simulations by improving domain-overlapping coupling schemes and reformulating energy and scalar transport to better capture transient and buoyancy-driven phenomena. The expanded verification and validation efforts—including natural convection loops and the MSRE—demonstrate that the integrated tools can accurately predict complex flow, heat transfer, and fission product transport behaviors critical to MSR operation.

Improvements in Pronghorn's corrosion and noble-metal plating models, supported by refined turbulence closures and buoyancy corrections, provide more realistic predictions of material degradation patterns, directly impacting reactor component longevity and maintenance planning. The implementation of a multiphase Euler–Euler model enables detailed simulation of two-phase flows, such as gas entrainment and bubble dynamics, which are essential for understanding operational safety and performance in MSR components like pump bowls. Updates to SAM's species transport framework, including noble gas migration and reactivity feedback integration, allow for comprehensive modeling of fission product behavior and its influence on reactor kinetics, thereby enhancing predictive capabilities for transient scenarios and shutdown conditions.

The impact of this work is multifaceted: it strengthens the predictive accuracy and confidence in MSR design and safety analyses, supports potential licensing efforts by providing validated, physics-based tools, and facilitates optimization of reactor operations through improved understanding of coupled thermal-fluid and chemical processes. By bridging multiple length scales and physics domains, these integrated modeling capabilities enable reactor designers and analysts to identify key sensitivities and mitigate risks associated with corrosion, mass transfer, and reactivity feedback, ultimately contributing to the commercialization and safe deployment of advanced MSR technologies.

Future work will focus on further refining coupling algorithms to enhance numerical convergence and physical consistency, extending validation to canonical multiphase benchmarks and complex geometries, and advancing redox corrosion modeling by incorporating diffusion kinetics within structural materials. Additional efforts will improve the representation of gas-salt interactions, dynamic stripping efficiencies, and bubble transport near porous graphite moderators. Integration of high-fidelity CFD-derived closure correlations will continue to strengthen multi-length scale coupling, while enhancements to user interfaces and input frameworks aim to broaden accessibility and practical application of these tools across the MSR community.

ACKNOWLEDGEMENTS

This work is supported by the U.S. DOE Office of Nuclear Energy's Nuclear Energy Advanced Modeling and Simulation program, under Contract No. DE-AC02-06CH11357. The INL portion of this work is supported by the U.S. Department of Energy, under Contract DE-AC07-05ID14517. The ORNL portion of this work is supported by the U.S. Department of Energy, under Contract DE-AC05-00OR22725. Accordingly, the U.S. Government retains a non-exclusive, royalty-free license to publish or reproduce the published form of this contribution or to allow others to do so for U.S. Government purposes. The development, demonstration, and validation of the integrated MSR modeling capabilities were greatly aided by additional efforts, discussions, and inputs from many colleagues and collaborators, especially Tingzhou Fei and Haomin Yuan at Argonne National Laboratory, Huihua Yang and Wei Ji at Rensselaer Polytechnic Institute.

This research made use of the resources of the High Performance Computing Center at INL, which is supported by the Office of Nuclear Energy of the U.S. Department of Energy and the Nuclear Science User Facilities under Contract No. DE-AC07-05ID14517.

List of Acronyms

ANL Argonne National Laboratory. 3

BC boundary condition. 14, 15, 118, 119

BlueCRAB Blue Comprehensive Reactor Analysis Bundle. 14, 17, 19

DNP delayed neutron precursor. 22, 27, 30

DO Domain Overlapping. xii, 14–19, 30–32

DOFs Degrees of Freedom. 104, 105

EOS equation of state. 4, 102

HTGR High-Temperature Gas-Cooled Reactor. 105

INL Idaho National Laboratory. 2

LWR light-water reactor. 104

MSR molten salt reactor. iii, 1–3, 7, 12, 96, 97, 100, 132

MSRE molten salt reactor experiment. iii, vii, 3, 14, 19, 21–23, 25–27, 29–32, 88, 90, 106, 120, 123–125, 128, 132

MSTDB-TP Molten Salt Thermal Properties Database-Thermophysical. iii, 3, 4, 7, 12, 24

NEAMS Nuclear Energy Advanced Modeling and Simulation. iii, 1, 2

ORNL Oak Ridge National Laboratory. 21

PB-FHR Pebble Bed-Fluoride Salt Cooled High Temperature Reactor. 104, 105

SAM System Analysis Module. viii, 14–17, 19

SIMPLE Semi-Implicit Method for Pressure Linked Equations. 5, 6

REFERENCES

[1] R. Hu, J. Fang, D. Nunez, M. Tano, G. Giudicelli, and R. Salko, "Development of integrated thermal fluids modeling capability for msre," tech. rep., Argonne National Laboratory (ANL), Argonne, IL (United States), 08 2022.

[2] A. Huxford, V. C. Leite, E. Merzari, L. Zou, V. Petrov, and A. Manera, "A hybrid domain overlapping method for coupling system thermal hydraulics and cfd codes," *Annals of Nuclear Energy*, vol. 189, p. 109842, 2023.

[3] A. J. Novak, R. W. Carlsen, S. Schunert, P. Balestra, D. Reger, R. N. Slaybaugh, and R. C. Martineau, "Pronghorn: A multidimensional coarse-mesh application for advanced reactor thermal hydraulics," *Nuclear Technology*, vol. 207, no. 7, pp. 1015–1046, 2021.

[4] S. Schunert, G. L. Giudicelli, A. D. Lindsay, P. Balestra, S. Harper, R. Freile, M. Tano, and J. Ragusa, "Deployment of the finite volume method in pronghorn for gas and salt cooled pebble bed reactors," tech. rep., Idaho National Laboratory (INL), Idaho Falls, ID (United States), 06 2021.

[5] A. Lindsay, G. Giudicelli, P. German, J. Peterson, Y. Wang, R. Freile, D. Andrs, P. Balestra, M. Tano, R. Hu, L. Zou, D. Gaston, C. Permann, and S. Schunert, "Moose navier–stokes module," *SoftwareX*, vol. 23, p. 101503, 2023.

[6] R. Hu, L. Zou, D. O'Grady, T. Mui, Z. J. Ooi, G. Hu, E. Cervi, G. Yang, D. Andrs, A. Lindsay, C. Permann, R. Salko, Q. Zhou, L. Fick, A. Heald, and H. Zhao, "SAM: A Modern System Code for Advanced Non-LWR Safety Analysis," *Nuclear Technology*, vol. 211, no. 9, p. 1883–1902, 2024.

[7] R. Hu, L. Zou, T. Mui, D. O'Grady, E. Cervi, Z. J. Ooi, G. Yang, T. Fei, G. Hu, G. Zhang, *et al.*, "Sam theory manual," Tech. Rep. ANL/NSE-17/4 Rev.2, Argonne National Laboratory (ANL), Argonne, IL (United States), 04 2025.

[8] R. Hu, "Three-dimensional flow model development for thermal mixing and stratification modeling in reactor system transients analyses," *Nuclear Engineering and Design*, vol. 345, pp. 209–215, 2019.

[9] R. Hu and Y. Yu, "A computationally efficient method for full-core conjugate heat transfer modeling of sodium fast reactors," *Nuclear Engineering and Design*, vol. 308, pp. 182–193, 2016.

[10] L. Zou, T. Hua, Z. J. Ooi, J. Fang, and R. Hu, "Thermal fluid modeling approaches in sam for high temperature gas-cooled reactor applications," *Nuclear Technology*, vol. 211, no. 9, pp. 1903–1920, 2025.

[11] S. Henderson, C. Agca, J. W. McMurray, and R. A. Lefebvre, "Saline: An api for thermophysical properties," tech. rep., Oak Ridge National Laboratory (ORNL), Oak Ridge, TN (United States), 09 2021.

[12] G. Giudicelli, C. Green, J. Hansel, D. Andrs, A. Novak, S. Schunert, B. Spaude, S. Isaacs, M. Kunick, R. Salko, S. Henderson, L. Charlot, and A. Lindsay, "The moose fluid properties module," *Computer Physics Communications*, vol. 307, p. 109407, 2025.

[13] R. K. Salko, T. Mui, L. Zou, and R. Hu, "Implementation of a drift flux model into sam with development of a verification and validation test suite for modeling of noncondensable gas mixtures," *Nuclear Technology*, pp. 1–23, 2024.

[14] R. Hu, L. Zou, T. Mui, D. O'Grady, E. Cervi, Z. J. Ooi, G. Yang, T. Fei, G. Hu, G. Zhang, *et al.*, "Sam user's guide," Tech. Rep. ANL/NSE-19/18 Rev.2, Argonne National Laboratory (ANL), Argonne, IL (United States), 04 2025.

[15] P. German, L. Harbour, R. Freile, A. Chaube, M. Tano, H. Giudicelli, Guillaume Tran-Kieu, and J. Salazar, "Moose-based thermal hydraulics capability deployment, cfd solver enhancements," 09 2025.

[16] V. Leite, D. Reger, R. Freile, M. Tano, V. Kyriakopoulosm, and L. Charlot, "Bluecrab domain overlapping coupling: Theory & verification," 09 2025.

[17] S. Schunert, M. E. Tano Retamales, and M. K. Mohammad Jaradat, "Overlapping domain coupling of multidimensional and system codes in neams - pronghorn and sam," Tech. Rep. INL/RPT-23-72874, Idaho National Laboratory, 5 2023.

[18] Y. Zvirin, "A review of natural circulation loops in pressurized water reactors and other systems," *Nuclear Engineering and Design*, vol. 67, no. 2, pp. 203–225, 1982.

[19] V. Coppo Leite, D. Reger, M. E. Tano Retamales, M. Q. T. Yaseen, E. Merzari, and S. Schunert, "Multiscale overlapping domain coupling for thermal hydraulics simulations within the bluecrab code suite," vol. Volume 2: Computational Fluid Dynamics (CFDTC); Micro and Nano Fluid Dynamics (MNFDTC); Flow Visualization, 07 2025. To be published.

[20] D. Bertolotto, A. Manera, S. Frey, H.-M. Prasser, and R. Chawla, "Single-phase mixing studies by means of a directly coupled cfd/system-code tool," *Annals of Nuclear Energy*, vol. 36, no. 3, pp. 310–316, 2009. PHYSOR 2008.

[21] R. Robertson, "Msre design and operations report; part i. description of reactor design 1965," *ORNL-TM-728. https://doi. org/10.2172/4654707*.

[22] P. Pfahl, M. K. Jaradat, M. Tano, R. O. Freile, S. Walker, and J. Ortensi, "Comparison of spatial dynamics and point kinetics approaches in multiphysics modeling of the molten salt reactor experiment," *Frontiers in Nuclear Engineering*, vol. 4, p. 1617048, 2025.

[23] M. Jaradat and J. Ortensi, "Thermal spectrum molten salt-fueled reactor reference plant model," *Idaho National Laboratory*, vol. INL/RPT-23-72875, 07 2023.

[24] G. L. Giudicelli, A. Abou-Jaoude, A. J. Novak, A. Abdelhameed, P. Balestra, L. Charlot, J. Fang, B. Feng, T. Folk, R. Freile, T. Freyman, D. Gaston, L. Harbour, T. Hua, W. Jiang, N. Martin, Y. Miao, J. Miller, I. Naupa, D. O'Grady, D. Reger, E. Shemon, N. Stauff, M. Tano, S. Terlizzi, S. Walker, and C. Permann, "The virtual test bed (vtb) repository: A library of

reference reactor models using neams tools," *Nuclear Science and Engineering*, vol. 0, no. 0, pp. 1–17, 2023.

[25] C. Agca, K. E. Johnson, J. W. Mcmurray, J. A. Yingling, and T. M. Besmann, "Fy21 status report on the molten salt thermal properties database (mstdb) development," tech. rep., Oak Ridge National Laboratory (ORNL), Oak Ridge, TN (United States), 2021.

[26] Idaho National Laboratory, "Moltensaltpropnet," 2025. Accessed: 2025-08-23. Available at: https://github.com/idaholab/MoltenSaltPropnet.

[27] B. Prince, S. Ball, J. Engel, P. Haubenreich, and T. Kerlin, "Zero-power physics experiments on the molten-salt reactor experiment.," tech. rep., Oak Ridge National Lab.(ORNL), Oak Ridge, TN (United States), 1968.

[28] H. Mochizuki, "Verification of neutronics and thermal-hydraulics coupling method for fluent code using the msre pump startup, trip data," *Nuclear Engineering and Design*, vol. 378, p. 111191, 2021.

[29] R. C. Steffy, Jr., "Experimental dynamic analysis of the msre with *sup*233u fuel.," Tech. Rep. ORNL-TM-2997, Oak Ridge National Lab., Tenn., 12 1969.

[30] T. Fei, M. Stempniewicz, F. Bertocchi, V. Pathirana, T. Hua, R. Hu, and F. Roelofs, "Msr transient simulation and msre transient benchmark with sam and spectra," *Nuclear Technology*, vol. 211, no. 9, pp. 2088–2104, 2025.

[31] D. Walter, T. Cisneros, K. Wardle, J. Walter, and S. Findlay, "Mcre design description in support of external model development," Tech. Rep. MCRE-ENG-PRSNT-0029, TerraPower, 2022.

[32] A. Troshko and Y. Hassan, "Law of the wall for two-phase turbulent boundary layers," *International journal of heat and mass transfer*, vol. 44, no. 4, pp. 871–875, 2001.

[33] W. Yue, C.-L. Lin, and V. C. Patel, "Numerical simulation of unsteady multidimensional free surface motions by level set method," *International journal for numerical methods in fluids*, vol. 42, no. 8, pp. 853–884, 2003.

[34] R. K.-C. Chan and R. L. Street, "A computer study of finite-amplitude water waves," *Journal of computational physics*, vol. 6, no. 1, pp. 68–94, 1970.

[35] C. C. Mei, *The applied dynamics of ocean surface waves*, vol. 1. World scientific, 1989.

[36] J. Martin and W. Moyce, "An experimental study of the collapse of fluid columns on a rigid horizontal plane, in a medium of lower, but comparable, density. 5.," *Philosophical Transactions of the Royal Society of London Series A-Mathematical and Physical Sciences*, vol. 244, no. 882, pp. 325–334, 1952.

[37] S. Hosokawa and A. Tomiyama, "Bubble-induced pseudo turbulence in laminar pipe flows," *International journal of heat and fluid flow*, vol. 40, pp. 97–105, 2013.

[38] M. Kim, J. H. Lee, and H. Park, "Study of bubble-induced turbulence in upward laminar bubbly pipe flows measured with a two-phase particle image velocimetry," *Experiments in Fluids*, vol. 57, no. 4, p. 55, 2016.

[39] Y. Liao, K. Upadhyay, and F. Schlegel, "Eulerian-eulerian two-fluid model for laminar bubbly pipe flows: Validation of the baseline model," *Computers & Fluids*, vol. 202, p. 104496, 2020.

[40] T. Mui, D. O'Grady, L. Zou, R. Hu, and R. Salko, "Sam code improvements for molten salt reactor transient and species transport modeling," Tech. Rep. ANL/NSE-24/73, Argonne National Laboratory, 2024.

[41] W. Ji, H. Yang, Q. Cheng, M. H. Sahadath, S. Walker, L. Zou, T. Mui, and R. Hu, "Neup final report: Material transport model development and integration in the system analysis module (sam) code," Tech. Rep. 21-24078, Rennselaer Polytechnic Institute, 12 2024.

[42] R. Kedl and A. Houtzeel, "Development of a model for computing xe-135 migration in the msre," Tech. Rep. ORNL-4069, Oak Ridge National Laboratory, 6 1967.

[43] P. Hubenreich, J. Engel, B. Prince, and H. Claiborne, "Msre design and operationrs report part iii. nuclear analysis," Tech. Rep. ORNL-TM-730, Oak Ridge National Laboratory, 2 1964.

[44] T. Price and O. Chvala, "The transfer of xenon-135 to molten salt reactor graphite," *Journal of Nuclear Engineering and Radiation Science*, vol. 10, no. 4, p. 041001, 2024.

[45] A. Malinauskas, J. Rutherford, and R. Evans III, "Gas transport in msre moderator graphite i. review of theory and counterdiffusion experiments," Tech. Rep. ORNL-4148, Oak Ridge National Laboratory, 9 1967.

[46] J. Engel and R. Steffy, "Xenon behavior in the molten salt reactor experiment," Tech. Rep. ORNL-TM-3464, Oak Ridge National Laboratory, 10 1971.

[47] J. Chen and C. S. Brooks, "Modeling of transient and steady state xenon behavior in the molten salt reactor experiment," *Annals of Nuclear Energy*, vol. 204, p. 110525, 2024.

[48] J. Bockris and A. Reddy, *Modern Electrochemistry: Volume 1: Ionics*. Plenum Press, 1998.

[49] G. Watson, R. Evans III, W. Grimes, and N. Smith, "Solubility of noble gases in molten fluorides. in lif-bef2.," *Journal of Chemical and Engineering Data*, vol. 7, no. 2, pp. 285–287, 1962.

[50] R. K. Salko, T. Mui, L. Zou, and R. Hu, "Implementation of a drift flux model into sam with development of a verification and validation test suite for modeling of noncondensable gas mixtures," *Nuclear Technology*, vol. 211, no. 9, pp. 1937–1959, 2025.

[51] T. H. Chilton and A. P. Colburn, "Mass transfer (absorption) coefficients prediction from data on heat transfer and fluid friction," *Industrial & engineering chemistry*, vol. 26, no. 11, pp. 1183–1187, 1934.

[52] H. Yuan and N. Hoyt, "Moscato solver development and integration plan," Tech. Rep. ANL/NSE-21/66, Argonne National Laboratory (ANL), Argonne, IL (United States), 09 2021.

[53] H. Yuan and N. Hoyt, "Moscato development and integration in fiscal year 2023," Tech. Rep. ANL/NSE-23/50, Argonne National Laboratory (ANL), Argonne, IL (United States), 09 2023.

[54] P. Calderbank and M. Moo-Young, "The continuous phase heat and mass transfer properties of dispersions," *Chemical Engineering Science*, vol. 16, pp. 39–54, 1961.

[55] T. Kress, "Mass transfer between small bubbles and liquids in cocurrent turbulent pipeline flow (thesis)," Tech. Rep. ORNL-TM-3718, Oak Ridge National Laboratory, 4 1972.

[56] S. Shahbazi, T. Fei, J. Fang, Y. Jeong, M. Tano, R. de Oliveira, S. Walker, D. Hartanto, and E. Davidson, "Towards the development of molten salt reactor multiphysics modeling capabilities: Depletion, thermochemistry, reactor dynamics, and species tracking," Tech. Rep. ANL/NSE-24/62, Argonne National Laboratory (ANL), Argonne, IL (United States), 09 2024.

[57] W. Pinczewski and S. Sideman, "A model for mass (heat) transfer in turbulent tube flow. moderate and high schmidt (prandtl) numbers," *Chemical engineering science*, vol. 29, no. 9, pp. 1969–1976, 1974.

[58] A. Inayatov, "Correlation of Data on Heat Transfer Flow Parallel to Tube Bundles at Relative Tube Pitches of $1.1 < s/d < 1.6$," *Heat Transfer-Soviet Research*, vol. 7, pp. 84–88, 1975.

[59] N. Wakao, S. Kaguei, and T. Funazkri, "Effect of Fluid Dispersion Coefficients on Particle-to-fluid Heat Transfer Coefficients in Packed Beds: Correlation of Nusselt Numbers," *Chemical engineering science*, vol. 34, no. 3, pp. 325–336, 1979.

[60] S. A. Walker and W. Ji, "Species transport analysis of noble metal fission product transport, deposition, and extraction in the molten salt reactor experiment," *Annals of Nuclear Energy*, vol. 158, p. 108250, 2021.

[61] S. S. Raiman, J. M. Kurley, D. Sulejmanovic, A. Willoughby, S. Nelson, K. Mao, C. M. Parish, M. S. Greenwood, and B. A. Pint, "Corrosion of 316h stainless steel in flowing flinak salt," *Journal of Nuclear Materials*, vol. 561, p. 153551, 2022.

[62] R. Hu, L. Zou, T. Mui, D. J. O'Grady, G. Hu, S. Chen, and T. Jayasankar, "Sam assessment report," Tech. Rep. ANL/NSE-23/93, Argonne National Laboratory (ANL), Argonne, IL (United States), 11 2023.

[63] T. Mui, R. Hu, Q. Zhou, T. Hua, and L. Zou, "Species transport framework development in sam for system-level tritium source term analysis," *Nuclear Technology*, pp. 1–16, 2025.

[64] P. W. Humrickhouse and B. J. Merrill, "Vacuum permeator analysis for extraction of tritium from dcll blankets," *Fusion Science and Technology*, vol. 68, no. 2, pp. 295–302, 2015.

[65] R. Hu, G. Hu, M. Gorman, J. Fang, T. Mui, D. O'Grady, T. Fei, and R. Salko, "Sam developments for msr modeling (fy21)," Tech. Rep. ANL/NSE-21/74, Argonne National Laboratory (ANL), Argonne, IL (United States), 09 2021.

Nuclear Science & Engineering Division
Argonne National Laboratory
9700 South Cass Avenue
Argonne, IL 60439

www.anl.gov

Argonne National Laboratory is a U.S. Department of Energy
laboratory managed by UChicago Argonne, LLC